

JSCSEN 90(10) 1147-1284(2025)

ISSN 1820-7421(Online)

Journal of the Serbian Chemical Society

Electronic

VOLUME 90

No 10

BELGRADE 2025

Available on line at



www.shd.org.rs/JSCS/

The full search of JSCS
is available through

DOAJ DIRECTORY OF
OPEN ACCESS
JOURNALS
www.doaj.org

The **Journal of the Serbian Chemical Society** (formerly Glasnik Hemijskog društva Beograd), one volume (12 issues) per year, publishes articles from the fields of chemistry. The **Journal** is financially supported by the **Ministry of Education, Science and Technological Development of the Republic of Serbia**.

Articles published in the **Journal** are indexed in **Clarivate Analytics products: Science Citation Index-Expanded™** – accessed via **Web of Science®** and **Journal Citation Reports®**.

Impact Factor announced on 28 June, 2023: **1.000; 5-year Impact Factor: 1.100**.

Articles appearing in the **Journal** are also abstracted by: **Scopus**, **Chemical Abstracts Plus (CAplus™)**, **Directory of Open Access Journals**, **Referativni Zhurnal (VINITI)**, **RSC Analytical Abstracts**, **EuroPub**, **Pro Quest** and **Asian Digital Library**.

Publisher: **Serbian Chemical Society**, Karmegijeva 4/III, P. O. Box 36, 1120 Belgrade 35, Serbia
tel./fax: +381-11-3370-467, E-mails: **Society** – shd@shd.org.rs; **Journal** – jscs@shd.org.rs
Home Pages: **Society** – <http://www.shd.org.rs/>; **Journal** – <http://www.shd.org.rs/JSCS/>
Contents, Abstracts and full papers (from Vol 64, No. 1, 1999) are available in the

Internet Service:

Former Editors:

electronic form at the Web Site of the **Journal** (<http://www.shd.org.rs/JSCS/>).
Nikola A. Pušin (1930–1947), **Aleksandar M. Leko** (1948–1954), **Panta S. Tutundžić** (1955–1961), **Miloš K. Mladenović** (1962–1964), **Đorđe M. Dimitrijević** (1965–1969), **Aleksandar R. Despić** (1969–1975), **Slobodan V. Ribnikar** (1975–1985), **Dragutin M. Dražić** (1986–2006).

Editor-in-Chief:

Deputy Editor:

Sub editors:

Organic Chemistry

BRANISLAV Ž. NIKOLIĆ, Serbian Chemical Society (E-mail: jscs-ed@shd.org.rs)
DUŠAN SLADIĆ, Faculty of Chemistry, University of Belgrade

*Biochemistry and
Biotechnology*

Inorganic Chemistry

Theoretical Chemistry

DEJAN OPSENICA, Institute of Chemistry, Technology and Metallurgy, University of Belgrade

JÁNOS CSANÁDI, Faculty of Science, University of Novi Sad

OLGICA NEDIĆ, INEP – Institute for the Application of Nuclear Energy, University of Belgrade

BILJANA GLIŠIĆ, Faculty of Science, University of Kragujevac

MATUJA ZLATAR, Institute of Chemistry, Technology and Metallurgy, University of Belgrade

Physical Chemistry

Electrochemistry

Analytical Chemistry

Polymers

Thermodynamics

Chemical Engineering

MILOŠ MILIČIĆ, Faculty of Chemistry, University of Belgrade

LJILJANA DAMJANOVIĆ-VASILJIĆ, Faculty of Physical Chemistry, University of Belgrade

SNEŽANA GOJKOVIĆ, Faculty of Technology and Metallurgy, University of Belgrade

RADA BAOŠIĆ, Faculty of Chemistry, University of Belgrade

BRANKO DUNJIĆ, Faculty of Technology and Metallurgy, University of Belgrade

MIRJANA KIJEVCANIN, Faculty of Technology and Metallurgy, University of Belgrade

TATJANA KALUĐEROVIĆ RADOIČIĆ, Faculty of Technology and Metallurgy,

University of Belgrade

Materials

*Metallic Materials and
Metallurgy*

*Environmental and
Geochemistry*

*History of and
Education in Chemistry*

RADA PETROVIĆ, Faculty of Technology and Metallurgy, University of Belgrade

ANA KOSTOV, Mining and Metallurgy Institute Bor, University of Belgrade

VESNA ANTIĆ, Faculty of Agriculture, University of Belgrade

DRAGICA TRIVIĆ, Faculty of Chemistry, University of Belgrade

**English Language
Editors:**

LYNNE KATSIKAS, Serbian Chemical Society

VLATKA VAJS, Serbian Chemical Society

JASMINA NIKOLIĆ, Faculty of Technology and Metallurgy, University of Belgrade

Technical Editors:

VLADIMIR PANIĆ, Institute of Chemistry, Technology and Metallurgy, University of

Belgrade, **MARIO ZLATOVIĆ**, Faculty of Chemistry, University of Belgrade

**Journal Manager &
Web Master:**

MARIO ZLATOVIĆ, Faculty of Chemistry, University of Belgrade

Office:

VERA ČUŠIĆ, Serbian Chemical Society

Editorial Board

From abroad: **R. Adžić**, Brookhaven National Laboratory (USA); **A. Casini**, University of Groningen (The Netherlands); **G. Cobb**, Baylor University (USA); **D. Douglas**, University of British Columbia (Canada); **G. Inzelt**, Eötvös Loránd University (Hungary); **J. Kenny**, University of Perugia (Italy); **Ya. I. Korenman**, Voronezh Academy of Technology (Russian Federation); **M. D. Lechner**, University of Osnabrueck (Germany); **S. Macura**, Mayo Clinic (USA); **M. Spiteller**, INFU, Technical University Dortmund (Germany); **M. Stratakis**, University of Crete (Greece); **M. Swart**, University of Girona (Cataluna, Spain); **G. Vunjak-Novaković**, Columbia University (USA); **P. Worsfold**, University of Plymouth (UK); **J. Zagal**, Universidad de Santiago de Chile (Chile).

From Serbia: **B. Abramović**, **V. Antić**, **R. Baošić**, **V. Beškoski**, **J. Csanadi**, **Lj. Damjanović-Vasilić**, **A. Dekanski**, **V. Dondur**, **B. Dunjić**, **M. Đuran**, **B. Glišić**, **S. Gojković**, **I. Gutman**, **B. Jovančičević**, **I. Juranić**, **T. Kaluđerović**, **Radiočić**, **L. Katsikas**, **M. Kijevcanin**, **A. Kostov**, **V. Leovac**, **S. Milonjić**, **V.B. Mišković-Stanković**, **O. Nedić**, **B. Nikolić**, **J. Nikolić**, **D. Opsenica**, **V. Panić**, **M. Petkovska**, **R. Petrović**, **I. Popović**, **B. Radak**, **S. Ražić**, **D. Sladić**, **S. Sovilj**, **S. Šerbanović**, **B. Šolaja**, **Ž. Tešić**, **D. Trivić**, **V. Vajs**, **M. Zlatović**.

Subscription: The annual subscription rate is **150.00 €** including postage (surface mail) and handling. For Society members from abroad rate is **50.00 €**. For the proforma invoice with the instruction for bank payment contact the Society Office (E-mail: shd@shd.org.rs) or see JSCS Web Site: <http://www.shd.org.rs/JSCS/>, option Subscription.

Godišnja preplata: Za članove SHD: **2.500,00 RSD**, za penzionere i studente: **1000,00 RSD**, a za ostale: **3.500,00 RSD**; za organizacije i ustanove: **16.000,00 RSD**. Uplate se vrše na tekući račun Društva: **205-13815-62**, poziv na broj **320**, sa naznakom “preplata za JSCS”.

Nota: Radovi čiji su svi autori članovi SHD prioritarno se publikuju.

Odlukom Odbora za hemiju Republičkog fonda za nauku Srbije, br. 66788/1 od 22.11.1990. godine, koja je kasnije potvrđena odlukom Saveta Fonda, časopis je uvršten u kategoriju međunarodnih časopisa (**M-23**). Takođe, aktom Ministarstva za nauku i tehnologiju Republike Srbije, 413-00-247/2000-01 od 15.06.2000. godine, ovaj časopis je proglašen za publikaciju od posebnog interesa za nauku. **Impact Factor** časopisa objavljen 2024. godine je **0,700**, a petogodišnji **Impact Factor 0,900**. **Journal Citation Indicator** časopisa za period 2020–2024 je **0,16**.

CONTENTS*

Biochemistry and Bioengineering

- J. Z. Marinković, M. D. Jakovljević, I. Stanisavljević, M. Obradović, K. Mijačić, N. Gajović, B. Simović Marković, M. Jovanović, M. Živković, S. Rajković and M. Jurišević: DNA/bovine serum albumin interaction studies and immunomodulatory effects of dinuclear platinum(II) complex with aromatic 1,5-naphthyridine bridging ligand 1147

Inorganic Chemistry

- K. B. Sakhare, K. N. Sarwade, H. U. Joshi and M. A. Sakhare: Green route for efficient synthesis of metal complexes of 4-bromo-2-((E)-((2-hydroxyphenyl)imino)methyl)-6-((E)-(3-nitrophenyl)diazenyl)phenol and its anti-hyperglycemia, anticancer and antimicrobial assessment 1161

Theoretical Chemistry

- A. Laoud, A. Belafriekh and M. Alaqrbeh: N-Phenyl-3-sulfamoyl-benzamide derivatives as anti-Hepatitis B virus agent candidates. Integrated computational studies 1175

Physical Chemistry

- N. Mustafayeva, E. Zeynalov, A. Huseynov, Y. Nagiyev, M. Nadiri and M. Maharramova: Investigation of multi-walled carbon nanotubes catalytic activity by means of the model aerobic oxidation reaction 1189

Analytical Chemistry

- N. H. Sazali, M. Miskam, F. B. M. Suah and N. Y. Rahim: Optimization of deep eutectic solvent based liquid phase microextraction of PAHs in environmental samples using response surface methodology 1203

Chemical Engineering

- G. Akar Şen: Synthesis of zeolite LTA from kaolin and its model CBC and WAC performance: Optimized by central composite design 1223

Geochemistry

- E. Hukić, M. Kašanin-Grubin, M. Subašić, T. Tosti, S. Đogo-Mračević, S. Štrbac and S. Stojadinović: Impact of drying, freezing and re-wetting events soil leachate in acidic versus calcareous soils 1241

Environmental Chemistry

- L. Imas-Garay, E. de Carvalho Lourenço, F. Rubio, A. T. Toci and M. Boroski: Unified method for multiresidue pesticide analysis in corn and sediment 1253

History of and Education in Chemistry

- G. Özveren, B. Turan, M. Ulucan and C. Tosun: University students' scientific knowledge levels regarding chemical reaction arrows and electron arrows 1267

Published by the Serbian Chemical Society
Karnegijeva 4/III, P.O. Box 36, 11120 Belgrade, Serbia
Printed by the Faculty of Technology and Metallurgy
Karnegijeva 4, P.O. Box 35-03, 11120 Belgrade, Serbia

* For colored figures in this issue please see electronic version at the Journal Home Page:
<http://www.shd.org.rs/JSCS/>



DNA/bovine serum albumin interaction studies and immunomodulatory effects of dinuclear platinum(II) complex with aromatic 1,5-naphthyridine bridging ligand

JOVANA Z. MARINKOVIĆ¹, MIRJANA D. JAKOVLJEVIĆ¹, ISIDORA STANISAVLJEVIĆ¹, MILICA OBRADOVIĆ¹, KATARINA MIJAČIĆ¹, NEVENA GAJOVIĆ¹, BOJANA SIMOVIĆ MARKOVIĆ¹, MILAN JOVANOVIĆ², MARIJA ŽIVKOVIĆ^{3**}, SNEŽANA RAJKOVIĆ^{4*} and MILENA JURIŠEVIĆ^{1,3}

¹University of Kragujevac, Faculty of Medical Sciences, Center for Molecular Medicine and Stem Cell Research, Svetozara Markovića 69, 34000 Kragujevac, Serbia, ²Military Medical Academy, Department of Abdominal Surgery, Crnotravska 117, 11000 Belgrade, Serbia, ³University of Kragujevac, Faculty of Medical Sciences, Department of Pharmacy, Svetozara Markovića 69, 34000 Kragujevac, Serbia and ⁴University of Kragujevac, Faculty of Sciences, Department of Chemistry, Radoja Domanovića 12, 34000 Kragujevac, Serbia

(Received 11 April, revised 24 April, accepted 16 July 2025)

Abstract: The DNA and bovine serum albumin binding evaluation of the dinuclear platinum(II) complex, [$\{\text{PtCl}(\text{NH}_3)_2\}_2(\mu\text{-1,5-nphe})\](ClO_4)₂ (1,5-nphe is the bridging 1,5-naphthyridine ligand) was investigated by UV–Vis and fluorescence emission spectroscopy. Influence of platinum(II) complex on immune response was also estimated. Peritoneal splenocytes isolated from BALB/c mice were treated with Concanavalin A (ConA) and platinum(II) complex. Concentrations of IFN- γ , IL-1 β , IL-17, TNF- α and IL-10 were measured and immunophenotyping was performed. Results showed notable immunomodulatory effects. Pt(II) complex has an inhibitory effect on the release of proinflammatory cytokines in ConA activated splenocytes and CD3⁺ T cells.$

Keywords: immune response; splenocytes; cytokines; platinum(II) complex.

INTRODUCTION

In addition to the widely utilized platinum-based drugs in clinical practice for cancer treatment – cisplatin, carboplatin and oxaliplatin – there is a growing array of compounds still under various stages of development.^{1–3} These platinum Pt(II) complexes have been evolving significantly, and research has demonstrated that direct DNA binding, though historically considered the primary mechanism of

*,** Corresponding authors. E-mail: (*)snezana.rajkovic@pmf.kg.ac.rs;
(**)mzivkovic@kg.ac.rs
<https://doi.org/10.2298/JSC250411049M>

action, is just one of many pathways to achieve antitumor activity.^{4,5} This opens up exciting opportunities for new therapeutic strategies.

For instance, Pt-based complexes show potential as photosensitizers in photodynamic therapy, enabling precise targeting of cancer cells when exposed to specific wavelengths of light.^{6–8} Additionally, they show promise as immune modulators for chemoimmunotherapy, especially when used in combination with immunotherapeutic agents. Together, these approaches have the potential to enhance anticancer immune responses by synergistically integrating different mechanisms of action.⁶

Such complexes could play a pivotal role in triggering the release and presentation of tumour antigens, which in turn activates immune effectors. This activation may lead to remodelling of the tumour microenvironment (TME), making it less hospitable to cancer growth and increasing overall antitumor efficacy.⁶ The multifaceted nature of these complexes' activity makes them particularly appealing for combinatorial treatment approaches.

DNA molecules play a crucial role in regulating cellular functions, making them an excellent drug target, especially in cancer therapy. Reactive ligands can form covalent bonds with DNA or interact non-covalently through electrostatic forces, hydrogen bonding and π - π stacking.^{9,1} The primary binding modes include intercalation and minor-groove binding. Minor-groove binding offers higher DNA sequence selectivity and efficiency, targeting AT-rich regions, while intercalation affects DNA conformation and is often directed at GC-rich regions.^{9–12} Proteins frequently bind in the major groove, but their biological activity can be influenced by minor-groove binding drugs. Additionally, highly-charged polynuclear platinum(II) complexes represent a novel class of antitumor agents with unique DNA binding mechanisms, such as backbone tracking and groove spanning.¹³ The interaction between metal complexes and blood components, such as human serum albumin (HSA), can significantly affect their bioavailability and the activity of biomolecules. Bovine serum albumin (BSA) is frequently used in studies due to its structural similarity to HAS. Investigation of BSA–drug interactions is crucial for understanding of drug activity in organism.

Building on previous findings, where the cytotoxic effects of dinuclear Pt(II) complexes with 1,5-naphthyridine-bridging ligands were demonstrated *in vitro*,¹⁴ further exploration has been conducted to examine their immunomodulatory effects. The results suggest that these complexes not only show promising cytotoxic capacity but could also unlock novel immunotherapeutic avenues, paving the way for innovative cancer treatment paradigms. The interaction of [*cis*-{Pt(L)Cl}₂(μ -1,5-nphe)](ClO₄)₂ complex with calf thymus DNA (CT-DNA) and BSA were examined using UV–Vis absorption and fluorescence spectroscopy techniques.

EXPERIMENTAL

All chemicals and chemical methods used in this study are presented in the Supplementary material to this paper.

Isolation of splenocytes

In order to determinate the effects of Pt-complex on cytokine production by splenocytes derived from healthy BALB/c mouse, isolation of splenocytes was performed according to a previously published protocol.¹⁵ Prepared suspension of freshly isolated splenocytes in complete DMEM medium was placed in 96-well microtiter plate (2×10^5 cells in a well). Based on treatment, there were four groups: control group treated with complete Dulbecco's modified eagle medium (DMEM) medium (complemented with 10 % heat-inactivated fetal bovine serum (FBS), 1 mmol/L penicillin-streptomycin, 1 mmol/L mixed nonessential amino acids (Sigma), and 2 mmol/L L-glutamine) only, platinum(II) complex treated group, Concanavalin A (ConA) treated group (0.5 μ g/ml), and ConA and platinum-complex co-treated group. The concentration of the platinum(II) complex used in the experiment was based on its IC_{50} value determined in our previous study.¹⁴ Cells were incubated for 24 h and then their viability was assessed using the trypan blue assay, which confirmed that viability exceeded 90 % in each well, with no differences observed between the groups (data not shown).

Measurement of cytokine concentrations

Cytokine concentrations were measured in supernatants of the cells using Elisa assay kits from R&D Systems (Minneapolis, MN, USA) according to the manufacturer's instructions. Levels of following cytokines were measured: interferon- γ (IFN- γ), interleukins (IL) IL-1 β , IL-17, tumor necrosis factor- α (TNF- α) and IL-10. The data are presented as mean \pm standard error of the mean (SEM).

Flow cytometric analysis of splenocytes

After incubation period, cells were collected and stained with fluorochrome-labeled anti-mouse antibodies specific for CD3 (cluster of differentiation 3) and CD69. For intracellular staining, cells were stimulated with phorbol 12-myristate 13-acetate (PMA) (50ng/ml, Sigma–Aldrich), ionomycin (500 ng/ml, Sigma–Aldrich) and GolgiPlug (BD Pharmingen, NJ) for 4 h and labeled with fluorochrome-conjugated anti-mouse antibodies specific for TNF α , IFN- γ , IL-10, IL-1 β and IL-17. FACSCalibur flow cytometer was used (BD Biosciences, San Jose, CA, USA) and the data were analyzed using FlowJo software (Tree Star).

Statistical analysis

The data were analyzed using SPSS (version 23.0). All results were analyzed using Student's t-test or Mann–Whitney U test, where appropriate. Data are presented as mean \pm standard error of the mean and statistical significance was set at $p < 0.05$.

RESULTS AND DISCUSSION

Dinuclear [*cis*-{PtCl(NH₃)₂}₂(μ -1,5-nphe)](ClO₄)₂ complex, which contains the bridging ligand 1,5-nphe, was synthesized.¹⁴ Fig. 1 depicts the structural formula for the synthesized platinum(II) complex, while the NMR spectra of 1,5-nphe and complex are given in Figs. S2 and S3 (Supplementary material). The interactions of [*cis*-{PtCl(NH₃)₂}₂(μ -1,5-nphe)]²⁺ complex with DNA were investigated using UV–Vis and fluorescence spectroscopy. Additional studies were focused on the immunomodulatory effect of this complex.

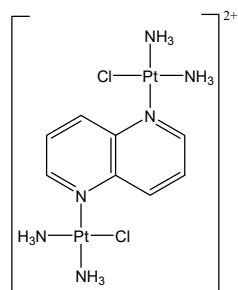


Fig. 1. Structural formula of $[cis-\{PtCl(NH_3)_2\}_2(\mu-1,5-nphe)]^{2+}$ complex.

Interactions of platinum(II) complex with CT-DNA

UV-Vis measurements. The UV-Vis spectra of the $[cis-\{PtCl(NH_3)_2\}_2(\mu-1,5-nphe)]^{2+}$ complex was recorded in the absence and presence of different concentrations of CT-DNA, $[Pt(II)]/[CT-DNA]$ in 0.0–1.6 range; Fig. 2A). Based on the UV-Vis spectroscopic data, it can be concluded that after the addition of CT-DNA to the solution of platinum(II) complex, a hyperchromic effect occurs, based on which it can be concluded that the complex interacts with CT-DNA. The intrinsic binding constant (K_b) was calculated based on the change in absorbance at 256 nm after the addition of CT-DNA according to the Eq. (S-1) of the Supplementary material and determined from the ratio of the slope of the line and the section on the y axis (Fig. 2A, Table I).

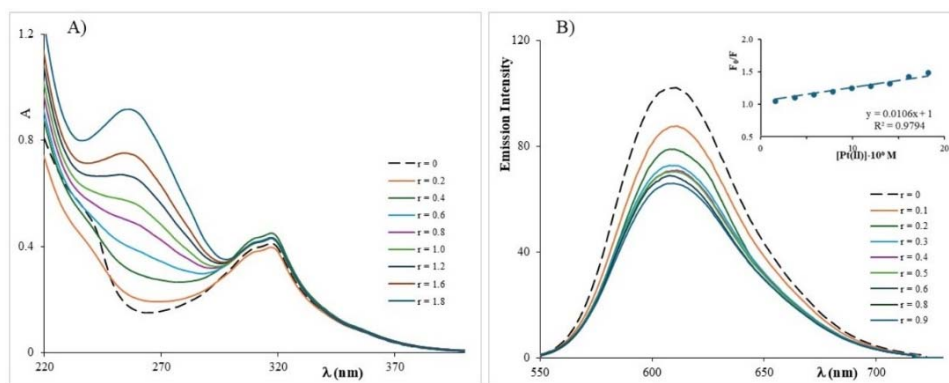


Fig. 2. A) UV-Vis spectra of the Pt(II) complex before and after addition of CT-DNA; B) emission spectra of CT-DNA/EB in the presence of Pt(II) complex (inset: plot of F_0/F versus $[Pt(II)]$; r is the mole ratio of Pt(II) and CT-DNA).

Based on the K_b value, it can be concluded that the studied Pt(II) complex, which has a rigid bridging 1,5-nphe ligand with CT-DNA achieves weak interactions. The negative value of the Gibbs energy indicate the spontaneity of the interactions of platinum(II) complex with CT-DNA (Table I). Based on the comparison of the K_b value of the tested complex with K_b of the classic intercalator

ethidium bromide (EB) for DNA, which is $1.23 \times 10^5 \text{ M}^{-1}$,¹⁶ it is clear that the K_b value obtained in experiments are lower (≈ 100 times) compared to K_b for EB, based on which it can be concluded that the interactions of the investigated complex is weaker compared to the interactions of EB. The assumption is that the examined complex with CT-DNA achieve interactions that are electrostatic in nature and are a consequence of the interaction of the positively charged complex cation (+2) and the negatively charged phosphate groups in CT-DNA.

TABLE I. Parameters obtained by investigating the reaction of Pt(II) complex with CT-DNA and BSA using UV-Vis and fluorescence measurements; $\%H = 100(A_\infty - A_0)/A_\infty$: hypochromism

Interaction	Method	Parameter	
CT-DNA	UV-Vis	K_b / M^{-1}	1.80×10^3
		$\Delta G_{298} / \text{kJ mol}^{-1}$	-19.30
	Fluorescence measurements (EB)	K_{sv} / M^{-1}	1.06×10^4
		K_a / M^{-1}	0.17×10^2
		n	0.3
	Fluorescence measurements (Hoe)	K_{sv} / M^{-1}	0.51×10^4
		K_a / M^{-1}	2.51×10^2
		n	0.5
BSA	UV-Vis	K_b / M^{-1}	7.30×10^3
		$\%H$	71.59
	Fluorescence measurements	K_{sv} / M^{-1}	1.72×10^4
		K_a / M^{-1}	1.70×10^4
		$k_q / \text{M}^{-1} \text{ s}^{-1}$	1.72×10^{12}
		n	1

Fluorescence spectroscopy. The interactions of Pt(II) complex with CT-DNA were investigated using emission fluorescence spectroscopy. Ethidium bromide (EB) acts as an intercalating agent by inserting itself between adjacent base pairs within the DNA double helix, resulting in strong fluorescence emission at 612 nm when excited at 527 nm, due to the formation of the CT-DNA/EB adduct. In contrast, Hoechst 33258 (Hoe) was used as a marker for minor groove binding, producing a fluorescent adduct that emits intensely at 486 nm upon excitation at 346 nm.¹⁷ Hence, the mode of interaction between the platinum(II) complex and CT-DNA can be assessed by monitoring changes in the fluorescence emission spectra of CT-DNA/EB and CT-DNA/Hoe adducts upon the incremental addition of the platinum(II) complex.

Fig. 2B shows the emission spectra of EB/CT-DNA in the presence of the Pt(II) complex. The addition of the Pt(II) complex solution leads to a decrease in the emission intensity at 612 nm, which indicates that there is a competitive reaction between EB and the examined Pt(II) complex in relation to CT-DNA. After the addition of the Pt(II) complex solution, the emission intensity at 612 nm decreases slightly, which indicates a very weak binding of the examined Pt(II) com-

plex to CT-DNA. The intensity of the interaction of the Pt(II) complex with CT-DNA was determined based on K_{SV} value obtained by using Eq. (S-2). The obtained results are shown graphically as the dependence of F_0/F on $[Pt(II)]$ (Fig. 2B). The Stern–Volmer constant was determined from the slope of the obtained line using the Eq. (S-2). The obtained value for K_{SV} , as well as for the stability constant (K_a), which was determined using Eq (S-3) (Table I), indicate that the tested complex is not good intercalator and that it has weak interaction with CT-DNA.

The DNA binding constant (K_a) of the investigated platinum(II) complex was found to be $0.17 \times 10^2 \text{ M}^{-1}$, which is significantly lower than that reported for a structurally related complex containing a 1,6-naphthyridine (1,6-nphe) ligand ($K_a = 5.3 \times 10^4 \text{ M}^{-1}$).¹⁸ This difference suggests that the position of the nitrogen atoms in aromatic naphthyridine ligands provide different interaction with DNA.¹⁷ In addition to the binding constant determined in this study, previously published molecular docking results provided further insight into the interaction between the complex and DNA, indicating that the binding is predominantly electrostatic in nature.¹⁴ This finding is consistent with the moderate binding constant observed experimentally and supports a non-intercalative binding mode.

The fluorescence emission spectra of the CT-DNA/Hoe in the absence and presence of increasing concentrations of the platinum(II) complex are shown in the Fig. S-4 of the Supplementary material. The gradual decrease in fluorescence intensity observed after adding the platinum(II) complex indicates its interaction with CT-DNA/Hoe. The obtained constant (K_a , Table I) values suggest that the studied complex is unable to effectively compete with the minor groove binding agent Hoe ($K_a \approx 1.4 \times 10^5 \text{ M}^{-1}$).¹⁹ Based on UV–Vis and fluorometric measurements, it can be concluded that the interactions between platinum(II) and CT-DNA occur from interactions between the positively charged complex ion and the negatively charged phosphate groups in DNA (electrostatic interactions).

Interactions of platinum(II) complex with BSA

UV–Vis spectroscopy. UV–Vis spectroscopy is applied to investigate conformational changes of proteins after their interaction with drugs or potential drugs.²⁰ In the UV–Vis spectrum of BSA a very strong absorption band in the 220–240 nm region can be observed. The absorption peak of lower intensity at 278 nm originates from the presence of aromatic amino acids (tryptophan, tyrosine and phenylalanine) in the BSA molecule.²¹ Therefore, this method is very sensitive to conformational changes of the BSA protein, as well as to changes in the microenvironment of aromatic amino acids. The UV–Vis spectra of BSA in the absence and presence of the Pt(II) complex are given in Fig. S-5A of the Supplementary material. After the addition of Pt(II) complex to the BSA solution, there is an increase in the absorption intensity at 278 nm, on the basis of which it can be concluded that the Pt(II) complex interact with BSA. These changes can be attributed to

electronic transitions of aromatic amino acids. In the examined reactions, a hyperchromic shift of the absorption maximum at 278 nm occurred. All this indicates that there are structural changes in BSA due to non-covalent interactions, which may be due to hydrogen bonding or electrostatic interactions.²² The value of the K_b was obtained on the basis of Eq. (S-4) (Table I) and calculated from the graphical dependence of $(A_\infty - A_0)/(A_x - A_0)$ on $1/[\text{Pt(II)}]$. Based on the obtained value of the constant, it can be concluded that the Pt(II) complex with BSA achieves strong interaction, which is a consequence of the presence of two condensed aromatic rings in the bridging 1,5-nphe ligand.

Fluorescence spectroscopy. The interactions of the Pt(II) complex with BSA were investigated using emission fluorescence spectroscopy. The solution of BSA gives intense fluorescent emission at $\lambda_{\text{em.max}} = 352$ nm, and when excited at 295 nm. After the addition of the Pt(II) complex to the BSA solution, it was observed that with increasing concentration of the complex, there is a decrease in fluorescence intensity (Fig. S-5B) indicating that complex interacts with this biomolecule. Changes in the emission spectra of BSA/Pt(II) complex indicate protein interactions with the complex, which lead to changes in the secondary structure of BSA.²³ Based on the decrease in BSA emission intensity with increasing concentrations of the Pt(II) complex, using the Eqs. (S5) and (S3) of the work, the following were determined: K_{sv} , k_q , K_a , as well as n (Table I). The average fluorescence time of BSA in the absence of the complex is $\tau_0 = 10^{-8}$ s, on the basis of which the fluorescence “quenching” rate constant (k_q , $\text{M}^{-1} \text{s}^{-1}$) was calculated. The K_{sv} and k_q values indicate that the tested complex can bind to BSA. The fluorescence quenching constant is greater than 10^{10} ($k_q > 10^{12} \text{ M}^{-1} \text{s}^{-1}$) indicating a static emission quenching mechanism.²⁴ The value of K_a and n were calculated based on Eq. (S3). Based on the K_a value, it can be concluded that Pt(II) complex can bind to BSA. The K_a value for the investigated complex is smaller compared to the K_a for avidin ($K_a = 10^{15} \text{ M}^{-1}$), which achieves the strongest non-covalent interactions with biomolecules, so the bond of the probe complex with BSA can be easily broken even before reaching the target site in the cell. Complex Pt(II) contains a 1,5-naphthyridine ligand with great steric hindrance resulting in weaker hydrogen bonding with BSA. The number of binding sites for Pt(II) is $n \approx 1$.

Lipid–water partition coefficient (log P). Drug lipophilicity represents a key pharmacokinetic parameter due to its crucial influence on the compound’s ability to traverse multiple layers of cells. Lipophilic drugs are typically associated with enhanced biological activity, faster metabolic processing and elimination, as well as stronger binding to plasma proteins.²⁵ The determined log P value of the investigated complex (log $P = -0.86$) indicates its hydrophilic nature. This result aligns well with previously reported data for similar platinum(II) complexes.²⁶ Incorporating aromatic, nitrogen-containing heterocyclic bridging ligands into the coordination environment of platinum(II) notably enhances the complex’s hydrophobicity.

Immunomodulatory effects

As the cytotoxic activities of the dinuclear Pt(II) complexes 1,5-naphthyrindine-bridging ligand were confirmed *in vitro*,¹⁴ we further examined the immunomodulatory effects of the complex with promising cytotoxic capacity.

First, cytokine production from splenocytes that were incubated for 24 h in medium only, medium with Pt(II) complex, ConA or co-stimulated with Pt(II) complex and ConA were analyzed (Fig. S-6A).

Treatment with Pt(II) complex significantly increased concentrations of IL-1 β ($p = 0.001$), IL-17 ($p = 0.004$), TNF- α ($p = 0.008$) and IL-10 ($p = 0.008$) compared to untreated splenocytes (Fig. S-6). ConA is an antigen-independent mitogen and leads to polyclonal proliferation and activation of T cells.²⁷ ConA significantly increased the concentration of proinflammatory cytokines IFN- γ ($p = 0.001$), IL-1 β ($p = 0.001$), IL-17 ($p = 0.001$), TNF- α ($p = 0.008$), and anti-inflammatory IL-10 ($p = 0.008$) in cell supernatants in comparison to untreated cells.

Co-stimulation of splenocytes with Pt(II) complex and ConA significantly reduced concentrations of IL-1 β ($p = 0.007$) and TNF- α ($p = 0.008$) compared to ConA. After Pt(II) complex and ConA co-treatment decreasing in concentrations of IFN- γ , IL-17 and IL-10 were also observed, but without statistical significance. Also, we observed ratios of cytokine production- Pt(II) complex/medium and Pt(II) complex + ConA/ConA (Fig. S-6). According to the results, the Pt(II) complex is more likely to exhibit its immunomodulatory effects on non-activated spleen cells, stimulating splenocytes to produce IL-1 β , IL-17, TNF- α and IL-10. *Vis-a-vis*, co-treatment with Pt(II) complex and ConA significantly reduced production of IL-1 β and TNF- α . IL-1 β is cytokine with strong inflammatory and immune-enhancing effects, mainly produced by leukocytes, especially monocytes and macrophages and plays a key role in inflammation, fever, and lymphocyte activation.²⁸ TNF- α cytokine is engaged in a promotion of inflammatory responses and is responsible for signaling events that lead to induction of apoptosis.²⁹ Beside inhibitory effect on the release of proinflammatory cytokines after ConA stimulation, it could be also concluded that immunomodulatory effects of Pt(II) complex were more prominent in non-activated cells, opening up the possibility that the investigated complex exerts effects on other splenocytes beside T cells. In order to determinate the relationship between proinflammatory and anti-inflammatory mediators in all groups we analyzed ratio of values of IFN- γ , IL-1 β , IL-17, TNF- α with values of IL-10 (Fig. 3). ConA significantly decreased the ratios of IFN- γ /IL-10 ($p = 0.001$), IL-17/IL-10 ($p = 0.001$) and TNF- α /IL-10 ($p = 0.001$) compared to medium (Fig. S-6A, C and D). Also, Pt(II) complex significantly decreased ratio of IFN- γ /IL-10 ($p = 0.001$), IL-1 β /IL-10 ($p = 0.002$), IL-17/IL-10 ($p = 0.001$) and TNF- α /IL-10 ($p = 0.001$) compared to medium. Co-treatment didn't significantly affect ratios of pro and anti-inflammatory cytokines compared to ConA. Based on these results Pt(II) complex could upregulate production of anti-inflammatory

cytokine IL-10. IL-10 is an anti-inflammatory cytokine that plays key role in limiting host immune response to pathogens.³⁰ IL-10 limits inflammation and enhances humoral immune responses. In IL-10-deficient mice, severe intestinal inflammation occurs, which can be alleviated by administering IL-10.³¹ Considering that IL-10 plays a key role in preventing inflammatory and autoimmune pathologies,³² results suggest that Pt(II) complex might have beneficial effects in treating autoimmune diseases.

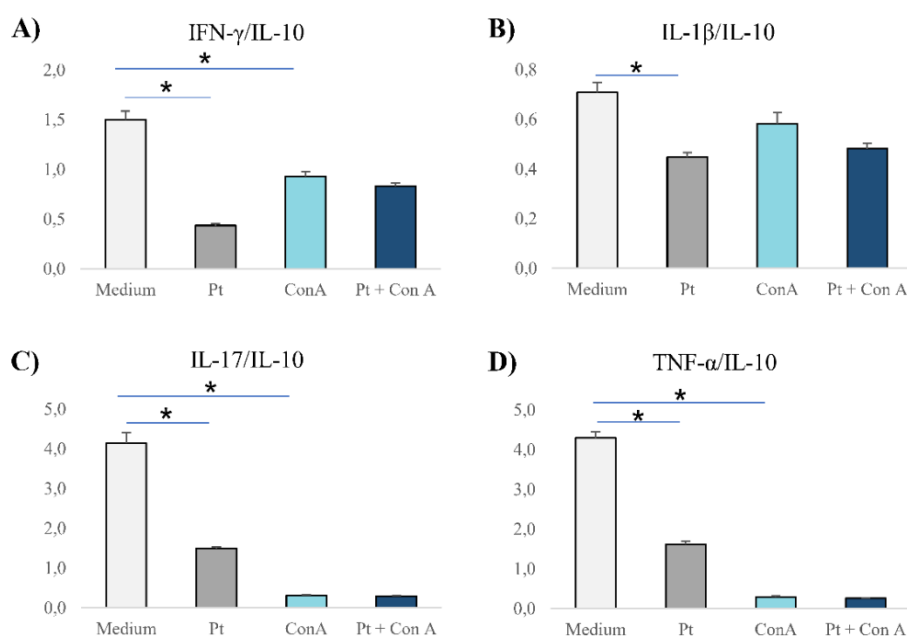


Fig. 3. Ratio of pro- and anti-inflammatory cytokine concentrations produced by splenocytes derived from healthy BALB/c mice after 24-h of incubation with DMEM medium only, Pt(II) complex, ConA, or a combination of Pt(II) complex and ConA. The data are shown as mean \pm SEM. Statistical significance was determined by student's *t*-test and Mann–Whitney U test, where appropriate (* $p < 0.05$).

With the intention of further understanding the immunomodulatory effects of Pt(II) complex, the functional phenotype of CD3⁺ splenocytes was analyzed using flow cytometry (Fig. 4A). CD3 complex is the subunit of T-cell receptor (TCR) and it's responsible for signal transduction necessary for activation of the T cells.³³ Activation and presence of CD3⁺ T lymphocytes is important prognostic factor for various types of cancer so potent immunomodulatory role of Pt(II) complex could contribute to its antitumor effects.^{33,34} ConA stimulation significantly increased the percentage of CD69⁺ ($p = 0.029$), IFN- γ ⁺ ($p = 0.001$), IL-1 β ⁺ ($p = 0.001$), IL-17⁺ ($p = 0.001$), TNF- α ⁺ ($p = 0.029$), IL-10⁺ ($p = 0.029$) CD3⁺ cells when compared to medium treated CD3⁺ cells. Cultivation with Pt(II) complex led to sig-

nificantly elevated percentage of CD69⁺ ($p = 0.029$), IFN- γ ⁺ ($p = 0.017$), IL-17⁺ ($p = 0.018$), TNF- α ⁺ ($p = 0.029$) CD3⁺ cells in comparison with medium treated CD3⁺ cells. CD69 is transmembrane type II C-lectin receptor and serves as an early indicator of lymphocyte activation. It is important for managing the differentiation of regulatory T cells (Tregs) and secretion of cytokines such as IFN- γ , IL-17 and IL-22.³⁵ It has been shown that increment of CD69⁺ T cells and significant increase in cytokines like: IFN- γ and TNF- α could be important for optimal anti-tumor response. Co-stimulation with Pt(II) complex and ConA significantly decreased percentage of CD69⁺ ($p = 0.029$), IFN- γ ⁺ ($p = 0.003$), IL-1 β ⁺ ($p = 0.002$), IL-17⁺ ($p = 0.001$) and TNF- α ⁺ ($p = 0.029$) CD3⁺ cells compared to ConA treated group. These results suggest that Pt(II) complex may reduce production of proinflammatory cytokines in previously ConA activated CD3⁺ splenocytes. Also, Pt(II) complex/medium and Pt(II) complex + ConA/ConA ratios of cytokine production by CD3⁺ splenocytes indicated that Pt(II) complex has pronounced effect in non-activated CD3⁺ splenocytes.

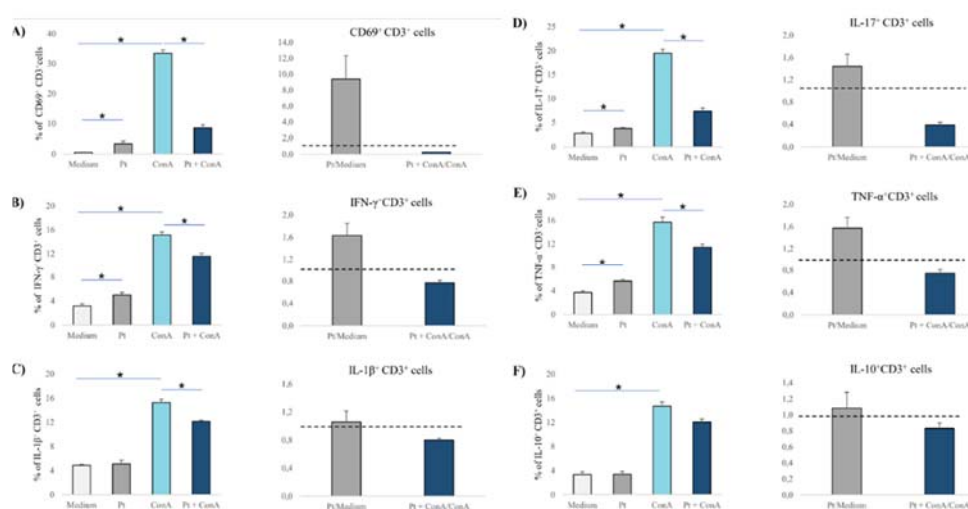


Fig. 4. Effects of Pt(II) complex on cytokine production of CD3⁺ splenocytes. The graphs show the percentage of CD3⁺CD69⁺ (A), CD3⁺IFN- γ ⁺ (B), CD3⁺IL-1 β ⁺ (C), CD3⁺IL17⁺ (D), CD3⁺TNF- α ⁺ (E) and CD3⁺IL-10⁺ (F) splenocytes derived from healthy BALB/c mice after 24-h of incubation with medium only, Pt(II) complex, ConA, or a combination of Pt(II) complex and ConA. Cytokine production ratios in splenocytes treated with Pt(II) complex/medium compared and treatment with Pt(II) complex + ConA/ConA were presented (A–F). The data are shown as mean \pm SEM. Statistical significance was determined by student's t-test and Mann–Whitney U test, where appropriate (* $p < 0.05$).

CONCLUSION

The DNA-binding evaluation of Pt(II) complex was carried out by UV–Vis and fluorescence emission spectroscopy. Electrostatic interactions between the positively charged platinum(II) complex and negatively charged DNA backbone could be detected based on a slight increase in the absorption intensity of the complex simultaneous with an increase in the concentration of CT-DNA. Further investigations were based on the immunomodulatory effect of this complex. Our study demonstrates that Pt(II) complex has an inhibitory effect on the release of proinflammatory cytokines in ConA activated splenocytes as well as CD3⁺ T cells derived from the spleens of BALB/c mice. Pronounced anti-inflammatory properties of Pt(II) complex may contribute to the confirmed antitumor effect, but also to illuminate the potential therapeutic effects in various inflammatory diseases, like multiple sclerosis, inflammatory bowel disease, Crohn's disease, systemic lupus erythematosus, gout and rheumatoid arthritis among others. Interestingly, significant immunomodulatory effects of Pt(II) complex were also expressed on previously non-activated splenocytes. Increases in cytokine production after incubation of splenocytes in the presence of the Pt(II) complex only insinuates that the complex might affect cytokine production patterns by other splenocytes except T cells. Further research is necessary in order to clarify the exact mechanism of action of this platinum(II) complex.

SUPPLEMENTARY MATERIAL

Additional data and information are available electronically at the pages of journal website: <https://www.shd-pub.org.rs/index.php/JSCS/article/view/13332>, or from the corresponding author on request.

Acknowledgements. This work was supported by the Ministry of Education, Science and Technological Development of the Republic of Serbia (Agreements No. 451-03-9/2021-14/200026; 451-03-9/2021-14/200122 and 451-03-9/2021-14/200111) and the Serbian Academy of Sciences and Arts under project No. F128. This research has also received funding from the Faculty of Medical Sciences, University of Kragujevac JP02/20.

ИЗВОД

ДНК/BSA ИНТЕРАКЦИЈЕ И ИМУНОМОДУЛАТОРНИ ЕФЕКТИ ДИНУКЛЕАРНОГ КОМПЛЕКСА ПЛАТИНЕ(II) СА АРОМАТИЧНИМ 1,5-НАФТИРИДИНСКИМ МОСТНИМ ЛИГАНДОМ

ЈОВАНА З. МАРИНКОВИЋ¹, МИРЈАНА Д. ЈАКОВЉЕВИЋ¹, ИСИДОРА СТАНИСАВЉЕВИЋ¹, МИЛИЦА ОБРДОВИЋ¹, КАТАРИНА МИЈАЧИЋ¹, НЕВЕНА ГАЈОВИЋ¹, БОЈАНА СИМОВИЋ МАРКОВИЋ¹, МИЛАН ЈОВАНОВИЋ², МАРИЈА ЖИВКОВИЋ³, СНЕЖАНА РАЈКОВИЋ⁴ и МИЛЕНА ЈУРИШЕВИЋ^{1,3}

¹Универзитет у Крајеву, Факултет медицинских наука, Центар за молекуларну медицину и истраживање матичних ћелија, Светозара Марковића 69, 34000 Крајевац, ²Војномедицинска академија, Одељење за абдоминалну хирургију, Црношавска 117, 11000 Београд, ³Универзитет у Крајеву, Факултет медицинских наука, Одсек за фармацију, Светозара Марковића 69, 34000 Крајевац и ⁴Универзитет у Крајеву, Природно-математички факултет, Одсек за хемију, Радоја Домановића 12, 34000 Крајевац

Евалуација интеракција динуклеарног платина(II) комплекса, $[cis-(PtCl(NH_3)_2)(\mu-1,5-nphe)](ClO_4)_2$ (1,5-nphe је мостни 1,5-нафтиридински лиганд) са ДНК и BSA испитивана је применом UV-Vis и флуоресцентне емисионе спектроскопије. Испитан је и утицај комплекса платине(II) на имунски одговор. Перитонеални спленоцити изоловани су из здравих мишева BALB/c соја и култивисани са конкавалином А (ConA) и платина(II) комплексом. Измерене су концентрације IFN- γ , IL-1 β , IL-17, TNF- α и IL-10 из добијених супернатанта и анализиран је фенотип култивисаних спленоцита. Резултати указују на имуномодулаторне ефекте испитиваног платина(II) комплекса. Платина(II) комплекс има инхибиторни ефекат на секрецију проинфламаторних цитокина у ConA активираним спленоцитима и CD3⁺ Т ћелијама.

(Примљено 11. априла, ревидирано 24. априла, прихваћено 16. јула 2025)

REFERENCES

1. C. Johnstone, K. Suntharalingam, S. J. Lippard, *Chem. Rev.* **116** (2016) 3436 (<https://doi.org/10.1021/acs.chemrev.5b00597>)
2. N. J. Wheate, S. Walker, G. E. Craig, R. Oun, *Dalton Trans.* **39** (2010) 8113 (<https://doi.org/10.1039/C0DT00292E>)
3. L. Kelland, *Nat. Rev. Cancer* **7** (2007) 573 (<https://doi.org/10.1038/nrc2167>)
4. E. R. Jamieson, S. J. Lippard, *Chem Rev.* **99** (1999) 2467 (<https://doi.org/10.1021/cr980421n>)
5. J. Reedijk, *Chem Rev.* **99** (1999) 2499 (<https://doi.org/10.1021/cr980422f>)
6. I. S. Mfouo-Tynga, L. D. Dias, N. M. Inada, C. Kurachi, *Photodiagnosis Photodyn. Ther.* **34** (2021) 102091 (<https://doi.org/10.1016/j.pdpdt.2020.102091>)
7. Z. F. Liu, H. Wang, Z. Zhang, *J. Inorg. Biochem.* **222** (2021) 111508 (<https://doi.org/10.1016/j.jinorgbio.2021.111508>)
8. Y. J. Wang, X. Shi, H. Fang, Z. Han, H. Yuan, Z. Zhu, L. Dong, Z. Guo, X. Wang, *J. Med. Chem.* **65** (2022) 7786 (<https://doi.org/10.1021/acs.jmedchem.2c00141>)
9. X. Han, X. Gao, *Curr. Med. Chem.* **8** (2001) 551 (<http://dx.doi.org/10.2174/0929867003373337>)
10. S. Neidle, C. M. Nunn, *Nature Prod. Rep.* **15** (1998) 1 (<https://doi.org/10.1039/A815001Y>)
11. G. Bischoff, S. Hoffmann, *Curr. Med. Chem.* **9** (2002) 312 (<https://doi.org/10.2174/0929867023371085>)

12. J. N. Lisgarten, M. Coll, J. Portugal, C. W. Wright, J. Aymami, *Nature Struct. Biol.* **9** (2002) 57 (<https://doi.org/10.1038/nsb729>)
13. N. Farrell, S. Spinelli, in *Uses of Inorganic Chemistry in Medicine*, N. Farrell, Ed., Royal Society of Chemistry, London, 1999, pp. 124–134 (<https://doi.org/10.1039/9781847552242-00124>)
14. B. Konovalov, M. D. Živković, J. Z. Milovanović, D. B. Djordjević, A. N. Arsenijević, I. R. Vasić, G. V. Janjić, A. Franich, D. Manojlović, S. Skrivanj, M. Z. Milovanović, M. I. Djuran, S. Rajković, *Dalton Trans.* **47** (2018) 15091 (<https://doi.org/10.1039/C8DT01946K>)
15. I. Stanisavljević, M. Živković, S. Rajković, M. Obradovic, M. Jurisevic, S. Pavlovic, B. Simovic Markovic, N. Gajovic, I. Corovic, M. Jovic, A. Kostic, I. Jovanovic, *Kragujevac J. Sci.* **46** (2024) 73 (<https://doi.org/10.5937/kgjsci2400003s>)
16. A. A. Recio Despaigne, J. G. Da Silva, P. R. da Costa, R. G. dos Santos, H. Beraldo, *Molecules* **19** (2014) 17202 (<https://doi.org/10.3390/molecules191117202>)
17. S. Dhar, M. Nethaji, A. R. Chakravarty, *J. Inorg. Biochem.* **99** (2005) 805 (<https://doi.org/10.1016/j.jinorgbio.2004.12.014>)
18. B. Konovalov, A. A. Franich, M. Jovanović, M. Jurisević, N. Gajović, M. Jovanović, N. Arsenijević, V. Maric, I. Jovanović, M.D. Živković, S. Rajković, *Appl. Organomet. Chem.* **35** (2021) e6112 (<https://doi.org/10.1002/aoc.6112>)
19. P. Smolenski, C. Pettinari, F. Marchetti, M. F. Guedes da Silva, G. Lupidi, G. V. Badillo Patzmay, D. Petrelli, L. A. Vitali, A. J. Pombeiro, *Inorg. Chem.* **54** (2015) 434 (<https://doi.org/10.1021/ic501855k>)
20. J. R. Lakowicz, *Principles of Fluorescence Spectroscopy*, Springer, New York, 2006 (e-ISBN-13: 978-0-387-46312-4)
21. M. Kumari, J. K. Maurya, U. K. Singh, A. B. Khan, M. Ali, P. Singh, R. Patel, *Spectrochim. Acta, A* **124** (2014) 349 (<https://doi.org/10.1016/j.saa.2014.01.012>)
22. P. Kumar, S. Gorai, M. K. Santra, B. Mondal, D. Manna, *Dalton Trans.* **41** (2012) 7573 (<https://doi.org/10.1039/C2DT30232B>)
23. M. Idowu, E. Lamprecht, T. Nyokong, *J. Photochem. Photobiol., A* **198** (2008) 7 (<https://doi.org/10.1016/j.jphotochem.2008.02.008>)
24. D. Čoćić, S. Jovanović, M. Nišavić, D. Baskić, D. Todorović, S. Popović, Ž. D. Bugarčić, B. Petrović, *J. Inorg. Biochem.* **175** (2017) 67 (<https://doi.org/10.1016/j.jinorgbio.2017.07.009>)
25. A. R. Timerbaev, C. G. Hartinger, S. S. Aleksenko, B. K. Keppler, *Chem. Rev.* **106** (2006) 2224 (<https://doi.org/10.1021/cr040704h>)
26. E. Rutkowska, K. Pajak, K. Jozwiak, *Acta Pol. Pharm.* **70** (2013) 3 (PMID: 23610954)
27. Y. Ando, C. Yasuoka, T. Mishima, T. Ikematsu, T. Uede, T. Matsunaga, M. Inobe, *In Vitro Cell. Dev. Biol.-Animal* **50** (2014) 313 (<https://doi.org/10.1007/s11626-013-9705-2>)
28. D. Boraschi, *Front. Immunol.* **13** (2022) 872155 (<https://doi.org/10.3389/fimmu.2022.872155>)
29. H. T. Idriss, J. H. Naismith, *Microsc. Res. Tech.* **50** (2000) 184 ([https://doi.org/10.1002/1097-0029\(20000801\)50:3<184::AID-JEMT2>3.0.CO;2-H](https://doi.org/10.1002/1097-0029(20000801)50:3<184::AID-JEMT2>3.0.CO;2-H))
30. A. Halimi, N. Mortazavi, A. Memarian, M. Zahedi, F. Niknejad, A. Sohrabi, S. J. Sarraf, *BMC Endocr. Disord.* **22** (2022) 296 (<https://doi.org/10.1186/s12902-022-01217-x>)
31. S. S. Iyer, G. Cheng, *Crit. Rev. Immunol.* **32** (2012) 23 (<https://doi.org/10.1615/critrevimmunol.v32.i1.30>)
32. S. Biswas, K. Bieber, R. A. Manz, *Front. Immunol.* **13** (2022) 970906 (<https://doi.org/10.3389/fimmu.2022.970906>)

33. A. P. Menon, B. Moreno, D. Meraviglia-Crivelli, F. Nonatelli, H. Villanueva, M. Barainka, A. Zheleva, H. M. van Santen, F. Pastor, *Cancers* **15** (2023) 1189 (<https://doi.org/10.3390/cancers15041189>)
34. N. Al-Rajhi, H. Soudy, S. A. Ahmed, T. Elhassan, S. F. Mohammed, H. A. Khoja, H. Ghebeh, *BMC Cancer* **20** (2020) 240 (<https://doi.org/10.1186/s12885-020-06757-w>)
35. D. Cibrián, F. Sánchez-Madrid, *Eur. J. Immunol.* **47** (2017) 946 (<https://doi.org/10.1002/eji.201646837>).



SUPPLEMENTARY MATERIAL TO
**DNA/bovine serum albumin interaction studies and
immunomodulatory effects of dinuclear platinum(II) complex
with aromatic 1,5-naphthyridine bridging ligand**

JOVANA Z. MARINKOVIĆ¹, MIRJANA D. JAKOVLJEVIĆ¹, ISIDORA
STANISAVLJEVIĆ¹, MILICA OBRADOVIĆ¹, KATARINA MIJAČIĆ¹, NEVENA
GAJOVIĆ¹, BOJANA SIMOVIĆ MARKOVIĆ¹, MILAN JOVANOVIĆ², MARIJA
ŽIVKOVIĆ^{3**}, SNEŽANA RAJKOVIĆ^{4*} and MILENA JURIŠEVIĆ^{1,3}

¹University of Kragujevac, Faculty of Medical Sciences, Center for Molecular Medicine and
Stem Cell Research, Svetozara Markovića 69, 34000 Kragujevac, Serbia, ²Military Medical
Academy, Department of Abdominal Surgery, Crnotravska 117, 11000 Belgrade, Serbia,
³University of Kragujevac, Faculty of Medical Sciences, Department of Pharmacy, Svetozara
Markovića 69, 34000 Kragujevac, Serbia and ⁴University of Kragujevac, Faculty of Sciences,
Department of Chemistry, Radoja Domanovića 12, 34000 Kragujevac, Serbia

J. Serb. Chem. Soc. 90 (10) (2025) 1147–1160

EXPERIMENTAL

Chemicals and methods

Commercially pure chemicals such as potassium tetrachloroplatinate(II) ($K_2[PtCl_4]$), 1,5-naphthyridine (1,5-nphe), calf thymus DNA(CT-DNA), ethidium bromide (EB), bisBenzimide (Hoechst 33258, Hoe), bovine serum albumin (BSA), phosphate-buffered saline (PBS, 10 mM, pH 7.40), deuterium oxide (D_2O), 1-octanol were purchased from the Sigma-Aldrich Chemical Co and used as received. All the other common chemicals were of reagent grade and used without purification. The platinum(II) complex, $[cis-\{PtCl(NH_3)_2(\mu-1,5-nphe)\}](ClO_4)_2$, was synthesized starting from the mononuclear $cis-[PtCl_2(NH_3)_2]$ complex and corresponding aromatic nitrogen-containing heterocyclic compound by following the literature reported methods.^{1,2} The stability of the platinum(II) complex in water and phosphate-buffered saline (PBS) was evaluated by monitoring changes in its UV-Vis absorption spectra over a 48 h at room temperature. Spectra were recorded in the 220–420 nm range using a PerkinElmer Lambda 35 spectrophotometer equipped with a thermostated 1.00 cm quartz cuvette. No changes were observed in the UV-Vis spectra of the studied complex (Fig. S1). Based on this, we concluded that the investigated Pt(II) complex remains stable in both water and phosphate-buffered saline (PBS) throughout the duration of the experiment. After dissolving the dinuclear platinum(II) complex in water, the UV-Vis spectra were acquired over the wavelength range of 200–600 nm using a Shimadzu double-beam spectrophotometer fitted with thermostated 1.00 cm quartz Suprasil cells. The Pt(II) complexes had a concentration of 50 μM . Fluorescence

*,** Corresponding authors. E-mail: (*)snezana.rajkovic@pmf.kg.ac.rs;
(**)mzivkovic@kg.ac.rs

measurements were performed using an RF-1501 PC spectrofluorometer (Shimadzu, Japan). The excitation and emission bandwidths were each 10 nm.

Interactions of dinuclear platinum(II) complex with CT-DNA

UV-Vis spectroscopy was used to study the interaction between the $[cis-\{PtCl(NH_3)_2\}_2(\mu-1,5-nphe)]^{2+}$ complex and CT-DNA. Based on these results, the Pt(II) complex's intrinsic binding constant (K_b) to CT-DNA was calculated. The UV-Vis measurements were performed using solutions prepared with a 10 mM phosphate buffer solution (pH = 7.4) and at 37 °C. An absorbance ratio of 1.8–1.9 at 260 and 280 nm (A_{260}/A_{280}) indicates that the CT-DNA was released from the protein part. The CT-DNA content was estimated using the UV absorbance at 260 nm and the extinction value $\varepsilon = 6600 \text{ M}^{-1}\text{cm}^{-1}$.³ The concentration of Pt(II) complex in Pt(II)/CT-DNA solution remained constant at 50.4 μM , whereas CT-DNA concentrations ranged from 10.1–80.7 μM . UV-Vis measurement was performed from 200 to 500 nm. The internal binding constants (K_b) were calculated using the equation:

$$\frac{[DNA]}{(\varepsilon_a - \varepsilon_f)} = \frac{[DNA]}{(\varepsilon_b - \varepsilon_f)} + \frac{1}{K_b}(\varepsilon_b - \varepsilon_f) \quad (\text{S-1})$$

where [DNA] are the concentration of CT-DNA, while ε_a and ε_b are the extinction coefficients of the free and bound complexes, respectively. The extinction coefficient ε_f is computed from a calibration curve that measures the absorption of the free complex at various concentrations. The results are visually represented as a dependence of $[DNK]/(\varepsilon_b - \varepsilon_f)$ on $[DNK]$. The slope of the resulting line is $1/(\varepsilon_b - \varepsilon_f)$, and the intercept on the y axis is $1/K_b (\varepsilon_b - \varepsilon_f)$. The Gibbs energy (ΔG) of the Pt(II)/CT-DNA complex was estimated using the equation: $\Delta G = -RT \ln K_b$.

Emission fluorescence spectroscopy was used to study the interaction between the Pt(II) complex and CT-DNA in the presence of ethidium bromide (EB) or bisBenzimide (Hoe). A solution of Pt(II) complex was added to the solution generated by mixing EB (or Hoe) CT-DNA in a 1:1 molar ratio, resulting in a concentration ratio of Pt(II) complex and CT-DNA ranging from 0.0 to 0.9. The above solutions were prepared using a 10 mM phosphate buffer solution (pH = 7.4). Emission spectra were recorded in the range of 550–750 nm for EB, with excitation at 527 nm and fluorescence emission observed at 612 nm.⁴ For Hoechst 33258 (Hoe), spectra were recorded from 360–600 nm, with excitation at 346 nm. The Stern-Volmer constant (K_{sv}) was calculated using the following equation:

$$\frac{F_0}{F} = 1 + K_{sv} \cdot [Pt(II)] \quad (\text{S-2})$$

where F_0 and F are the fluorescence intensities before and after adding the Pt(II) complex to the EB/CT-DNA solution, respectively. The obtained results can be shown visually as F_0/F versus $[Pt(II)]$. The Scatchard equation was used to determine the stability constant (K_a) and the number of binding sites (n).

$$\log \frac{(F_0 - F)}{F} = \log K_a + n \cdot \log [Pt(II)] \quad (\text{S-3})$$

The obtained results are shown graphically as the dependence of $\log(F_0 - F)/F$ on $\log[Pt(II)]$.

Interactions of dinuclear platinum(II) complex with bovine serum albumin

UV-Vis spectroscopy was employed to study the interactions between [Pt(II) complexes and BSA. The absorption spectra of BSA- Pt(II) complex were recorded in the 220–450 nm region, where the BSA concentration was constant (8 μ M) and the Pt(II) complex concentration ranged from 0 to 120 μ M. The binding constant (K_{app}) was determined using the Benesi-Hildebrand equation.⁵

$$\frac{(A_{\infty} - A_0)}{(A_x - A_0)} = 1 + \frac{1}{K_{app}} [Pt(II)] \quad (S-4)$$

where A_0 is the absorbance of BSA at 278 nm, A_x is the absorbance of BSA after addition of the complex at the same wavelength, A_{∞} is the absorbance of BSA fully bound to the Pt(II) complex.

Emission fluorescence spectroscopy was used to study the interactions between the Pt(II) complex and serum albumin obtained from bovine blood (BSA). Emission spectra were recorded in the 300–500 nm range, with extinction at 295 nm.⁶ The binding effect of the tested complex to BSA was observed based on the decrease in the emission intensity of albumin (8 μ M in 10 mM PBS) at 366 nm after the addition of the Pt(II) complex. The emission spectrum was collected under identical experimental conditions. The Stern-Volmer constant (K_{sv}) was determined employing the equation:

$$\frac{F_0}{F} = 1 + K_{SV} \cdot [Pt(II)] = 1 + k_q \cdot \tau_0 \cdot [Pt(II)] \quad (S-5)$$

where F_0 is the initial fluorescence intensity of tryptophan in BSA, F is the fluorescence intensity of tryptophan in BSA after addition of the Pt(II) complex into the protein solution, k_q is the fluorescence quenching constant, τ_0 is the average fluorescence time of albumin in the absence of the complex and $[Pt(II)]$ is the complex concentration. The binding constant (K_a) and the number of binding sites (n) were determined using equation S3.

Lipid–water partition coefficient (logP)

The lipophilicity of the investigated dinuclear platinum(II) complex was evaluated by determining the partition coefficient using the shake-flask method. The biphasic system consisted of 1-octanol and a 10 mM phosphate buffer (pH 7.4; 137 mM NaCl and 2.7 mM KCl). The absorbance of the platinum(II) complex in the aqueous phase was measured spectrophotometrically at his absorption maxima (A_{max} 309 nm). The concentration of each complex was calculated based on its previously determined molar extinction coefficient at the absorption maximum.

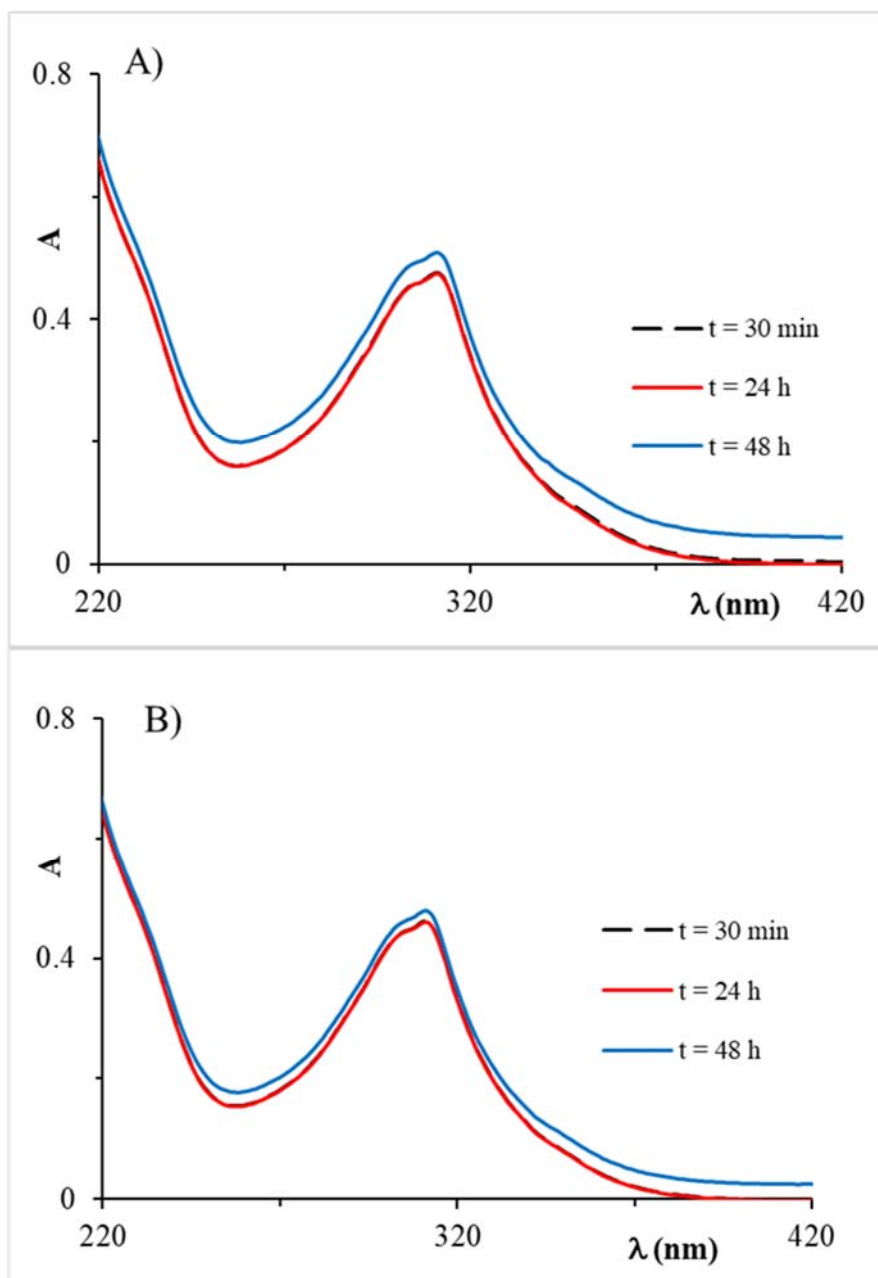


Fig. S-1. A) Stability of $[cis-\{PtCl(NH_3)_2(\mu-1,5-nphe)\}]^{2+}$ complexes followed by UV-Vis spectrophotometry in 0.01 M PBS at pH 7.40; B) Stability of $[cis-\{PtCl(NH_3)_2(\mu-1,5-nphe)\}]^{2+}$ complexes followed by UV-Vis spectrophotometry in H₂O. All measurements were performed at different time intervals and room temperature.

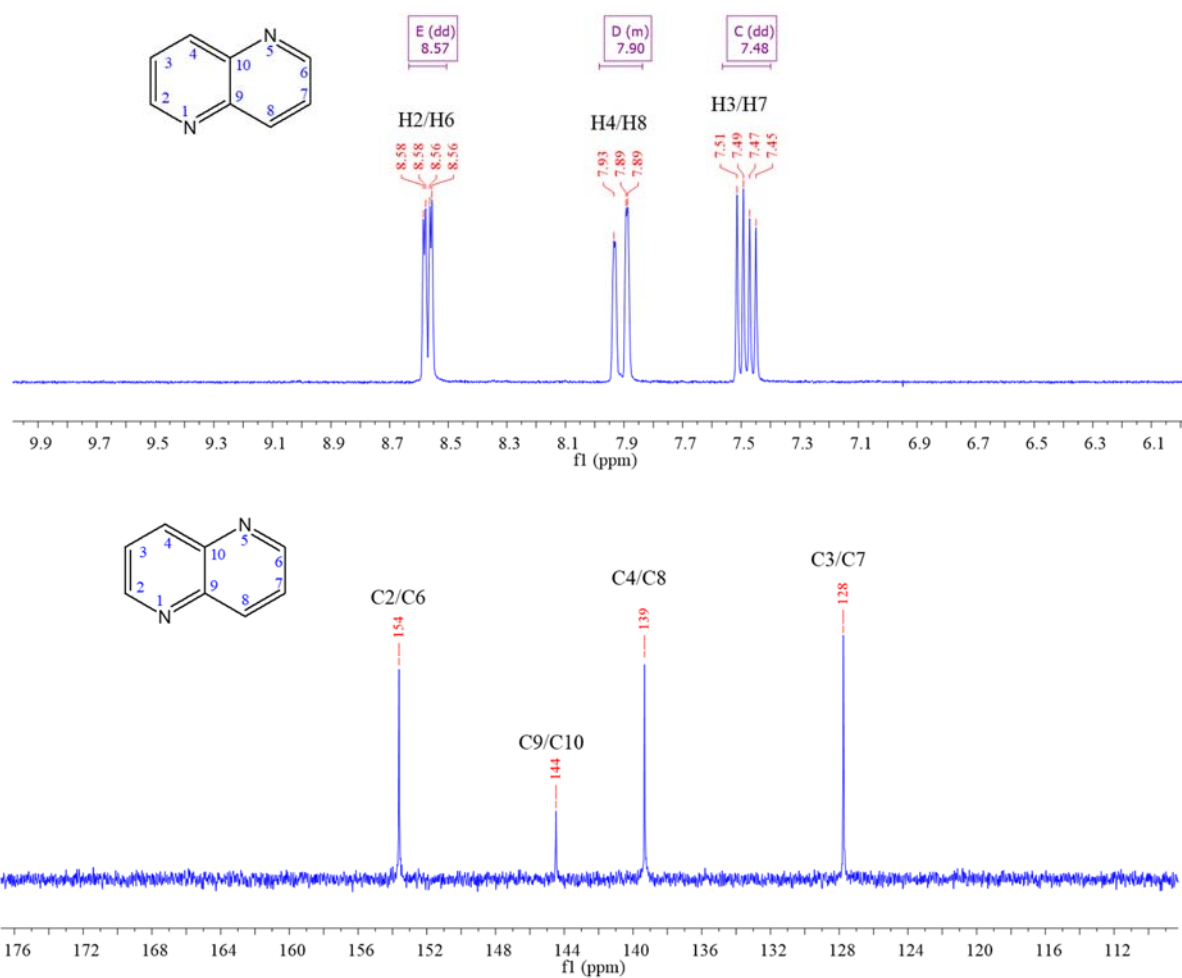


Fig. S-2. ^1H and ^{13}C NMR spectrum of 1,5-naphthyridine (200 MHz (^1H), 50 MHz (^{13}C), D_2O , 298 K).

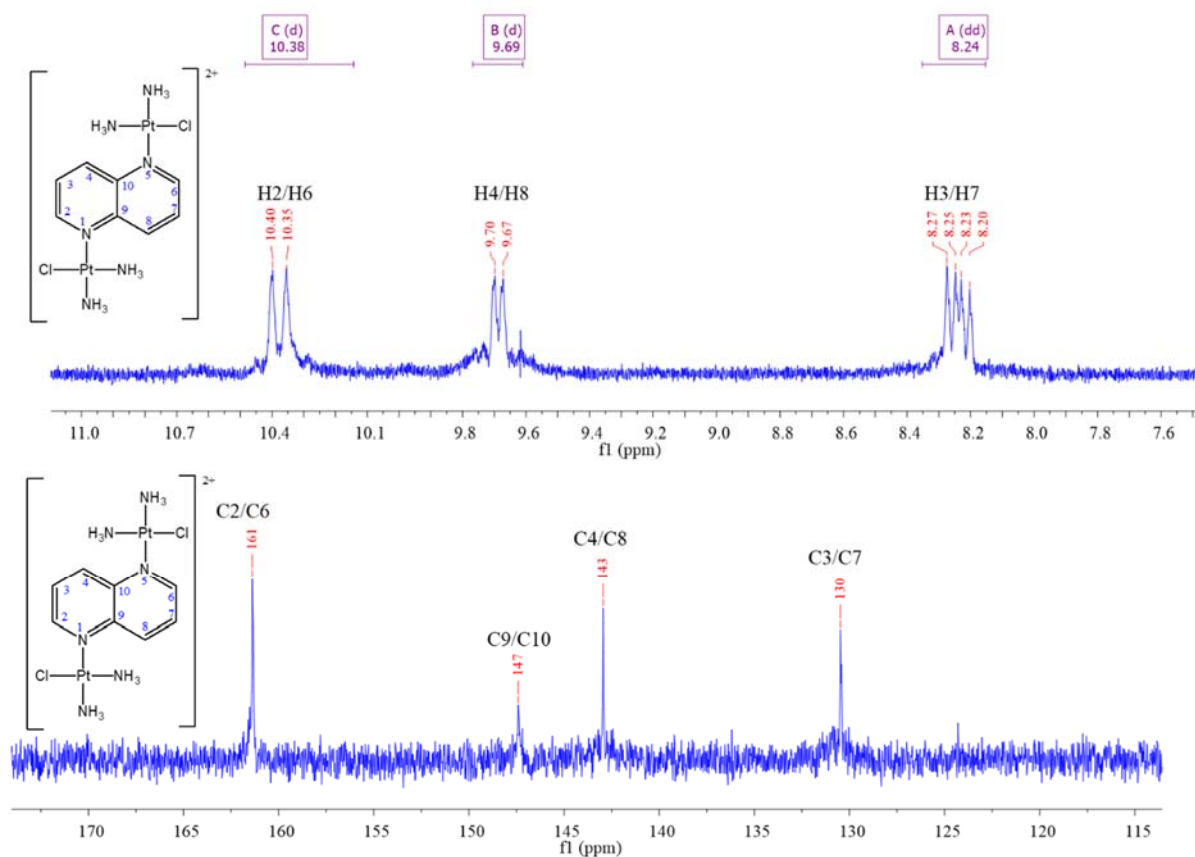


Fig. S-3. 1H and ^{13}C NMR spectrum of $[cis-\{PtCl(NH_3)_2\}(\mu-1,5-nphe)]^{2+}$ complex (200 MHz (1H), 50 MHz (^{13}C), D_2O , 298 K).

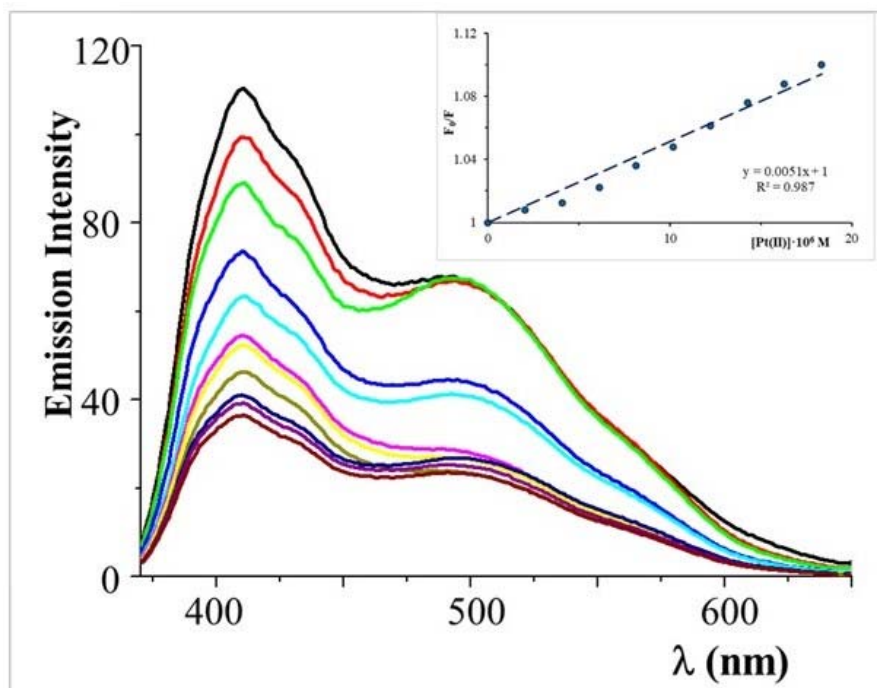


Fig. S-4. Emission spectra of CT-DNA/Hoe in the presence of Pt(II) complex (The inserted graph represents the Stern–Volmer plot of the F_0/F versus $[Pt(II)]$)

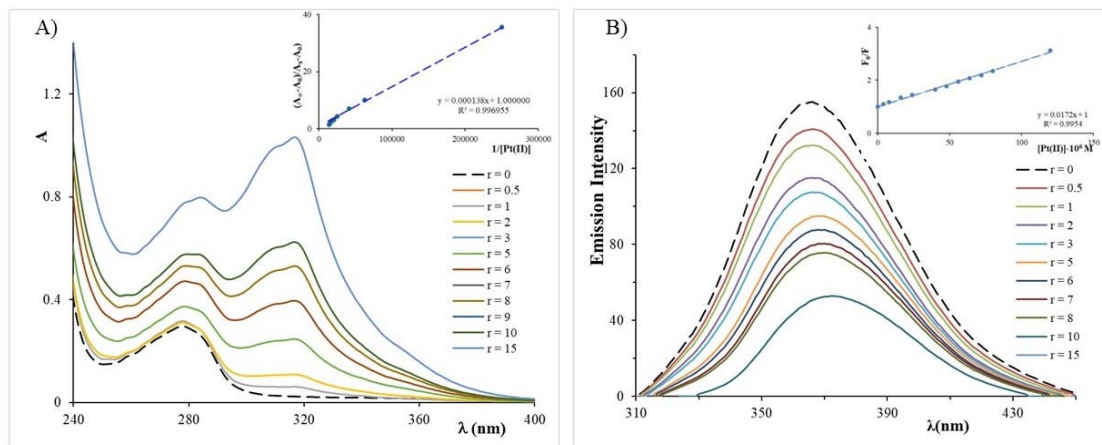


Fig. S-5. A) UV-Vis absorption of BSA in the presence of increasing concentrations of Pt(II) complex (Inset graph: Plot of $(A_\infty - A_0)/(A_x - A_0)$ versus $1/[Pt(II)]$); B) Emission spectra of BSA in the presence of Pt(II) complex (Inset graph: Plot of F_0/F versus $[Pt(II)]$).

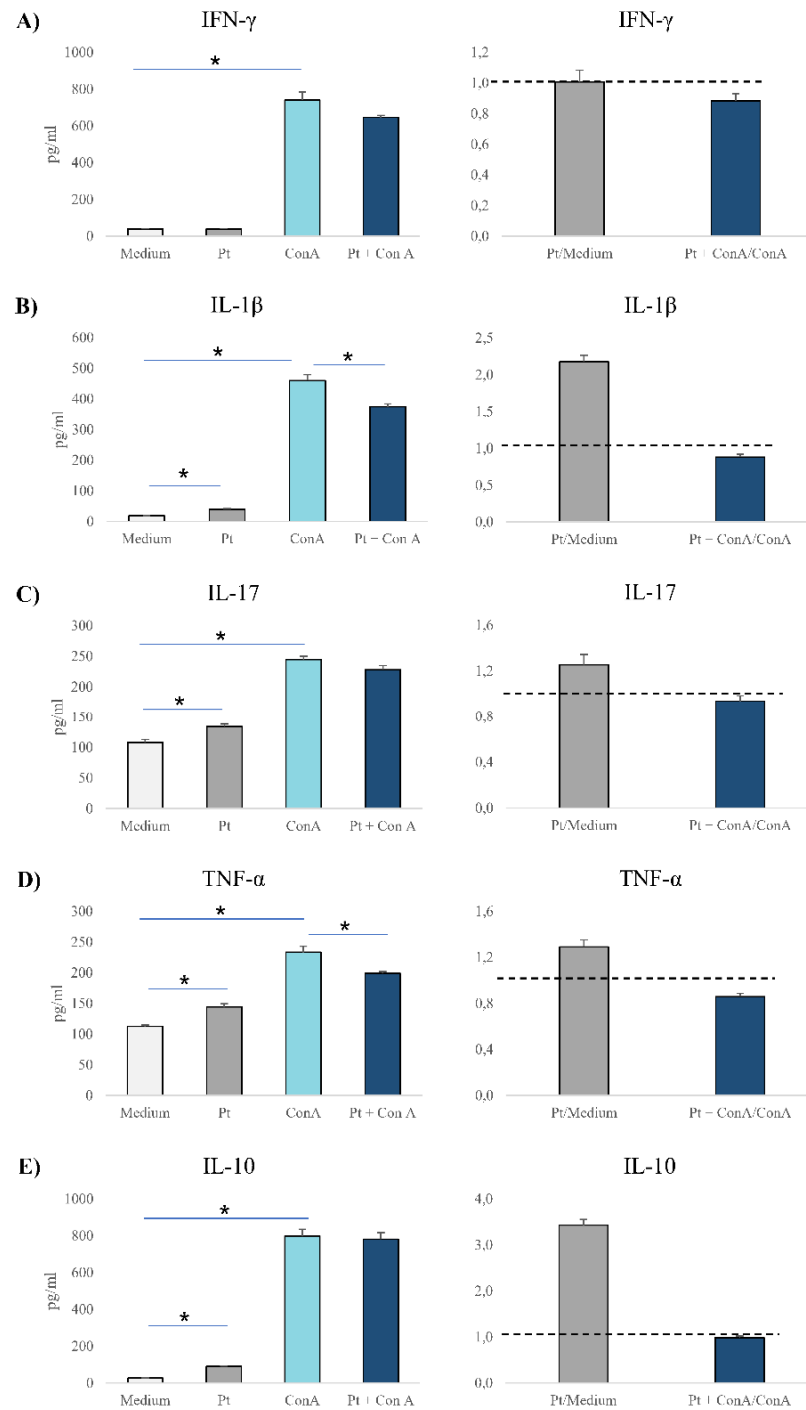


Fig. S-6. Impact of Pt(II) complex on cytokine production by splenocytes. The graphs show the concentration of IFN- γ (A), IL-1 β (B), IL-17 (C), TNF- α (D) and IL-10 (E) determined by ELISA in the supernatants of splenocytes derived from healthy BALB/C mice after 24-hours of incubation with DMEM medium only, Pt(II) complex, ConA, or a combination of Pt(II) complex and ConA. Cytokine production ratios in splenocytes -Pt(II) complex/medium and treatment with Pt(II) complex + ConA/ConA (A-E). The data are shown as mean \pm SEM. Statistical significance was determined by Student's t-test and Mann-Whitney U test, where appropriate (* $p < 0.05$).

REFERENCES

1. B. Konovalov, M. D. Živković, J. Z. Milovanović, D. B. Djordjević, A. N. Arsenijević, I. R. Vasić, G. V. Janjić, A. Franich, D. Manojlović, S. Skrivanj, M. Z. Milovanović, M. I. Djuran, S. Rajković, *Dalton Trans.* **47** (2018) 15091 (<https://doi.org/10.1039/C8DT01946K>)
2. S. C. Dhara, *Indian J. Chem.* **8** (1970) 193
3. F. Dimiza, F. Perdihi, V. Tangoulis, I. Turel, D. P. Kessissoglou, G. Psomas, *J. Inorg. Biochem.* **105** (2011) 476 (<https://doi.org/10.1016/j.jinorgbio.2011.10.014>)
4. M. Liu, W. Yuan, Q. Zhang, L. Yan, R. Yang, *Spectrochim. Acta Part A Mol. Biomol. Spectrosc.* **70** (2008) 1114 (<https://doi.org/10.1016/j.saa.2007.10.023>)
5. K. Sakthikumar, R. V. Solomon, J. D. Raja, *RSC Advances* **9** (2019) 14220 (<https://doi.org/10.1039/C8RA09218D>)
6. A. A. Franich, M. Živković, T. Ilić-Tomić, S. I. Đorđević, J. Nikodinović-Runić, A. Pavić, G. V. Janjić, S. Rajković, *J. Biol. Inorg. Chem.* **25** (2020) 395 (<https://doi.org/10.1007/s00775-020-01770-7>).



J. Serb. Chem. Soc. 90 (10) 1161–1173 (2025)
JSCS–5446

Green route for efficient synthesis of metal complexes of 4-bromo-2-((*E*)-((2-hydroxyphenyl)imino)methyl)-6-((*E*)-(3-nitrophenyl)diazenyl)phenol and its anti-hyperglycemia, anticancer and antimicrobial assessment

KULDEEP B. SAKHARE¹, KIRTI N. SARWADE¹, HANSARAJ U. JOSHI²
and MAHADEO A. SAKHARE^{1*}

¹Department of Chemistry, Balbhim Arts, Science & Commerce College, Beed, Maharashtra, India and ²Department of Chemistry, Swa. Sawarkar College, Beed, Maharashtra, India

(Received 8 April, revised 29 April, accepted 8 August 2025)

Abstract The world is battling cancer and diabetes, prompting global research into effective drugs. Studies show coordination compounds, especially substituted salicylaldehydes, exhibit strong biological activity, which increases when treated with amines. In the presented article, the preparation of metal complexes involving Mn(II), Co(II), Ni(II), Cu(II), Zn(II) and VO(II) was carried out using a Schiff base ligand that had been previously synthesized by grinding method of (*E*)-5-bromo-2-hydroxy-3-((3-nitrophenyl)diazenyl)benzaldehyde and 2-amino-phenol. The synthesized Schiff base ligand was confirmed by mass, ¹H-NMR and FT-IR spectra. The confirmation of the Schiff base ligand was followed by synthesis of metal complexes using metal salts of Mn(II), Co(II), Ni(II), Cu(II), Zn(II) and VO(II). The synthesized metal complexes were analyzed by elemental analysis, FT-IR and electronic spectra, thermal analysis, X-ray powder diffraction, molar conductivity, *etc.* In the course of the biological studies, anti-hyperglycaemia and anticancer assessments of Schiff base ligand and metal complexes were carried out by alpha amylase inhibition assay and MTT assay against standard reference drug acarbose and 5-fluorouracil (5-FU), respectively. The findings of the anti-hyperglycaemia suggest that Co(II) shows higher activity than other metals, whereas all metal complexes show more significant activity than free ligand. In the anticancer activity it is clear that Co(II) shows higher activity than other metal complexes; also, all metal complexes show higher activity than that of free ligand. In addition to this, the antimicrobial properties were examined against two Gram-positive bacterial strains (*Staphylococcus aureus* and *Bacillus subtilis*), two Gram-negative bacterial strains (*Klebsiella pneumoniae* and *Pseudo-*

*Corresponding author. E-mail: sakharema.chem@gmail.com
<https://doi.org/10.2298/JSC250408064S>

monas aeruginosa) and three fungal strains (*Penicillium chrysogenum*, *Trichoderma viride* and *Aspergillus niger*). From all the results and observations, it is clear that metal complexes exhibit better biological activity than Schiff base ligand.

Keywords: acarbose; 5-flourouracil; tetracycline; Schiff-base; anti-diabetic.

INTRODUCTION

The diseases, cancer and diabetes, have emerged as significant global health challenges, affecting population worldwide over the past three decades. Developing effective pharmaceutical interventions to combat these diseases presents a complex and critical task for researchers. Over the last two decades, coordination chemistry has gathered substantial scientific interest due to its extensive applications in the fields of biology and medicine. Schiff base ligands, when coordinated with transition metal ions, exhibit remarkable bioactive properties that amplify various pharmacological activities including anticancer,¹ antidiabetic,² antifungal,³ antibacterial,^{4–6} antioxidant,^{2,7} antiviral, antimalarial, antitumor, antituberculosis,⁸ anthelmintic, anti-HIV, antidiuretic, anti-inflammatory, antiprotozoal, anticonvulsant, analgesic, anti-Alzheimer's, anti-hypertensive, anti-ulcerative and other therapeutic functions. The versatility and efficacy of Schiff base metal complexes highlight their potential as promising candidates in drug discovery and development.^{9–21} The azomethine linkage, in the presence of oxygen, nitrogen and sulfur donor atoms, plays a critical role in enhancing biological properties and facilitating the coordination of metal complexes. The interaction of metal ions with such biologically active compounds can significantly augment their pharmacological efficacy.²² Green chemistry provides a sustainable alternative to traditional methods of drug molecule synthesis, emphasizing eco-friendly and non-toxic approaches. This methodology not only minimizes environmental hazards but also enhances reaction efficiency by reducing time consumption and achieving a product yield of 70–90 %. Furthermore, green chemistry promotes environmental sustainability by eliminating the use of harmful solvents and excessive energy consumption, aligning with the principles of resource conservation and ecological balance.

The Azo-Schiff base ligand has garnered significant scientific attention for its role in the formation of coordination compounds, as well as its broad spectrum of biological activities when complexed with metal ions. These activities include antibacterial, antifungal, anticonvulsant, antimalarial and anticancer properties.^{23–26} Previously, various types of Azo-Schiff base ligands, along with their metal complexes, have been effectively employed as catalysts in numerous organic reactions, such as the oxidation and reduction of both saturated and unsaturated compounds.^{27–29} Building on this foundation and after an extensive literature review, we synthesized the ligand 4-bromo-2-((*E*)-((2-hydroxyphenyl)imino)methyl)-6-

-((*E*)-(3-nitrophenyl)diazenyl)phenol using the azo aldehyde (*E*)-5-bromo-2-hydroxy-3-((3-nitrophenyl)diazenyl)benzaldehyde. The synthesis was accomplished *via* a green chemistry approach using a simple grinding method and was characterized through various spectroscopic techniques to confirm the structure of the products. Furthermore, we coordinated this ligand with transition metal salts to generate corresponding metal complexes.

These metal complexes, along with the ligand, were subjected to an array of biological assays, including antimicrobial, anticancer and anti-hyperglycemic evaluations, against standard drugs references. The results revealed that the metal complexes exhibit superior pharmacological potential compared to the Schiff base ligand alone when benchmarked against standard drugs.

EXPERIMENTAL

Material and methods

All the chemicals such as aldehyde (5-bromosalicylaldehyde), amines (2-aminophenol) were used as received from the Sigma Aldrich Private Limited. The various metal salts such as manganese (II), cobalt (II), nickel (II), copper (II) and zinc (II) acetate and vanadium (II) oxy-sulphate were procured from Sigma Aldrich and utilized without any further modifications. The solvents like ethyl alcohol, *n*-hexane, ethyl acetate, and petroleum ether were demanded from the local vendor and used after purification by distillation method. The reaction progress was periodically monitored using thin layer chromatography (TLC) with silica gel coated on aluminum foil. A mixture of *n*-hexane and ethyl acetate served as the mobile phase. The physical constant of the synthesized Schiff base ligand as well as metal complexes were taken on digital melting point instrument named as Optic Technology. The elemental analysis was carried out on Vario EL Cube. ¹H-NMR spectra were recorded on the instrument Bruker 400 MHz ¹H-NMR by using CDCl₃ solvent. The MALDI TOF-mass spectrum instrument was utilized for the observation of EI-MS spectrum of the Schiff base ligand. The Bruker Alpha T. FTIR spectrophotometer was used to obtain FTIR spectra of Schiff base ligand as well as metal complexes by utilizing potassium bromide disk. The electronic spectrum has been recorded on the instrument Perkin Elmer UV light level meter. To check the stability of synthesized metal complexes stability test was done by using TGA instrument in the nitrogen atmosphere. The instrument utilized powder X-ray diffraction analysis using the Rigaku-Japan Miniflex 600.

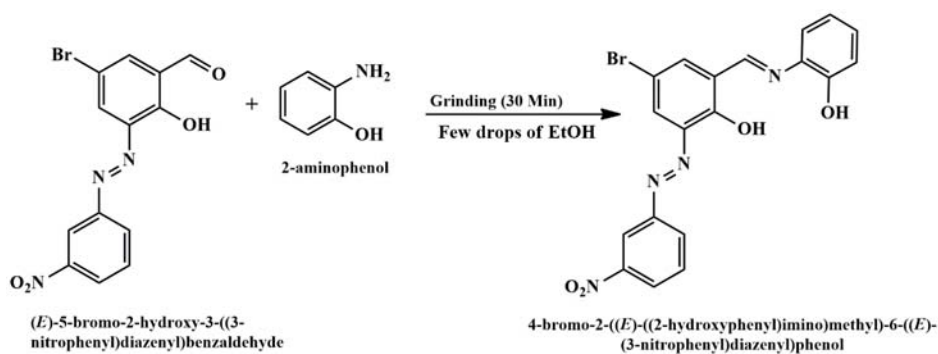
Synthesis of Schiff base ligand (L)

The Schiff base ligand B106 was synthesized by utilizing 3.501 g (0.01 mol) of (*E*)-5-bromo-2-hydroxy-3-((3-nitrophenyl)diazenyl)benzaldehyde and 1.090 g (0.01 mol) of 2-aminophenol ground with pestle in mortar at a ambient temperature for 30 min by adding few drops of ethyl alcohol (Scheme 1). The reaction progress was periodically tracked using thin layer chromatography (TLC). After the 30 min brown colored paste was obtained and poured in to crushed ice, the solid product observed. Filtration was used to separate this solid product. To obtain an analytically pure product with high yields, the material was vacuum-dried overnight using anhydrous CaCl₂.³⁰

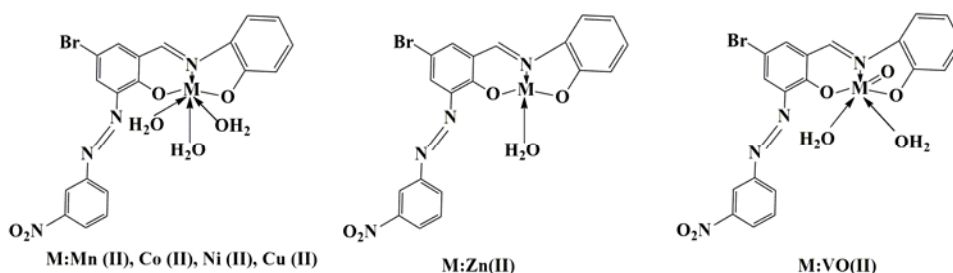
Synthesis of metal complex (M)

A mixture of 0.440 g (0.001 mol) of the Schiff base ligand B106 and 0.001 mol of metal acetate salts, including Mn (II), Co (II), Ni (II), Cu (II), Zn (II) and VO (II) sulfate, was ground together in a mortar with a pestle at ambient temperature for 40–45 min, few drops of ethanol

were added during the process of grinding for mixing the reactant (Scheme 2). Various coloured metal complexes formed.³⁰



Scheme 1. Synthesis of Schiff base ligand (L).



Scheme 2. Synthesis of metal complexes.

Anti-hyperglycemia assessment

The anti-hyperglycemia assessment of Schiff base ligand B106 and Mn (II), Co (II), Ni (II), Cu (II), Zn (II) and VO(II) complexes was done by utilizing amylase inhibition assay. For this study, 500 μ L of 0.1 M phosphate buffer solution having pH of 6.9 containing 0.5 % α -amylase enzyme was made first. The test sample of 500 μ L was taken and added in the above solution allowed to react and incubated for 10 min at 25 $^{\circ}$ C. After this 500 μ L of 1 % starch solution, extra pure 0.1 M phosphate buffer was mixed and placed in incubator for 10 min at 25 $^{\circ}$ C. The comparable procedure was conducted for the controls where 500 μ L of the enzyme were substituted with buffer. After incubation, 1000 μ L of DNS was transferred to both test and control samples. The drug acarbose was used as standard drug. The absorbance at 540 nm was recorded using a spectrophotometer, and the percentage inhibition of the α -amylase enzyme was determined using the specified formula:

$$\text{Inhibition (\%)} = \frac{\text{Abs}_{540}(\text{control}) - \text{Abs}_{540}(\text{extract})}{\text{Abs}_{540}(\text{control})} \times 100 \quad (1)$$

Anticancer activity

The MTT assay has been used to test of the anticancer assessment of the synthesized Schiff base ligand B106 along with the Mn (II), Co (II), Ni (II), Cu (II), Zn (II) and VO(II) complexes on the MCF-7 human breast cancer cell line. The growing cell line was incubated for 24 h in a

medium with 10 % FBS and L-glutamine at 37 °C, 5 % CO₂, 5 % air and 100 % relative humidity. The Mn (II), Co (II), Ni (II), Cu (II), Zn (II) and VO(II) complexes and ligand B106 were diluted in water to a maximum of 100 µg/mL and dissolved in to 1mg/mL of DMSO before being applied to the microtiter wells and placed in incubator for 48 h. After adding trichloroacetic acid (TCA) to finish the procedure, the cell line was fixed and incubated for an hour at 4 °C. 1 % acetic acid was used to create the MTT solution and after 20 min of incubation at room temperature, the unbound dye was removed. MCF-7 cells were seeded at a density of 5×10³ cells per well in a 96-well plate. 10 mM trizma base was used to elute the bound dye stain. The analysis was done on the different concentration such as 10, 40 and 100 µg/mL. A reference wavelength of 690 and 540 nm were used to measure absorbance and calculated by using following formula:

$$\text{Inhibition (\%)} = 100(\text{Control OD} - \text{Sample OD})/\text{Control OD} \quad (2)$$

Antimicrobial activity

The National Committee for Clinical Laboratory Standards (NCCLS) 2002 standards were followed for conducting the antimicrobial assessment using the agar disc diffusion method. In order to prepare McFarland turbidity standards, first sterilize the PDA+MHA mediums and autoclave them for the time of 15 min. Then added 0.5 mL of 1.175 % BaCl₂·2H₂O solutions to 99.5 mL of 0.18 mol/L sulfuric acid and stirring continuously. Standardized bacterial and fungal inoculums were swabbed onto Petri dishes containing MHA + PDA to initiate the inoculation process. After applying the sample to the inoculated agar plate, the plates have been then kept in an incubator that had been preheated to 30 °C. Each plate was carefully inspected after 24 h and we discovered that the inhibition zone was uniformly round with a lawn of growth. We were able to measure the inhibition zone diameter with our unaided eyes. Sliding callipers are used to measure the zones in mm on the reverse side of a petri dish.

RESULTS AND DISCUSSION

Sophisticated techniques such as mass spectrometry, ¹H-NMR and FTIR were employed to analyze the synthesized Schiff base ligand and its associated complexes labeled A1 through A6 (A1 = Mn (II), A2 = Co (II), A3 = Ni (II), A4 = Cu (II), A5 = Zn (II), A6 = VO(II)). For biological assessments, including anti-hyperglycemia, anticancer and antimicrobial assessment, various instruments were utilized. The Schiff base ligand B106 along with its complexes A1 to A6 exhibits a range of distinct colors. The A1–A6 complexes are not soluble in water, ethyl alcohol and methyl alcohol but are soluble in various organic solvents including chloroform, dimethylsulfoxide and dimethylformamide.

Physical and spectral data

Physical and spectral data are given in Supplementary material to this paper.

Spectroscopic analysis

Mass spectra of Schiff base ligand B106. The mass spectrometry analysis reveals molecular ion peaks at *m/z* 440.34, 441.15 (M+1) and 443.15 (M+3). These peaks are attributed to the successful formation of Schiff base ligand B106 as shown in Fig. S-1 of the Supplementary material.

¹H-NMR of Schiff base ligand B106. The ¹H-NMR of Schiff base ligand B106 was recorded in CDCl₃ solvent. The spectrum revealed the important signal, the signal at 8.65 ppm attributed to imine proton (HC=N-). Peaks found at 12.37 and 5.72 ppm, which correspond to the phenolic-OH groups are observed within the salicylaldehyde and amine moiety. Peaks observed at 6.94–7.58 ppm attributed to presence of proton of aromatic ring³¹ as shown in Fig. S-2 of the Supplementary material.

IR spectra of Schiff base ligand B106 and A1–A6 complexes. The imine group (>C=N-) in the Schiff base ligand B106 exhibited a band at 1619 cm⁻¹ which shifted to lower frequencies ranging between 1580–1615 cm⁻¹ in the A1–A6 complexes. This change is attributed to the metal ion and nitrogen of the Schiff base ligand B106 in the coordination and resulting in the formation of complexes.³² The band of phenolic-OH group was found at 3432 and 3502 cm⁻¹, this band disappeared in all A1–A6 complex indicating that the phenolic oxygen atom coordinated by deprotonation and this was further corroborated by the IR spectra of the Schiff base ligand B106, where the >C–O band observed at 1271 cm⁻¹ shifted to higher frequencies ranging from 1275 to 1292 cm⁻¹ in all A1–A6 complexes.^{33,34} The >C–Br band was found at 742–747 cm⁻¹. The band of azo group (–N=N–) was found at 1368–1381 cm⁻¹. The –OH rocking band found at 821–828 cm⁻¹ suggests that all A1–A6 complexes contain coordinated water molecule.³⁵ According to overall data, Schiff base ligand chelated to the central metal ion by tridentate manner as shown in Figs. S-3–S-9 of the Supplementary material.

UV–Vis spectra, magnetic susceptibility of A1–A6 complexes

The UV–Vis spectra of A1–A6 complexes are presented in the Figs. S-10–S-14 of the Supplementary material. The A1 complex shows band at 335 nm and indicates an octahedral geometry around the central metal atom suggesting metal to ligand charge transfer transition (MLCT). The UV spectra of the A2 complexes display broad absorption bands at 383, 350 and 267 nm, corresponding to the transitions ⁴T_{1g}→⁴T_{2g}, ⁴T_{1g}→⁴T_{1g}(P) and ⁴T_{1g}→⁴A_{2g}, respectively. The magnetic moment (μ) value of 3.90 μ_B indicates a paramagnetic nature and suggests an octahedral geometry. The UV spectra of A3 complexes exhibit bands at 398, 366 and 335 nm which attributed to ³A_{2g}→³T_{2g}, ³A_{2g}→³T_{1g}(f) and ³A_{2g}→³T_{1g}(P). The value of magnetic moment (μ) at 3.05 μ_B indicates paramagnetic nature and suggests an octahedral geometry. The A4 complexes exhibit bands at 435 and 363 nm which attributed to ²E_g→²T_{2g} and ligand to metal charge transitions (LMCT). The magnetic moment value of 1.70 μ_B indicates a paramagnetic nature and points to a distorted octahedral geometry likely influenced by Jahn–Teller distortion. The absorption band of the A5 complexes observed at 396 nm is attributed to the metal to ligand charge transfer (MLCT). The diamagnetic property indicates the presence of a tetrahedral geometry. The A6 complex exhibits absorption bands at 435 and

325 nm potentially corresponding to the ${}^2B_2 \rightarrow {}^2E$ and ${}^2B_2 \rightarrow {}^2B_1$ transitions. The magnetic moment value of $1.72 \mu_B$ indicates a square pyramidal geometry.³¹

Molar conductivity of A1–A6 complexes

The molar conductance of A1–A6 complexes were measured at ambient temperature in a 10^{-3} M dimethylsulfoxide (DMSO) solution. The findings were obtained by utilizing the relation $\Lambda_M = K/C$. The molar conductance values ranged between 7.2 to $19.5 \text{ S} \cdot \text{mol}^{-1} \cdot \text{cm}^2$ clearly indicate that A1–A6 complex are non-electrolytic in nature. This is consistent with non-electrolyte molar conductivity values in DMSO solution being less than $50 \text{ S} \cdot \text{mol}^{-1} \cdot \text{cm}^2$. The structure of stable metal complexes does not dissociate into ions in DMSO, leading to non-electrolytic properties of the metal complexes³⁶ shown in Table I.

TABLE I. Magnetic moment and molar conductance of A1–A6 complexes

Sr. No.	Complex	Conductance $\text{S} \cdot \text{mol}^{-1} \cdot \text{cm}^2$	Magnetic moment μ_B	Assigned geometry
1.	A1	15.20	5.00	Octahedral
2.	A2	14.35	3.90	Octahedral
3.	A3	17.25	3.05	Octahedral
4.	A4	19.5	1.70	Octahedral
5.	A5	7.2	Diamagnetic	Tetrahedral
6.	A6	13.20	1.72	Square pyramidal

Thermal analysis of A1–A6 complexes

For the stability of synthesized A1–A6 complexes; the complexes were tested by thermogravimetric analysis in presence of nitrogen atmosphere. For this test the temperature was changed from ambient to 800°C . As a result of decomposition, it was observed that the A1–A6 complexes decompose at two distinct steps, Table

TABLE II. Thermogravimetric data

Sr. No.	Complex	TG range, $^\circ\text{C}$	Mass loss in % (Calc. %)	Decomposition of molecule	Metallic residue
1.	A1	27–190	9.13(9.85)	H_2O	MnO
		240–580	77.78(77.19)	$\text{C}_{19}\text{H}_{11}\text{BrN}_4\text{O}_4$	
2.	A2	27–200	9.14(9.78)	H_2O	CoO
		250–580	77.06(76.63)	$\text{C}_{19}\text{H}_{11}\text{BrN}_4\text{O}_4$	
3.	A3	27–190	9.65(9.80)	H_2O	NiO
		240–540	76.18(76.58)	$\text{C}_{19}\text{H}_{11}\text{BrN}_4\text{O}_4$	
4.	A4	27–190	10.76 (9.71)	H_2O	CuO
		200–550	75.25(76.08)	$\text{C}_{19}\text{H}_{11}\text{BrN}_4\text{O}_4$	
5.	A5	27–195	3.10(3.44)	H_2O	ZnO
		200–570	81.65(81.04)	$\text{C}_{19}\text{H}_{11}\text{BrN}_4\text{O}_4$	
6.	A6	27–150	5.67(6.64)	H_2O	VO
		180–520	81.98(80.99)	$\text{C}_{19}\text{H}_{11}\text{BrN}_4\text{O}_4$	

II. In the initial stage, the loss of the coordinated water molecule occurs between ambient temperature and 200 °C influenced by the nature of the metal to water bonds. In the second step consecutive loss of Schiff base ligand takes place from the temperature range of 200 to 600 °C and at temperatures exceeding 600 °C the formation of metal oxides takes place.³⁷ The graphs derived from the data are presented in Figs. S-15–S-17 of the Supplementary material.

Powder X-ray diffraction

The powder X-ray diffraction study was carried out by sophisticated instrument in the 2θ range of 20–80° at wavelength of 1.540 Å. This is given in Table III and Figs. S-18–S-20 of the Supplementary material. The A1 and A2 complex shows monoclinic crystal system. The metal complexes A3 and A6 complex show orthorhombic crystal system; A4 and A5 complexes show the triclinic crystal system.³⁵

TABLE III. XRD spectral data of metal complexes; M – monoclinic; O – orthorhombic; T – triclinic

Complex	No. of reflections	Maxima ($2\theta / ^\circ$)	d -Value nm	Lattice constant, Å	Unit cell volume, Å ³	Axis and axis angle	Z- Value	Crystal system
A1	14	5.53	15.962	$a = 15.9729$ $b = 17.5388$ $c = 11.5710$	3229.366	$a \neq b \neq c$ and $\alpha = \gamma = 90^\circ$ $\neq \beta$	4	M
A2	17	10.50	8.415	$a = 8.4087$ $b = 13.6230$ $c = 17.1860$	1631.359	$a \neq b \neq c$ and $\alpha = \gamma = 90^\circ$ $\neq \beta$	2	M
A3	9	22.10	4.018	$a = 6.9600$ $b = 7.8514$ $c = 9.5124$	337.154	$a \neq b \neq c$ and $\alpha = \beta = \gamma$ $= 90^\circ$	4	O
A4	13	6.82	12.956	$a = 26.3197$ $b = 9.4184$ $c = 13.3606$	3260.708	$a \neq b \neq c$ and $\alpha \neq \beta \neq \gamma$ $\neq 90^\circ$	8	T
A5	14	7.31	17.627	$a = 14.3633$ $b = 12.2982$ $c = 11.7339$	3521.568	$a \neq b \neq c$ and $\alpha \neq \beta \neq \gamma$ $\neq 90^\circ$	2	T
A6	17	6.97	12.672	$a = 15.3440$ $b = 8.4152$ $c = 11.2140$	3021.568	$a \neq b \neq c$ and $\alpha = \beta = \gamma$ $= 90^\circ$	4	O

Biological studies of Schiff base ligand(L) and its metal complexes(M)

Anti-hyperglycemia assessments. The anti-hyperglycemia assessments of synthesized Schiff base ligand and A2, A4 and A5 complexes was done by α -amylase inhibition assay and demonstrated in Table IV. The A2 complex shows higher inhibition than Schiff base ligand. Cobalt is commonly known to show the good antidiabetic activity. Other metal complexes such as A4 and A5 also exhibit better inhibition than Schiff base ligand compared with standard drug acarbose.³⁸

Anticancer assessments. The anticancer assessments of Schiff base ligand as well as the A2, A4 and A6 complexes have been performed by utilizing the MTT (3-[4,5-dimethylthiazol-2-yl]-2,5-diphenyltetrazolium bromide) test by using MCF-7 human breast cancer cell line. The metal complexes of copper and zinc are commonly known to exhibit good anticancer activities than other metals. The metal complexes involving A1, A4 and A5 demonstrated significantly superior anticancer assessment compared to Schiff base ligand B106 against standard drug 5-FU³⁹ shown in Table V.

TABLE IV. Anti-hyperglycemia assessment of Schiff base ligand and A2, A4 and A5 complexes

Sr. No.	Compound	Concentration, $\mu\text{g/mL}$	Cell viability, %
1	Standard acarbose	250	54.54
		500	61.93
		1000	74.43
2	B106	250	28.97
		500	35.22
		1000	44.31
3	A2 Complex	250	35.79
		500	43.18
		1000	56.81
4	A4 Complex	250	35.22
		500	44.88
		1000	53.97
5	A5 Complex	250	38.63
		500	44.31
		1000	47.72

TABLE V. Anticancer assessment of Schiff base ligand and A2, A4 and A5 complexes

Sr. No.	Compound	Concentration of sample, $\mu\text{g/mL}$	Cell inhibition, %
1	Standard 5-FU	10	79.14
		40	83.29
		100	88.79
2	B106	10	38.06
		40	59.14
		100	66.52
3	A2 Complex	10	42.75
		40	57.62
		100	71.81
4	A4 Complex	10	38.56
		40	62.81
		100	70.83
5	A5 Complex	10	41.34
		40	60.83
		100	69.84

Antimicrobial activities. The Schiff base ligand and metal complexes were investigated against antifungal and antibacterial activities.³⁵ The observation suggest that the metal complexes are more active than the Schiff base ligand (L).

The antimicrobial properties of the synthesized Schiff base ligand B106 and its A1–A6 complexes were evaluated using the disc diffusion method against Gram-positive bacteria (*Bacillus subtilis*, *Staphylococcus aureus*) as well as Gram-negative bacteria (*Klebsiella pneumoniae*, *Pseudomonas aeruginosa*) and three fungi (*Penicillium chrysogenum*, *Trichoderma viride* and *Aspergillus niger*). The findings of the antibacterial assessments indicate that all complexes except A5 show better inhibition than Schiff base ligand B106 and standard reference drug tetracycline. In antifungal activity no metal complex shows better or higher inhibition than Schiff base ligand B106 and standard reference drug fluconazole 40, Table VI.

TABLE VI. Antimicrobial assessment of Schiff base ligand and metal complexes; interpretation key: “–” (resistant) = up to 8 mm; intermediate sensitive: 8–12 mm; sensitive: 12–18 mm; highly sensitive: ≥ 18 mm

Sr. No.	Compound	Antibacterial activity				Antifungal activity		
		<i>S. aureus</i>	<i>B. subtilis</i>	<i>K. pneumoniae</i>	<i>P. aeruginosa</i>	<i>P. chrysogenum</i>	<i>T. viride</i>	<i>A. niger</i>
1	B106	8	8	8	8	8	8	8
2	A1 complex	22	21	19	21	8	8	8
3	A2 complex	13	14	11.5	17	8	8	8
4	A3 complex	17.5	20	20.5	16	8	8	8
5	A4 complex	18	19	15	16.5	8	8	8
6	A5 complex	8	8	8	8	8	8	8
7	A6 complex	21	15	18	15	8	8	8
8	Tetracycline	19	25	20	19	–	–	–
9	Fluconazole	–	–	–	–	25	35	26

CONCLUSION

The current study utilized a green synthetic approach to produce Schiff base ligand and its corresponding transition metal complexes. This environmentally friendly methodology demonstrated notable advantages over conventional techniques, including significantly higher yields ranging from 80 to 90 %. Moreover, the green approach considerably reduced reaction times and eliminates the necessity of hazardous solvents, thereby enhancing safety and sustainability. These factors collectively contribute to a substantial decrease in the overall cost of the reaction process, emphasizing the economic and ecological benefits of the method. The spectroscopic analyses revealed that the Schiff base ligand exhibited tridentate behaviour. Furthermore, powder X-ray diffraction (XRD) studies highlighted the presence of distinct crystal systems such as monoclinic for A1 and A2, triclinic for

A4 and A5 and orthorhombic for A3 and A6 configurations in the metal complexes, suggesting structural diversity. By the molar conductance measurements, it is confirmed that the metal complexes are non-electrolytic in nature. In the view of biological activity, the synthesized transition metal complexes, labelled A1 to A6, displayed significantly superior biological activities than Schiff base ligand (B106) in comparison with different standard drugs. This enhancement in activity highlights the potential applications of these complexes in various fields, paving the way for advancements in coordination chemistry and material science.

SUPPLEMENTARY MATERIAL

Additional data and information are available electronically at the pages of journal website: <https://www.shd-pub.org.rs/index.php/JSCS/article/view/13329>, or from the corresponding author on request.

Acknowledgements. We the authors are greatly appreciate to The University Grant Commission's financial support and the Principal of Balbhim Arts, Science and Commerce College, Beed (M.S.) India, for providing laboratory facility. We are also thankful to the Biocyte Institute of Research for providing us with results of biological activities.

ИЗВОД

ЗЕЛЕНИ ПРИСТУП У ЕФИКАСНОЈ СИНТЕЗИ КОМПЛЕКСА МЕТАЛА СА 4-БРОМО-2-((Е)-((2-ХИДРОКСИФЕНИЛ)ИМИНО)МЕТИЛ)-6-((Е)-(3-НИТРОФЕНИЛ)ДИАЗЕНИЛ)-ФЕНОЛОМ И ИСПИТИВАЊЕ ЊИХОВЕ АНТИХИПЕРГЛИКЕМИЈСКЕ, АНТИТУМОРСКЕ И АНТИМИКРОБНЕ АКТИВНОСТИ

KULDEEP B. SAKHARE¹, KIRTI N. SARWADE¹, HANSARAJ U. JOSHI² и МАНАДЕО А. SAKHARE¹

¹Department of Chemistry, Balbhim Arts, Science & Commerce College, Beed, Maharashtra, India u

²Department of Chemistry, Swa. Sawarkar College, Beed, Maharashtra, India

У данашње време, свет се бори против рака и дијабетеса, што је подстакло глобална истраживања у правцу развоја ефикасних лекова за лечење ових болести. Истраживања показују да координациона једињења, посебно са супституисаним салицилалдехидима, показују значајну биолошку активност, која се додатно повећава након додатка амина. У овом раду приказана је синтеза комплекса метала, Mn(II), Co(II), Ni(II), Cu(II), Zn(II) и VO(II), са Шифовом базом, која је претходно синтетисана методом млевења из (Е)-5-бромо-2-хидрокси-3-((3-нитрофенил)дiazенил)бензалдехида и 2-аминофенола. Синтетисана Шифова база је окарактерисана применом масене спектрометрије, као и ¹H-NMR и FT-IR спектроскопије. Након тога, синтетисани су комплекси метала са овом Шифовом базом у реакцији са одговарајућим Mn(II), Co(II), Ni(II), Cu(II), Zn(II) и VO(II) солима. Добијени комплекси метала су испитивани применом елементарне микроанализе, FT-IR и електронских спектра, термалне анализе, дифракцијом X-зрака са праха, моларне проводљивости и др. У току биолошких испитивања, одређена је антихипергликемијска и анти туморска активности Шифове базе и комплекса метала применом теста инхибиције α-амилазе и МТТ теста, користећи стандардне референтне лекове акарбозу и 5-флуороурацил (5-FU). Резултати антихипергликемијског испитивања указују да Co(II) комплекс показује већу активност у поређењу са осталим комплексима, док сви синтетисани комплекси показују већу активност од слободне Шифове базе. Када је реч о анти туморској активности, Co(II) комплекс показује већу активност у односу на остале комплексе, а сви комплекси метала су активнији од некоординоване Шифове базе. Поред тога, испитивана

је и антимикробна активност синтетисаних једињења према две Грам-позитивне бактеријске врсте (*Staphylococcus aureus* и *Bacillus subtilis*), две Грам-негативне врсте (*Klebsiella pneumoniae* и *Pseudomonas aeruginosa*), као и три врсте гљивица (*Penicillium chrysogenum*, *Trichoderma viride* и *Aspergillus niger*). На основу добијених резултата, закључено је да комплекси метала показују бољу биолошку активност у односу на одговарајућу Шифову базу.

(Примљено 8. априла, ревидирано 29. априла, прихваћено 8. августа 2025)

REFERENCES

1. E. S. Aazam, R. Thomas, *J. Mol. Struct.* **1295** (2024) 136669 (<https://doi.org/10.1016/j.molstruc.2023.136669>)
2. R. Gandhimathi, S. Anbuselvi, R. Saranya, *J. Indian Chem. Soc.* **100** (2023) 101033 (<https://doi.org/10.1016/j.jics.2023.101033>)
3. S. Sharma, S. P. Yadav, S. Kumari, M. Ranka, *J. Indian Chem. Soc.* **100** (2023) 100997 (<https://doi.org/10.1016/j.jics.2023.100997>)
4. H. L. Singh, S. Khaturia, V. S. Solanki, N. Sharma, *J. Indian Chem. Soc.* **100** (2023) 100945 (<https://doi.org/10.1016/j.jics.2023.100945>)
5. P. Tiwari, S. Phadte, S. Chandavarkar, B. Biradar, S. M. Desai, *J. Indian Chem. Soc.* **100** (2023) 100951 (<https://doi.org/10.1016/j.jics.2023.100951>)
6. M. R. A. Mohameed, A. H. Hasan, R. D. Kareem, *J. Garmian Univ.* **155** (2017) 453 (<https://doi.org/10.24271/garmian.155>)
7. H. Katouah, A. M. Hameed, A. Alharbi, F. Alkhatib, R. Shah, S. Alzahrani, R. Zaky, N. M. El-Metwaly, *Chem. Select* **5** (2020) 10256 (<https://doi.org/10.1002/slct.202002388>)
8. G. More, S. Bootwala, S. Shenoy, J. Mascarenhas, K. Aruna, *Int. J. Pharm. Sci.* **9** (2018) 3029 ([http://dx.doi.org/10.13040/IJPSR.0975-8232.9\(7\).3029-35](http://dx.doi.org/10.13040/IJPSR.0975-8232.9(7).3029-35))
9. K. N. Sarwade, K. B. Sakhare, M. A. Sakhare, S. V. Thakur, *Heterocyclic Lett.* **14** (2024) 797 (<https://www.heteroletters.org/issue144/Paper-8.pdf>)
10. B. Debaraj, P. Raj, R. Badekar, K. I. Momin, A. S. S. Bondge, *J. Appl. Organomet. Chem.* **4** (2024) 76 (<https://doi.org/10.48309/JAOC.2024.434283.1156>)
11. V. P. Radha and M. Prabakaran, *Appl. Organomet. Chem.* **36** (2022) e6872 (<https://doi.org/10.1002/aoc.6872>)
12. S. A. Halim, M. Shebl, *J. Coord. Chem.* **74** (2021) 2984 (<https://doi.org/10.1080/00958972.2021.2020259>)
13. M. Shebl, *J. Coord. Chem.* **69** (2016) 199 (<https://doi.org/10.1080/00958972.2015.1116688>)
14. O. M. I. Adly, M. Shebl, E. M. Abdelrhman, B. A. El-Shetary, *J. Mol. Struct.* **1219** (2020) 128607 (<https://doi.org/10.1016/j.molstruc.2020.128607>)
15. K. Tahmineh, H. Mohammad, H. Hassan, A. H. Hasan, *Chem. Methodol.* **7** (2023) 748 (<https://doi.org/10.48309/chemm.2023.414603.1718>)
16. C. Dolan, R. Glynn, S. Griffin, C. Conroy, C. Loftus, *Diabet. Med.* **35** (2018) 871 (<https://doi.org/10.1111/dme.13639>)
17. R. Miyazaki, H. Yasui, Y. Yoshikawa, *Open J. Inorg. Chem.* **6** (2016) 114 (<https://doi.org/10.4236/ojic.2016.62007>)
18. E. Akila, M. Usharani, P. Maheswaran, R. Rajavel, *Int. J. Rec. Sci. Res.* **4** (2013) 1497 (https://www.recentscientific.com/sites/default/files/Download_629.pdf)
19. C. Veeravel, K. Rajasekar, P. Chakkaravarthy, R. Selvarani, A. Kosiha, V. Sathya, *Research Square* (2023) 2693 (<https://doi.org/10.21203/rs.3.rs-2680647/v1>)

20. P. Wanjari, A. Bharati, V. Ingle, *Malaysian J. Chem.* **23** (2021) 23 (<https://ikm.org.my/publications/malaysian-journal-of-chemistry/view-abstract.php?abs=J0035-C0R305>)
21. L. M. R. Ummi, K. Karima, M. T. Amalina, K. Y. Muhamad, N. A. Zakaria, *Malaysian J. Chem.* **24** (2022) 250 (<https://doi.org/10.55373/mjchem.v24i2.250>)
22. V. P. Nisha, N. Subhadrambika, S. S. Swathy, K. Mohanan, *J. Indian Chem. Soc.* **89**(2012) 761 (https://www.researchgate.net/publication/288108395_Synthesis_spectroscopic_characterization_thermal_decomposition_and_antimicrobial_studies_of_manganeseIII_ironIII_and_cobaltIII_complexes_with_Schiff_base_derived_from_thiophene-2-carboxaldehyde_and_2-)
23. M. Bal, G. Ceyhan, B. Avar, M. Kose, A. Kayraldiz, M. Kurtoglu, *Turkish J. Chem.* **38** (2014) 222 (<https://doi.org/10.3906/kim-1306-28>)
24. M. Kurtoglu, E. Ispir, N. Kurtoglu, S. Serin, *Dyes Pigments* **77** (2008) 75 (<https://doi.org/10.1016/j.dyepig.2007.03.010>)
25. F. Dimiza, A. N. Papadopoulos, V. Tangoulis, V. Psycharis, C. P. Raptopoulou, D. P. Kessissoglou, G. Psomas, *Dalton Transact.* **39** (2010) 4517 (<https://doi.org/10.1039/B927472C>)
26. M. M. Abd-Elzaher, S. A. Moustafa, A. A. Labib, M. M. Ali, *Monatsh. Chem.* **141** (2010) 387 (<https://doi.org/10.1007/s00706-010-0268-6>)
27. E. Ispir, *Dyes Pigments* **82** (2009) 13 (<https://doi.org/10.1016/j.dyepig.2008.09.019>)
28. M. Ozdemir, *Inorg. Chim. Acta* **421** (2014) 1 (<https://doi.org/10.1016/j.ica.2014.05.024>)
29. S. Urus, M. Dolaz, M. Tumer, *J. Inorg. Org. Poly. Mat.* **20** (2010) 706 (<http://dx.doi.org/10.1007/s10904-010-9394-1>)
30. V. Anusuya, N. Muruganatham, P. Anitha, S. Mahesh, *Oriental J. Chem.* **38** (2022) 1525 (<https://doi.org/10.13005/ojc/380626>)
31. K. N. Sarwade, K. B. Sakhare, M. A. Sakhare, S. V. Thakur, *Eurasian J. Chem.* **30** (2025) 4 (<https://doi.org/10.31489/2959-0663/1-25-8>)
32. K. Singh, Y. Kumar, P. Puri, C. Sharma, K. R. Aneja, *Arabian J. Chem.* **10** (2017) 978 (<http://dx.doi.org/10.1016/j.arabjc.2012.12.038>)
33. Z. H. Abd El-Waheb, M. M. Mashaly, A. A. Faheim, *Chem. Papers* **59** (2005) 25 (<https://www.chemicalpapers.com/?id=7&paper=55>)
34. Y. N. Bharate, K. B. Sakhare, S. A. Survase, M. A. Sakhare, *Heterocyclic Lett.* **13** (2023) 45 (<https://www.heteroletters.org/issue131/Paper-5.pdf>)
35. K. N. Sarwade, K. B. Sakhare, M. A. Sakhare, S. V. Thakur, *Mong. J. Chem.* **25** (2024) 10 (<https://doi.org/10.5564/mjc.v25i52.3537>)
36. R. Sawant, J. Wadekar, R. Ukirde, G. Barkade, *Pharmaceut. Sci.* **27** (2021) 345 (<http://dx.doi.org/10.34172/PS.2020.95>)
37. G. Sasikumar, T. N. Balaji, A. K. Ibrahim Sheriff, *World J. Pharm. Res.* **7** (2018) 564 (https://www.wjpr.net/abstract_file/9977)
38. H. R. Afzal, N. U. H. Khan, K. Sultana, A. Mobashar, A. Lareb, A. Khan, A. Gull, H. Afzaal, M. T. Khan, M. Rizwan, M. Imran, *ACS Omega* **6** (2021) 4470 (<https://doi.org/10.1021/acsomega.0c06064>)
39. L. H. Abdel-Rahman, A. M. Abu-Dief, R. M. El-Khatib, S. M. Abdel-Fatah, *Bioorg. Chem.* **69** (2016) 140 (<https://doi.org/10.1016/j.bioorg.2016.10.009>)
40. K. N. Sarwade, K. B. Sakhare, M. A. Sakhare, Y. N. Bharate, S. V. Thakur, *Curr. Bioact. Comp.* (2025) e15734072349875 (<https://doi.org/10.2174/0115734072349875250224092826>).



J. Serb. Chem. Soc. 90 (10) S381–S395 (2025)

SUPPLEMENTARY MATERIAL TO
**Green route for efficient synthesis of metal complexes of
4-bromo-2-((*E*)-((2-hydroxyphenyl)imino)methyl)-6-((*E*)-(3-
-nitrophenyl)diazenyl)phenol and its anti-hyperglycemia,
anticancer and antimicrobial assessment**

KULDEEP B. SAKHARE¹, KIRTI N. SARWADE¹, HANSARAJ U. JOSHI²
and MAHADEO A. SAKHARE^{1*}

¹Department of Chemistry, Balbhim Arts, Science & Commerce College, Beed, Maharashtra, India and ²Department of Chemistry, Swa. Sawarkar College, Beed, Maharashtra, India

J. Serb. Chem. Soc. 90 (10) (2025) 1161–1173

LIST OF CONTENT

No	Figure	Page No.
1.	Figure S-1. Mass spectrum of Schiff base ligand B106	S2
2.	Figure S-2. ¹ H NMR of Schiff base ligand B106	S2
3.	Figure S-3-S-9. FTIR of Schiff base ligand B106 and A1-A6 complexes	S3-S6
4.	Figure S-10-S-14. Uv of A1-A6 complexes	S6-S8
5.	Figure S-15-S-17. TGA of metal complex	S9
6.	Figure S-18-S-20. P-XRD of metal complex	S10
7.	Photos of antimicrobial assessments	S11
8.	Photos of anti-hyperglycemia assessments	S11-S12
9.	Photos of anticancer assessments	S13

*Corresponding author. E-mail: sakharema.chem@gmail.com

Schiff base ligand (B106). Colour: Brown; Time : 30 min; Yield: 84%; M. P.: 210-230 °C; FT-IR in cm^{-1} : 3432, 3502 (-OH stretching), 1619 (>C=N Stretching), 1372 (-N=N Stretching), 1271 (>C-O stretching), 647 (>C-Br stretching); ^1H NMR (400 MHz, CDCl_3) δ 12.37 (s, 1H), 8.65 (s, 1H), 7.58 (d, J = 2.4 Hz, 1H), 7.51 (dd, J = 8.8, 2.4 Hz, 1H), 7.29 (s, 2H), 7.28 – 7.22 (m, 2H), 7.17 (dd, J = 7.9, 1.4 Hz, 1H), 7.05 (d, J = 8.3 Hz, 1H), 7.01 – 6.94 (m, 2H), 5.72 (s, 1H); MS (ESI): m/z for $\text{C}_{19}\text{H}_{13}\text{BrN}_4\text{O}_4$ Calculated: 440.01 Found: 440.; Elemental analysis : Found (Calculated) C=51.72(51.35), H=2.97(2.75), N=12.70(12.12).

Mn(II) complex (A1 complex)

Colour: Maroon; Time: 40-42 min; Yield: 68%; M.P.: >300°C; FT-IR in cm^{-1} : 1590 (>C=N Stretching), 1370 (-N=N Stretching), 1288 (>C-O stretching), 742 (>C-Br stretching), 824(-OH Rocking); Elemental analysis : Found (Calculated) C=41.63(41.06), H=3.13(3.10), N=10.22(10.01); Uv-vis λ_{max} in nm: 335.

Co(II) complex (A2 complex)

Colour: Brown; Time: 40-45 min; Yield: 82%; M.P.: >300°C; FT-IR in cm^{-1} : 1588 (>C=N Stretching), 1370 (-N=N Stretching), 1291 (>C-O stretching), 743 (>C-Br stretching), 823(-OH Rocking); Elemental analysis : Found (Calculated) C=41.33(41.44), H=3.10(3.00), N=10.15(10.24); Uv-vis λ_{max} in nm: 383, 350, and 267.

Ni(II) complex (A3 complex)

Colour: Light Brown; Time: 40-45 min; Yield: 86%; M.P.: >300°C; FT-IR in cm^{-1} : 1580 (>C=N Stretching), 1368 (-N=N Stretching), 1292 (>C-O stretching), 742 (>C-Br stretching), 821(-OH Rocking); Elemental analysis : Found (Calculated) C=41.34(41.25), H=3.10(3.09), N=10.15(10.08); Uv-vis λ_{max} in nm: 398, 366 and 335.

Cu(II) complex (A4 complex)

Colour: Faint green; Time: 40-45 min; Yield: 71%; M.P.: >300°C; FT-IR in cm^{-1} : 1615 (>C=N Stretching), 1368 (-N=N Stretching), 1275 (>C-O stretching), 743 (>C-Br stretching), 825(-OH Rocking); Elemental analysis : Found (Calculated) C=40.90(40.72), H=3.08(3.00), N=10.06(10.00); Uv-vis λ_{max} in nm: 435 and 363.

Zn(II) complex (A5 complex)

Colour: Dark yellow; Time: 40-45 min; Yield: 84%; M.P.: >300°C; FT-IR in cm^{-1} : 1603 (>C=N Stretching), 1374 (-N=N Stretching), 1284 (>C-O stretching), 744 (>C-Br stretching), 828(-OH Rocking); Elemental analysis : Found (Calculated) C=43.67(43.82), H=2.51(2.37), N=10.72(10.46); Uv-vis λ_{max} in nm: 396.

VO(II) complex (A6 complex)

Colour: Green; Time: 40-45 min; Yield: 59%; M.P.: >300°C; FT-IR in cm^{-1} : 1593 (>C=N Stretching), 1381 (-N=N Stretching), 1288 (>C-O stretching), 746 (>C-Br stretching), 828 (-OH Rocking); Elemental analysis : Found (Calculated) C=42.09(41.91), H=2.79(2.58), N=10.33(10.17); Uv-vis λ_{max} in nm: 435 and 325.

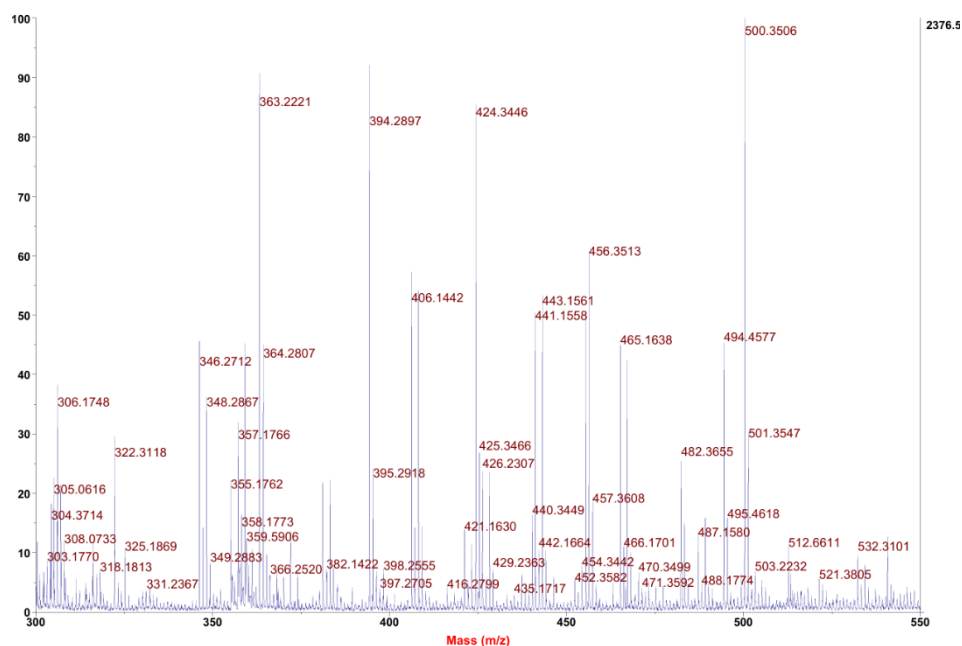


Figure S-1. Mass spectrum of Schiff base ligand B106

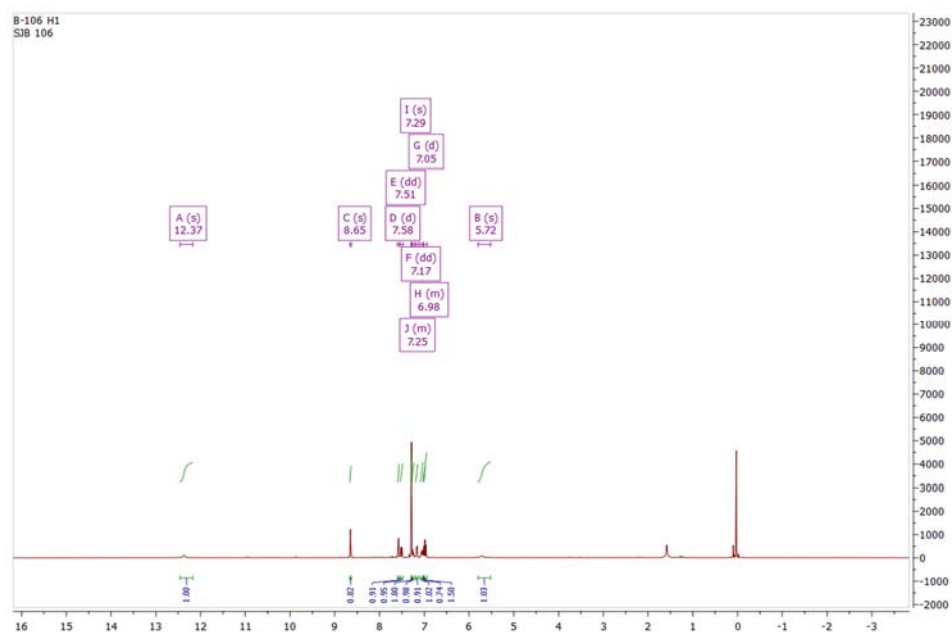
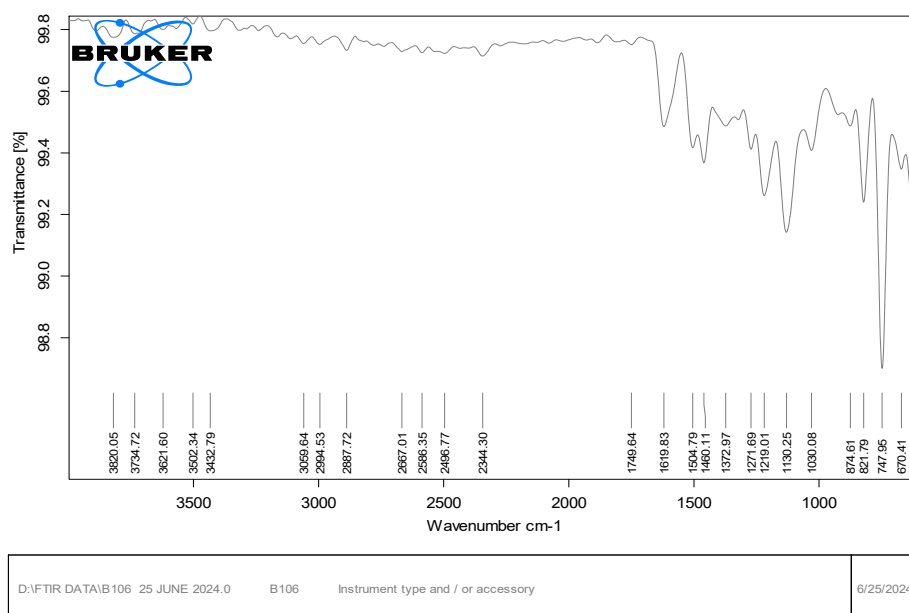
Figure S-2. ^1H NMR of Schiff base ligand B106

Figure S-3. FTIR of Schiff base ligand B106

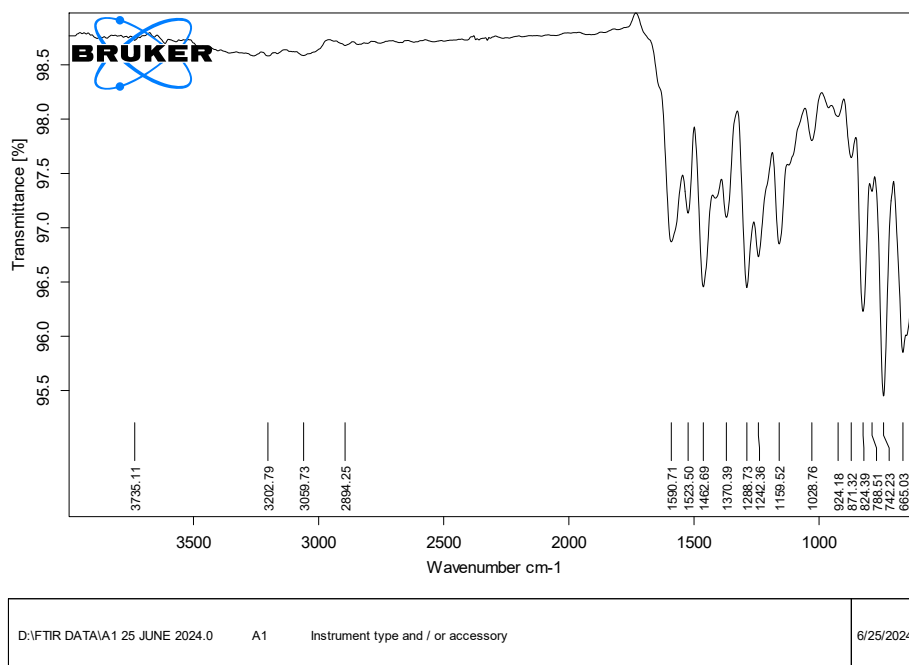


Figure S-4. FTIR of A1 complex

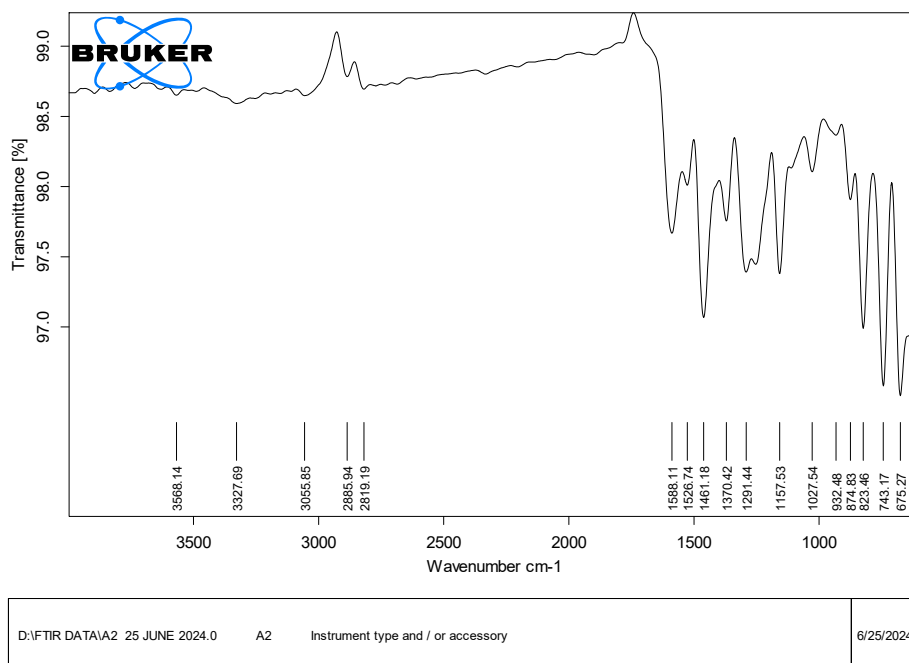


Figure S-5. FTIR of A2 complex

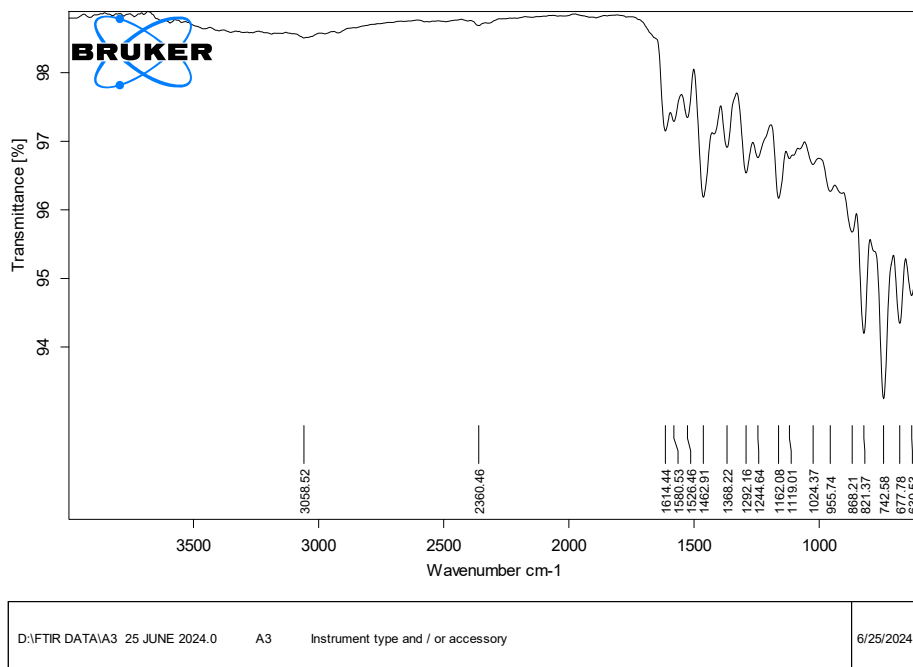


Figure S-6. FTIR of A3 complex

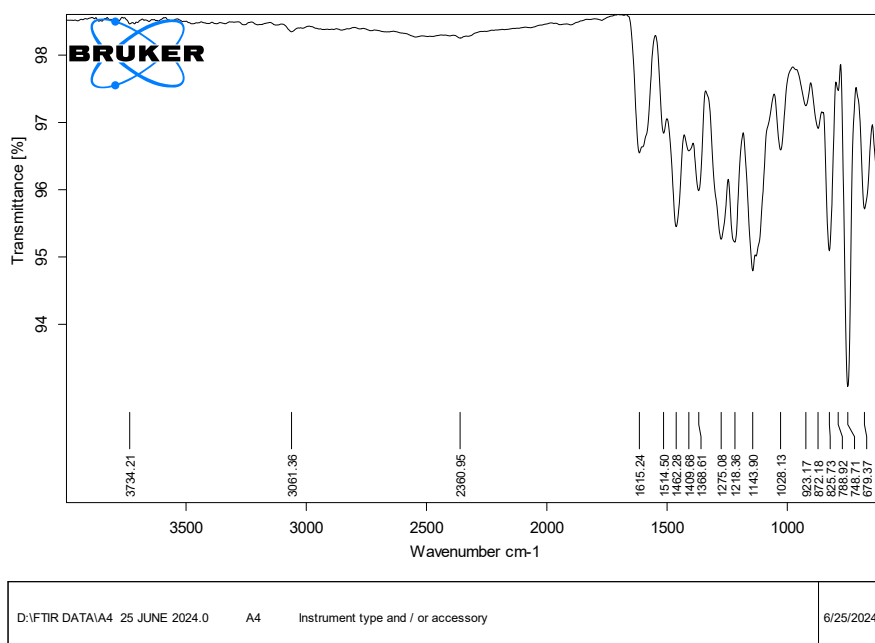


Figure S-7. FTIR of A4 complex

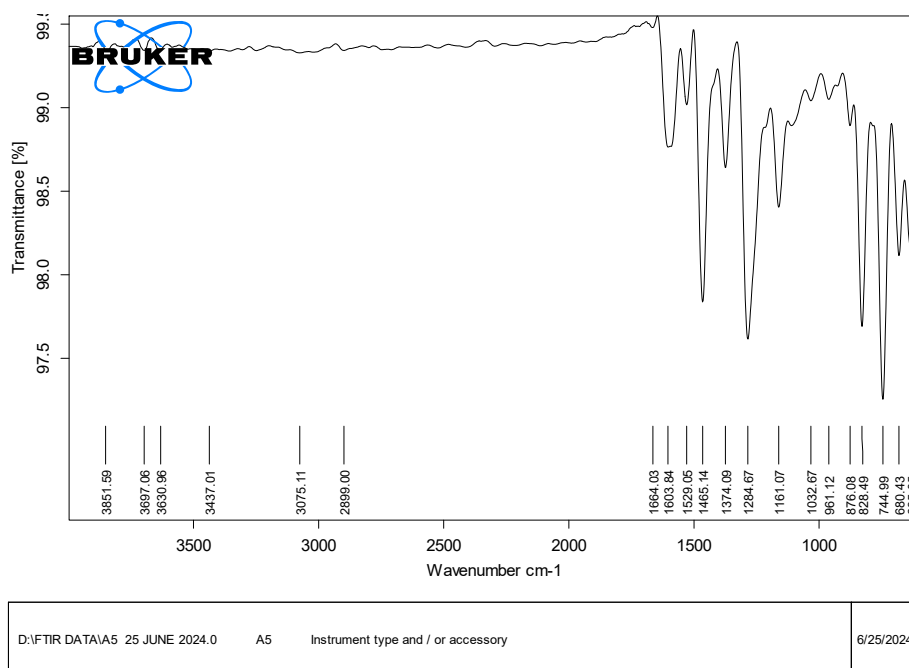


Figure S-8. FTIR of A5 complex

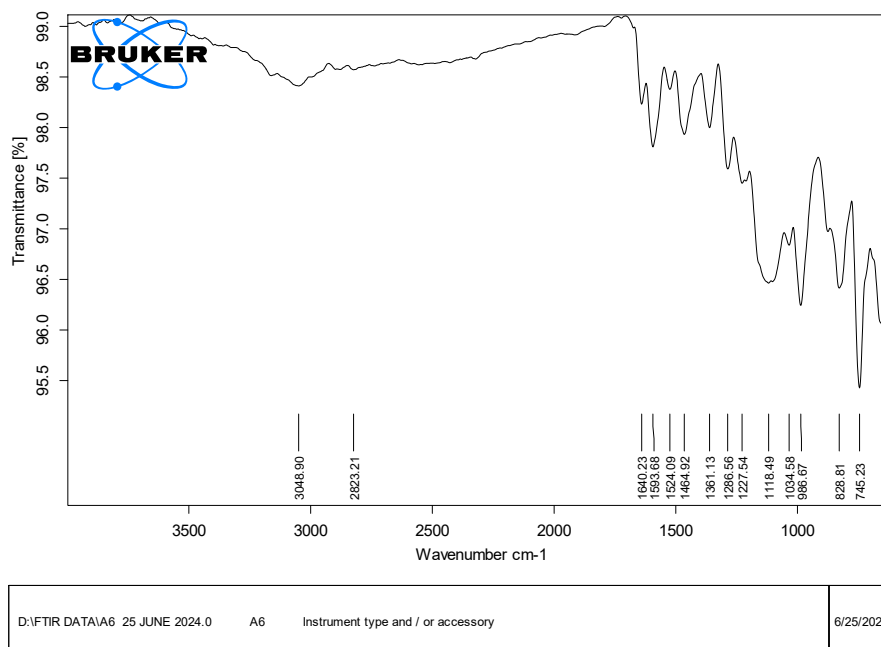


Figure S-9. FTIR of A6 complex

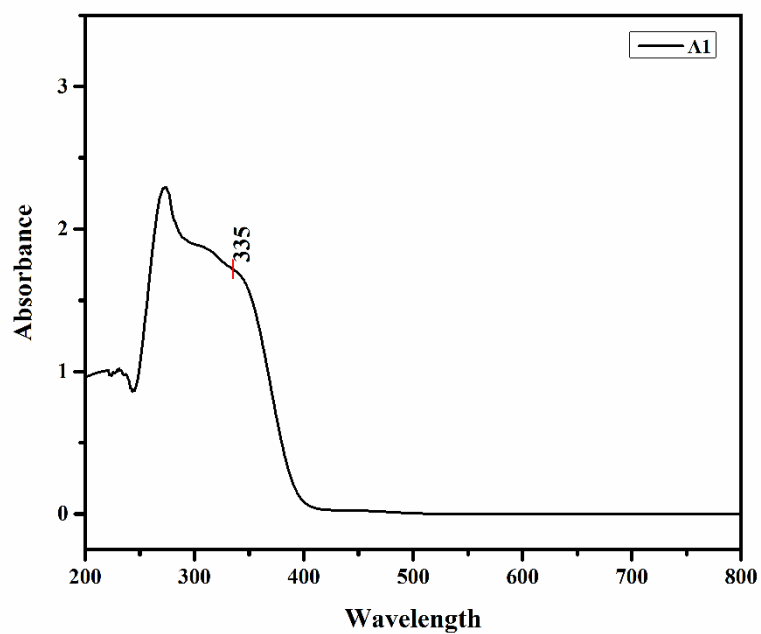


Figure S-10. UV spectra of A1 complex

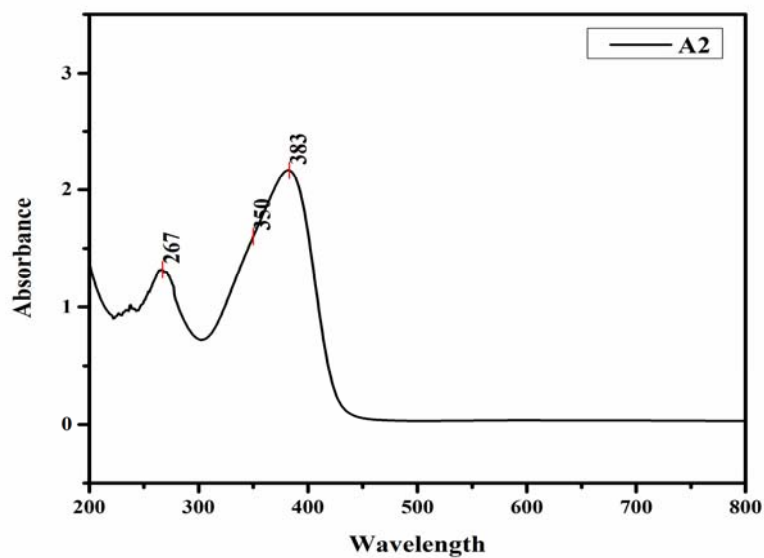


Figure S-11. Uv spectra of A2 complex

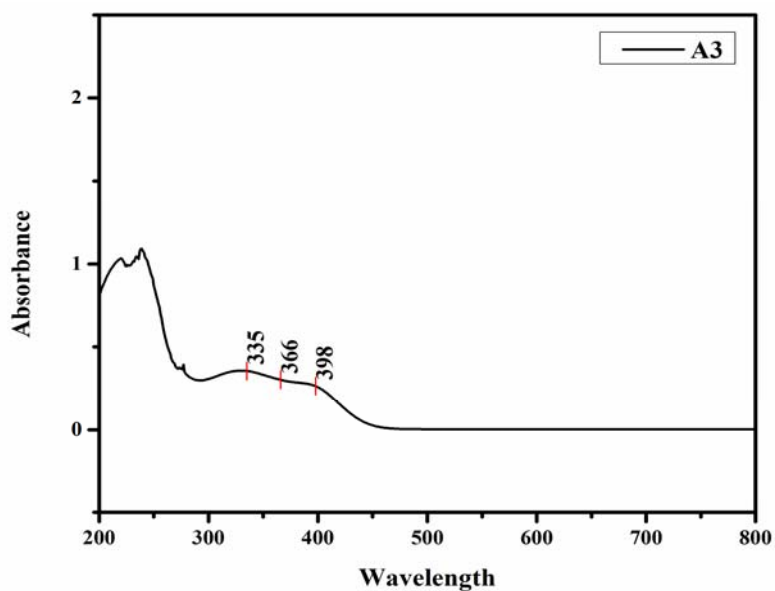


Figure S-12. Uv spectra of A3 complex

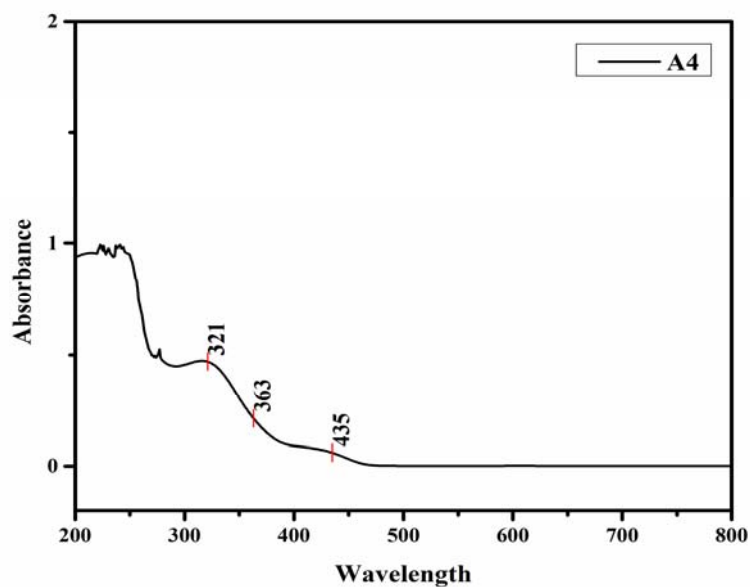


Figure S-13. Uv spectra of A4 complex

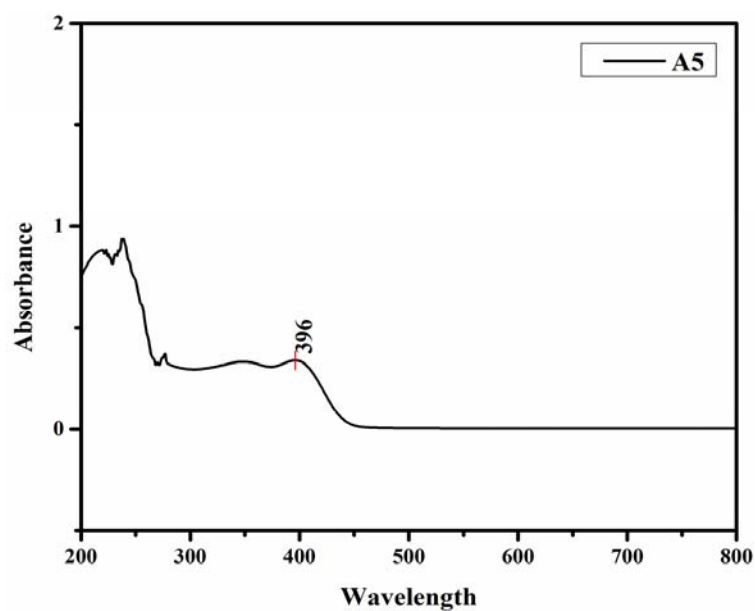


Figure S-14. Uv spectra of A5 complex

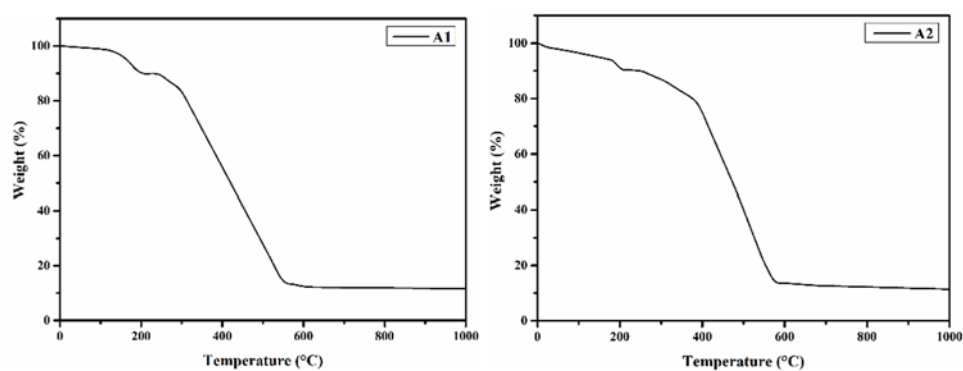


Figure S-15. TGA of A1 and A2 complex

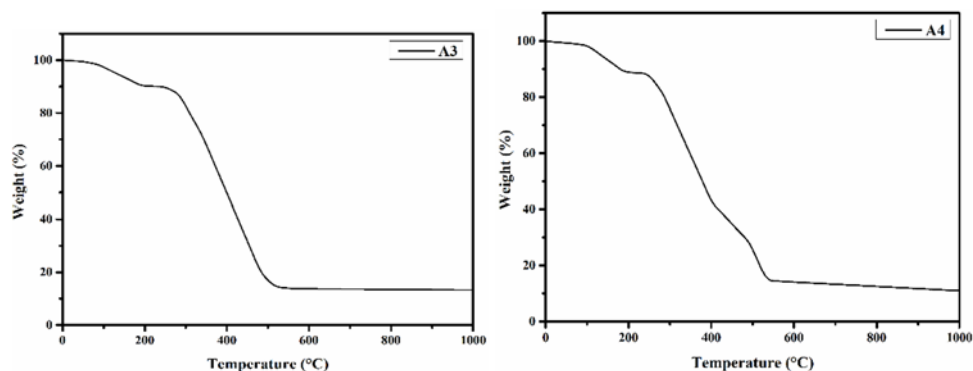


Figure S-16. TGA of A3 and A4 complex

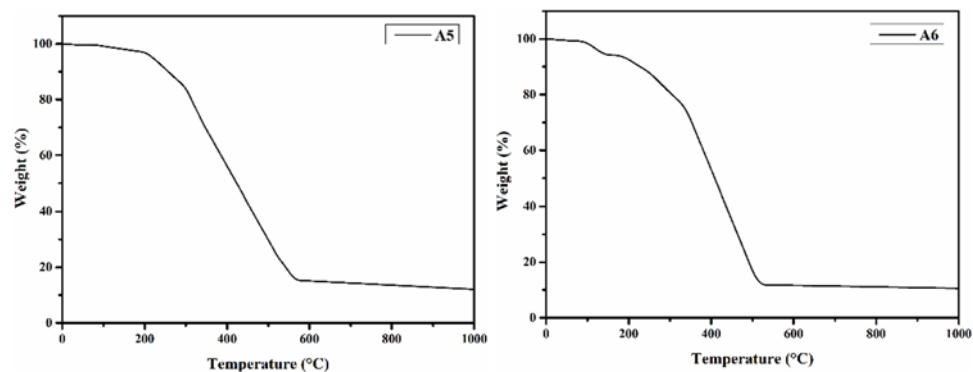


Figure S-17. TGA of A5 and A6 complex

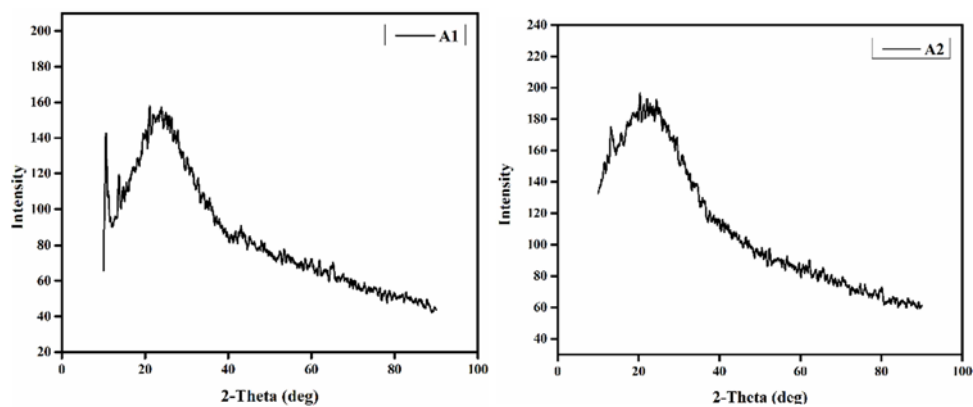


Figure S-18. P-XRD of A1 and A2 complex

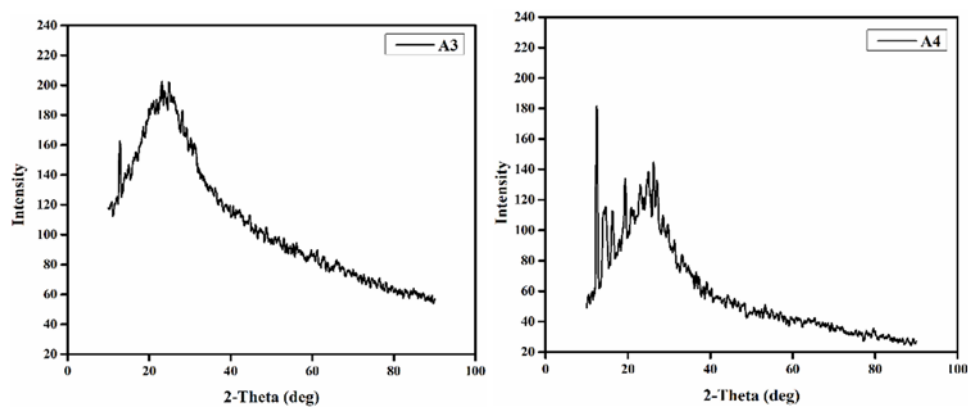


Figure S-19. P-XRD of A3 and A4 complex

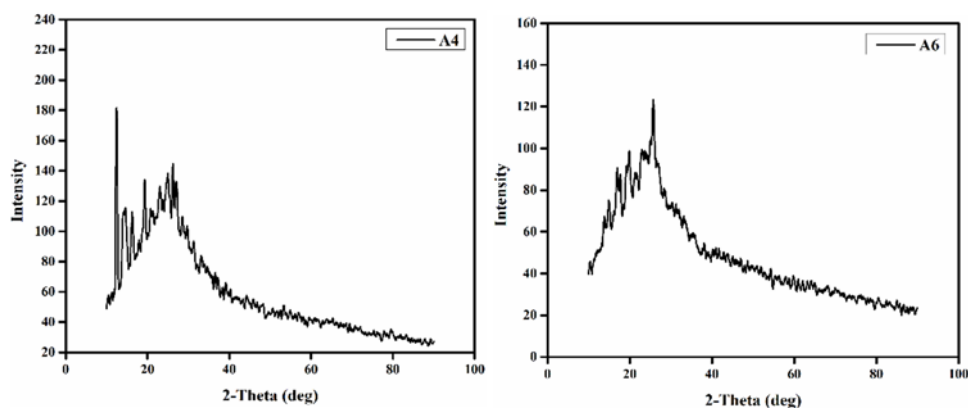
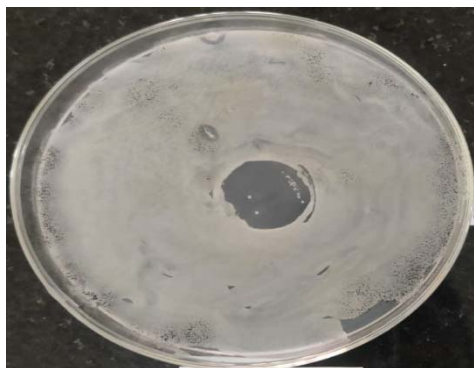


Figure S-20. P-XRD of A5 and A6 complex

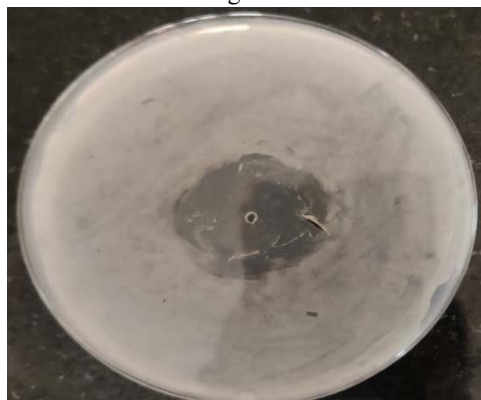
PHOTOS OF ANTIMICROBIAL ASSESSMENTS



Ligand B106



A1 complex



A2 complex



A3 complex



A4 complex



A5 complex



A6 complex

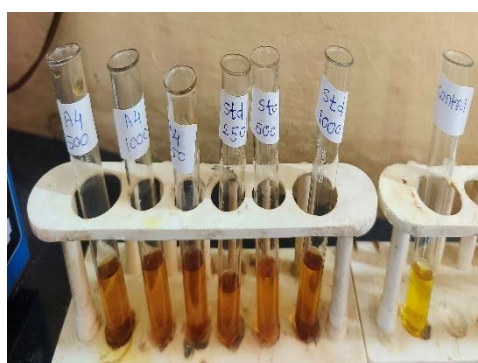
PHOTOS OF HYPERGLYCEMIA ASSESSMENTS



Ligand B106



A2 complex

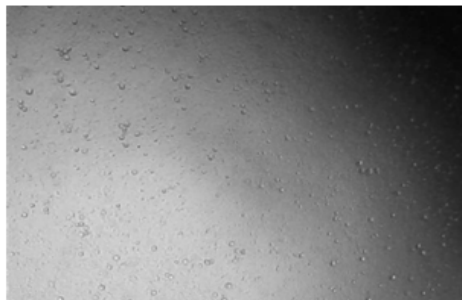


A4 complex

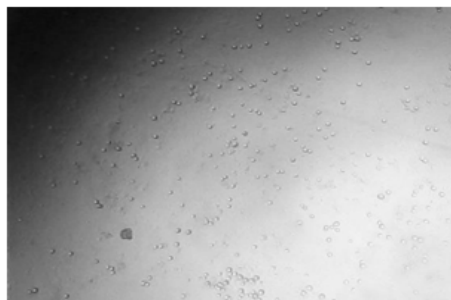


A5 complex

PHOTOS OF ANTICANCER ACTIVITY



Ligand B106



A2 complex



A4 complex



A5 complex

N-Phenyl-3-sulfamoyl-benzamide derivatives as anti-Hepatitis B virus agent candidates. Integrated computational studies

AICHA LAOUD¹, ABDE RAHMANE BELAFRIEKH^{2*} and MARWA ALAQARBEH³

¹Chemical Engineering Department, Faculty of Chemical Engineering, University of Salah Boubnider Constantine 3, Constantine, 25000, Algeria, ²Laboratory of LCPMM, Chemistry Department, Faculty of Sciences, University of Blida1, P.O. Box 270 Blida, 09000, Algeria and ³Basic Science Department, Prince Al Hussein Bin Abdullah II Academy for Civil Protection, Al-Balqa Applied University, Al-Salt, Jordan

(Received 30 April, revised 19 June, accepted 4 August 2025)

Abstract: This study used a combined approach of atom-based 3D-QSAR modeling and molecular docking to investigate 44 *N*-phenyl-3-sulfamoyl-benzamide derivatives as potential inhibitors of the hepatitis B virus (HBV). The developed QSAR model demonstrated strong statistical robustness, with a good correlation coefficient for the training set ($R^2 = 0.94$), a cross-validated coefficient ($Q^2_{cv} = 0.65$), and a correlation coefficient for the test set ($R^2 = 0.85$) using three PLS-components. Contour maps explained the modified areas within the compounds, clarifying hydrogen bond donors, hydrophobic interactions and electrostatic effects. The docking studies supported the findings of the 3D-QSAR model and explained the molecule's interactions with the receptors. Overall, the model and the docking analysis provide valuable insights into designing molecules with enhanced activity against the hepatitis B virus.

Keywords: molecular docking; HBV; 3D-QSAR; coefficient.

INTRODUCTION

The Hepatitis B virus (HBV) is the etiological agent of Hepatitis B, a serious viral infection that represents a significant global public health concern.¹ This disease primarily affects the liver and has the potential to progress to chronic hepatitis, cirrhosis and hepatocellular carcinoma.² HBV is easily transmitted through blood by sexual contact and from mother to child during pregnancy, underscoring the critical importance of implementing robust prevention strategies.³ Recent advancements in vaccines and antiviral therapies have substantially reduced the transmission of HBV and the mortality associated with it. Despite these positive developments, significant challenges persist, particularly in resource-constrained

*Corresponding author. E-mail: a.belafriekh@gmail.com
<https://doi.org/10.2298/JSC250430060L>

environments where access to medical care and vaccinations is limited.⁴ Furthermore, recent medicinal alternatives cannot eradicate covalently closed circular DNA (cccDNA), which serves as a reservoir for persistent viral infection, effectively complicating efforts to annihilate the disease.⁵

Current antiviral medications are effective in inhibiting the replication of viruses; however, they are incapable of completely eradicating them. This study underscores the necessity for innovative therapeutic strategies.^{6,7} The primary objective of this research is to enhance our understanding of the mechanisms by which the Hepatitis B virus (HBV) operates and to develop novel antiviral agents that can effectively prevent viral transmission, circumvent drug resistance and progress toward a definitive cure. The current study aims to predict the anti-Hepatitis B activity of forty-four *N*-phenyl-3-sulfamoyl-benzamide derivatives⁸ using an atom-based 3D-QSAR model and molecular docking to understand binding interactions with key HBV proteins. In this research, several computational methods, such as molecular docking and quantitative structure–activity relationship (QSAR) modeling, were used in identifying potential HBV inhibitors by analyzing the relationship between molecular structures and their antiviral effectiveness.^{9,10}

EXPERIMENTAL

Dataset

A series of forty-four *N*-phenyl-3-sulfamoyl-benzamide derivatives (Table S-I of the Supplementary material to this paper) were identified from the literature as inhibitors of the Hepatitis B virus (HBV).⁸ The half-maximal effective concentration (EC_{50}) values were transformed into their corresponding pEC_{50} values ($pEC_{50} = -\log (EC_{50} \times 10^{-6})$) to reduce data skewness and facilitate analysis. The dataset was subsequently divided into two subsets to develop a 3D-QSAR model: randomly, 33 compounds were selected to be the training set for building the model. The other 11 compounds were used as the test set to see how well the proposed model could predict the future.¹¹

Ligand preparation

ChemDraw Ultra drew all the 2D structures in the dataset and then imported them into the Maestro interface to generate 3D structures.¹² The generated 3D structures were prepared using the LigPrep module with an OPLS-2005 force field.¹³ To ensure comprehensive representation, multiple tautomers and potential ionization states were generated and considered within a pH range of 7 ± 2 , with all other parameters kept at their default settings.¹⁴

Molecular docking

The crystal structure of the Hepatitis B virus core protein (PDB ID: 5T2P, resolution: 1.69 Å) was retrieved from the Protein Data Bank (<https://www.rcsb.org/structure>). Protein preparation was performed using the Protein Preparation Wizard module in Maestro.¹⁵ During this process, all water molecules were removed, and hydrogen atoms were added. The protein structure was energy-minimized using the OPLS-2005 force field, with a root-mean-square deviation (*RMSD*) threshold of 0.30 Å.¹⁶ A receptor grid was generated using the Co-crystallized ligand (K89) as the centroid, with de coordinates $X = -0.96$ Å, $Y = 40.16$ Å, and $Z = -6.88$ Å.¹⁷ Molecular docking techniques help scientists to predict binding modes and interaction

profiles with the virus. The Glide extra-precision (XP) module was then used for docking studies to check ligand docking scores and binding affinities at the target protein's active site.^{18,19}

Atom-based 3D-QSAR model generation

A 3D-QSAR model was developed using the atom-based QSAR feature in the Phase module to predict the anti-Hepatitis B inhibitory activity of selected compounds.²⁰ The dataset was initially divided into training and test sets using a random selection method, with a ratio of 75:25.²¹ The model development was carried out using partial least squares (PLS) regression with a grid spacing of 1 Å.²² The primary criterion for selecting the optimal model was statistical robustness, further visualized through contour maps. The performance and stability of the model were evaluated using metrics such as SD , R^2 , R^2_{cv} , stability, F , P , $RMSE$, Q^2 and Pearson- r . Internal validation of the training set was performed using a leave-one-out (LOO) cross-validation method to calculate R^2 and R^2_{cv} .^{23,24} External validation with the test set confirmed the model's predictive accuracy, as assessed by Q^2 and other relevant parameters.²⁵ A scatter plots was created to depict the relationship between predicted and observed activity values for both the training and test sets. Finally, the QSAR model was applied to predict the biological activity of newly designed molecules.

ADMET prediction and activity predicted (pEC_{50})

The newly designed compounds were subjected to Atom-based 3D-QSAR to predict their biological activity (pEC_{50}) based on the generated 3D-QSAR model. Additionally, the QikProp module in Schrödinger was used to predict the absorption, distribution, metabolism and excretion (ADME) properties of these compounds. These predictions provided insights into the pharmacokinetic profiles of the compounds, which are critical for assessing their potential as drug candidates.^{26,27}

RESULTS AND DISCUSSION

Molecular alignment

Molecular alignment at the structural level is important for ensuring the accuracy of a 3D-QSAR model and the trustworthiness of the resulting contour maps. Consequently, a flexible alignment approach was utilized to align all selected anti-hepatitis compounds in this study. We chose the most active compound **8** as the template and aligned the remaining compounds based on their shared substructure (Fig. 1).

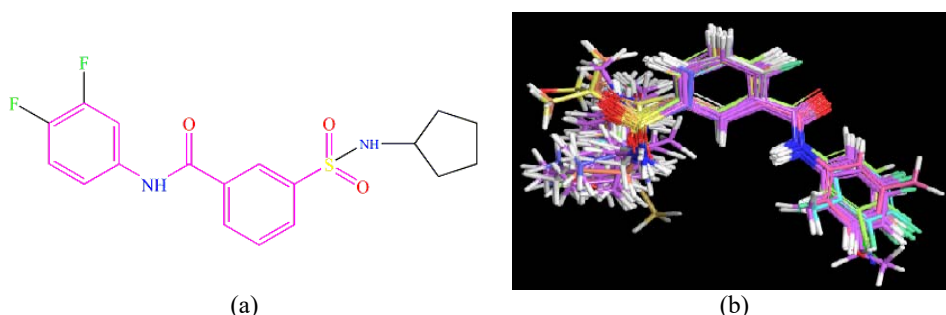


Fig 1. a) Template used for molecular alignment of anti-Hepatitis B virus. b) Structural alignment of the dataset chosen for the QSAR model.

The binding affinity of the ligand Co-crystalline K89 (sulfamoylbenzamide, or SBA) was -44.40 kJ/mol. This ligand formed hydrogen bonds with the amino residues TRP102, LEU140 and THR128 (Fig. 2). The binding affinity for the *N*-phenyl-3-sulfamoyl-benzamide derivatives was similar to that of the ligand co-crystalline K89, ranging from -42.34 to -27.66 kJ/mol. These derivatives formed hydrogen bonds with the residues TRP102 and THR128 (refer to Fig. 2). These conserved hydrogen bonding interactions appear to be key determinants for the binding of this chemical series to the HBV core protein, suggesting a common binding mode and contributing significantly to the observed binding affinities. Beyond hydrogen bonding, a range of other important interactions contributed to the overall binding stability. Significant hydrophobic interactions were noted with the residues PHE23, TYR118, PRO25, ILE105, PRO138, TRP102, LEU101 and LEU140. These extensive hydrophobic contacts play a crucial role in anchoring the non-polar portions of the ligands within the hydrophobic pockets of the active site, thereby enhancing binding affinity through the hydrophobic effect. Furthermore, electrostatic interactions were observed, with a negatively charged interaction noted with ASP29 and a positively charged interaction with the residue ARG127.



Fig. 2. 3D and 2D interaction between the Hepatitis B virus core protein (PDB ID: 5T2P) and the co-crystalline ligand (K89), as well as compound **8**.

These charged interactions contribute to the specificity and strength of binding, particularly when the ligand possesses complementary charges. Additionally, Polar interactions occurred with the amino acid residues SER106, SER121 and THR33, further supporting the overall ligand-receptor recognition.

Notably, compounds that exhibited higher predicted anti-HBV activity (higher pEC₅₀ values from the QSAR model) consistently showed more favorable (lower) docking scores. It formed a greater number of these crucial stabilizing interactions (*e.g.*, hydrogen bonds with TRP102/THR128, extensive hydrophobic contacts and favorable electrostatic interactions). For instance, beyond compound **8** (illustrated in Fig. 2), compounds **5**, **7**, **38**, **39** and **42** demonstrated the most favorable binding affinities, aligning well with their predicted high biological activity.

In this study, a 3D-QSAR model was developed using the atom-based 3D-QSAR approach within the phase module. The model underwent internal validation with an R^2 value for the training set and external validation with a Q^2 value for the test set. Table I summarizes the statistical parameters. The results revealed a strong correlation between the predicted and actual activity values, as shown in Table II, demonstrating the model's predictive capability. The QSAR model exhibited strong predictive performance, with key values of $R^2 = 0.94$, $R^2_{cv} = 0.61$, and $Q^2 = 0.85$, indicating its reliability. Furthermore, the low standard deviation (SD) of 0.17 and $RMSE$ of 0.18 underscored the high quality of the dataset for QSAR analysis. Fig. 3 illustrates the correlation between the training and test sets' actual and predicted pEC₅₀ values. These findings pave the way for further research into optimizing compound design and enhancing drug efficacy in future studies.

TABLE I. PLS Statistics parameters of the 3D-QSAR model

PLS statistics	3D-QSAR model	Threshold
<i>PLS</i> : partial least square	3	N training set: 5
<i>SD</i> : standard deviation	0.17	Smaller value
R^2 : Regression coefficient	0.94	>0.6
R^2_{cv} : cross-validated correlation coefficient	0.61	>0.5
Stability	0.755	Maximal value of 1
F : ratio of the model variance	151.8	High value
P : significance level of variance ratio	7.94e-18	Smaller value
$RMSE$: root-mean-square error	0.18	Smaller value
Q^2 : Correlation coefficient for the test set	0.85	>0.6
Pearson- r : correlation between the predicted and observed activity	0.85	—
Contribution, %		
H-bond donor	7	—
Hydrophobic	68	—
Positive ionic	2.9	—
Electrostatic	17.8	—
Other	4.3	—

3D-QSAR study

Four contributions were applied in the construction of the model: H-bond donor, hydrophobic, positive and electrostatic. Table I shows that the hydrophobic (68 %) and electrostatic (17.8 %) groups contributed most to anti-Hepatitis B activity.

TABLE II. Actual (pEC_{50}) and predicted (pEC_{50pred}) values along with the residual of the dataset

<i>N</i>	EC_{50}	pEC_{50}	pEC_{50Pred}	Residual	<i>N</i>	EC_{50}	pEC_{50}	pEC_{50Pred}	Residual
Training Set					32	2.22	5.65	5.72	0.07
2	0.78	6.11	6.26	0.15	33	3.63	5.44	5.46	0.02
4	0.60	6.22	6.12	-0.10	34	0.38	6.08	6.29	0.21
5	0.36	6.44	6.40	-0.04	36	2.33	5.63	5.91	0.28
7	0.27	6.57	6.36	-0.21	37	0.07	7.16	7.10	-0.06
8	0.038	7.41	6.99	-0.42	38	0.31	6.51	6.50	0.01
11	1.99	5.70	5.90	0.20	39	0.21	6.68	6.80	0.12
13	26.5	4.58	4.40	-0.18	40	1.40	5.85	5.88	0.03
14	7.10	5.15	5.07	-0.08	41	0.32	6.50	6.28	-0.21
15	8.49	5.07	5.06	-0.01	42	2.74	6.92	6.89	-0.03
16	4.53	5.34	5.29	-0.05	44	3.06	5.51	5.65	0.14
18	0.75	6.13	6.23	0.10	Test set				
20	0.34	6.47	6.29	-0.18	1	2.60	5.86	5.63	0.05
22	2.10	6.08	6.06	-0.02	3	0.66	6.18	6.38	0.20
23	0.96	5.68	5.87	0.20	6	4.18	5.38	5.25	-0.13
24	1.18	6.02	5.82	-0.20	9	0.28	6.55	6.25	-0.30
25	0.54	5.93	6.04	0.12	10	0.10	7.00	6.93	0.07
26	6.77	6.27	6.40	0.13	12	4.50	5.35	5.13	-0.22
27	5.30	5.17	5.13	-0.04	17	0.74	6.13	5.99	-0.14
28	0.93	5.27	5.16	-0.12	19	0.75	6.13	6.16	0.03
29	0.12	6.03	6.23	0.20	21	1.21	5.91	5.93	0.02
30	2.10	6.92	6.77	-0.15	35	0.81	6.09	6.16	0.07
31	0.29	6.54	6.67	0.13	43	3.06	5.56	5.95	0.38

Contour plots of the 3D-QSAR model

Contour plots from a quantitative structure–activity relationship (3D-QSAR) model are valuable tools for gaining a deeper understanding of how the molecular properties of compounds influence their biological activity.^{28,29} It is particularly important in the context of 3D-QSAR analysis. These plots can show regions where specific interactions (such as hydrogen bond donor, electrostatic or hydrophobic interactions) are favorable or unfavorable for biological activity.³⁰ The results contribute to the development of new selective agents and inhibitors for the hepatitis B virus. In Fig. 4, the contour plots utilize compound **8** as a reference to illustrate how hydrogen bond donor, electrostatic, and hydrophobic interactions influence the compound's effectiveness in combating the virus.

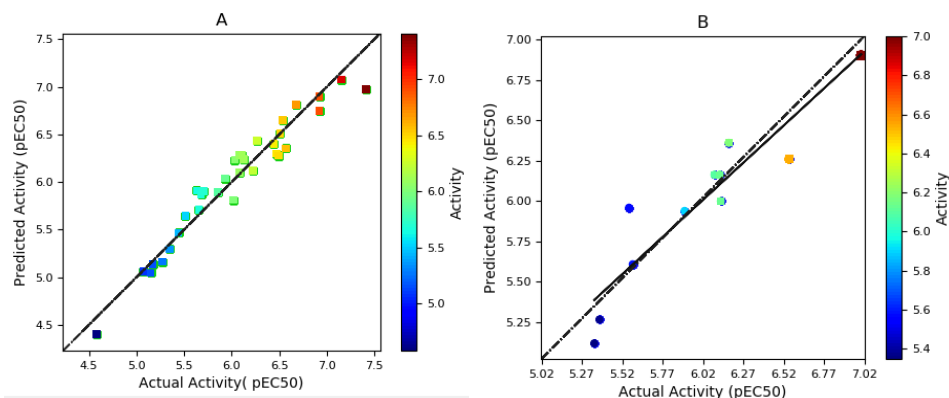


Fig. 3. Graph of predicted vs. actual pEC_{50} values for the training set (A) and test set (B).

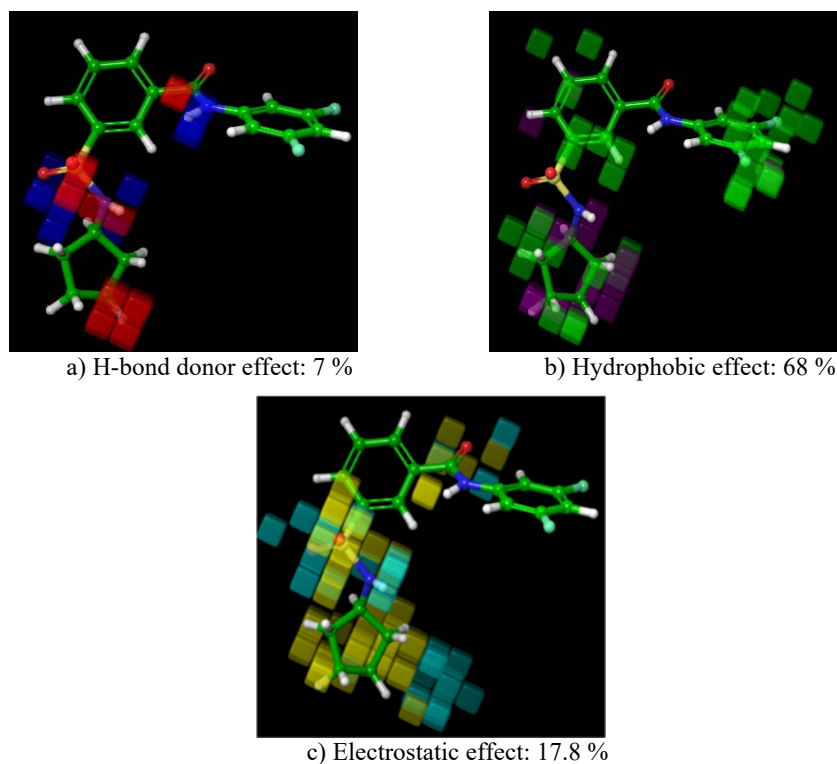


Fig. 4. Visualization of atom-based 3D-QSAR contour maps for the most active compound **8**.

In the hydrogen bond donor effect (Fig. 4a), the blue cube suggests that the hydrogen bond donor groups (such as $-NH$ or $-OH$ groups) can improve biological activity, while the red cube suggests that some of these groups can be detrimental to biological activity. The blue cubes are located near the amid group ($-CO-NH-$)

and sulfonamide ($-\text{NH}-\text{SO}_2-$) group compounds. The location suggests that these groups can interact favorably with the biological target *via* hydrogen bonds, thereby increasing the compound's activity.

In the hydrophobic effect (Fig. 4b), the green cubes indicate regions where hydrophobic interactions can enhance biological activity. Green cubes are near the compound's phenyl and cyclopentane groups. These hydrophobic interactions may promote the compound's adhesion to the biological target or help stabilize the active conformation. Purple cubes indicate regions where hydrophobic interactions are unfavorable and impair biological activity. Also, the green cubes seen near the fluorinated groups on the phenyl group show that these hydrophobic interactions are good for activity.

In the electrostatic effect (Fig. 4c), the yellow cubes indicate that electrostatic groups enhance biological activity. Electrostatic groups withdraw electrons, making the compound more reactive and improving its interaction with the biological target. The presence of yellow cubes near the sulfonamide group and the amid group suggests that these groups promote beneficial interactions for activity. In contrast, the cyan cubes show regions where electrostatic groups can impair biological activity.

Design of new inhibitors of Hepatitis B

The molecular docking analysis of the new compounds (Fig. S-1 of the Supplementary material) revealed a $\pi-\pi$ interaction with the amino acid PHE110. While a hydrogen bond acceptor interaction was observed at residue THR196, hydrogen bond donor interactions were noted at residues THR33, THR128 and LEU140. The binding affinity for the newly designed compounds (ranging from -44.14 to -39.24 kJ mol^{-1}) was analogous to that of the *N*-phenyl-3-sulfamoyl-benzamide derivatives (range: -42.34 to -26.02 kJ mol^{-1}), suggesting that the newly designed compounds exhibited a higher binding affinity for the inhibition of Hepatitis B. The 2D ligand interaction diagram for the newly designed compounds is shown in Fig S-1. Additionally, the docking results of the newly designed compounds and their predicted pEC_{50} values are detailed in Table III.

TABLE III. Molecular docking results and predicted pEC_{50} values of the newly designed compounds

Design	XP-Gscore (kJ/mol^{-1})	E-model (kJ/mol^{-1})	Key interacting residues	pEC_{50} Predict
D1	-44.14	-388.40	LEU140, PHE110, THR128, TRP102, THR38	5.46
D2	-42.84	-364.30	LEU140, PHE110, THR128, TRP102, THR38	5.60
D3	-42.47	-369.66	LEU140, PHE110, THR128, TRP102, THR38	5.56
D4	-42.09	-374.22	LEU140, PHE110, THR128, TRP102	5.81

TABLE III. Continued

Design	XP-Gscore (kJ/mol ⁻¹)	E-model (kJ/mol ⁻¹)	Key interacting residues	pEC ₅₀ Predict
D5	-42.05	-335.31	LEU140, PHE110, THR128, TRP102	5.62
D6	-41.09	-389.07	LEU140, PHE110, THR128, TRP102	5.82
D7	-40.71	-378.69	LEU140, PHE110, THR128, TRP102	6.17
D8	-39.24	-355.56	LEU140, PHE110, VAL124, TRP102	5.87
K89	-44.60	-417.06	LEU140, THR128, TRP102	/
08	-42.34	-303.13	THR128, TRP102	/

ADME-Tox of the newly designed molecules

The evaluated ADME properties indicate that the newly designed molecules exhibit favorable pharmacokinetic characteristics (Tables IV and V).

TABLE IV. Results of drug-likeness parameters; *MW*: molecular weight; *HBD*: hydrogen bond donor; *HBA*: hydrogen bond acceptor; *PSA*: polar surface area

Design	<i>MW</i>	<i>HBA</i>	<i>HBD</i>	<i>PSA</i>	Rule of five	Rule of three
D1	377.43	3.50	8.00	110.85	0	0
D2	378.42	3.00	7.75	107.18	0	0
D3	378.42	3.00	7.75	106.63	0	0
D4	396.41	3.00	7.75	106.49	0	0
D5	378.42	3.00	7.75	107.33	0	0
D6	378.42	3.00	7.75	105.53	0	0
D7	396.41	3.00	7.75	105.52	0	0
D8	377.43	3.50	8.00	108.76	0	0
Rule	>500	0 to 6	2 to 20	140	N. Viol 1	N. Viol 1

All molecules show high human oral absorption (*HOA* = 3) and an acceptable percentage of oral absorption (*PHOA*, 75–83 %). The permeability across Caco-2 and MDCK cell lines varies, with some molecules, such as D6 and D7, demonstrating high permeability. This suggests they could be beneficial for transport across the intestinal and blood–brain barriers. Additionally, the *SASA* values fall within the optimal range (300–1000 Å²), indicating that the molecular size and polarity are suitable. *QPlogBB* indicates that some molecules have limited penetration into the brain, which can be advantageous if we want to avoid unwanted central nervous system (CNS) side effects. Predicted metabolic reactions (*metab*) fall within an acceptable range of 1 to 3, suggesting that the metabolic profiles are manageable. *QPlogK_{hsa}* values show standard binding to human serum albumin, which influences drug distribution. *QPlogS* values demonstrate good solubility, supporting oral bioavailability. Additionally, *QPlogP_w* and *QPlogP_{o/w}* values fall

within ideal ranges, indicating favorable lipophilicity and permeability. The *QPlogHERG* value for most compounds is below -5.0 , suggesting potential for *hERG* channel inhibition, which is a marker for cardiotoxicity risk. Additionally, no reactive functional groups (*RtvFG* = 0) were identified, which reduces the likelihood of off-target toxicity. These newly designed compounds show strong ADME profiles and exhibit drug-like potential.

TABLE V. Results of ADMET properties; *QPlogKp*: log *Kp* for skin permeability (< -2.5 for good permeability); *HOA*, human oral absorption (1 low, 3 high); *PHOA*, percent human oral absorption (80 % high, 25 % low); *QPPCaco*; predicted apparent Caco-2 cell permeability in nm s^{-1} (<25 poor, >500 great). *QPPMDCK*; Predicted apparent MDCK cell permeability in nm s^{-1} (<25 poor, >500 great); *SASA*, solvent-accessible surface area ($300\text{--}1000 \text{ \AA}^2$); *QPlogBB*, predicted blood–brain partition coefficient (-1.5 to 1.5); *QPlogKha*, log *Khsa* serum protein binding (-1.5 to 1.5); *QPlogP_{0/w}*, octanol–water partition coefficient (-2 to 6.5); *QPlogPw*, predicted water/gas partition coefficient (4 to 45); *metab*, prediction of metabolic activity (1 to 8); *QPlogS*, predicted aqueous solubility, logarithm in mol dm^{-3} (-6.5 to 0.5); *Rotor*, number of rotatable bonds (0 to 15); *QPlogHERG*, for blocking *HERG* K^+ channel in terms of IC_{50} value (< -5.0); *RtvFG*, related to specific toxicity parameters (0 to 1 , 0 indicating non-toxicity)

Parameter	D1	D2	D3	D4	D5	D6	D7	D8
<i>QPlogKp</i>	−3.66	−3.657	−3.322	−3.491	−3.497	−3.266	−3.386	−3.601
<i>HOA</i>	3	3	3	3	3	3	3	3
<i>PHOA</i>	76.97	79.17	80.74	81.75	79.73	81.86	83.06	77.59
<i>QPPCaco</i>	149.68	173.36	204.85	202.19	177.59	234.00	234.12	156.4
<i>QPPMDCK</i>	108.56	128.78	127.75	244.42	131.94	178.76	303.05	113.5
<i>SASA</i>	649.59	646.28	640.963	648.92	645.92	634.20	641.49	652.4
<i>QPlogBB</i>	−1.64	−1.566	−1.488	−0.051	−0.059	−0.090	−0.058	−0.114
<i>QPlogKha</i>	−0.13	−0.083	−0.07	−0.051	−0.059	−0.090	−0.058	−0.114
<i>QPlogP_{0/w}</i>	1.90	1.895	2.123	2.311	2.138	2.137	2.340	1.942
<i>QPlogPw</i>	15.879	14.864	14.913	14.65	14.87	14.75	14.55	15.91
<i>metab</i>	2	1	2	1	1	2	1	3
<i>QPlogS</i>	−4.444	−4.462	−4.342	−4.804	−4.462	−4.462	−4.804	−4.324
<i>Rotor</i>	6	6	6	6	6	6	6	6
<i>QPlogHERG</i>	−5.710	−5.706	−5.562	−5.535	−5.645	−5.527	−5.403	−5.752
<i>RtvFG</i>	0	0	0	0	0	0	0	0

CONCLUSION

The current study successfully utilized a combination of atom-based 3D-QSAR modeling and molecular docking to investigate the efficacy of various *N*-phenyl-3-sulfamoyl benzamides as treatments for Hepatitis B and their mechanisms for inhibiting the virus. The developed 3D-QSAR model demonstrated a strong predictive capability with high correlation coefficients ($R^2 = 0.94$ for the training set, $Q^2_{\text{cv}} = 0.61$, and $Q^2 = 0.85$ for the test set), reflecting a good agreement between experimental and theoretical results. The molecular docking studies were conducted to elucidate the binding interactions further and analyze how these molecules bind to the target HBV core protein. Additionally, ADMET predictions

suggested that the newly designed molecules possess favorable pharmacokinetic properties and drug-likeness, indicating their potential as promising candidates for further development. While these computational results provide strong theoretical support, it is important to acknowledge that *in silico* predictions have their limitations and require experimental validation. Future studies will focus on the synthesis and *in vitro* and *in vivo* testing of these promising compounds to experimentally confirm their anti-HBV activity and pharmacokinetic profiles. Overall, integrating QSAR modeling, docking studies, and ADMET profiling provides valuable insight into the rational design of novel antiviral agents targeting Hepatitis B.

SUPPLEMENTARY MATERIAL

Additional data and information are available electronically at the pages of journal website: <https://www.shd-pub.org.rs/index.php/JSCS/article/view/13358>, or from the corresponding author on request.

ИЗВОД

N-ФЕНИЛ-3-СУЛФАМОИЛ-БЕНЗАМИДНИ ДЕРИВАТИ КАО КАНДИДАТИ ЗА АНТИВИРУСНЕ АГЕНСЕ ПРОТИВ ХЕПАТИТИСА Б: ИНТЕГРИСАНЕ РАЧУНАРСКЕ СТУДИЈЕ

AICHA LAOUD¹, ABDERAHMANE BELAFRIKH² и MARWA ALAQARBEN³

¹Chemical Engineering Department, Faculty of Chemical Engineering, University of Salah Boubnider Constantine 3, Constantine, 25000, Algeria, ²Laboratory of LCPMM, Chemistry Department, Faculty of Sciences, University of Blida1, P.O. Box 270 Blida, 09000, Algeria и ³Basic Science Department, Prince Al Hussein Bin Abdullah II Academy for Civil Protection, Al-Balqa Applied University, Al-Salt, Jordan

У овом раду примењен је комбиновани приступ атомистички заснованог 3D-QSAR моделовања и молекулског докинга за испитивање 44 N-фенил-3-сулфамоил-бензамидних деривата као потенцијалних инхибитора вируса хепатитиса Б (HBV). Развијени QSAR модел показао је снажну статистичку поузданост, са високим коефицијентом корелације за тренинг сет ($R^2 = 0,94$), унакрсно валидираним коефицијентом ($Q^2_{cv} = 0,65$), и коефицијентом корелације за тест сет ($R^2 = 0,85$), коришћењем три PLS-компоненте. Контурним мапама објашњени су модификовани региони једињења, прецизирајући доноре водоничних веза, хидрофобне интеракције и електростатичке ефекте. Докинг је потврдио резултате 3D-QSAR модела и објаснио интеракције молекула са рецепторима. Генерално, 3D-QSAR модел и анализа докинг резултата пружају важан увид у дизајн молекула са побољшаном активношћу против вируса хепатитиса Б.

(Примљено 30. априла, ревидирано 19. јуна, прихваћено 4. августа 2025)

REFERENCES

1. M. Kirstgen, S. F. Müller, K. Alessandra, A. Theresa, N. Goldmann, F. Lehmann, S. Alakurtti, J. Yli-kauhaluoma, K. Baringhaus, R. Krieg, D. Glebe, J. Geyer, *Viruses* **13** (2021) 1489 (<https://doi.org/10.3390/v13081489>)
2. C. Huang, Y. Jin, P. Fu, K. Hu, M. Wang, W. Zai, T. Hua, X. Song, J. Ye, Y. Zhang, G. Luo, H. Wang, J. Liu, J. Chen, X. Li, Z. Yuan, *Acta. Pharm. Sin., B* **14** (2024) 4914 (<https://doi.org/10.1016/j.apsb.2024.07.019>)

3. T. Ruengstra, A. Meeprasert, E. Rattanangkool, S. Deesiri, J. Srisa, U. Udomnilobol, W. Dunkoksung, N. Chuaypen, R. Kiatbumrung, P. Tangkijvanich, S. Vimolmangkang, K. Pudhom, T. Prueksaritanont, *RSC Adv.* **13** (2023) 29004 (<https://doi.org/10.1039/D3RA04720B>)
4. G. C. Fanning, F. Zoulim, J. Hou, A. Bertoletti, *Nat. Rev. Drug. Discov.* **18** (2019) 827 (<https://doi.org/10.1038/s41573-019-0037-0>)
5. X. Zhang, J. Cheng, J. Ma, Z. Hu, S. Wu, N. Hwang, J. Kulp, Y. Du, J. T. Guo, J. Chang, *ACS Infect. Dis.* **5** (2019) 759 (<https://doi.org/10.1021/acsinfecdis.8b00269>)
6. J. Sanchitra, A. Debnath, A. K. Singh, A. K. Jha, R. K. Singh, *Sci. Rep.* **15** (2025) 13054 (<https://doi.org/10.1038/s41598-025-97242-6>)
7. A. Mohebbi, S. P. T. Nabavi, M. Naderi, K. Sharifian, F. Behnezhad, M. Mohebbi, A. Gholami, F. S. Askari, A. Mirarab, S. H. Monavari, *In Silico Pharmacol.* **13** (2025) 35 (<https://doi.org/10.1007/s40203-025-00314-8>)
8. K. Vandyck, G. Rombouts, B. Stoops, A. Tahri, A. Vos, W. Verschueren, Y. Wu, J. Yang, F. Hou, B. Huang, K. Vergauwen, P. Dehertogh, J. M. Berke, P. Raboisson, *J. Med. Chem.* **61** (2018) 6247 (<https://doi.org/10.1021/acs.jmedchem.8b00654>)
9. S. Ejeh, A. Uzairu, G. A. Shallangwa, S. E. Abechi, *Future J. Pharm. Sci.* **7** (2021) 219 (<https://doi.org/10.1186/s43094-021-00373-6>)
10. S. Ejeh, A. Uzairu, G. A. Shallangwa, S. E. Abechi, M. T. Ibrahim, *Bull. Natl. Res. Cent.* **46** (2022) 109 (<https://doi.org/10.1186/s42269-022-00796-y>)
11. A. Laoud, F. Ferkous, L. Maccari, G. Maccari, Y. Saihi, K. Kraim, *Comput. Biol. Chem.* **72** (2018) 122 (<https://doi.org/10.1016/j.compbiolchem.2017.12.003>)
12. H. Nour, O. Daoui, O. Abchir, S. Elkhatabi, S. Belaidi, S. Chtita, *Helvion* **8** (2022) e11991 (<https://doi.org/10.1016/j.helivon.2022.e11991>)
13. O. Mafethe, T. Ntseane, T. H. Dongola, A. Shonhai, N. J. Gumede, F. Mokoena, *ACS Omega* **8** (2023) 38220 (<https://doi.org/10.1021/acsomega.3c04494>)
14. S. Mirzaei, R. Ghodsi, F. Hadizadeh, A. Sahebkar, *Biomed. Res. Int.* **6** (2022) 9761279 (<https://doi.org/10.1155/2021/6480804>)
15. N. Chahbaoui, S. Khamouli, M. Alaqarbeh, S. Belaidi, L. Sinha, S. Chtita, M. Bouachrine, *J. Biomol. Struct. Dyn.* **42** (2024) 12021 (<https://doi.org/10.1080/07391102.2023.2266502>)
16. D. A. Omoboyowa, *Chem. Africa* **5** (2022) 871 (<https://doi.org/10.1007/s42250-022-00373-w>)
17. C. Hanwarinroj, N. Phusi, B. Kamsri, P. Kamsri, A. Punkvang, S. Kettrat, P. Saparpakorn, S. Hannongbua, K. Suttisintong, P. Kittakoo, J. Spencer, A. J. Mulholland, P. Pungpo, *Future Med. Chem.* **14** (2022) 717 (<https://doi.org/10.4155/fmc-2021-0348>)
18. A. Belafriekh, A. Laoud, L. Mchichi, M. Bouachrine, *Phys. Chem. Res.* **12** (2024) 729 (<https://doi.org/10.22036/pcr.2024.425052.2448>)
19. F. Olawale, O. Iwaloye, K. Olofinisan, O. M. Ogunyemi, G. A. Gyebi, I. M. Ibrahim, *Chem. Pap.* **76** (2022) 3729 (<https://doi.org/10.1007/s11696-022-02128-w>)
20. A. K. Maurya, V. Mulpuru, N. Mishra, *ACS Omega* **5** (2020) 32234 (<https://doi.org/10.1021/acsomega.0c03871>)
21. A. Ali, M. H. Abdellatif, A. Ali, O. Abuali, M. Shahbaaz, M. J. Ahsan, M. A. Hussien, *Molecules* **26** (2021) 5932 (<https://doi.org/10.3390/molecules26195932>)
22. A. Laoud, F. Ali-Rachedi, F. Ferkous, *Phys. Chem. Res.* **11** (2023) 459 (<https://doi.org/10.22036/pcr.2022.342259.2106>)

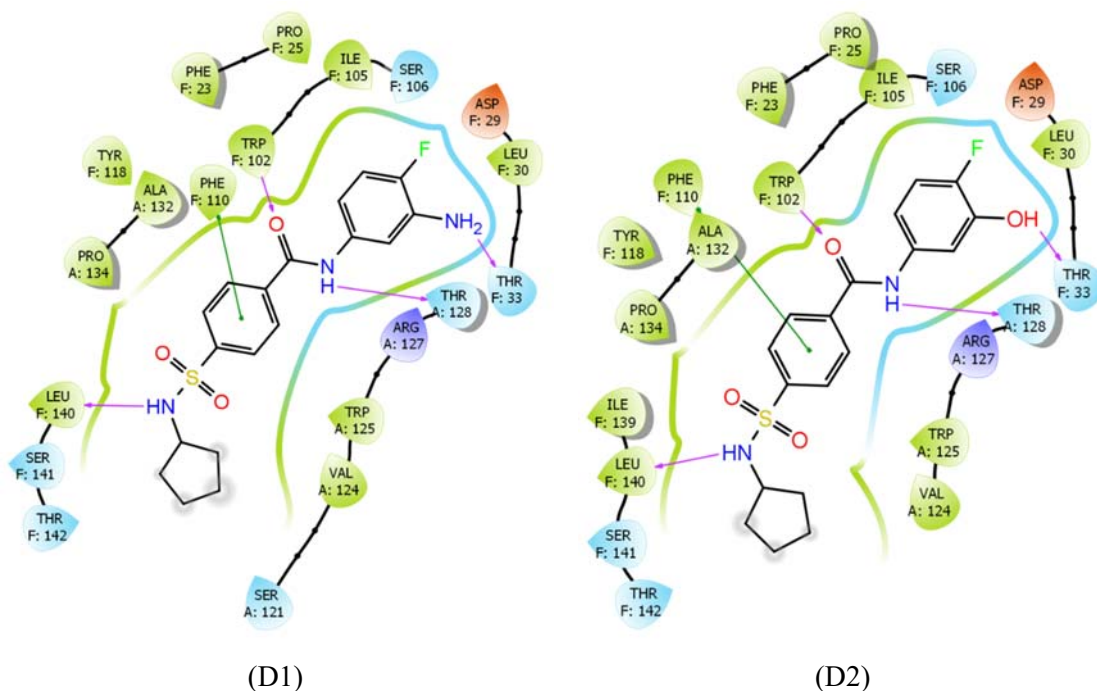
23. A. A. Poola, P. S. Prabhu, T. P. K. Murthy, M. Murahari, S. Krishna, M. Samantaray, A. Ramaswamy, *Front. Mol. Biosci.* **10** (2023) 1106128 (<https://doi.org/10.3389/fmolb.2023.1106128>)
24. K. Tabti, S. Baammi, A. Sbair, H. Maghat, M. Bouachrine, *J. Biomol. Struct. Dyn.* **41** (2023) 13798 (<https://doi.org/10.1080/07391102.2023.2183032>)
25. M. A. Azam, J. Thathan, S. Jupudi, *Comput. Biol. Chem.* **84** (2020) 107197 (<https://doi.org/10.1016/j.compbiolchem.2019.107197>)
26. M. Elbouhi, K. Tabti, M. Ouabane, M. Alaqarbeh, K. Elkamel, T. Lakhli, A. Sbair, M. Bouachrine, *Chem. Heterocycl. Compd.* **60** (2024) 627 (<https://doi.org/10.1007/s10593-025-03386-8>)
27. S. Ahmad, D. Gupta, T. Ahmed, A. Islam, *J. Biomol. Struct. Dyn.* **41** (2023) 14016 (<https://doi.org/10.1080/07391102.2023.2176361>)
28. U. Panwar, S. K. Singh, *Struct. Chem.* **32** (2021) 337 (<https://doi.org/10.1007/s11224-020-01628-3>)
29. R. Dias, W. F. J. de Azevedo, *Curr. Drug Targets* **9** (2008) 1040 (<https://doi.org/10.2174/138945008786949432>)
30. V. M. Kulkarni, S. Bhansali, *Res. Reports Med. Chem.* **4** (2014) 1 (<https://doi.org/10.2147/rrmc.s50738>).

SUPPLEMENTARY MATERIAL TO
***N*-Phenyl-3-sulfamoyl-benzamide derivatives as anti-Hepatitis B virus agent candidates. Integrated computational studies**

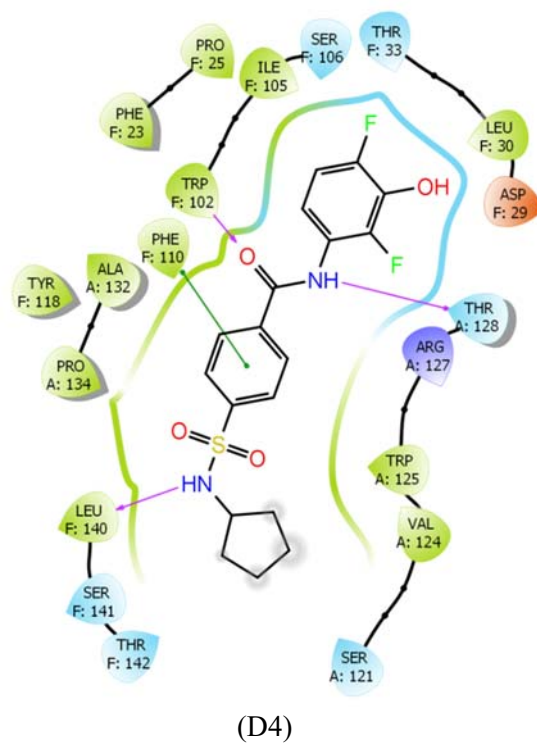
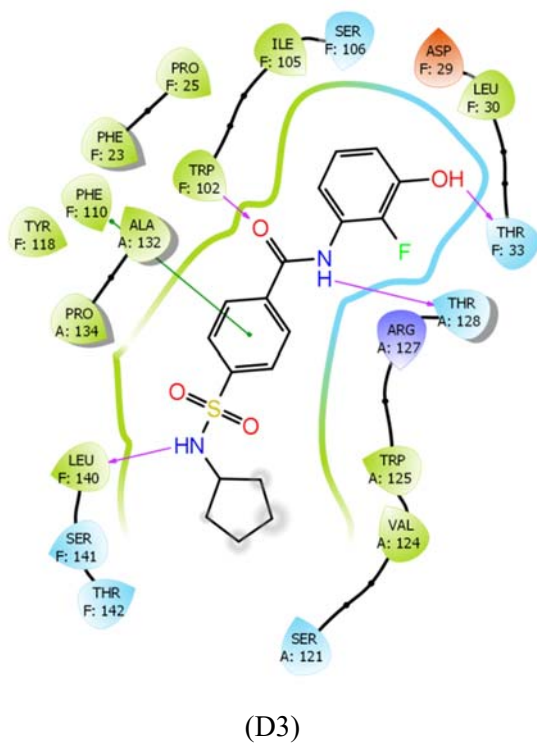
AICHA LAOUD¹, ABDERAHMANE BELAFRIEKH^{2*} and MARWA ALAQARBEH³

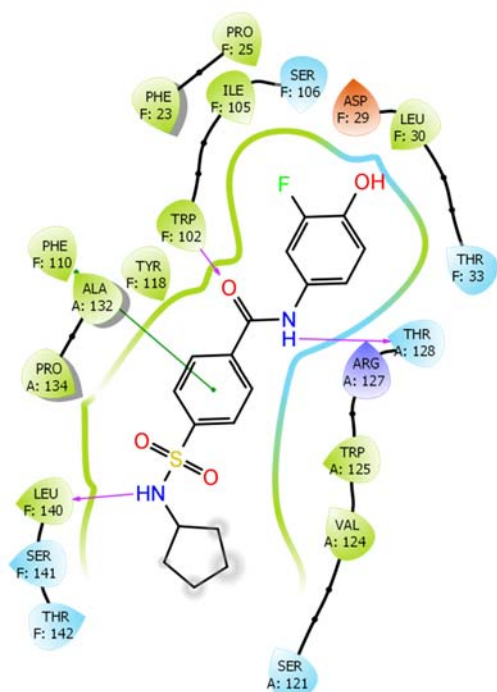
¹Chemical Engineering Department, Faculty of Chemical Engineering, University of Salah Bounider Constantine 3, Constantine, 25000, Algeria, ²Laboratory of LCPMM, Chemistry Department, Faculty of Sciences, University of Blida1, P.O. Box 270 Blida, 09000, Algeria and ³Basic Science Department, Prince Al Hussein Bin Abdullah II Academy for Civil Protection, Al-Balqa Applied University, Al-Salt, Jordan

J. Serb. Chem. Soc. 90 (10) (2025) 1175–1187

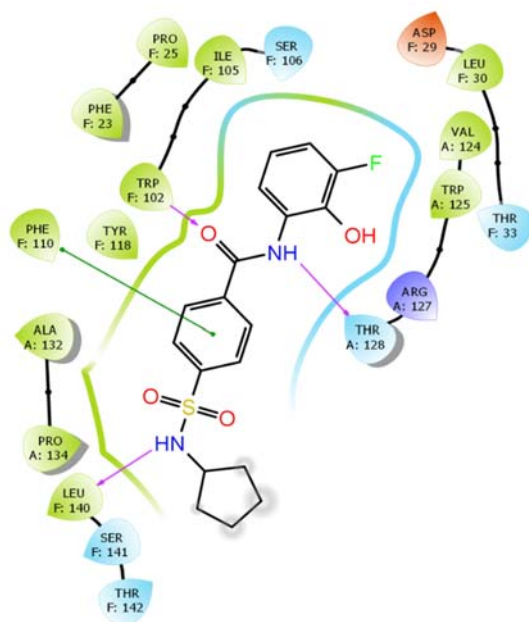


* Corresponding author. E-mail: a.belafriekh@gmail.com





(D5)



(D6)

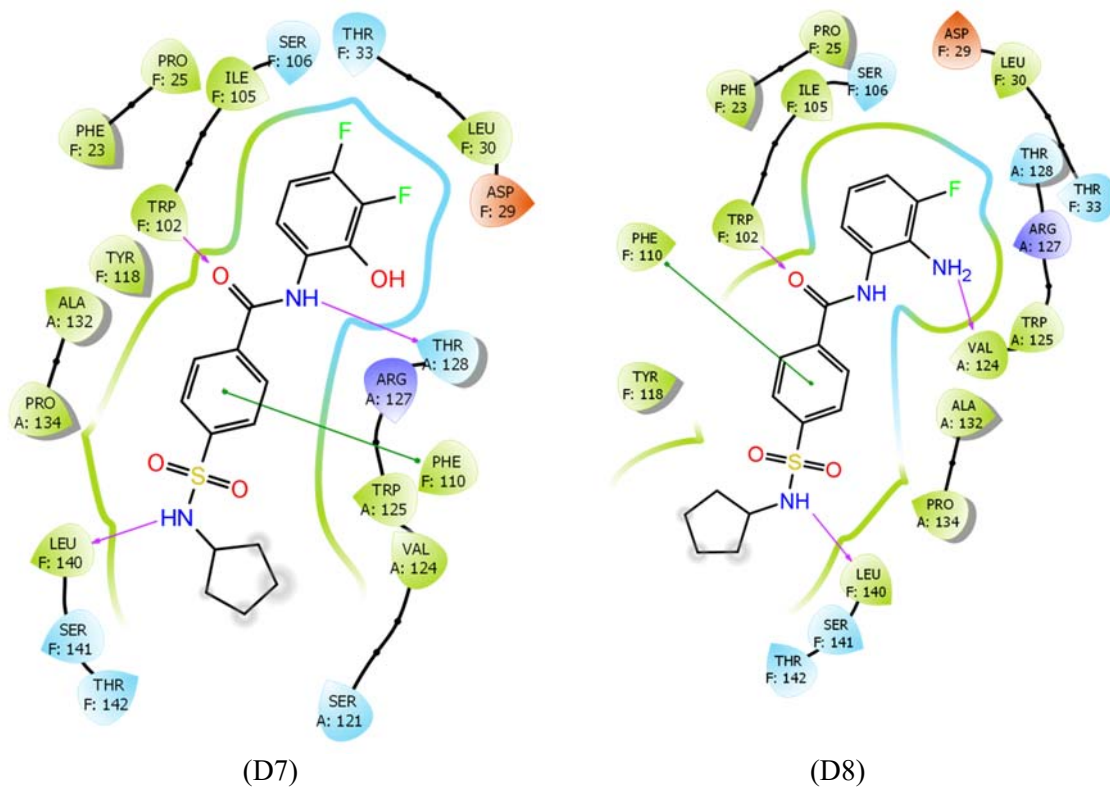
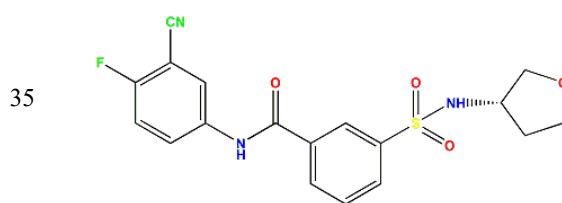
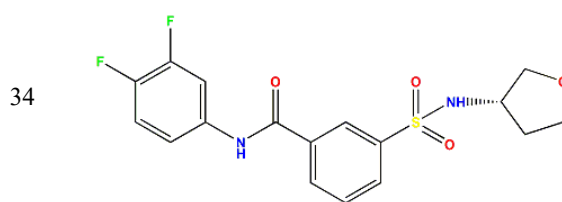
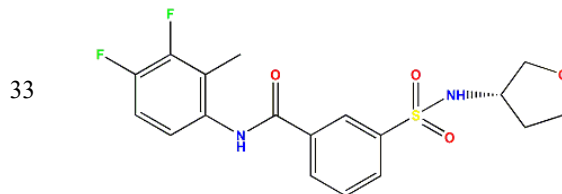
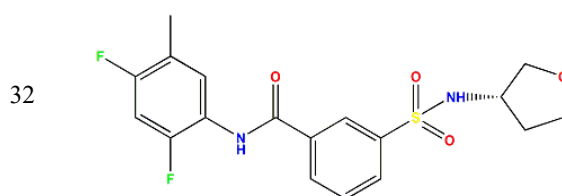
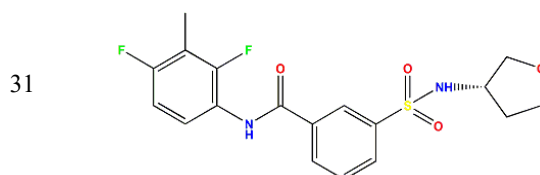
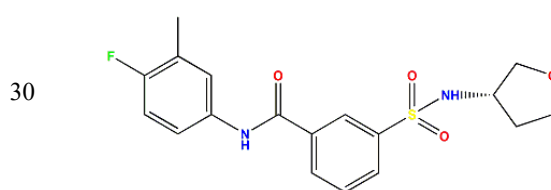
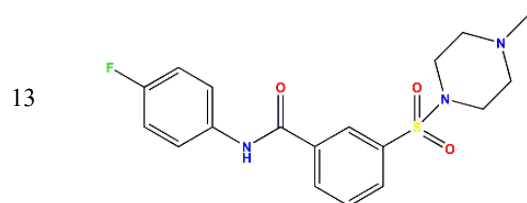
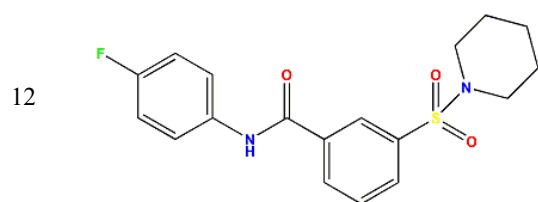
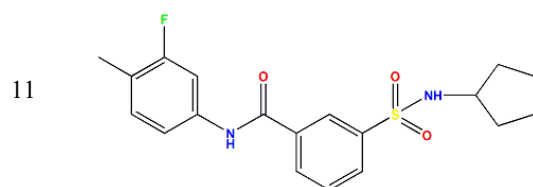
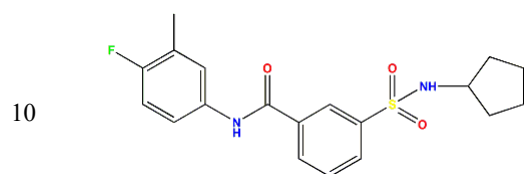
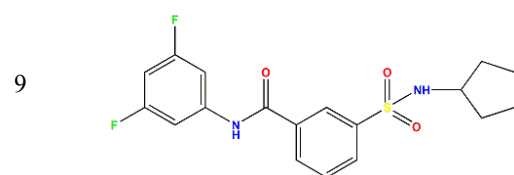
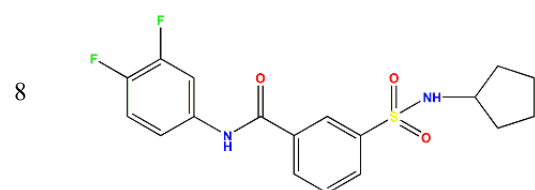
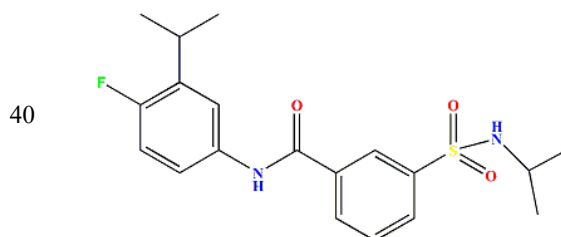
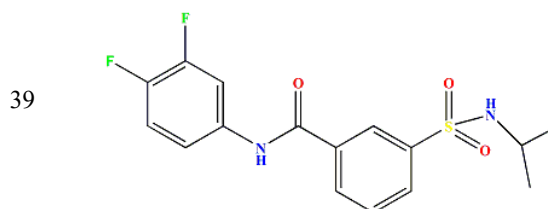
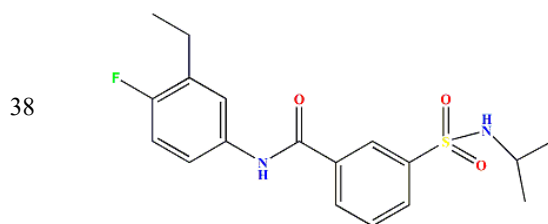
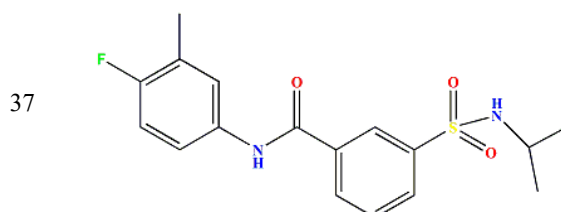
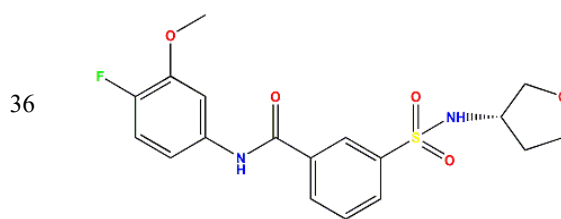
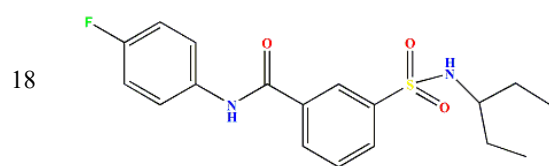
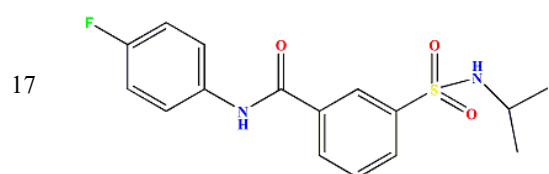
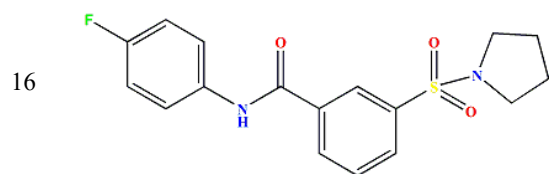
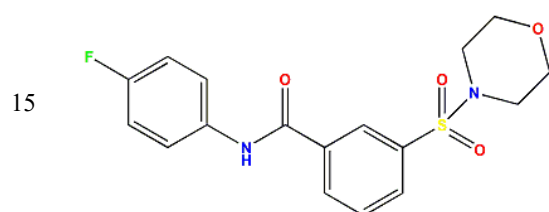
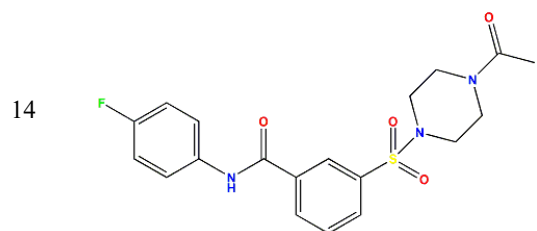


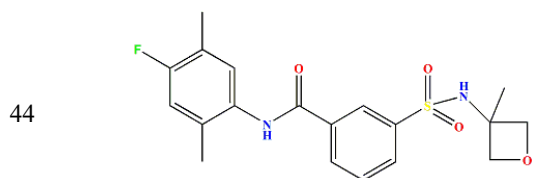
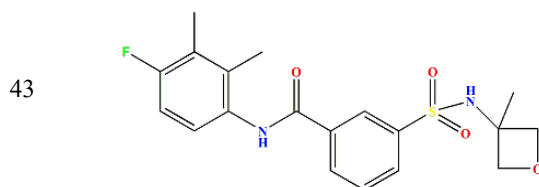
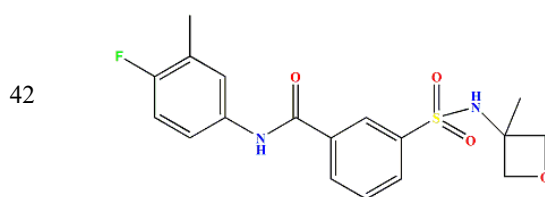
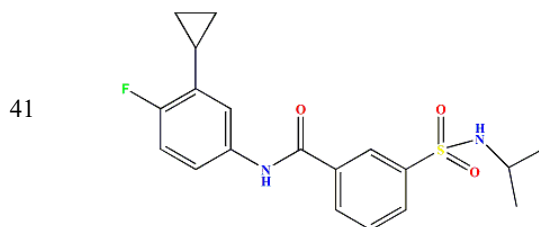
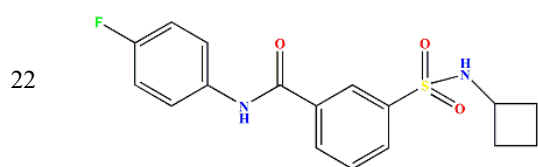
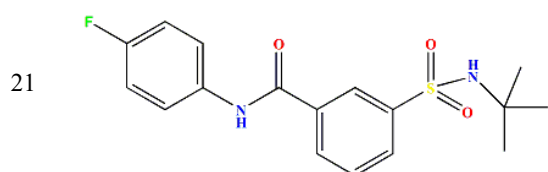
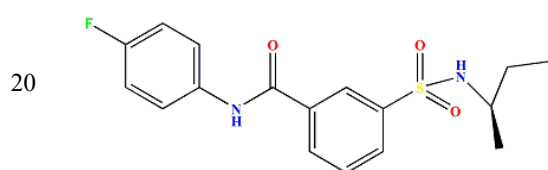
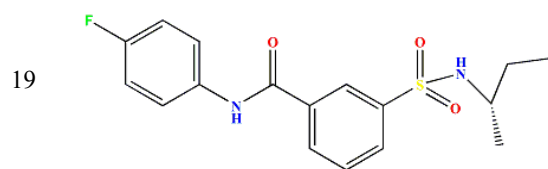
Fig. S-1. 2D interaction diagram of selected designed compounds with the HBV core protein (PDB: ID:2T5P).

TABLE S-I. Chemical structures of N-Phenyl-3-sulfamoyl-benzamide derivatives.

compound		compound	
1		23	
2		24	
3		25	
4		26	
5		27	
6		28	
7		29	









J. Serb. Chem. Soc. 90 (10) 1189–1201 (2025)
JSCS–5448

Investigation of multi-walled carbon nanotubes catalytic activity by means of the model aerobic oxidation reaction

NARMIN MUSTAFAYEVA*, ELDAR ZEYNALOV, ASGAR HUSEYNOV,
YAGUB NAGİYEV, MEHPARA NADİRİ and MATANAT MAHARRAMOVA

Ministry of Science and Education of the Republic of Azerbaijan, Institute of Catalysis and Inorganic Chemistry named after Academician Murtuza Nagiyev, AZ1143 Baku, Azerbaijan

(Received 23 January, revised 30 March, accepted 3 August 2025)

Abstract: This study investigates the synthesis of multi-walled carbon nanotubes (MWCNTs) *via* chemical vapor deposition (CVD) using propane gas and evaluates their catalytic efficiency in oxidation reactions. The MWCNTs were synthesized in a laboratory-scale CVD reactor under optimized conditions, with ferrocene used as a precursor to incorporate 9.8 wt. % iron into the nanotube structure. The catalytic activity of the synthesized MWCNTs was evaluated in the cumene oxidation reaction, demonstrating remarkable performance even at relatively low temperatures. This enhanced catalytic efficiency is attributed to the presence of iron compounds within the MWCNT channels, which are presumed to act as active sites for the reaction. Among the catalysts studied, the G-CVD-1 sample containing 9.8 wt. % iron showed the highest performance, accelerating the oxidation reaction by a factor of 23 compared to the uncatalyzed process. In comparison, the L-CVD-184 sample, with a lower iron content of 3.7 wt. %, achieved a 16-fold increase in reaction rate relative to the same uncatalyzed baseline. These values indicate that the iron concentration within MWCNTs plays a crucial role in determining their catalytic efficiency, with higher iron loading providing significantly better activity. This study demonstrates that iron-modified MWCNTs possess significant potential as durable and efficient catalysts for oxidation reactions.

Keywords: metal-containing carbon nanotubes; CVD reactor; catalyst; cumene; kinetic parameters; oxygen rate.

INTRODUCTION

Carbon nanotubes (CNTs) have emerged as distinctive allotropes of carbon, exhibiting substantial applications across various domains, including technology and catalysis. Their applications predominantly encompass nanotechnology, nanomedicine,¹ transistors, actuators, sensors,² membranes and capacitors.³

*Corresponding author. E-mail: nabdurrehmanova@mail.ru
<https://doi.org/10.2298/JSC250123061M>

In recent years, carbon nanotubes have garnered significant attention in the realm of nanocatalysis, drawing extensive investigation from researchers worldwide. Notable characteristics of CNTs include their lightweight nature, diminutive size, coupled with high surface area, impressive tensile strength, non-toxicity, and excellent electrical conductivity. These properties render CNTs highly advantageous as fillers in diverse materials such as polymers, metal surfaces and ceramics.^{4,5} Furthermore, numerous studies have demonstrated that the incorporation of various functional groups^{6–11} and metal atoms^{12–16} into CNTs yields catalysts with markedly enhanced catalytic activity compared to other carbon allotropes.

For instance, nitrogen-doped carbon nanotubes have been effectively utilized as catalysts in the aerobic oxidation of cyclohexane to adipic acid, along with its precursors, cyclohexanol and cyclohexanone.¹⁷ Multi-walled carbon nanotubes have been directly employed by Wang and colleagues as more durable and environmentally friendly catalyst for the conversion of ethanol to acetaldehyde in the presence of molecular oxygen. The C=O groups generated on the nanocarbon surface have been identified as active sites for the selective oxidation of ethanol to acetaldehyde, achieving approximately 60 % ethanol conversion with 93 % selectivity for acetaldehyde at an optimized temperature of 270 °C. Notably, the catalytic activity exhibited remarkable stability over a duration of 500 h, comparable to that of supported gold catalysts. This robust catalytic performance underscores the potential industrial applications of CNTs in catalysis. Further investigations have revealed that nanocarbon materials function as effective catalysts for activating C–H bonds in carbon nanotubes, short-chain alkanes in either the gas or liquid phase or ethylbenzene. A prominent example is the oxidative dehydrogenation of ethylbenzene to styrene facilitated by oxygen atoms. The absence of strong Lewis acid metal cations minimizes coke formation, thus preserving catalyst activity.¹⁸

In another study, carbon nanotubes functionalized with oxygen-containing groups were developed as novel catalyst types (*e.g.*, V₂O₅/TiO₂–CNTs–OH, V/Ti–CNTs–OH, V₂O₅/TiO₂–CNTs–COOH, V/Ti–CNTs–COOH and V₂O₅/TiO₂–CNTs, V/Ti–CNTs). These catalysts were employed to catalytically degrade 1,2-dichlorobenzene at low temperatures (150 °C). The findings revealed that the modification with oxygen-containing functional groups significantly enhanced the catalytic activity of V/Ti–CNTs, particularly highlighting the exceptional performance of the V/Ti–CNTs–COOH catalyst at low temperatures.¹⁹

In a separate investigation, researchers focused on iron and nitrogen atoms, developing two distinct CNT catalysts: single-walled CNTs (Fe–N–SWCNT) and double-walled CNTs (Fe–N–DWCNT). They conducted both experimental and theoretical studies on CO₂ conversion, emphasizing the effects of electrical energy on CO₂ conversion with increasing CNT diameter. The study established

that Fe–N–DWCNT exhibited superior catalytic activity for CO₂ adsorption compared to Fe–N–SWCNT while maintaining catalyst stability. Notably, Fe–N–DWCNT demonstrated potential for selective HCOOH production from CO₂ conversion.²⁰

Moreover, the catalytic activity of the Fe₂O₃/CNT catalyst in the selective oxidation of ammonia was examined in a constant flow reactor. Results indicated that the incorporation of iron(III) oxide onto carbon nanotubes effectively enhanced the electronic properties of the CNTs. Under the influence of this catalyst, NO conversion exceeded 90 % within a temperature range of 200–325 °C. Furthermore, studies indicated that the Fe₂O₃/CNTs catalyst displayed resistance to SO₂/H₂O, demonstrating considerable reaction stability.²¹

As highlighted, research into nanocarbon-based catalysts suggests their significant potential for industrial applications, presenting a viable alternative to metal-based catalysts with relatively high economic value. The field of nanocatalysis stands on the cusp of significant growth as a new area of inquiry. However, several limitations, particularly concerning production costs, impede the large-scale application of carbon nanotubes.³

Various methods have been employed for synthesizing carbon nanotubes, with parameters such as sample purity, structural integrity, surface area, surface load, particle size distribution, surface chemistry and agglomeration conditions significantly influencing the reactivity of CNTs.²² The most widely accepted synthesis methods for carbon nanotubes include: 1) chemical vapor deposition,^{23,24} 2) laser ablation^{25,26} and 3) carbon arc discharge.^{27–29} Each method presents distinct advantages and drawbacks; however, CVD is regarded as the most economically feasible approach for large-scale, high-purity CNT production, primarily due to its ability to yield high-purity samples and facilitate straightforward control of the reaction medium.^{22,30}

The predominant hydrocarbon sources utilized in CNT production *via* the CVD method include petrochemical products such as methane, ethane and acetylene, as well as petroleum derivatives like natural gas and kerosene.³¹ The selection of hydrocarbon precursors plays a critical role in determining the growth, physicochemical and thermodynamic properties of CNTs. The gas-phase synthesis method is particularly advantageous, yielding less contaminated CNTs while also permitting large-scale production.^{32,33}

Given these considerations, the catalytic oxidation of hydrocarbons utilizing CNTs represents a novel priority, with ongoing developments in its fundamental and applied aspects. Nonetheless, the inefficiencies associated with large-scale CNT production remain a principal challenge. This article elucidates the production of carbon nanotubes from inexpensive raw materials and explores their catalytic activity in the oxidation reaction of isopropylbenzene.

EXPERIMENTAL

This study commenced with the synthesis of multi-walled carbon nanotubes from a gas feedstock (propane) through chemical vapor deposition in the gas phase. The selection of the propane gas mixture as a precursor for carbon nanotube synthesis is justified by its potential for multi-tonnage production within our country, as well as its ability to yield cleaner, flatter, and relatively larger carbon nanotubes.

To facilitate this process, an expanded laboratory setup was established, leading to the synthesis of various samples of MWCNT (G-CVD-1). The apparatus (Fig. 1) comprises five primary components.

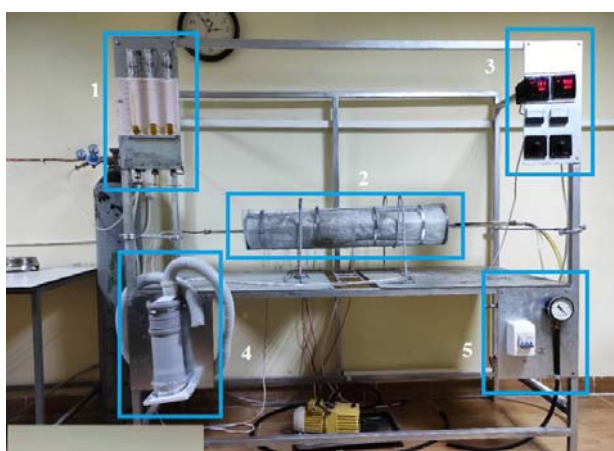


Fig. 1. MWCNT synthesis device; 1 – gas raw material preparation unit: the gas raw material (propane, butane, their mixture) is diluted with argon to the required concentration and fed to the reactor zone at a certain speed. 2 – Reactor block: it consists of 2 parts, each of which is heated independently by a tubular furnace with a quartz reactor inside. The furnace heats the reactor to a temperature of 1000 °C. 3 – Furnace temperature control unit block: this consists of a temperature regulator that automatically controls and maintains the set temperature in the reactor and two regulators to supply current to the furnace coil. 4 – air supply block. 5 – Vacuum block: to create a vacuum in the reactor, the block is designed for the synthesis of CNT at reduced pressures (80–20 kPa). The unit consists of a vacuum pump, a valve and a manometer.

Preparation of G-CVD-1 catalyst using chemical vapor deposition in the gas phase

During the process, propane gas is mixed with argon in the primary gas mixture preparation block. The flow rate of propane is $q_{\text{propane}} = 6 \text{ L h}^{-1}$, while that of argon is $q_{\text{argon}} = 60 \text{ L h}^{-1}$, resulting in an argon-to-propane volume ratio of 10:1. The prepared gas mixture is directed into a quartz reactor housed within a furnace. In the first section of the reactor, the temperature is maintained at 200 °C. Here, 1 g of ferrocene is placed in a specialized ceramic container, where it serves as the precursor for the catalyst. At this stage, the argon-propane mixture is combined with ferrocene vapor and introduced into the second section of the reactor, where the temperature is increased to 900 °C. At 900 °C, ferrocene vapor undergoes decomposition, leading to the release of iron atoms, which form nanoscale clusters within the reactor. These clusters play a crucial role in the synthesis of carbon nanotubes. It is noteworthy that

the synthesis of carbon nanotubes primarily occurs via the growth mechanism facilitated by iron atoms derived from ferrocene. However, ferrocene itself does not directly participate in the reaction mechanism. These clusters act as catalysts during the synthesis process. Simultaneously, propane undergoes cracking in the second section of the reactor. The resulting carbon deposits grow on the Fe clusters, leading to the formation of multi-walled carbon nanotubes. Upon completion of the synthesis process, which lasts for 40–60 min, the flow of propane is stopped. The system is allowed to cool, after which the quartz tube is removed from the reactor (furnace). The MWCNTs deposited on the inner walls of the tube are collected using a metal rod. A fraction of the Fe catalyst used during the synthesis remains embedded within the MWCNTs. The mass fraction of the catalyst in the nanotubes was determined through combustion analysis.³⁴ The catalytic activity of the newly synthesized sample containing 9.8 wt. % Fe atoms (MWCNT (G-CVD-1)) was evaluated using the model reaction of cumene oxidation. Oxidation experiments were conducted in a gasometric device,^{12,13} where molecular oxygen (atmospheric oxygen) was employed to investigate the kinetic characteristics of cumene oxidation. The measurements were carried out by the volumetric method, based on the rise of the liquid level in the burette due to the adsorption of oxygen. The total volume of the reaction mixture was 10 mL, and the reaction was conducted at a constant temperature of 60 °C. The oxygen pressure in the system was maintained at 20 kPa (under air atmosphere). As the reaction was performed in a gasometric setup without the use of any solvents (under pure conditions), the starting concentration of cumene reflects that of its undiluted liquid form at the specified conditions ($\approx 6.9 \text{ mol L}^{-1}$).

These pressure values were selected to ensure that oxygen actively participates as a reactive component. Initially, the reaction was carried out under control conditions without the addition of carbon nanotubes to the reaction mixture. In this case, the catalyst sample was not involved in the reaction, and the reaction rate depended solely on the intrinsic properties of the reactants.

In the second stage, the reaction was performed by introducing the MWCNT (G-CVD-1) catalyst sample into the mixture at a concentration of 0.005 g L^{-1} . In the third stage, the MWCNT (G-CVD-1) catalyst was added at two different concentrations (0.01 and 0.02 g L^{-1}) to the reaction mixture. The volume of oxygen adsorbed during the reaction was the primary parameter used to evaluate the reaction rate and the efficiency of the catalyst. Using the same methodology,¹³ investigations were conducted with the L-CVD-184 catalyst sample synthesized *via* the CVD method from a liquid carbon source, containing 3.7 wt. % Fe. Unlike the previous catalyst sample, the initiation of the reaction with L-CVD-184 involved the use of azobisisobutyronitrile (AIBN) as a radical initiator. AIBN decomposes at elevated temperatures, triggering the initiation stage of the reaction mechanism.

RESULTS AND DISCUSSION

The scanning electron microscope (SEM, Fig. 2A), transmission electron microscope (TEM, Fig. 2B) and energy-dispersive X-ray (EDX) imaging (Fig. 2C) of the synthesized MWCNT (G-CVD-1) are presented below.

The SEM image of the MWCNT (G-CVD-1) catalyst sample illustrates the surface and morphology of the synthesized multi-walled carbon nanotubes. The fibers or tubular structures visible in the image correspond to multi-walled carbon nanotubes, which are tubular carbon materials with diameters measured in nanometers and lengths in the micrometer range. The magnification factor used in

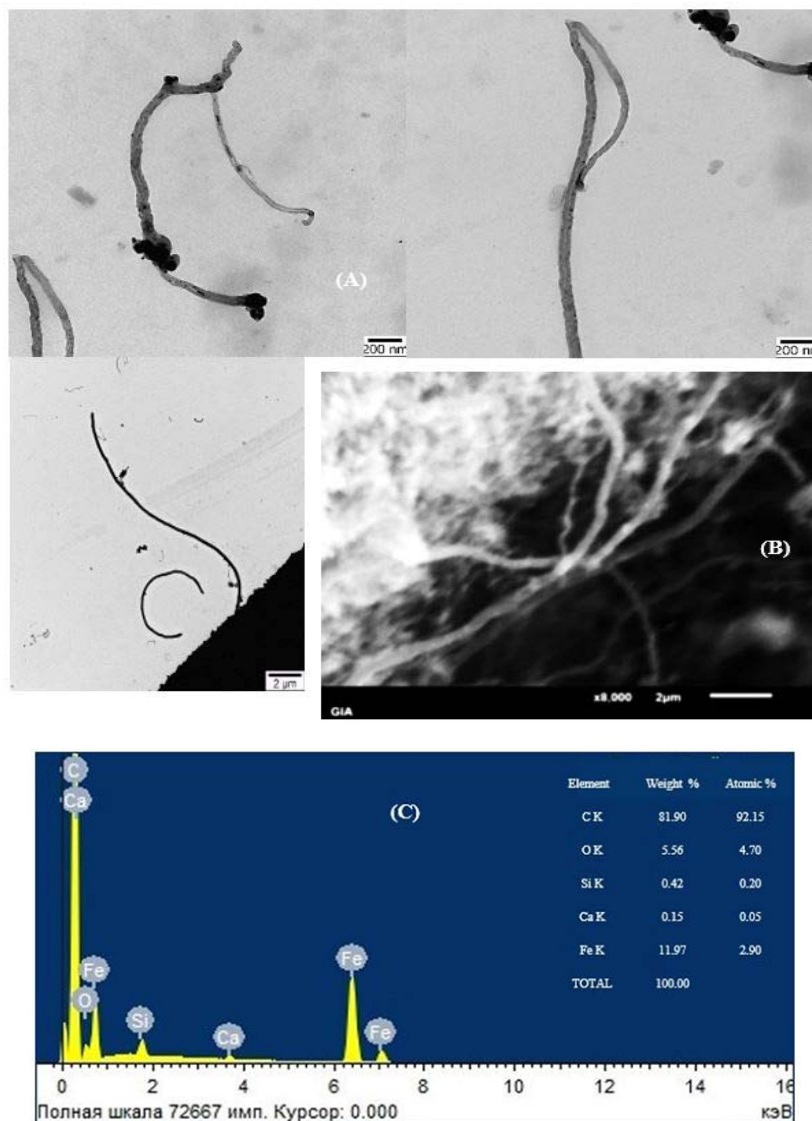


Fig. 2. Synthesized MWCNT (G-CVD-1) images: SEM (A), TEM (B) and EDX (C). (Scanning electron microscope JEOL, JSM6610LV. Oxford Instrument; Transmission Electron Microscope JEM-1400 (JEOL, Japan)).

the analysis was 8,000 \times , allowing for detailed observation of the sample's nanostructures. The diameters of the tubular structures range approximately from a few to 100 nm. The surface of the tubes appears smooth, indicating the high quality of the synthesis method. Furthermore, the tubes are observed to be entangled with one another, demonstrating their high surface area and nanoscale pro-

perties. As shown in the provided images, the synthesized MWCNT (G-CVD-1) exhibits a smooth surface, is free from visible defects, and features a linear morphology characterized by minimal bending and cracking. These observations suggest that the synthesized MWCNT (G-CVD-1) is of high quality and possesses minimal structural imperfections (Fig. 2A).

The TEM images depict the structural characteristics of the synthesized multi-walled carbon nanotubes (MWCNT (G-CVD-1)). The tubular structures, a defining feature of MWCNTs, are clearly visible. These structures consist of concentric graphene layers wrapped around each other. The images reveal that the MWCNTs are long, thin, and tubular in shape, with diameters measured on the nanometer scale (indicated by a 200 nm scale bar). In the first image, some of the tubes appear slightly bent or deformed. This deformation could be attributed to the conditions of the synthesis process or subsequent sample processing. In the second image, a straighter and more uniform tube is observed, indicative of a higher-quality structure with fewer defects. In both images, dark dot-like structures can be seen at the ends or along certain sections of the tubes. These are metal catalyst particles (Fe) used during the synthesis process. These particles act as nucleation points for the growth of MWCNTs, enabling carbon deposition through catalytic decomposition (Fig. 2B). The EDX analysis indicates that the primary component of the sample is carbon, comprising 81.90 mass % and 92.15 at. %. This confirms that the material is carbon-based. The iron content is measured at 11.97 mass % and 2.90 at. %, demonstrating the presence of iron in the sample, likely in the form of oxides (Fig. 2C).

Recent studies highlight that the unique physical properties of carbon nanotubes provide a solid foundation for the development of novel and efficient heterogeneous catalytic systems. Laboratory experiments have led to the creation of a new multi-walled carbon nanotube formulation containing iron, which exhibits high selectivity and efficiency. This catalyst serves as a versatile system, demonstrating significant effectiveness in the oxidation of various homologous hydrocarbons. The structural integrity of the MWCNT (G-CVD-1) catalyst, synthesized *via* the chemical vapor deposition method using propane, was confirmed through SEM analysis (Fig. 2A). Energy-dispersive X-ray spectroscopy analysis further revealed a substantial iron content (11.97 wt. %), emphasizing its critical role in the material. The incorporation of iron atoms during synthesis through the use of ferrocene as a catalyst precursor is particularly noteworthy.

In this study, the catalytic activity of iron-containing multi-walled carbon nanotubes in the aerobic oxidation reaction of cumene was analyzed. Experiments were conducted at a temperature of 60 °C, and the oxygen adsorption kinetics of the MWCNT (G-CVD-1) catalyst, synthesized from propane gas, were comparatively investigated to evaluate their effect on the oxidation reaction of

cumene. The catalyst contains 9.8 wt. % Fe, which significantly influences the reaction rate and kinetics.

Reaction rate without catalyst

The reaction rate without the catalyst was measured as $y = 0.0072x$. This value indicates that the reaction proceeds very slowly without a catalyst and can only occur at high temperatures and over a long period. The reaction under uncatalyzed conditions exhibits very low kinetics, which demonstrates the necessity of a catalyst to accelerate the process. From the given data, it is clear that the iron-containing MWCNT (G-CVD-1) catalyst lowers the activation energy of the reaction, significantly increases the reaction rate, and this effect is further enhanced as the iron content increases (Fig. 3).

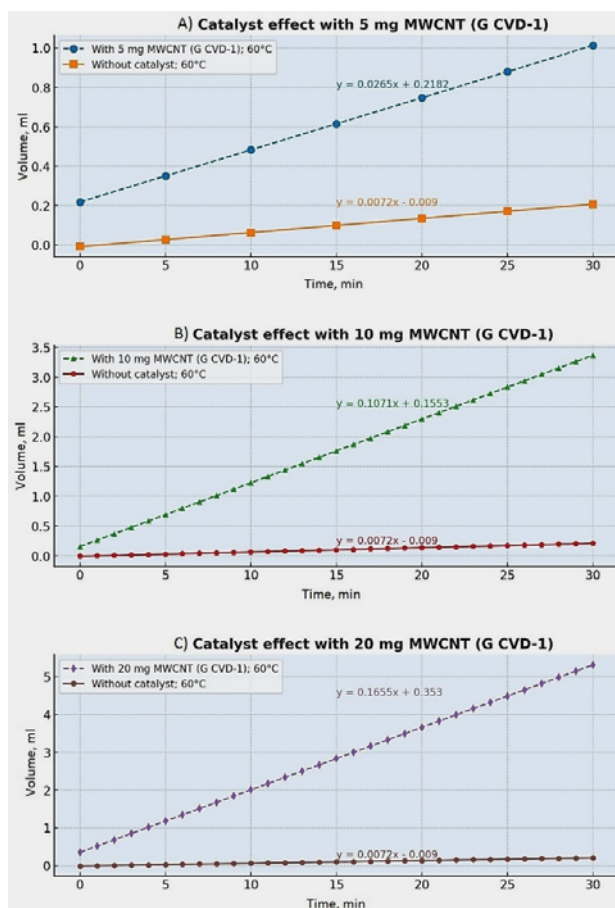


Fig. 3. Kinetic dependences of oxygen adsorption in aerobic oxidation reaction in the liquid phase of cumene in the presence of MWCNT (G-CVD-1) (9.8 wt. % Fe) catalysts synthesized from propane gas.

Effect of MWCNT catalyst quantity on reaction rate

In an experiment where 5, 10 and 20 mg quantities of MWCNT (G-CVD-1) catalyst were used, it was observed that as the quantity increased, the reaction rate also increased. With 5 mg of MWCNT (G-CVD-1) catalyst, the reaction rate was measured as $y = 0.0265x$ (Fig. 3A), while with 10 mg, it increased to $y = 0.1071x$ (Fig. 3B). This caused the reaction to accelerate by approximately 3 and 15 times, respectively. With 20 mg of MWCNT (G-CVD-1), the oxygen adsorption rate further increased, and a 23-fold acceleration was observed, with $y = 0.1655x$ (Fig. 3C). This is due to the increase in the number of active sites on the catalyst surface as the amount of catalyst increases, leading to more collisions of reactive molecules with the surface, thus speeding up the reaction. However, when a certain threshold is reached, increasing the catalyst amount may not significantly affect the reaction rate. This is due to limitations related to the concentration of reactive species (substrate saturation).

Effect of Fe content on reaction rate

Experiments show that the high Fe content (9.8 wt. %) in the MWCNT (G-CVD-1) catalyst further accelerates the reaction compared to the MWCNT (L-CVD-184) catalyst sample with 3.7 wt. % Fe. The rate constant is 1.2 times higher ($0.1304/0.1086 \approx 1.2$, Fig. 4). This difference can be explained by the following mechanism: Fe nanoclusters on the surface of the carbon nanotube exhibit high catalytic activity. It is clear that the catalyst sample with a higher amount of Fe nanoclusters (e.g., 9.8 wt. % Fe) provides more active sites,

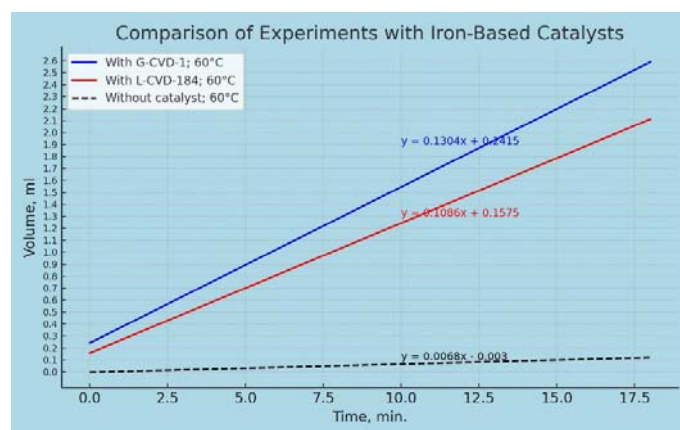


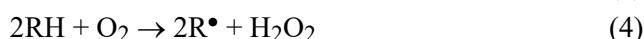
Fig. 4. Kinetic dependences of oxygen adsorption in the liquid phase aerobic oxidation reaction in the presence of catalysts MWCNT (G-CVD-1) and MWCNT (L-CVD-184) in the liquid phase of cumene. MWCNT (G-CVD-1) – carbon nanotubes synthesized from propane gas in the gas phase (9.8 wt. % Fe); MWCNT (L-CVD-184) – carbon nanotubes synthesized from cyclohexane in the liquid phase (3.7 wt. % Fe). Experimental conditions: cumene – 10 ml; AIBN – 10 mg; catalyst (G-CVD-1 or L-CVD-184) – 20 mg.

accelerating the reaction rate. More Fe clusters increase effective collisions with reactive molecules, thus reducing the activation energy and speeding up the reaction. This leads to the conclusion that Fe facilitates electron transfer in oxidation processes and promotes the formation of reactive oxygen species.

Reaction mechanisms and effective oxidation rate

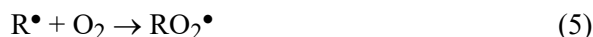
The general pathway for the aerobic catalytic oxidation of cumene in the presence of MWCNT (G-CVD-1) is illustrated as follows, where W_{O_2} represents the effective oxidation rate. The overall reaction steps (Eqs. (1)–(11)) follow the conventional numbering and notation system commonly used for hydrocarbon oxidation chain reactions in the scientific literature:^{35,36}

Chain nucleation (formation of alkyl R^\bullet radicals, rate W_o):

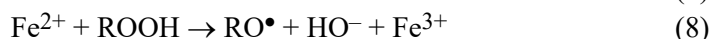
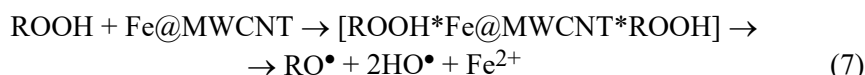


where M is a metal (Fe).

Continuation and development of the chain (rate W_d):



The presence of a carbon nanocatalyst results in the decomposition of the intermediate catalytic complex (hydroperoxide-Fe@MWCNT), leading to the formation of additional active radicals and the propagation of the reaction chain according to the following mechanism:



Open circuit (rate W_i):



The kinetic equation that describes the proposed scheme can be represented as follows:

$$W_{O_2} = (W_o + W_d)^{1/2} k_3 k_6^{1/2} [RH] \quad (11)$$

The high surface area of such nanotube structures provides more active sites, ensuring more reactions occur. The catalytic role of Fe makes the reaction faster and more efficient, which increases the potential for using MWCNTs in industrial oxidation processes.

4. Y. Yibo, M. Jianwei, Y. Zhihong, X. Fang-Xing, H. B. Yang, B. Liu, Y. Yang, *Chem. Soc. Rev.* **44** (2015) 3295 (<https://doi.org/10.1039/C4CS00492B>)
5. I. Khan, Kh. Saeed, *Carbon Letters* **14** (2013) 131 (<https://doi.org/10.5714/CL.2013.14.3.131>)
6. A. Sivaranjani, C. Lakshmi Devi, *Mater. Res. Express* **6** (2019) 1050e3 (<https://doi.org/10.1088/2053-1591/ab42ff>)
7. E. B. Zeynalov, E. R. Huseynov, N. I. Salmanova, N. A. Abdurahmanova, *Chem. Probl.* **3** (2020) 351 (<https://doi.org/10.32737/2221-8688-2020-3-351-360>)
8. E. B. Zeynalov, Y. M. Nağıyev, F. M. Mammedov, S. A. Aliyeva, M. I. Nadiri, L. I. Ahmedova, M. Y. Maharramova, N. A. Abdurehmanova, G. Sh. Asadzade, *News Baku State Univer.* **1** (2017) 18 (<http://static.bsu.az/w1/pdf%202017%20N1/1.pdf>)
9. N. A. Mustafayeva, *Azer. Chem. J.* **2022** (2022) 87 (<https://doi.org/10.32737/0005-2531-2022-3-87-92>)
10. Ya. M. Nagiyev, *Proc. Petrochem. Oil Ref.* **1** (2021) 99 (<https://www.ppor.az/jpdf/8-Naghiyev-1-2021.pdf>)
11. E. B. Zeynalov, A. B. Huseynov, S. G. Abdullayeva, N. A. Abdurahmanova, in *Proceedings of 6th International Caucasian Symposium on Polymers and Advanced Materials*, 2019, Batumi Shota Rustaveli State University, Georgia, Ivane Javakhishvili Tbilisi State University Press, Batumi, 2019, p. 115 (https://www.icsp6.tsu.ge/ge/x3_185s4csfh92rm)
12. N. A. Abdurahmanova, *Proc. Petrochem. Oil Ref.* **21** (2020) 268 (<https://ppor.az/jpdf/11-Abdurahmanova-2-2020.pdf>)
13. E. Zeynalov, A. Huseynov, E. Huseynov, N. Salmanova, Y. Nagiyev, N. Abdurakhmanova, *Chem. Chem. Technol.* **15** (2021) 479 (<https://doi.org/10.23939/chcht15.04.479>)
14. E. B. Zeynalov, Ya. M. Nagiyev, A.B. Huseynov, M. I. Nadiri, M. Kh. Abbasov, A. D. Guliyev, N. Salmanova, *SOCAR Proc.* **4** (2022) 134 (https://proceedings.socar.az/uploads/pdf/89/10.5510_OGP20220400794.pdf)
15. Ya. M. Nagiev, R. R. Apaeva, M. I. Nadiri, A. B. Guseinov, E. B. Zeynalov, *SOCAR Proc.* **3** (2023) 182 (<https://doi.org/10.5510/OGP20230300900>)
16. E. B. Zeynalov, N. S. Allen, Ya. M. Naghiev, A. B. Huseinov, F.G. Rzaev, *J. Phys. Chem. Solids* **195** (2024) 112263 (<https://doi.org/10.1016/j.jpcs.2024.112263>)
17. H. Yu, F. Peng, J. Tan, X. Hu, H. Wang, J. Yank, W. Zheng, *Angew. Chem. Int. Ed. Engl.* **50** (2011) 3978 (<https://doi.org/10.1002/anie.201007932>)
18. W. Jia, H. Rui, F. Zhenbao, L. Hongyang, S. Dangsheng, *ChemSusChem* **9** (2016) 1820 (<https://doi.org/10.1002/cssc.201600234>)
19. W. Qiulin, Z. Jianchao, T. Minghui, P. Yaqi, D. Cuicui, Y. Jianhua, L. Shengyong, *Environ. Prog. Sustain.* **38** (2019) 13221 (<https://doi.org/10.1002/ep.13221>)
20. H. S. Yoon, P. Hyunwoong, O. N. Elbashir, H. S. Dong, *Sust. Mat. Tech.* **26** (2020) e002244 (<https://doi.org/10.1016/j.susmat.2020.e00224>)
21. Q. Zhenping, M. Lei, W. Hui, F. Qiang, *Chem. Commun.* **51** (2015) 956 (<https://doi.org/10.1039/C4CC06941B>)
22. E. Ali, D. Hadis, K. Hamzeh, K. Mohammad, N. Zarghami, A. Akbarzadeh, M. Abasi, Y. Hanifehpour, S. W. Joo, *Nanoscale Res. Lett.* **9** (2014) 393 (<https://doi.org/10.1186/1556-276X-9-393>)

23. E. Abbasi, F. A. Sedigheh, A. Abolfazl, M. Morteza, H. T. Nasrabadi, S. W. Joo, Y. Hanifehpour, K. Nejati-Koshki, R. Pashaei-Asl, *Nanoscale Res. Lett.* **9** (2014) 247 (<https://doi.org/10.1186/1556-276X-9-247>)
24. Y. M. Jose., Y. M. Miki, L. Rendon, J. G. Santiesteban, *Appl. Phys. Lett.* **62** (1993) 202 (<https://doi.org/10.1063/1.109315>)
25. L. Chico, V. H. Crespi, L. X. Benedict, S. G. Louie, M. L. Cohen, *Phys. Rev. Lett.* **76** (1996) 971 (<https://doi.org/10.1103/PhysRevLett.76.971>)
26. P. M. Ajayan, T. W. Ebbesen, *Rep. Prog. Phys.* **60** (1997), 1025 (<https://doi.org/10.1088/0034-4885/60/10/001>)
27. A. Thess, R. Lee, P. Nikolaev, H. Dai, P. Petit, J. Robert, C. Xu, H. L. Young, G. K. Seong, A. G. Rinzler, D. T. Colbert, G. E. Scuseria, D. Tománek, J. E. Fischer, R. E. Smalley, *Science* **273** (1996) 483 (<https://doi.org/10.1126/science.273.5274.483>)
28. R. Hirlekar, M. Yamagar, H. Garse, M. Vij, V. Kadam, *Asian J. Pharm. Clin. Res.* **2** (2009) 17 (<https://www.innovareacademics.in/journal/ajpcr/Vol2Issue4/238.pdf>)
29. P. X. Hou, S. Bai, Q. H. Yang, C. Liu, H. M. Cheng, *Carbon* **40** (2002) 81 ([https://doi.org/10.1016/S0008-6223\(01\)00075-6](https://doi.org/10.1016/S0008-6223(01)00075-6))
30. S. P. Patole, P. S. Alegaonkar, H. C. Lee, J. B. Yoo, *Carbon* **46** (2008) 1987 (<https://doi.org/10.1016/j.carbon.2008.08.009>)
31. A. Hayder, R. Irmawati, I. Ismayadi, Y. Nor Azah, *Pertanika J. Sci. Technol.* **25** (2017) 379 (https://www.researchgate.net/publication/316988879_Hydrocarbon_Sources_for_the_Carbon_Nanotubes_Production_by_Chemical_Vapour_Deposition_A_Review)
32. E. T. Thostenson, Z. Ren, T. W. Chou, *Comp. Sci. Technol.* **6** (2001) 1899 ([https://doi.org/10.1016/S0266-3538\(01\)00094-X](https://doi.org/10.1016/S0266-3538(01)00094-X))
33. R. J. Hynes, R. Sankaranarayanan, M. Kathiresan, P. Sentharamaikkannan, in *Nanocarbon and its Composites*, A. Khan, M. Jawaaid, Inamuddin, A. M. Asiri, Eds., Woodhead Publishing, Cambridge, 2019, pp. 805–830 (<https://doi.org/10.1016/B978-0-08-102509-3.00027-4>)
34. Federal Agency for Technical Regulation and Metrology (OOO EO Engineering Safety), +7 and R 58356, 2019 (ГОСТ Р 58356-2019: Наноматериалы. Нанотрубки углеродные одностенные. Технические требования и методы испытаний (standartgost.ru))
35. N. S. Kobotaeva, T. S. Skorokhodova, N. V. Ryabova, *Russ. J. Phys. Chem., A* **89** (2015) 462 (<https://doi.org/10.1134/S0036024415030164>)
36. A. Bhattacharya, *J. Chem. Eng.* **137** (2008) 308 (<https://doi.org/10.1016/j.cej.2007.04.043>).



J. Serb. Chem. Soc. 90 (10) 1203–1221 (2025)
JSCS–5449

Optimization of deep eutectic solvent based liquid phase microextraction of PAHs in environmental samples using response surface methodology

NUR HIDAYAH SAZALI¹, MAZIDATULAKMAM MISKAM², FAIZ BUKHARI MOHD SUAH² and NURUL YANI RAHIM^{2*}

¹*Institute of Sustainable Energy and Resources, Universiti Teknologi PETRONAS, 32610 Seri Iskandar, Perak, Malaysia, and* ²*School of Chemical Sciences, Universiti Sains Malaysia, 11800 USM, Pulau Pinang, Malaysia*

(Received 24 January, revised 17 April, accepted 5 August 2025)

Abstract: The presence of polycyclic aromatic hydrocarbons (PAHs) in wastewater poses significant health risks. To address this, a novel deep eutectic solvent-based ferrofluid (DES-ferrofluid) was developed for liquid phase microextraction with back extraction (LPME-BE) to detect PAHs. The DES-ferrofluid was characterised for its physicochemical properties and morphology using FTIR, VSM and SEM-EDX. Key parameters in the LPME-BE process were optimised using response surface methodology (RSM) based on a Box–Behnken design (BBD). Optimal conditions included 15 mg of tetraethyl orthosilicate-coated magnetic nanoparticles (MNPTEOS), 25 μL of DES 1 (caprylic acid and lauric acid), 800 mg NaCl and a 10 min extraction time. Analysis of variance (ANOVA) confirmed strong alignment between experimental data and the model, with an R^2 of 0.8799 and adj. R^2 of 0.7395. The method achieved limits of detection (LODs) of 0.4–1.7 ng mL^{-1} and limits of quantification (LOQs) of 1.33–5.67 ng mL^{-1} . Recoveries for spiked samples ranged from 75.78 to 118.65 %, with $RSD < 15$ %. This DES-ferrofluid LPME-BE method with BBD optimization shows promise as an effective alternative for PAH detection in wastewater samples.

Keywords: ferrofluid; fatty acid-based deep eutectic solvent; green microextraction; Box–Behnken design.

INTRODUCTION

Polycyclic aromatic hydrocarbons (PAHs) are among the most common organic pollutants disposed of into the environment, resulting in serious environmental concerns. PAHs are chemical compounds with two or more fused benzene rings insoluble in water. PAHs with fewer than four rings are considered light

*Corresponding author. E-mail: nurulyanirahim@usm.my
<https://doi.org/10.2298/JSC250124062S>

PAHs, while PAHs with more than four rings are considered heavy PAHs. Heavy PAHs are more stable and dangerous than light PAHs.¹ PAHs result from thermal deterioration, which occurs due to the incomplete combustion of organic materials and the geochemical creation of fossil fuels. Power plants, domestic heating, waste incineration, industrial activities and, most importantly, automotive exhaust emissions are the principal sources of anthropogenic pollution.

Given by the occurrence and adverse side effects of PAHs, the development of effective analytical methods for identifying PAHs in samples is highly desired. PAHs analysis is typically conducted in various samples using chromatographic techniques such as high-performance liquid chromatography^{2,3} and gas chromatography.^{4,5} Despite their high sensitivity, the presence of PAHs at low concentrations in samples and complex matrices has hindered their direct application. A sensitive and selective sample pretreatment technique is required to clean up and pre-concentrate the analytes before chromatographic analysis.^{1,6}

Liquid-phase microextraction (LPME), a novel method for complex matrices pretreatment, can be considered an environmentally friendly, simple, easy-to-operate and highly sensitive method for preconcentration. A miniaturised preparation method allows trace determination of target compounds in complex matrices.⁷ Recently, green solvents, namely ionic liquids and deep eutectic solvents, have been significantly adopted in LPME as a substitute for hazardous solvents. The utilisation of deep eutectic solvents (DES) has garnered heightened interest in LPME.⁸ DES is a combination of two compounds: a hydrogen-bonding donor and a hydrogen-bonding acceptor, which form a eutectic mixture. Deep eutectic solvents (DES) exhibit characteristics similar to ionic liquids (IL), such as high thermal stability, viscosity and high tunability, rendering them a good substitute for hazardous solvents.^{9,10} Owing to their distinctive physicochemical characteristics, DES are advantageous in diverse extraction processes, such as serving as coating agents or carrier liquids in producing ferrofluids.^{4,11,12}

Ferrofluid liquid-phase microextraction (LPME) is a novel and environmentally friendly method that utilizes magnetic nanoparticles (MNPs) dispersed in a carrier fluid. This technique does not require centrifugation or advanced equipment, allowing for rapid phase separation with the aid of an external magnetic field. Surface coating techniques that use surfactants or ionic charges to preserve colloidal stability are employed to stop MNPs sediment and clumping together due to their high reactivity. Because of their low toxicity, affordability, environmental sustainability and capacity to modify the physicochemical characteristics of ferrofluids for improved extraction performance, deep eutectic solvents (DESs) have become the preferred choice for the carrier fluid.

Numerous experiments have shown that DES-based ferrofluids can extract analytes from complicated matrices. Dil *et al.* developed a hydrophobic octanoic acid–DL–menthol DES ferrofluid to determine the amount of doxycycline in urine,

blood plasma and milk.¹³ This method achieved excellent extraction efficiency using 150 μL of ferrofluid and 7 min of vortex. Zarei *et al.* created a magnetic clay nanoparticle coated with a menthol–decanoic acid DES to remove explosives from water, producing recovery rates ranging from 88 to 104 %.¹⁴ Similarly, Jouyban *et al.* extracted 16 PAHs from urine and saliva using a toner-based ferrofluid modified with choline chloride–stearic acid DES, with recoveries ranging from 61 to 84 %.⁴ In a different application, PAHs were extracted from grilled meat using a ternary DES (phosphocholine:menthol:decanoic acid) ferrofluid, which produced excellent recovery and selectivity.¹² Mohebbi *et al.* extracted pesticides such as diazinon, deltamethrin and fenpropathrin using a choline chloride–stearic acid ferrofluid, achieving recovery rates of 82–94 % and enrichment factors of 1643–1884.¹⁵ To extract PAHs from coffee, Fan *et al.* created a ternary DES (menthol–borneol–camphor) ferrofluid, which achieved recovery rates of 91–121 % and detection limits of 0.31–5.9 ng L^{-1} .¹⁶

Tamoxifen and its active metabolites were extracted from plasma more recently by Abarbakouh *et al.* using a ferrofluid dispersive solid-phase microextraction in conjunction with LC–UV.¹⁷ They achieved low detection limits (0.2–200 $\mu\text{g/L}$), precision (intra-day ≤ 7.5 %; inter-day ≤ 11.2 %), and accuracy (94–105 %). For the quantification of remdesivir in human plasma, Morovati *et al.* used a DES–IL ferrofluid microextraction approach, which produced a linear range of 0.5–500 $\mu\text{g L}^{-1}$, low detection limits (0.2 $\mu\text{g L}^{-1}$), and good precision (intra-day ≈ 9 %; inter-day ≈ 17 %) and accuracy (90–107 %).¹⁸ Due to their avoidance of centrifugation and external dispersive solvents, these techniques align with the principles of green analytical chemistry. Therefore, they are ideal for regular pharmaceutical tests, therapeutic monitoring, and clinical pharmacokinetic research.

Despite significant advancements, little is known about the long-term stability, reusability and environmental impact of ferrofluids based on deep eutectic solvents (DES). There are also few studies investigating their compatibility with automated platforms, potential toxicity profiles, and comparative performance across different analyte classes and matrices. Further research is needed to fully demonstrate the scope, reliability and sustainability of ferrofluid-based microextraction procedures.

Several important parameters, such as the type of solvents, pH and solvent volume, must be optimised to establish optimal extraction procedure conditions. Previous research has presented the “trial and error” strategy, in which one parameter is changed at a time while other parameters must remain constant to achieve effective analyte separation.^{19,20} Due to the enormous number of experimental steps and organic solvent consumption, testing the parameters at such levels is time-consuming and cost-ineffective, resulting in unsatisfactory results. Conversely, this approach does not demonstrate the interactive response at the extreme values of independent parameters.²⁰

Hence, response surface methodology (RSM) is critical in determining the ideal combination of parameters that produces the best chromatographic responses, such as sensitivity, recovery, and peak area. RSM is a statistical technique that is a significant tool for modelling and analysing the impacts of various process parameters. The underlying principle is to get the best conditions by doing the fewest trials possible and estimating interactions between the independent variables. Several previous studies have combined sample pretreatment methods with statistical analysis tools to optimise their experimental process by reducing the number of experiments while improving the accuracy of the results. The use of RSM to optimise experimental conditions has been widely used in various extraction techniques, including PAHs determination^{21,22} and organo-phosphate pesticide determination.^{23–25} Response surface methodology (RSM), which includes central composite design (CCD), Box–Behnken design (BBD) and Doehlert design, is used to optimise the most important independent parameter and determine the optimum amount of each factor.²⁶ BBD is primarily a factorial design used in RSM to examine the quadratic response surface and construct second-order polynomial models. BBD is a spherical, three-level fractional factorial design comprised of a central point and the middle points of the circle's circumscribed edges of the sphere.^{26,27} BBD needs fewer experimental runs than other factorial designs, making it more practical and cost-effective.^{26,28}

Further research is imperative to understand the effect of independent variables on the LPME-BE technique utilising DES-based ferrofluids with Box–Behnken design. Therefore, this work aims to investigate RSM experimental design approaches for optimising independent parameters and validate the method for quantifying PAHs determination using the DES-based ferrofluids LPME method. In addition, DES-based ferrofluid LPME with back extraction was employed to analyse extracted PAHs in various environmental samples.

EXPERIMENTAL

Chemicals and reagents

All fatty acids (caprylic acid ($\geq 99.0\%$), capric acid ($\geq 98.0\%$), pelargonic acid ($\geq 97.0\%$) and lauric acid ($\geq 98.0\%$) were purchased from Sigma–Aldrich. Iron (III) chloride hexahydrate ($\text{FeCl}_3 \cdot 6\text{H}_2\text{O}$) and ammonium iron (II) sulphate hexahydrate ($(\text{NH}_4)_2\text{Fe}(\text{SO}_4)_2 \cdot 6\text{H}_2\text{O}$) were obtained from QRec (Auckland, New Zealand). Tetraethyl orthosilicate ($\geq 98.0\%$) was purchased from Merck. HPLC-grade acetonitrile and methanol were purchased from QRec (Auckland, New Zealand). Analytical grade solvents such as ammonia solution (28 %), hexane, dichloromethane, ethanol and isopropyl alcohol were also supplied by QRec (Auckland, New Zealand). Ultrapure water was prepared by the Millipore water purification system (Molsheim, France).

Polycyclic aromatic hydrocarbons (PAHs) analytical standards (naphthalene, ($\geq 99.7\%$), biphenyl, ($\geq 98.0\%$), acenaphthylene ($\geq 99.0\%$), anthracene ($\geq 98.0\%$) and pyrene ($\geq 98.0\%$) were provided by Sigma–Aldrich. The individual stock solution for each PAH ($1000\text{ }\mu\text{g mL}^{-1}$) in acetonitrile and stored in dark at $4\text{ }^\circ\text{C}$. The working standard solution containing the PAH

mixtures of a concentration of $10 \mu\text{g mL}^{-1}$ was prepared by appropriate dilution of the stock solution with acetonitrile.

Synthesis of magnetic nanoparticles (MNP)

The magnetic nanoparticles (MNP) was prepared using previous methods.²⁹ About 4.8 g of $(\text{NH}_4)_2\text{Fe}(\text{SO}_4)_2 \cdot 6\text{H}_2\text{O}$ and 9.6 g of $\text{FeCl}_3 \cdot 6\text{H}_2\text{O}$ were mixed with 120 mL of deionised water. The mixture was stirred in a pre-heated solution (60°C) for 5 min in an N_2 atmosphere. The ammonia solution was then added dropwise and stirred for 1 h. The solid products were recovered using an external magnet and rinsed with excess deionised water until the pH reached neutral and dried in an oven for 24 h.

The magnetic nanoparticles with tetraethyl orthosilicate (MNPTEOS) was produced by sonicating the synthesised MNP in a 200 mL mixture of ethanol and deionised water (1:1 volume ratio) for 20 min.¹² Ammonia (15 mL) and tetraethyl orthosilicate (TEOS, 6.3 mL) were gradually added into the mixture. The mixture was then agitated for 8 hours in a pre-heated solution (50°C) under an N_2 atmosphere. The solid products were gathered using an external magnet after cooling at room temperature, washed thrice with ethanol and deionised water (30:70 volume ratio) and dried in the oven for 24 h.

Synthesis of deep eutectic solvent (DES)

The selected fatty acid-based deep eutectic solvent (DES) synthesis was carried out using a previously published method.³⁰

Preparation of DES-based ferrofluids

About 15 mg of MNPTEOS was mixed into 25 μL of DES 1 and sonicated for 15 min to produce stable DES-based ferrofluid (MNPDES). The MNPDES was rinsed with deionised water to eliminate unreacted compound.¹²

Characterisation

The vibrational frequencies of each functional group in all MNP, MNPTEOS and MNPDES were analysed using Fourier transform-infrared spectroscopy (FTIR). The study was conducted with a Perkin Elmer 2000 instrument (Waltham, USA). The FTIR spectrum has been acquired in the range of $400\text{--}4000 \text{ cm}^{-1}$ to analyse and determine the unique chemical properties within the sample. The magnetic properties of the synthesised MNP, MNPTEOS and MNPDES were analysed using a Lake Shore 4700 series VSM (Westerville, OH, USA). The magnetic field was applied within the range of -8000 to 8000 G . The QuantaTM 650 FEG SEM (Hillsboro, OR, USA) was used to analyse the surface morphology and elemental dispersion of the MNP, MNPTEOS and MNPDES. EDX analysis offers elemental analysis to characterise the components present in the sample. The EDX spectra reveal the elemental composition and distribution found in MNP, MNPTEOS and MNPDES. The analysis was conducted using an operating voltage of $10.00\text{--}15.00 \text{ kV}$, a magnification of $100,000\times$, and a working distance (*WD*) of $9.7\text{--}9.8 \text{ mm}$.

Liquid phase microextraction with back extraction (LPME-BE) procedure

Initially, 25 μL of MNPDES was added into a 20 mL sample bottle followed by $5 \mu\text{g mL}^{-1}$ of PAHs mixtures and 800 mg of NaCl, and vortexed for 10 min using a vortex mixer. An external magnet was used to separate the ferrofluid from the sample solution. The PAHs were extracted back into 500 μL of acetonitrile by vortex for 1 min and then using an external magnet to achieve phase separation. The eluate was transferred to a 1.5 mL centrifuge tube before being injected into the GC-FID for analysis.

GC-FID analysis

A Perkin Elmer Clarus500 gas chromatograph (Waltham, MA, USA) with a flame ionisation detector (FID) and a split/splitless injector was used to analyse the samples. The PAHs were separated using an Elite-5 fused silica capillary column (30 m×0.32 mm I.D, 1 µm film thickness) from J&W Scientific. The carrier gas was hydrogen at a 1.0 mL/min flow rate. The injection volume was set to 2 µL, and the sample injection mode was splitless. The GC oven temperature programme was set to begin at 70 °C (1 min), ramp to 170 °C at 7 °C/min, ramp to 290 °C at 15 °C/min, and hold at this temperature for 3 min. The injection port and detector were adjusted to 270 and 300 °C, respectively.

Box–Behnken design (BBD)

The extraction process was optimised using Box–Behnken design, and the statistical analysis of the experimental results was performed using Minitab® statistical software, version 21 (Minitab Inc., State College, PA, USA). Box BBD experiments were used to evaluate four independent parameters that could affect extraction efficiency, including the amount of MNPT EOS (5–15 mg), the volume of DES 1 (25–90 µL), salt addition (0–800 mg) and extraction time (1–10 min). To perform a quadratic regression on the model coefficients, 27 BBD experiment runs with four variables and three levels were utilised to develop a second-order polynomial model to describe the response variables and their interactions. The prediction equation was generated by fitting the experimental data to the BBD model in Eq. (1), which provides an empirical link between the response (total peak area) and the tested variables (coded level) at a confidence level greater than 95%:

$$Y = \beta_0 + \beta_1 X_1 + \beta_2 X_2 + \beta_{12} X_1 X_2 + \beta_{11} X_1^2 + \beta_{22} X_2^2 \quad (1)$$

where Y is the measure response (peak area), X_1 and X_2 are significant independent variables, β_1 and β_2 are the linear regression coefficients, β_{12} is the interactive regression coefficient and β_0 is a constant term. Further, to get maximum peak area, BBD was considered to analyse the effect of a significant independent variable on response.

The variables were coded as follows: X_1 (amount of MNPT EOS), X_2 (volume of DES 1), X_3 (addition of salt) and X_4 (extraction time). Table S-I of the Supplementary material to this paper contains the coded-level design variables and the predicted and experimental response values.

ANOVA, coefficient of determination (R^2), model significance (P -value of 0.05), non-significant lack of fit and response surface plots were used to validate the mathematical model generated by the BBD approach.

Analytical method validation and performance characteristics

The developed and optimised method has been validated employing SANTE guidelines for linearity, precision, limit of detection (LOD) and limit of quantification (LOQ).³¹

Real samples analysis

The wastewater samples were collected from the Kulim Hi-Tech industrial area in Kedah and Batu Kawan in Penang, Malaysia. The specimens were maintained at 4 °C under darkness until they were utilised. Prior to the LPME-BE procedure, the water samples were filtered with 0.45 µm membrane filters to remove contaminants. Roadside leaf samples continuously exposed to automobile air pollutants were randomly collected from various locations in Sungai Dua, Gelugor, Penang. The methodology employed for the preparation of leaf samples in this study was adapted from the previously reported procedure.²² Initially, the leaves were minced

and subsequently pulverised using a mortar. Subsequently, roughly 0.5 g of leaves were subjected to introducing analytes at concentrations of 0.2, 0.5 and 1.0 $\mu\text{g mL}^{-1}$, followed by 15 min of diffusion. Subsequently, a volume of approximately 2 mL of acetonitrile was introduced into the mixture and agitated for 3 min using a vortex mixer. After centrifugation at 4000 rpm for 5 min, the supernatant was gathered and subjected to microextraction.

RESULTS AND DISCUSSION

Characterisation results

Fourier-Transform Infrared (FTIR) analysis. The confirmation of the presence of functional groups on the surface of the synthesised materials was conducted using FTIR analysis in the range of 400–4000 cm^{-1} . Fig. 1a–e displays the FTIR spectra of MNP, MNPTEOS and DES-based ferrofluids. Previous research has documented the FTIR spectra of various fatty acids and synthesised DES. Based on FTIR spectra in Fig. 1a and b, two prominent peaks associated with the Fe–O bond in MNP were seen at 577 and 611 cm^{-1} , respectively.^{32,33} Furthermore, there are noticeable peaks in the O–H bending region at 3418 and 3422 cm^{-1} for MNP and MNPTEOS, respectively. MNPTEOS has a prominent peak at 1104 cm^{-1} ,

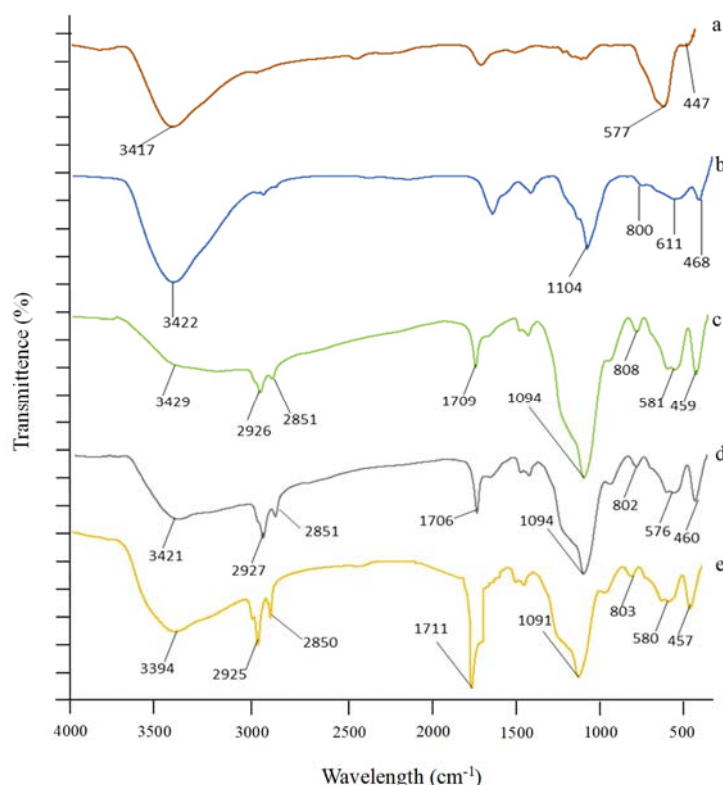


Fig. 1. FTIR spectra of (a) MNP, (b), MNPTEOS, (c) MNPDES 1, (d) MNPDES 2, (e) MNPDES 3.

representing the stretching of Si–O–Si bonds. This peak demonstrated the successful application of coating silanol groups on MNP cores.³³

The FTIR spectra of the synthesised DES-based ferrofluids (MNPDES 1, 2 and 3) are displayed in Fig. 1c–e. The location of the O–H vibration peaks is affected by the analytes' structure and content. Carboxylic acids commonly form dimer associations due to hydrogen bonding.³⁴ The hydroxyl and carbonyl groups of DES-based ferrofluids are within the range of 3398 to 3407 cm^{-1} and 1705 to 1709 cm^{-1} , respectively. Characteristic peaks at 1094 (MNPDES 1), 1096 (MNPDES 2) and 1104 cm^{-1} (MNPDES 3) correspond to the Si–O–Si stretching vibration band, revealing the presence of TEOS in these synthesised DES ferrofluids. Peaks at 2925 to 2927 cm^{-1} and 2851 to 2857 cm^{-1} , corresponding to the CH_3 and CH_2 groups, were found in all DES-based ferrofluids. This indicates that the DES successfully coated the MNP core.

Vibrating sample magnetometer (VSM) analysis. The magnetic properties of MNP, MNPTEOS and MNPDES were analysed at room temperature. The measurements were conducted within a magnetic field range of –8000 to 8000 G. The saturation magnetisation (M_s) and coercive field (H_c) were evaluated as critical magnetic properties. The magnetic properties predominantly dictate the behaviour of nanoparticles and ferrofluids. Fig. S-1a–e of the Supplementary material depicts the magnetic hysteresis of MNP, MNPTEOS and MNPDES, which have an S-shaped curve. M_s values for MNP and MNPTEOS were determined to be 55.86 and 35.67 emu g^{-1} , respectively. The magnetisation values for the synthesised MNPDES were measured to be 1.45, 1.51 and 1.50 emu g^{-1} for MNPDES 1, 2 and 3, respectively. The magnetic susceptibility of MNPTEOS and MNPDES is lower than that of the MNP. The presence of TEOS and DES on the surface of the MNP may lead to a decrease in the M_s , as predicted by Jayabharathi *et al.*³⁵ Furthermore, synthesising ferrofluid could contribute to the decrease in M_s .³⁶ Nevertheless, the decline in M_s seen in MNPDES suggests that the DES has successfully formed a coating on the surface of the magnetic nanoparticles (MNP). Despite having a lower M_s compared to MNP and MNPTEOS, MNPDES nevertheless fall within an acceptable range for simple separation using an external magnetic field.³⁵ The MNP, MNPTEOS and MNPDES exhibit superparamagnetism at room temperature, indicated by the lack of hysteresis, retentivity (M_r) and H_c .

Scanning electron microscopy – energy dispersive X-ray (SEM-EDX) analysis. The surface morphology of MNP, MNPTEOS and MNPDES was examined using SEM-EDX analysis. Fig. S-2a–e of the Supplementary material illustrates that MNP, MNPTEOS and MNPDES have a roughly spherical shape with a uniform distribution spanning 553.8 to 1.468 μm . The SEM analysis revealed that the synthesised MNPDES exhibited particle sizes ranging from 1.13 to 1.468 μm , greater than those of MNP (553.8 nm) and MNPTEOS (767.9 nm). The enlarged particle size in MNPDES is caused by the coating of the MNP core with DES.

Lenin *et al.*³⁷ observed that the application of DES coating on the surface of MNP's leads to an increase in the particle size of ferrofluids.

EDX analysis assessed the elemental composition of MNP, MNPTEOS and DES-based ferrofluids. The EDX spectra in Fig. S-3a of the Supplementary material indicate that the MNP is composed of 61.49 % Fe and 30.37 % O. MNPTEOS (Fig. S-3b) comprises 35.73 % Fe, 39.35 % O and 20.04 % Si. In the case of MNPDES (as shown in Fig. S-3c–e), all of them had a composition consisting of 32.41–36.96 % Fe, 37.07–39.20 % O and 15.50–21.57 % Si. Furthermore, MNPDES 3 contains the highest carbon content (13.04 %) compared to other compounds. This is attributed to a combination of lauric acid and capric acid in a mole ratio of 1:3, which results in the longest alkyl chain. The SEM-EDX results confirm the successful application of the DES coating on the surface of the MNPs.

Selection of fatty acid-based DES

The selection of an ideal DES as a carrier of ferrofluid is important in the proposed method. DES should have an appropriate interaction with the MNP to form a stable ferrofluid, thus enhancing the extraction efficiency of the developed method. Therefore, a hydrophobic DES should stabilise in an aqueous solution during microextraction. Moreover, the solubility of desired analytes in the extractant solvent, assisted with the presence of steric interaction, should be considered to achieve an optimum extraction efficiency. For these reasons, caprylic acid (C₈), pelargonic acid (C₉) and capric acid (C₁₀) acted as hydrogen bond donor (HBD) and were used to produce nine different eutectic solvents with lauric acid (C₁₂) by varying their molar ratio to investigate their extraction performance. The DES consist of caprylic acid, pelargonic acid, capric acid, and lauric acid incorporated with MNPTEOS, were listed in Table I.

TABLE I. Types of DES and their mole ratio; HBA: lauric acid

HBD	HBA:HBD mole ratio	Abbreviation
Caprylic acid	1:3	MNPDES 1
Pelargonic acid	1:3	MNPDES 2
Capric acid	1:3	MNPDES 3
Caprylic acid	1:2	MNPDES 4
Caprylic acid	1:4	MNPDES 5
Pelargonic acid	1:2	MNPDES 6
Pelargonic acid	1:4	MNPDES 7
Capric acid	1:2	MNPDES 8
Capric acid	1:4	MNPDES 9

Fig. 2 shows the effect of the type of DES on the LPME method. Generally, DES with longer alkyl chains and a high hydrogen bond donor (HBD) ratio, such as MNPDES 7 and 9, are expected to achieve higher recovery percentages for hydrophobic polycyclic aromatic hydrocarbons (PAHs), with the exception of

anthracene when using MNPDES 7. As illustrated in Fig. 2, both MNPDES 7 and 9 tend to self-coacervate and agglomerate in highly hydrophobic environments, which leads to a decrease in recovery percentages.²² This behaviour suggests that MNPDES, containing longer alkyl chains and a higher HBD ratio, demonstrate increased viscosity. The elevated viscosity hinders the dispersion of MNP in the solution, thereby limiting the mass transfer of PAHs.³⁸

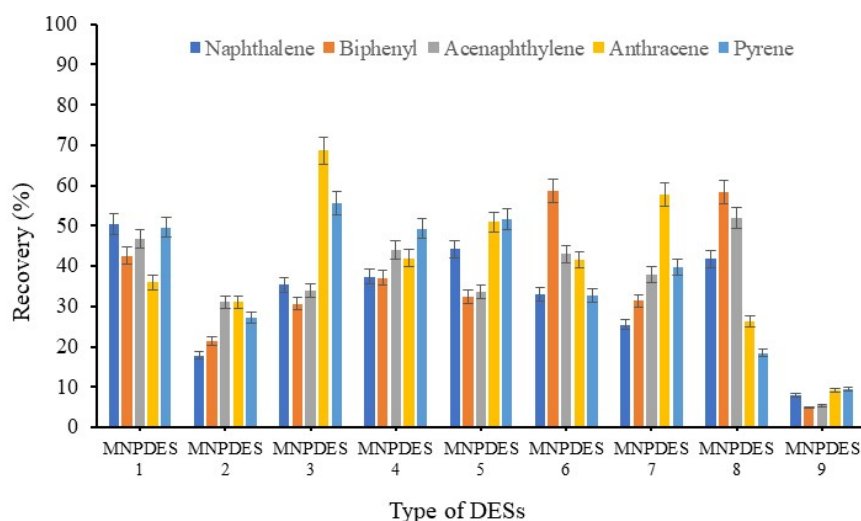


Fig. 2. The effect of type of DES with their mole ratio on extraction efficiency. Extraction condition: sample volume: 10 mL, amount of MNP: 10 mg, volume of DES: 50 μ L, salt addition: 200 mg, extraction time: 5 min, back extraction solvent: ACN, volume of ACN: 300 μ L, back-extraction time: 1 min.

Conversely, most PAHs displayed satisfactory recovery percentages when using DESs with shorter alkyl chains and a lower HBD ratio, specifically MNPDES 1, 4, 5 and 6. The results indicate that PAHs exhibit enhanced solubility in these MNPDESs, a phenomenon attributed to their lower viscosity and suitable hydrophobicity. This results in improved dispersion of MNPDES in the solution, facilitating mass transfer through stable hydrogen bonding and hydrophobic interactions between the PAHs and the alkyl chain of MNPDES 1. Additionally, the CH- π interaction between the benzene ring of PAHs and the CH₃ group of MNPDES also plays a crucial role in the efficient extraction process.^{5,22} Several studies have highlighted the importance of these interactions between hydrophobic DES and analytes that contributed to more efficient extraction of non-polar compounds due to favourable dispersion interactions and phase compatibility.^{4,5,22} Additionally, an increase in PAH solubility in DES formulated with hydrophobic DES, attributing this phenomenon to van der Waals and hydrophobic interact-

ions.^{4,12,22} The DES, composed of long-chain components, effectively encapsulates non-polar analytes through hydrophobic inclusion or micelle-like domains, stabilizing them within the DES-rich phase. The observed selectivity and efficiency in PAH extraction can be linked to these interactions, even in the absence of strong polar interactions.^{39,40}

As seen from Fig. 2, MNPDES 3 obtained a higher extraction efficiency on anthracene and pyrene, which are known as high molecular weight PAHs, owing to the optimal ratio of hydrogen bond donors and acceptors, which facilitated enhanced hydrophobic interactions with these compounds. Thus, the type and molar ratio of HBD are critical factors for effective extraction. After thorough analysis, MNPDES 1, consisting of a mixture of C₁₂:C₈ in a 1:3 ratio, has been identified as the most suitable carrier liquid for MNP. The extraction capability for all PAHs is enhanced due to its lower viscosity and satisfactory hydrophobic properties. The characteristics of DES 1 facilitate stable hydrogen bonding and hydrophobic interactions with PAHs, enabling efficient extraction from aqueous solutions.

Statistical analysis

The optimisation of independent parameters influencing the extraction efficiency was performed using BBD. The interaction and significance of each factor were determined by analysis of variance (ANOVA). The significance of each coefficient was determined using the *F*-test and *p*-value (Table S-II of the Supplementary material). The quadratic regression model indicated it was significant, as evidenced by the *F*-test with a low probability value (*p*-value of 0.05). The *F*-value of the model was 6.28, with a *p*-value of 0.001 (less than 0.05), implying a linear relationship between the amount of MNPT EOS (X_1), the volume of DES 1 (X_2), the addition of salt (X_3) and the extraction time (X_4). Notably, parameters such as X_1 and X_3 exhibited significant linear effects. Additionally, the quadratic term of X_2 and the interaction between X_2 and X_3 were also identified as significant. In contrast, X_4 and specific higher-order interactions did not reach statistical significance, indicating that their removal may enhance the model's simplicity.

The Lack-of-fit's *F*-value of 1.37 was observed insignificant (greater than 0.05) compared to the pure error. Furthermore, the reliability of the proposed model was assessed using R^2 and adjusted- R^2 , which were 0.8799 and 0.7395, respectively, showing that the quadratic model is still suitable for data fitness and appropriate for the current study.^{41,42} Despite low value of adjusted R^2 , the model is statistically significant ($p = 0.001$) and generally exhibits a good fit. The lower adjusted R^2 suggests that not all predictors strongly influence the response variable.⁴³ As a result, the analysis demonstrates the significant importance of the model used to describe the relationship between the extraction conditions and the responses given, as shown in Eq. (2):

$$\begin{aligned}
 Y \text{ (Total peak area)} = & 16047 - 1251X_1 - 264X_2 + 36.2X_3 - 997X_4 + \\
 & + 79.5X_1^2 + 4.27X_2^2 - 0.00898X_3^2 + 53.3X_4^2 - 7.0X_1X_2 + \\
 & + 0.770X_1X_3 + 70.9X_1X_4 - 0.372X_2X_3 - 11.9X_2X_4 - 0.005X_3X_4 \quad (2)
 \end{aligned}$$

The 3D response surfaces of the relationship between the amount of MNPTEOS, the volume of DES, the addition of salt, and the extraction time are shown in Fig. 3. According to Fig. 3a, adding 15 mg of MNPTEOS to a lower volume of DES 1 (25 μ L) enhanced PAHs extraction efficiency. This behaviour indicates that the ferrofluid is more stable and provides higher MNP dispersion in the sample solution despite the low DES volume. Furthermore, Fig. 3b demonstrates that a high extraction efficiency of PAHs was obtained when 15 mg of MNPTEOS and 800 mg of NaCl were applied. Increasing the MNPTEOS provides more adsorption sites for PAHs. With the addition of salt, the solubility of PAHs in the aqueous phase decreases due to the salting out effect, thus increasing their extraction. The extraction efficiency of PAHs was low when a large volume of MNPDES 1 was used, and no salt was added (Fig. 3c). This is explained by the fact that increasing the volume of DES 1 increases the diluting impact of PAHs. Fig. 3d and e show that using a small amount of DES 1 and a large amount of MNP with a longer extraction period results in higher efficiency. Furthermore, as demonstrated in Fig. 3f, the extraction efficiency of PAHs increases with the addition of NaCl and the length of the extraction time. A higher concentration of NaCl and a longer extraction time may aid in developing equilibrium during the extraction process. It can be concluded that the overall results indicated the most optimal condition was using 15 mg of MNPTEOS, 25 μ L of DES 1, 800 mg of NaCl and 10 min of extraction time.

It is crucial to acknowledge the variability in peak areas observed across experimental runs. These discrepancies can be attributed to sample handling and analytical drift factors. Minor variations in sample preparation, such as inconsistencies in vortex, pipetting, nanoparticle dispersion or magnetic separation, lead to fluctuations in analyte recovery, ultimately affecting chromatographic responses. Furthermore, analytical drift, which is characterized by gradual changes in instrument response over time, may stem from factors including temperature variations or detector instability. Such changes can compromise peak shape, baseline stability, and detector sensitivity.^{44,45}

Analytical method validation and performance characteristics

The LPME-BE method for determining PAHs using DES-based ferrofluid was validated under optimum circumstances, as indicated in Table S-III of the Supplementary material. All PAHs demonstrated strong linearity between 0.005 and 5 μ g mL⁻¹, with R^2 values larger than 0.9730. The detection and quantitation limits of detection (LOD) were determined to be 0.40–1.70 ng mL⁻¹ and 1.33–5.67 ng mL⁻¹, respectively. The precision of the LPME-BE method was determined by

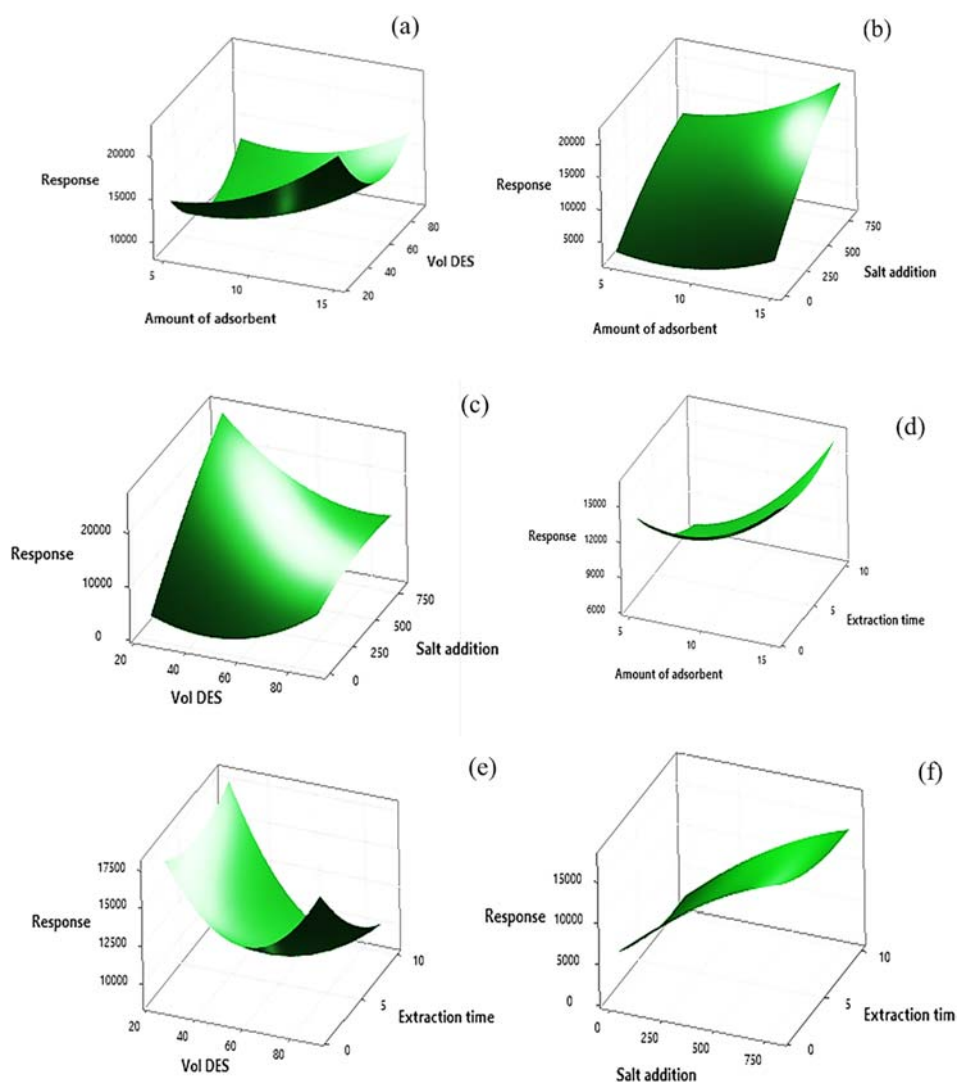


Fig. 3. Three-dimensional response surface plot in the peak area of PAHs. a) Amount of MNP-volume of DES. b) Amount of MNP-salt addition. c) Volume of DES-salt addition. d) Amount of MNP-extraction time. e) Volume of DES-extraction time. f) Salt addition-extraction time.

measuring the relative standard deviation (*RSD*) for intra-day (repeatability) and inter-day (reproducibility). The *RSD* ranges for intra-day (repeatability) and inter-day (reproducibility) precisions were 13.05–16.89 % and 9.37–15.84 %, respectively. It is notable that the intra- and inter-day precision values for the target PAHs ranged from 15–17 %, with recoveries as high as 118 %. According to SANTE

guidance document criteria, the *RSD* values should be fewer than 20 %, and the precision obtained with this approach is acceptable.³¹ Considering the method demonstrated acceptable performance, however, increased variability in specific replicates might be contributed to minor inconsistencies in sample preparation. Additionally, analytical drift over time, particularly fluctuations in detector response and baseline shifts in GC-FID, may have contributed to signal variability across runs. These factors likely influenced the reproducibility of peak areas.^{44,45} Although the precision values were generally acceptable for most analytes, these findings highlight the need for improved procedural consistency and the potential introduction of internal standards in future studies to enhance method robustness. Furthermore, the enrichment factor values for this method ranged from 26.66 to 40.05, indicating that the low concentration of PAHs was successfully preconcentrated utilising this extraction method.

Application to real samples

To evaluate the potential of the MNPDES, wastewater samples from industrial effluents (Batu Kawan, Seberang Perai, Penang and Kulim Hi-Tech industrial area, Kedah) and random roadside plant leaves samples, that were continuously exposed to air pollutants in automobile areas in Sungai Dua, Gelugor, Penang, were obtained and used to analyse the DES-based ferrofluid LPME-BE effectiveness by spiking PAHs into the samples with known amounts (0.2, 0.5 and 1.0 $\mu\text{g mL}^{-1}$). Table II shows the results of the extraction of PAHs for each spiked sample. No endogenous PAHs were detected in the wastewater and leaf samples; however, significant peaks appeared after adding exogenous PAHs. The method's extraction recoveries and repeatability were evaluated through triplicate analysis of samples spiked at concentration levels of 0.2, 0.5 and 1 $\mu\text{g mL}^{-1}$ of each PAHs. The data presented in Table II indicate that the recoveries of PAHs from environmental samples fall within the range from 75.78 to 118.65 %, with relative standard deviations (*RSDs*) ranging from 0.08 to 13.21 %. As per the guidelines provided by SANTE, the outcomes of the recovery were deemed satisfactory.³¹ The research findings demonstrated that the LPME-BE using MNPDES is a viable technique for efficiently separating, extracting, and quantifying trace amounts of PAHs in diverse, complex environmental matrices.

TABLE II. Determination of analytes using the proposed method in different real samples; ACN – acenaphthylene; Ww – wastewater; L – leaves

Sample	Spiked conc. $\mu\text{g/mL}$	Relative recovery, % (<i>RSD</i> / %), <i>N</i> = 3				
		Naphthalene	Biphenyl	ACN	Anthracene	Pyrene
Ww 1	0.2	98.68 (9.81)	79.26 (4.02)	85.08 (1.03)	105.45 (1.07)	80.91 (9.87)
	0.5	92.42 (1.01)	82.10 (7.29)	89.04 (7.72)	104.93 (0.47)	89.85 (1.21)
	1	92.05 (0.41)	82.14 (5.45)	86.14 (2.14)	109.40 (7.52)	89.14 (7.87)

TABLE II. Continued

Sample	Spiked conc. $\mu\text{g/mL}$	Relative recovery, % (<i>RSD</i> / %), <i>N</i> = 3				
		Naphthalene	Biphenyl	ACN	Anthracene	Pyrene
Ww 2	0.2	99.33 (5.23)	77.78 (1.41)	85.10 (0.03)	110.40 (8.66)	89.15 (0.02)
	0.5	95.60 (6.81)	97.23 (6.10)	82.56 (5.27)	106.25 (1.91)	89.31 (0.24)
	1	97.18 (2.73)	89.58 (13.21)	89.45 (4.26)	117.44 (0.42)	89.62 (0.93)
Ww 3	0.2	101.86 (9.05)	81.20 (7.31)	90.41 (10.21)	117.50 (0.51)	89.40 (0.48)
	0.5	93.21 (7.75)	84.78 (8.60)	85.30 (0.46)	117.56 (0.59)	93.18 (7.52)
	1	101.13 (9.40)	78.96 (4.29)	93.05 (9.95)	112.77 (5.49)	92.49 (6.27)
Ww 4	0.2	109.39 (11.64)	87.94 (11.20)	86.38 (2.61)	115.91 (1.86)	89.25 (0.11)
	0.5	102.85 (12.13)	81.14 (8.83)	97.99 (12.32)	117.15 (0.56)	89.27 (6.92)
	1	101.65 (10.22)	82.04 (5.66)	86.90 (1.91)	118.65 (2.19)	94.33 (6.62)
Ww 5	0.2	96.08 (0.77)	77.53 (2.26)	88.53 (6.74)	107.07 (9.91)	90.06 (0.92)
	0.5	94.95 (1.05)	83.23 (10.59)	85.46 (0.64)	113.55 (4.48)	99.06 (14.16)
	1	99.47 (6.65)	75.78 (1.63)	85.28 (0.40)	110.60 (10.27)	94.23 (9.36)
Ww 6	0.2	95.07 (0.86)	76.30 (1.30)	76.48 (0.95)	114.58 (6.89)	90.57 (2.73)
	0.5	99.50 (6.66)	76.47 (0.61)	85.41 (0.68)	108.92 (6.80)	89.50 (0.70)
	1	96.06 (0.61)	77.66 (1.20)	87.11 (3.30)	118.10 (1.12)	89.56 (0.66)
Ww 7	0.2	101.78 (8.52)	77.38 (0.70)	85.45 (0.62)	117.29 (0.16)	89.26 (0.20)
	0.5	96.47 (1.20)	75.94 (5.09)	86.04 (1.57)	118.65 (1.78)	89.15 (0.92)
	1	95.59 (0.08)	82.37 (9.94)	86.21 (2.0)	116.96 (0.23)	89.47 (0.53)
L 1	0.2	95.72 (0.11)	77.61 (1.10)	85.01 (1.02)	117.10 (0.72)	88.90 (1.92)
	0.5	96.20 (0.80)	77.38 (0.70)	85.00 (1.20)	114.93 (2.74)	89.54 (0.63)
	1	96.35 (1.03)	76.00 (1.88)	81.83 (5.60)	110.88 (8.00)	88.74 (0.64)
L 2	0.2	94.72 (1.38)	76.20 (1.50)	84.71 (0.61)	113.01 (5.18)	88.25 (1.43)
	0.5	95.31 (0.50)	71.24 (11.44)	84.70 (0.62)	114.78 (2.92)	85.83 (5.45)
	1	90.88 (7.41)	71.07 (11.80)	77.88 (13.07)	112.27 (6.15)	88.04 (1.76)
L 3	0.2	89.10 (10.38)	75.06 (3.64)	82.20 (4.96)	113.53 (4.51)	86.44 (4.40)
	0.5	95.15 (0.73)	76.56 (0.82)	80.98 (7.15)	112.52 (5.82)	88.58 (0.90)
	1	94.83 (1.22)	77.2 (0.624)	87.28 (3.57)	115.61 (1.99)	85.22 (6.95)

CONCLUSION

The proposed work showed that the application of the Box–Behnken design optimized independent parameters impacting the DES-based ferrofluid LPME-BE method and achieved appropriate PAHs determination in environmental samples. The primary goal of this work is to determine the maximum peak area by evaluating significant independent parameters that affect the PAHs peak area. The successful DES coating on MNP has been conclusively validated through FTIR, VSM and SEM-EDX analyses. The ANOVA test indicated that these parameters substantially impacted the extraction efficacy of PAHs using DES-based ferrofluids. The optimum extraction performance within the experimental range was expected to be 15 mg of MNPT EOS, 25 μL of DES 1, 800 mg of NaCl and 10 min of extraction time. Validation of analytical performances such as precision, accuracy, enrichment factor and recovery were evaluated under optimal extraction circum-

stances. The proposed extraction method is suitable for measuring PAHs in environmental samples. The *LOD* and *LOQ* values for PAHs were 0.4–1.70 ng mL⁻¹ and 1.33– 5.67 ng mL⁻¹, respectively, which made the approach dependable for reliably and precisely determining PAHs. The recoveries obtained were ranged from 75.78 to 118.65 % with *RSD* < 15 %. As a result, it has been demonstrated that the established approach is straightforward and reliable for quantifying PAHs in environmental samples.

This study introduces a promising green extraction method for the determination of PAHs that utilises DES-based ferrofluids. However, it is important to recognise certain limitations. The method was assessed with a limited selection of PAHs and examined solely in spiked matrices, potentially failing to exhibit the actual environmental sample applications. Intra- and inter-day precision variability may result from slight inconsistencies in sample handling and analytical drift. The application of GC-FID, although practical, is insufficient in selectivity for dependable analyte identification within complex matrices. The statistical model demonstrated moderate explanatory power and variability in response despite its utility. Future research should enhance the method's applicability by incorporating validation with certified reference materials (CRMs) and real contaminated samples, integrating internal standards, assessing matrix effects *via* spiking or standard addition and confirming results through mass spectrometry (GC-MS or LC-MS/MS) to achieve greater selectivity. The proposed enhancements will increase the method's robustness, reliability and relevance for trace-level environmental analysis.

SUPPLEMENTARY MATERIAL

Additional data and information are available electronically at the pages of journal website: <https://www.shd-pub.org.rs/index.php/JSCS/article/view/13221>, or from the corresponding author on request.

Acknowledgements. The authors would like to thank the editors and reviewers for their helpful suggestions for this manuscript. The authors gratefully acknowledge the financial support from the Ministry of Higher Education Malaysia (FRGS/1/2018/STG01/USM/03/1).

ИЗВОД

ОПТИМИЗАЦИЈА ТЕЧНЕ МИКРОЕКСТРАКЦИЈЕ РАН ЗАСНОВАНЕ НА ДУБОКОМ ЕУТЕКТИЧКОМ РАСТВОРАЧУ У УЗОРЦИМА ЖИВОТНЕ СРЕДИНЕ КОРИШЋЕЊЕМ МЕТОДОЛОГИЈЕ ПОВРШИНЕ ОДЗИВА

NUR HIDAYAH SAZALI¹, MAZIDATULAKMAM MISKAM², FAIZ BUKHARI MOHD SUAH²

и NURUL YANI RAHIM²

¹*Institute of Sustainable Energy and Resources, Universiti Teknologi PETRONAS, 32610 Seri Iskandar, Perak, Malaysia* и ²*School of Chemical Sciences, Universiti Sains Malaysia, 11800 USM, Pulau Pinang, Malaysia*

Присуство полициклических ароматических углеводородов (ПАХ) в отпадних водама представља значајан ризик по здравље. У циљу решавања овог проблема, развијен је нови ферофлуид на бази дубоког еутектичког растварача (DES-ферофлуид) за микроекстракцију у течном фазном стању са повратном екстракцијом (LPME-BE) ради детекције ПАХ.

DES-ферофлуид је карактерисан у погледу својих физичко-хемијских особина и морфологије помоћу FTIR, VSM и SEM-EDX. Кључни параметри у процесу микроекстракције у течном фазном стању са повратном екстракцијом (LPME-BE) оптимизовани су применом методологије површине одзива (RSM), засноване на Бох–Бехнкен дизајну (BBD). Оптимални услови укључивали су 15 mg магнетних наночестица премазаних тетраетилорто-силикатом (MNPTEOS), 25 μ L DES 1 (мешавина каприлне и лауринске киселине), 800 mg NaCl и време екстракције од 10 min. Анализа варијансе (ANOVA) је потврдила добро поклапање експерименталних података са моделом, са R^2 од 0,8799 и прилагођеним R^2 од 0,7395. Метод је постигао границу детекције (LOD) у опсегу од 0,4 до 1,7 ng mL⁻¹ и границу квантификације (LOQ) од 1,33 до 5,67 ng mL⁻¹. Приноси за узорке са додатим стандардом кретали су се од 75,78 до 118,65 %, са релативним стандардним одступањем (RSD) мањим од 15 %. Овај LPME-BE метод са DES-ферофлуидом и BBD оптимизацијом представља обећавајућу и ефикасну алтернативу за детекцију PAHs у узорцима отпадних вода.

(Примљено 24. Јануара, ревидирано 17. априла, прихваћено 5. августа 2025)

REFERENCES

1. N. Manousi, E. Rosenberg, E. Deliyanni, G. A. Zachariadis, V. Samanidou, *Molecules* **25** (2020) 1148 (<https://doi.org/10.3390/molecules25051148>)
2. M. A. Farajzadeh, M. R. Afshar Mogaddam, M. Aghanassab, *Anal. Methods* **8** (2016) 2576–2583 (<https://doi.org/10.1039/c5ay03189c>)
3. L. Foan, F. Ricoul, S. Vignoud, *Int. J. Environ. Anal. Chem.* **95** (2015) 1171 (<https://doi.org/10.1080/03067319.2014.994617>)
4. A. Jouyban, M. A. Farajzadeh, M. Nemati, A. A. Alizadeh Nabil, M. R. Afshar Mogaddam, *Microchem. J.* **154** (2020) 104631 (<https://doi.org/10.1016/j.microc.2020.104631>)
5. N. N. Naing, S. F. Yau Li, H. K. Lee, *J. Chromatogr., A* **1440** (2016) 23 (<https://doi.org/10.1016/j.chroma.2016.02.046>)
6. S. K. Mahmad Rozi, S. Bakhshaei, N. S. Abdul Manan, S. Mohamad, *RSC Adv.* **6** (2016) 87719 (<https://doi.org/10.1039/c6ra15319d>)
7. M. Carabajal, C. M. Teglia, S. Cerutti, M. J. Culzoni, H.C. Goicoechea, *Microchem. J.* **152** (2020) 104436 (<https://doi.org/10.1016/j.microc.2019.104436>)
8. J. S. da S. Burato, D. A. V. Medina, A. L. de Toffoli, E. V. S. Maciel, F. M. Mauro Lanças, *J. Sep. Sci.* **43** (2020) 202 (<https://doi.org/10.1002/jssc.201900776>)
9. P. Makoš, E. Słupek, J. Gębicki, *Microchem. J.* **152** (2020) 104384 (<https://doi.org/10.1016/j.microc.2019.104384>)
10. C. Florindo, L. Romero, I. Rintoul, L. C. Branco, I. M. Marrucho, *ACS Sustain. Chem. Eng.* **6** (2018) 3888 (<https://doi.org/10.1021/acssuschemeng.7b04235>)
11. E. A. Dil, M. Ghaedi, A. Asfaram, *Talanta* **202** (2019) 526 (<https://doi.org/10.1016/j.talanta.2019.05.027>)
12. A. Jouyban, M. A. Farajzadeh, M. R. Afshar Mogaddam, M. Nemati, A. A. Alizadeh Nabil, *Anal. Methods* **12** (2020) 1522 (<https://doi.org/10.1039/d0ay00073f>)
13. E. A. Dil, M. Ghaedi, A. Asfaram, L. Tayebi, F. Mehrabi, *J. Chromatogr., A* **1613** (2020) 460695 (<https://dx.doi.org/10.1016/j.chroma.2019.460695>)
14. A. R. Zarei, M. Nedaei, S. A. Ghorbanian, *J. Chromatogr., A* **1553** (2018) 32 (<https://dx.doi.org/10.1016/j.chroma.2018.04.023>)
15. M. A. Farajzadeh, A. Mohebbi, M. Reza, A. Mogaddam, *J. Sep. Sci.* **43** (2020) 1119 (<https://dx.doi.org/10.1002/jssc.201901000>)

16. C. Fan, X. Cao, T. Han, H. Pei, G. Hu, W. Wang, C. Qian, *Microchim. Acta* **186** (2019) 560 (<https://dx.doi.org/10.1007/s00604-019-3651-y>)
17. M. P. Abarbakouh, H. Faraji, H. Shahbaazi, M. Miralinaghi, *J. Mol. Liq.* **399** (2024) 124421 (<https://dx.doi.org/10.1016/j.molliq.2024.124421>)
18. S. Morovati, K. Larijani, M. Helalizadeh, L. G. Mohammadkhani, H. Faraji, *J. Chromatogr., A* **1712** (2023) 464468 (<https://dx.doi.org/10.1016/j.chroma.2023.464468>)
19. S. R. Chaudhari, A. A. Shirkhedkar, *J. Anal. Sci. Technol.* **11** (2020) 48 (<https://doi.org/10.1186/s40543-020-00246-2>)
20. A. Czyrski, J. Sznura, *Sci. Rep.* **9** (2019) 19458 (<https://doi.org/10.1038/s41598-019-55761-z>)
21. J. S. Cvetkovic, V. D. Mitic, V. P. Stankov Jovanovic, M. V Dimitrijevic, G. M. Petrovic, S. D. Nikolic-Mandic, G. S. Stojanovic, *Anal. Methods* **8** (2016) 1711 (<https://doi.org/10.1039/C5AY03248B>)
22. B. Yih Hui, N. N. Mohamad Zain, S. Mohamad, P. Varanusupakul, H. Osman, M. Raoov, *Food Chem.* **314** (2020) 126214 (<https://doi.org/10.1016/j.foodchem.2020.126214>)
23. B. Maddah, M. Soltaninezhad, K. Adib, *Sep. Sci. Technol.* **52** (2017) 700 (<https://doi.org/10.1080/01496395.2016.1221432>)
24. V. W. O. Wanjeri, S. Gbashi, J. C. Ngila, P. Njobeh, M. A. Mamo, P. G. Ndungu, *Int. J. Anal. Chem.* **2019** (2019) 4564709 (<https://doi.org/10.1155/2019/4564709>)
25. P. Zohrabi, M. Shamsipur, M. Hashemi, B. Hashemi, *Talanta* **160** (2016) 340 (<https://doi.org/10.1016/j.talanta.2016.07.036>)
26. M. A. Bezerra, R. E. Santelli, E. P. Oliveira, L. S. Villar, L. A. Escalera, *Talanta* **76** (2008) 965 (<https://doi.org/10.1016/j.talanta.2008.05.019>)
27. M. Kumari, S. K. Gupta, *Sci. Rep.* **9** (2019) 18339 (<https://doi.org/10.1038/s41598-019-54902-8>)
28. S. N. Azizi, N. Asemi, *J. Environ. Sci. Heal., B* **47** (2012) 692 (<https://doi.org/10.1080/03601234.2012.669260>)
29. L. I. Abd Ali, W. A. Wan Ibrahim, A. Sulaiman, M. A. Kamboh, M. M. Sanagi, *Talanta* **148** (2015) 191 (<https://doi.org/10.1016/j.talanta.2015.10.062>)
30. N. H. Sazali, M. Miskam, F. B. M. Suah, N. Y. Rahim, *Int. J. Environ. Anal. Chem.* **104** (2022) 2465 (<https://doi.org/10.1080/03067319.2022.2062570>)
31. SANTE/11945/2015: *Guidance Document on Analytical Quality Control and Method Validation Procedures for Pesticides Residues Analysis in Food and Feed*, 2017
32. M. Imran, A. R. Ansari, A. H. Shaik, Abdulaziz, S. Hussain, A. Khan, M. R. Chandan, *Mater. Res. Express* **5** (2018) 036108 (<https://doi.org/10.1088/2053-1591/aab4d7>)
33. S. Bandgar, J. Dhumal, S. Bandgar, K. Zipare, G. Shahane, *Int. J. Mater. Chem. Phys.* **1** (2015) 141 (<http://www.aiscience.org/journal/paperInfo/ijmcp?paperId=1819>)
34. K. Zhang, C. Liu, S. Li, Y. Wang, G. Zhu, J. Fan, *Anal. Lett.* **53** (2020) 1204 (<https://doi.org/10.1080/00032719.2019.1700422>)
35. J. Jayabharathi, P. Ramanathan, V. Thanikachalam, C. Karunakaran, *New J. Chem.* **39** (2015) 3801 (<https://doi.org/10.1039/c4nj02068e>)
36. Y. Hadadian, H. Masoomi, A. Dinari, C. Ryu, S. Hwang, S. Kim, B. K. Cho, J. Y. Lee, J. Yoon, *ACS Omega* **7** (2022) 15996 (<https://doi.org/10.1021/acsomega.2c01136>)
37. R. Lenin, A. Dadwal, P. A. Joy, *Bull. Mater. Sci.* **41** (2018) 120 (<https://doi.org/10.1007/s12034-018-1638-7>)
38. S. M. Majidi, M. R. Hadjmohammadi, *Talanta* **222** (2021) 121649 (<https://doi.org/10.1016/j.talanta.2020.121649>)

39. A. García, E. Rodríguez-Juan, G. Rodríguez-Gutiérrez, J. J. Rios, J. Fernández-Bolaños, *Food Chem.* **197** (2016) 554 (<https://dx.doi.org/10.1016/j.foodchem.2015.10.131>)
40. N. R. Rodriguez, P. F. Requejo, M. C. Kroon, *Ind. Eng. Chem. Res.* **54** (2015) 11404 (<https://dx.doi.org/10.1021/acs.iecr.5b02611>)
41. Y. An, W. Ma, K. H. Row, *Anal. Lett.* **53** (2020) 262 (<https://doi.org/10.1080/00032719.2019.1646754>)
42. M. Shirani, B. Akbari-adergani, M. B. Jazi, A. Akbari, *Microchim. Acta* **186** (2019) 674 (<https://doi.org/10.1007/s00604-019-3763-4>)
43. E. F. Elkady, M. A. Fouad, A. N. Mozayad, *BMC Chem.* **16** (2022) 1 (<https://dx.doi.org/10.1186/s13065-022-00908-9>)
44. A. Drolc, P. Djinović, A. Pintar, *Accredit. Qual. Assur.* **18** (2013) 225 (<https://dx.doi.org/10.1007/s00769-013-0980-0>)
45. V. J. Barwick, *J. Chromatogr., A* **849** (1999) 13 ([https://dx.doi.org/10.1016/S0021-9673\(99\)00537-3](https://dx.doi.org/10.1016/S0021-9673(99)00537-3)).

SUPPLEMENTARY MATERIAL TO
**Optimization of deep eutectic solvent based liquid phase
microextraction of PAHs in environmental samples using
response surface methodology**

NUR HIDAYAH SAZALI¹, MAZIDATULAKMAM MISKAM², FAIZ BUKHARI MOHD
SUAH² and NURUL YANI RAHIM^{2*}

¹Institute of Sustainable Energy and Resources, Universiti Teknologi PETRONAS, 32610 Seri
Iskandar, Perak, Malaysia, and ²School of Chemical Sciences, Universiti Sains Malaysia,
11800 USM, Pulau Pinang, Malaysia

J. Serb. Chem. Soc. 90 (10) (2025) 1203–1221

Table S-I. Factors, actual and coded levels, and design matrix used in BBD for extraction of PAHs.

	Factors				Levels	
					Low (-1)	High (+1)
					Central (0)	
Amount of MNP (X ₁)					5 mg	15 mg
Volume of DES 1 (X ₂)					25 µL	90 µL
Addition of salt (X ₃)					0 mg	800 mg
Extraction time (X ₄)					1 min	10 min

Run	X ₁	X ₂	X ₃	X ₄	Total Peak Area
1	0	1	1	0	12791.4
2	0	0	1	-1	13475.01
3	0	0	-1	-1	4956.06
4	0	0	0	0	10409.47
5	0	-1	-1	0	4301.17
6	0	0	0	0	7232.75
7	-1	0	0	1	5663.43
8	0	0	0	0	12951.61
9	0	-1	1	0	30499.95
10	1	0	0	-1	17902.92
11	1	0	1	0	21445.59
12	-1	0	-1	0	5608.21
13	-1	0	0	-1	14281.39
14	0	1	-1	0	5938.1
15	0	1	0	-1	18590.96
16	1	-1	0	0	20089.58

* Corresponding author. E-mail: nurulyanirahim@usm.my

17	1	0	0	1	15669.13
18	-1	0	1	0	14115.98
19	-1	-1	0	0	9925.93
20	1	1	0	0	18459.84
21	0	0	1	1	12002.42
22	0	0	-1	1	3519.91
23	1	0	-1	0	6777.07
24	0	1	0	1	11623.2
25	0	-1	0	1	18922.02
26	0	-1	0	-1	18955.6
27	-1	1	0	0	12873.51

Table S-II. ANOVA results obtained by BBD.

Source	Degree of freedom (DF)	Sum of Square (SS)	Mean Square (MS)	F-value	P-value
Model	14	944374587	67455328	6.28	0.001
Linear	4	644230114	161057529	15	0.000
X ₁	1	119547261	119547261	11.13	0.006
X ₂	1	41877721	41877721	3.9	0.072
X ₃	1	446884000	446884000	41.61	0.000
X ₄	1	35921132	35921132	3.34	0.092
X ₁ ²	1	21044575	21044575	1.96	0.187
X ₂ ²	1	108300369	108300369	10.08	0.008
X ₃ ²	1	11002371	11002371	1.02	0.331
X ₄ ²	1	6221976	6221976	0.58	0.461
X ₁ X ₂	1	5237965	5237965	0.49	0.498
X ₁ X ₃	1	9488710	9488710	0.88	0.366
X ₁ X ₄	1	10189407	10189407	0.95	0.349
X ₂ X ₃	1	93561899	93561899	8.71	0.012
X ₂ X ₄	1	12020713	12020713	1.12	0.311
X ₃ X ₄	1	332	332	0	0.996
Lack-of-Fit	10	112457625	11245762	1.37	0.494
Pure Error	2	16419795	8209898		
Total SS		1073252007			
R ²		0.8799			
Adj R ²		0.7398			

Table S-III. Analytical performance of the proposed method

	Linearity ($\mu\text{g mL}^{-1}$)		y-intercept	R^2	LOD (ng/mL^{-1})	LOQ (ng mL^{-1})	EF	Interday	Intraday
	slope							n=5	n=15
Naphthalene	0.005 – 5	126103	-13702	0.9915	1.70	5.67	32.88	15.85	16.90
Biphenyl	0.005 – 5	140933.2	37004.56	0.9997	1.52	5.08	26.67	15.59	16.05
Acenaphthylene	0.005 – 5	144895.1	61485.88	0.9738	1.48	4.94	29.36	11.98	14.56
Anthracene	0.005 – 5	534834.5	-54043.2	0.9831	0.40	1.33	40.05	9.92	13.06
Pyrene	0.005 – 5	386375.5	-34810	0.9921	0.55	1.85	30.71	9.37	15.21819

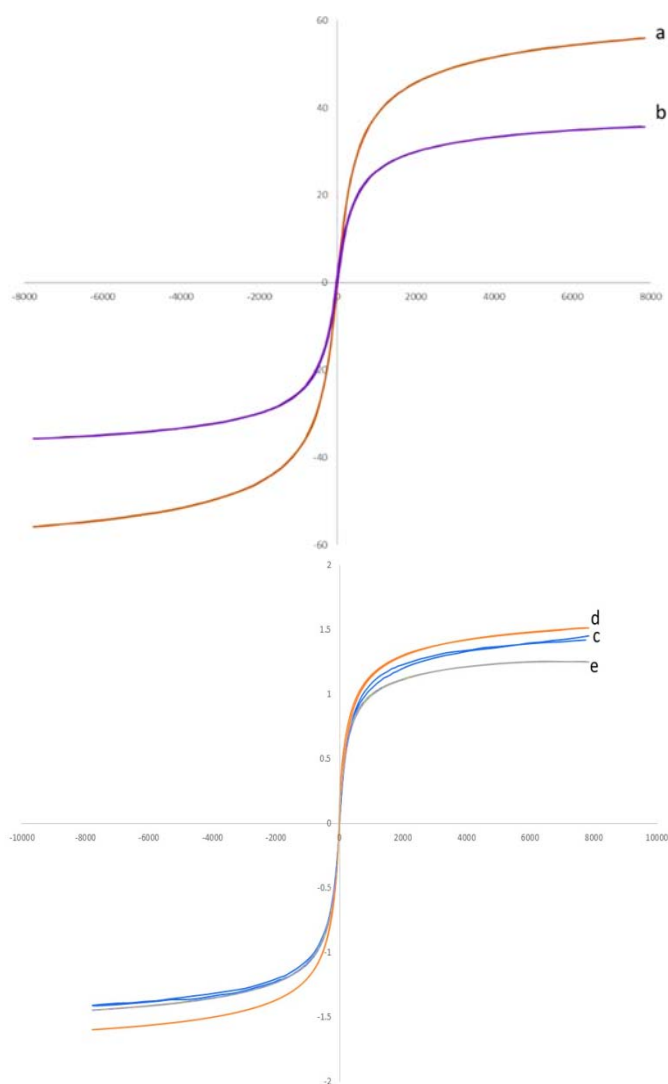


Fig. S-1. Hysteresis loops of (a) MNP, (b) MNPTEOS, (c) MNPDES 1, (d) MNPDES 2, (e) MNPDES 3.

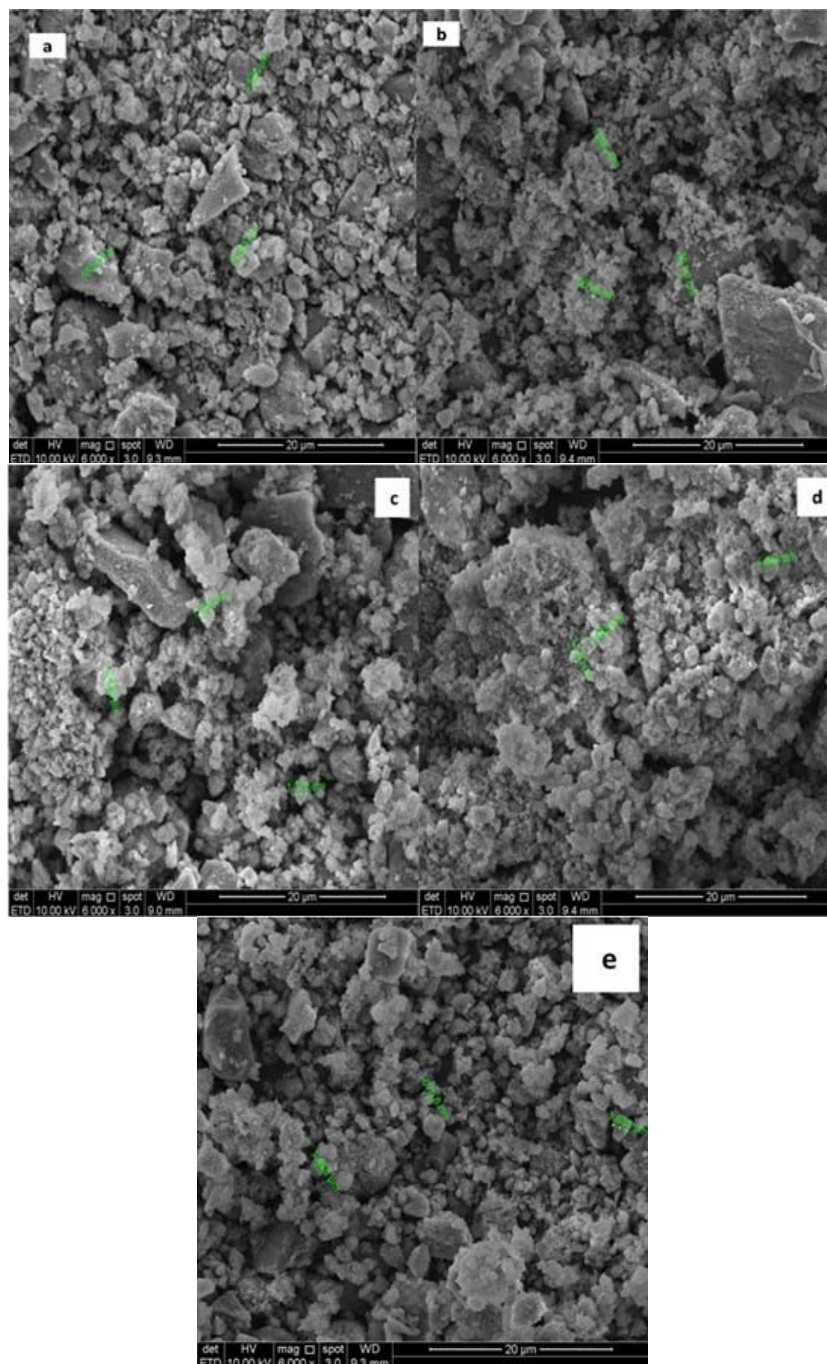


Fig.S-2. SEM images of (a) MNP, (b) MNPTEOS, (c) MNPDES 1, (d) MNPDES 2, (e) MNPDES 3.

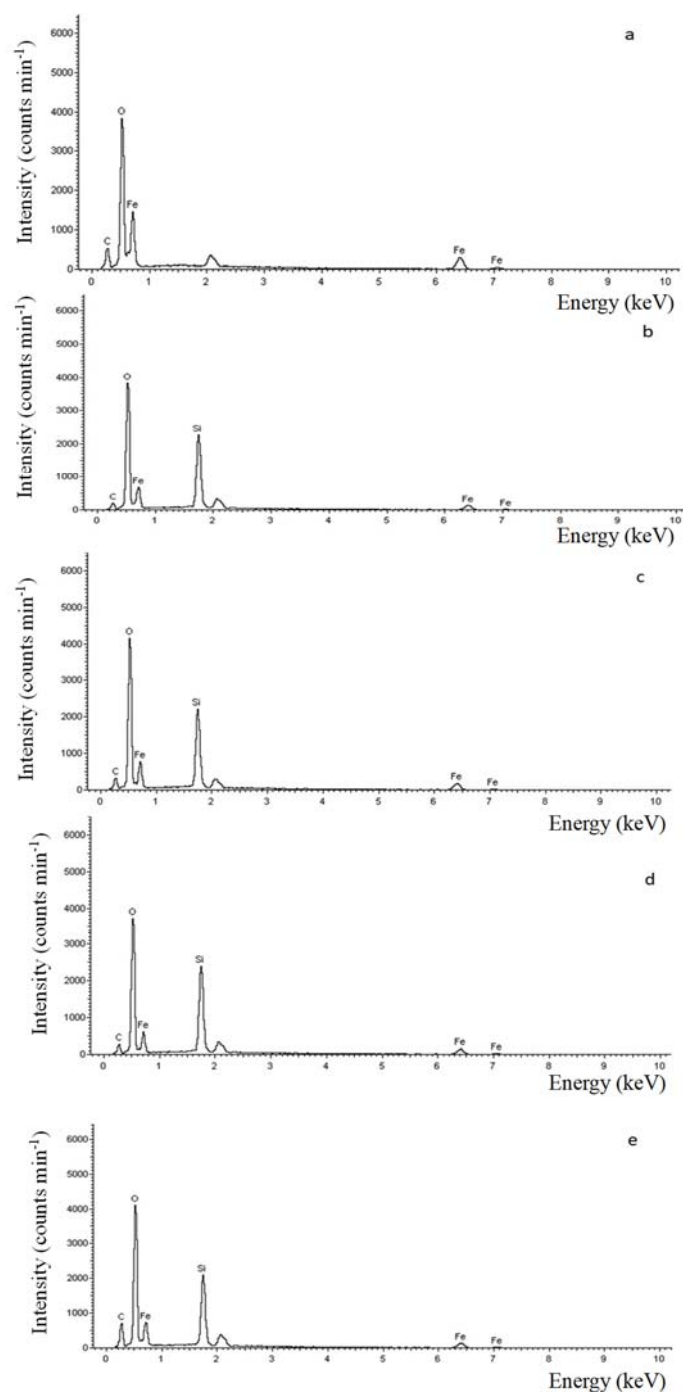


Fig. S-3. EDX images of (a) MNP, (b) MNPTEOS, (c) MNPDES 1, (d) MNPDES 2, (e) MNPDES 3.



J. Serb. Chem. Soc. 90 (10) 1223–1239 (2025)
JSCS–5450

Synthesis of zeolite LTA from kaolin and its model CBC and WAC performance: Optimized by central composite design

GÜL AKAR ŞEN*

Dokuz Eylul University, Faculty of Engineering, Mining Engineering Department, İzmir, Türkiye

(Received 10 March, revised 8 April, accepted 22 July 2025)

Abstract: In this study, a cost-effective route to synthesizing LTA-type zeolite from Balıkesir-region kaolin was demonstrated. Kaolin was calcined at 800 °C to obtain metakaolin, which was then treated hydrothermally in the presence of NaOH under optimized conditions determined by a Box–Behnken experimental design. The process variables NaOH concentration, temperature, and solid to liquid ratio were systematically investigated to maximize both water adsorption capacity and cation-exchange capacity (CEC). Quadratic regression models and ANOVA confirmed that NaOH concentration and temperature exert the most significant impact on zeolite formation and performance. Characterization by XRD, SEM and FTIR confirmed that the synthesized product under optimal conditions predominantly consisted of LTA-type zeolite crystals, as evidenced by the characteristic diffraction peaks, morphology and vibrational bands. The best performing sample showed a CEC of up to 192 mg CaCO₃ g⁻¹ and a water adsorption capacity of nearly 29 g H₂O per 100 g adsorbent. These results highlight the potential of locally sourced kaolin for producing high value zeolites, offering a sustainable alternative to imported raw materials.

Keywords: synthesis of zeolite; zeolite LTA; kaolin; hydrothermal synthesis; ANOVA.

INTRODUCTION

Rapid urbanization and industrial growth have significantly increased environmental pollution, especially due to industrial waste disposal.¹ Energy-intensive industries notably contribute to environmental degradation.^{2,3} Zeolites, owing to their interconnected micro and mesoporous framework that confers highly selective adsorption and ion-exchange behavior, play a pivotal role in industrial separations, environmental remediation and heterogeneous catalysis. They are crystalline aluminosilicates formed by tetrahedral units of silicon, aluminum and oxygen,

* Correspondence E-mail: gul.akar@deu.edu.tr
<https://doi.org/10.2298/JSC250310054A>

where the negative charge from Al is balanced by cations (Na^+ , K^+ , Ca^{2+}).⁴⁻⁸ Their adsorption capacity,⁹ molecular sieving, and ion-exchange properties make zeolites valuable in various applications,⁹⁻¹² including hydrocarbon separation, heavy metal removal, water softening through ammonium removal by ion-exchange,^{13,14} and catalysis/sensor supports.¹⁵

Both natural and synthetic zeolites contain aluminosilicates incorporating elements from groups I and II. According to the International Zeolite Association Structure Commission, more than 260 unique zeolite framework types have now been officially approved and assigned three-letter codes.¹⁶ Synthetic zeolites have been produced through microwave, vapor, and hydrothermal methods from diverse silica/alumina sources.¹⁷⁻²¹ Among materials explored (kaolin, clay, fly ash, feldspar, bauxite), kaolin is highlighted for its economic viability and high silica/alumina content, making it an ideal precursor for synthesizing LTA-type zeolites.^{22,23} The synthesis involves converting kaolin into reactive metakaolin by calcination, followed by hydrothermal crystallization. Important parameters include silica-to-alumina ratio, reaction time, temperature, hydrodynamics and pH. Due to their uniform pore size, crystallinity, and robust structure, LTA-type zeolites (such as zeolite 4A) are widely utilized in ion-exchange, adsorption and catalysis.²⁴

Turkey imports a variety of synthetic zeolites: around fifty thousand tons per year for detergents, ten thousand tons per year for insulating glass applications, and approximately five thousand tons annually for use as petrochemical catalysts. Local production is minimal, primarily due to higher production costs linked to imported raw materials. The main goal of this study is to synthesize zeolite 4A (LTA) from locally available Turkish kaolin, which may differ from international sources. Previous research on synthesizing zeolites from kaolin has focused on optimizing the process for environmental applications, such as pollutant removal.²⁵⁻²⁷ In line with this, the present work aims to synthesize LTA-type zeolites from Balıkesir-region kaolin and optimize their cation exchange capacity (CEC) and water adsorption capacity using response surface methodology (RSM). A central composite design (CCD) was employed to identify the best set of synthesis conditions, and the resulting materials were characterized extensively, including structural and adsorption properties.

EXPERIMENTAL

Materials and methods

A Balıkesir-region kaolin (K) was used as the starting material. Wet chemical analyses in aqua regia were performed using an Analytik Jena NovaA 300 AAS to determine the oxide compositions of the samples. The raw sample is labeled "K". To remove impurities, the raw material was treated with sodium dithionite ($\text{Na}_2\text{S}_2\text{O}_4$) at a concentration of 0.3 g per 100 g of kaolin (pH adjusted to 3 with H_2SO_4).²⁸ The treated kaolin is labeled "TK". After drying and sieving, synthetic zeolite LTA was obtained from TK, which was first converted to metakaolin (MK) by calcination at 800 °C for 2 h, followed by hydrothermal synthesis. Particle size distri-

butions (volume based D_{80}) were measured with a Horiba LA-950 V2 laser diffraction analyser. Samples were dispersed in isopropanol and ultrasonicated for 2 min at 40 W prior to measurement to ensure uniform particle dispersion. Specific gravity was determined with a Micromeritics AccuPyc II 1340 helium gas pycnometer (five measurement cycles; precision $\pm 0.002 \text{ g cm}^{-3}$). Hardness was assessed on pelletised specimens using a Vickers micro-hardness tester (Shimadzu HMV-2), reported as average of five indents. pH measured on a 10 wt. % solid suspension with a pH meter (calibrated at 25 °C with NBS buffers 4.00/7.00). Elemental composition of major oxides determined by flame AAS (Analytik Jena novAA 300) and expressed on an LOI-free basis. X-ray diffraction (XRD) analyses were performed on a Rigaku Miniflex II diffractometer with $\text{CuK}\alpha$ radiation (30 kV, 15 mA, 2θ range: 3–55°). Morphological studies were conducted using a Jeol JXA-733 Superprobe SEM. FT-IR analyses of selected products used a Perkin Elmer Spectrum BX in the range of 500–4000 cm^{-1} with 4 cm^{-1} resolutions. All chemicals ($\text{Na}_2\text{S}_2\text{O}_4$, NaOH, HCl and H_2SO_4) were Sigma–Aldrich grade and used without further purification. Deionized water was produced via a Millipore Milli-Q system.

Calcination (metakaolinization)

Calcination is critical in transforming kaolin into metakaolin by destroying the layered kaolinite lattice.^{24,29} This process typically occurs at 600–900 °C. The transition starts near 600 °C, and near 800 °C, kaolin is mostly converted into an amorphous metakaolin.³¹ Optimization of temperature and duration depends on the raw material's quality, which in turn depends on mining sites.²⁴ In this work, TK was calcined in a muffle furnace at a heating rate of 3 °C/min up to 800 °C, held for 2 h, then cooled naturally. The product is labelled MK.

Synthesis of zeolite LTA using central composite experimental design

Zeolite LTA was synthesized from TK-derived metakaolin under hydrothermal conditions. Based on literature findings that crystallinity increases significantly after 3–4 h, a reaction time of 24 h was chosen. Temperatures below 50 °C were deemed unsuitable for crystallization.^{24,28–33} Temperature, NaOH concentration and solid-to-liquid (S/L) ratio, known to affect crystallization, were selected as the experimental variables in a Box–Behnken design (BBD) combined with RSM. BBD allows the sequential examination of parameters while keeping others constant.³⁴ The selected variables and their levels, as shown in Table I, were defined as follows: NaOH concentration (2, 2.5 and 3 M), solid-to-liquid ratio (20, 25 and 30 %) and temperature (60, 75 and 90 °C).

TABLE I. Box–Behnken design parameters and experimental conditions; –1: factor at low level; 0: factor at medium level; +1: factor at high level

Variable	Symbol	–1	0	+1
NaOH (mol/L as M)	A	2	2.5	3
Temperature, °C	B	60	75	90
Solid/liquid ratio, %	C	20	25	30

A key advantage of the BBD with RSM methodology is its ability to analyse multiple parameters with fewer experimental trials compared to other methods.³⁴ In this study, three factors at three levels (low, medium and high) were evaluated, represented by –1, 0 and +1, respectively. The test variables were designated as NaOH concentration (A), temperature (B), and solid-to-liquid ratio (C), while the responses, water adsorption (Y_1) and cation exchange capacity (CEC , Y_2), were investigated.

The second-order polynomial equation was used to predict the relationship between the independent variables and the response, as represented by:

$$Y_{1,2} = b_0 + b_1A + b_2B + b_3C + b_{12}AB + b_{13}AC + b_{23}BC + b_{11}A^2 + b_{22}B^2 + b_{33}C^2 \quad (1)$$

where Y is the predicted response, b_0 is the constant term, A , B , C are the independent variables, b_1 , b_2 , b_3 are linear coefficients, b_{12} , b_{13} , b_{23} are interaction coefficients, and b_{11} , b_{22} , b_{33} are quadratic coefficients. ANOVA and 3D surface plots (Stat-Ease 360 software) were used to determine model fit and analyse parameter interactions.

Following the experimental design, 5.0 g of metakaolin was mixed with NaOH at the specified S/L ratios and stirred at 250 rpm for 24 h. The resulting gel was subjected to hydrothermal synthesis at different temperatures. After the reaction, the gel was washed until reaching pH 9–10, filtered, and dried at 100 °C for 12 h. The synthesis route is summarized in Fig. 1.

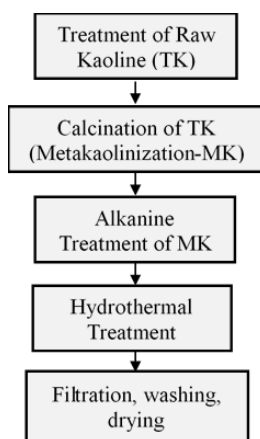


Fig 1. Schematic representation of hydrothermal synthesis procedure of zeolites.

Cation-exchange capacity (CEC) and water adsorption amounts

Cation-exchange capacity (CEC) was determined by Ca^{2+} exchange following Hui & Chao (2006) with minor modifications.²¹ Precisely 0.100 ± 0.001 g of each sample (pre-dried at 105 °C for 2 h) was contacted with 50.0 mL of 0.010 M CaCl_2 in a 100 mL polyethylene conical flask. Suspensions were agitated in an orbital shaker (IKA KS-4000) at 25 ± 0.2 °C, 150 rpm for 24 h. Supernatants were centrifuged (10 min) and filtered (0.45 μm nylon); Ca^{2+} was analysed with a PCA-1-01 ion selective electrode calibrated from 0.5×10^{-3} to 5×10^{-3} M:

$$CEC = 100.08V(C_0 - C_1) / m \quad (2)$$

where CEC represents the calcium ion-exchange capacity of the product ($\text{mg CaCO}_3 \text{ g}^{-1}$), 100.08 is the molar mass of CaCO_3 (g/mol or mg/mmol), C_0 is the initial Ca^{2+} concentration in the CaCl_2 solution (mol/L), C_1 is the Ca^{2+} concentration in the filtrate (mol/L), V is the volume of the CaCl_2 solution (mL), and m is the mass of the sample (g).

For water-adsorption tests the exchanged solids were re-dried at 60 °C for 24 h, then placed in a Binder KBF 115 climate chamber at 25 ± 0.3 °C, 68 ± 0.2 % RH with 0.3 m s^{-1} airflow. Mass gain after 24 h was recorded and expressed as $\text{g H}_2\text{O}$ per 100 g adsorbent. This method allows for the quantification of the water adsorption amounts of the synthesized zeolites, providing insight into their potential applications in moisture-sensitive environments.

RESULTS AND DISCUSSION

Physical and chemical characterization

Raw Balıkesir kaolin was crushed, ground below 106 μm , and analyzed for specific gravity, hardness, pH and particle size. Table II shows that metakaolin (MK) had increased density and hardness, and reduced particle size compared to treated kaolin (TK), primarily due to removal of structurally bound water. During calcination at 800 $^{\circ}\text{C}$, the dehydroxylation of kaolinite removes structural $-\text{OH}$ groups, leading to the collapse of the layered lattice into an amorphous, highly brittle metakaolin. This structural collapse, combined with the release of interlayer water, weakens inter-particle cohesion and promotes fragmentation.³⁵ Consequently, even mild grinding and dispersion steps after calcination generate much finer platelets, which accounts for the observed D_{80} drop from 102.15 (TK) to 3.65 μm (MK).

TABLE II. Some physical properties of TK and MK samples

Samples	Specific gravity, g/cm^3	Hardness	pH	Particle size, $D_{80} / \mu\text{m}$
TK	2.609	1.72	6.91	102.15
MK	2.615	6.22	6.91	3.65

Wet chemical analyses were conducted using an Analytik Jena NovaA 300 atomic absorption spectrometer (AAS) to determine the concentration of applicable elements in the final solutions. The chemical composition of T, TK and MK are shown in Table III

TABLE III. Chemical composition of samples kaoline (K) and treated kaoline (TK); *LOI* = loss on ignition

Sample	SiO_2	Al_2O_3	Fe_2O_3	CaO	MgO	Na_2O	K_2O	TiO_2	MnO	<i>LOI</i>
Kaoline (K)	51.37	36.95	0.45	0.43	0.11	0.01	0.34	0.47	0.01	9.12
Treated Kaoline (TK)	52.18	37.68	0.11	0.22	0.08	0.01	0.14	0.24	0.01	8.18
Metakaoline (MK)	58.38	38.95	0.10	0.19	0.11	0.08	0.12	0.23	0.01	1.06

The Si/Al mole ratio of MK was 1.50, which is within the typical range (1.0–1.8) associated with the formation of low-silica zeolite frameworks such as LTA and sodalite. While the synthesis mixture can accommodate a broader range, this ratio in the final product is often considered favorable for achieving high LTA crystallinity.^{36,37}

Mineralogical and morphological characterization of TK and MK

The XRD pattern of TK and MK is shown in Fig. 2. The XRD pattern of treated kaolin exhibits the diagnostic basal reflections of kaolinite at $2\theta \approx 12.3^{\circ}$ ($d001 \approx 7.15 \text{ \AA}$) and 24.9° ($d002 \approx 3.57 \text{ \AA}$), assigned to the (001) and (002) planes,

confirming the layered kaolinite structure.³¹ Upon a single calcination step at 800 °C for 2 h, the XRD patterns exhibit the expected significant change in comparison to the pattern of TK, the characteristic kaolinite peaks at $2\theta \sim 12.3^\circ$ (001) and $\sim 24.9^\circ$ (002) disappear, and the diffractogram develops a broad hump centred at $\sim 25^\circ$, consistent with the formation of largely amorphous metakaolin which was characterized by the disappearance of the diffraction peaks of kaolinite, accompanied by the appearance of amorphous aluminosilicate (Fig. 2). These findings are consistent with the related literature.³¹

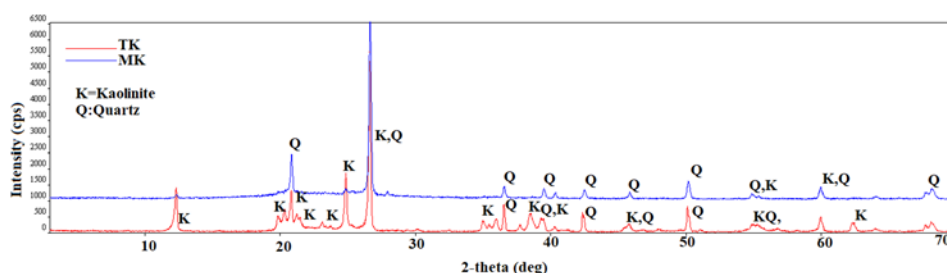


Fig. 2. XRD pattern of treated kaolin (TK) and metakaoline (MK).

SEM analyses were carried out to assess the samples' morphological features. In Fig. 3a, the typical layered, plate-like structure of kaolinite is evident. However, after calcination (Fig. 3b), this layered structure was lost, and particle size was notably reduced, leaving behind an irregular, disorganized plate morphology. Calcination promotes the dehydroxylation of kaolinite, altering the local environment of the aluminum atoms as they transition from octahedral to tetrahedral coordination. As a result, the material becomes amorphous and more reactive.³⁸

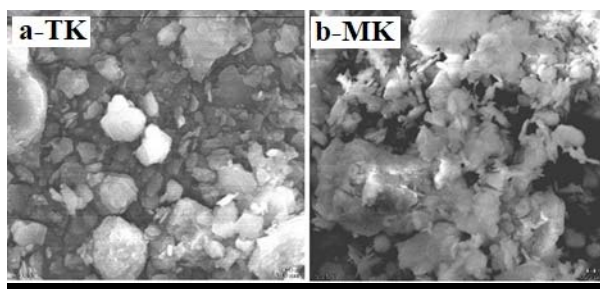


Fig. 3. SEM pictures of treated kaolin (TK) and metakaoline (MK).

Results of synthesis of zeolite LTA using Box–Behnken design with RSM methodology

Seventeen experimental runs and three control trials were carried out to evaluate the effects of the three variables. The actual data obtained from these tests

were utilized to derive mathematical equations describing how the independent variables influence the *CEC* and water adsorption capacity of the synthesized LTA. Table IV presents the conditions of the design matrix, along with the corresponding experimental outcomes. Notably, the experimental program produced an LTA sample with a *CEC* of up to 186.82 mg CaCO₃ g⁻¹ and a water adsorption capacity of 29.09 g H₂O per 100 g of adsorbent.

TABLE IV. BBD with RSM designed experimental results

Run	Factor 1 A: NaOH (mol/L)	Factor 2 B: Temperature °C	Factor 3 C: S/L ratio %	Response 1 Water absorbed, g H ₂ O/100 g adsorbent		Response 2 <i>CEC</i> mg CaCO ₃ g ⁻¹	
				Actual	Predicted	Actual	Predicted
1	2	60	25	25.45	25.29	142.25	142.84
2	2.5	60	20	26.65	26.75	170.91	171.56
3	2.5	60	30	26.52	26.56	168.53	167.10
4	3	60	25	26.91	26.88	175.41	175.39
5	2	75	20	26.35	26.39	155.34	154.05
6	2	75	30	26.21	26.31	149.98	150.81
7	2.5	75	25	29.08	29.03	185.03	185.79
8	2.5	75	25	29.06	29.03	186.55	185.72
9	2.5	75	25	29.05	29.03	185.96	185.79
10	2.5	75	25	29.09	29.04	186.82	185.79
11	2.5	75	25	28.87	29.03	184.61	185.79
12	3	75	20	27.75	27.66	185.19	184.36
13	3	75	30	27.23	27.17	182.52	183.82
14	2	90	25	27.78	27.81	165.39	165.45
15	2.5	90	20	28.92	28.85	188.91	190.34
16	2.5	90	30	28.53	28.43	191.78	191.07
17	3	90	25	28.15	28.31	192.43	192.84

Fig. 4 shows the solid linear relationship between the experimental and predicted values of the responses. The determination coefficients R^2 of 0.9940 and 0.9963 of the water adsorbed amounts (g H₂O/100 g⁻¹) and *CEC* (mg CaCO₃ g⁻¹), respectively, shows that the fit is reasonably good. The actual and predicted values of both the water adsorbed amounts and *CEC* obtained using model equations are presented in Fig. 4a and b. The predicted values are in good agreement with the experimental values.

Table V shows the analysis of variance of the developed models for the *CEC* and water adsorption amounts of synthesized zeolite LTA. Fisher's test with corresponding (P) values was used to study the effect of different parameters on two responses on the result of analysis by ANOVA analysis model. The models are significant as the F value is high, the $Prob>F$ value is less than 0.05 and the standard deviation is very small: 0.14 for the water adsorption amounts and 1.42 for the *CEC*:

$$Y_1 = 28.64 + 0.6208A + 0.9189B - 0.1258C - 0.1867AB - 0.0950AC - 0.0433BC - 1.36A^2 - 0.2622B^2 - 0.7850C^2 \quad (3)$$

$$Y_2 = 182.00 + 16.00A + 8.04B - 1.38C - 0.3533AB + 0.6725AC - 0.8750BC - 13.85A^2 - 0.9220B^2 - 3.69C^2 \quad (4)$$

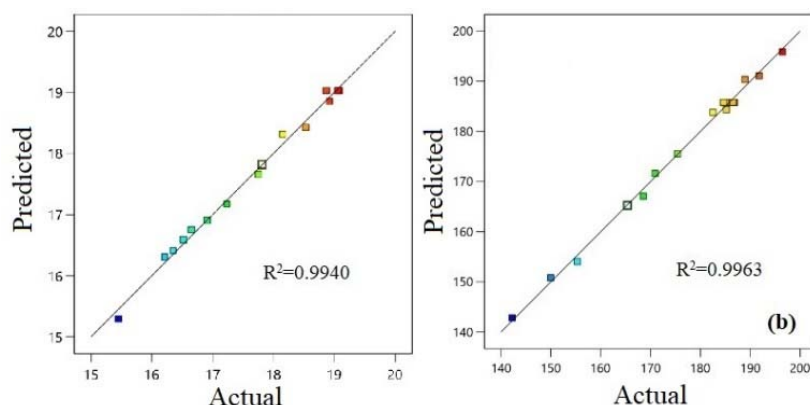


Fig. 4. Relationship between observed and predicted values (a: water adsorbed amounts, b: CEC).

TABLE V. ANOVA for the parameters of RSM-BBD

Statistics	Water absorbed g H ₂ O/100 g adsorbent	CEC / mg CaCO ₃ g ⁻¹
Sum of square	23.54	3861.23
Degree of freedom	9	9
Mean square	2.62	429.03
F-Value	129.60	211.80
Prob>F	<0.0001	<0.0001
Standard deviation	0.14	1.42
R ²	0.9940	0.9963
Lack of fit (p-values)	0.093	0.112

The model *F*-value of 129.60 indicates that the model is significant for Response 1 (water adsorption, g H₂O/100 g adsorbent). There is only a 0.01 % likelihood that an *F*-value of this magnitude could arise due to random variation. A *p*-value below 0.0500 indicates that the corresponding model term is significant. Accordingly, *A*, *B*, *AB*, *A*², *B*² and *C*² are well agreed, whereas terms with *p*-values above 0.1000 are considered insignificant. The lack of fit *F*-value of 4.38 suggests there is a 9.39 % chance that such a high lack of fit *F*-value could be due to noise.

Similarly, the model *F*-value of 211.80 signifies that the model is significant for Response 2 (CEC). Again, there is only 0.01 % probability that such an *F*-value could be noise-driven. Terms with *p*-values below 0.0500 are deemed significant, namely *A*, *B*, *C*, *A*², *B*² and *C*² in this case. Terms with *p*-values above 0.1000 are

deemed insignificant. The lack of fit F -value of 3.86 implies that the lack of fit is not significant relative to pure error, with an 11.23 % likelihood that this F -value could result from noise.

Based on these experiments (Table VI), the lowest water adsorption was 25.45 g H₂O/100 g adsorbent and the highest was 29.09 g H₂O/100 g adsorbent. Meanwhile, the CEC varied from a minimum of 142.25 mg CaCO₃ g⁻¹ to a maximum of 192.43 mg CaCO₃ g⁻¹.

TABLE VI. Statistical analysis for responses (water adsorbed amounts and CEC value)

Variable	Std. Dev.	Low	High
A : NaOH (mol/L)	0	2	3
B : Temperature, °C	0	60	90
C : S/L ratio, %	0	20	30
Water absorbed, g H ₂ O/100 g adsorbent	0.14	25.475	29.09*
CEC / mg CaCO ₃ g ⁻¹	1.42	142.35	192.43

Effect of variables on water adsorbed amounts and CEC value

To more thoroughly explore how synthesis parameters affect the adsorption properties of LTA-type zeolite, three-dimensional (3D) response surface plots were generated (Fig. 5). These plots demonstrate how NaOH concentration (A), temperature (B) and solid-to-liquid ratio (C) collectively influence both water adsorption capacity and cation exchange capacity.

The first row of Fig. 5 demonstrates the effects of process parameters on water adsorption (g H₂O/100 g adsorbent). NaOH concentration and temperature significantly influence water adsorption, whereas the solid-to-liquid ratio has a minor impact. Water adsorption increases with NaOH concentration up to around 2.5 M, then declines, reflecting the optimal concentration suggested by the negative quadratic coefficient ($-1.36A^2$). Temperature positively influences water adsorption ($+0.9189B$) initially, but diminishes at higher levels. The minimal effect of solid-to-liquid ratio is indicated by its small linear coefficient ($-0.1258C$).

The second row of Fig. 5 shows the response surfaces for cation-exchange capacity (CEC). Increasing NaOH concentration greatly enhances CEC ($+16.00A$), but overly high concentrations negatively affect it ($-13.85A^2$), possibly due to structural degradation. Temperature similarly shows a positive effect initially ($+8.04B$), slightly decreasing at higher temperatures ($-0.9220B^2$). The solid-to-liquid ratio has the smallest effect ($-1.38C$), indicating minimal influence on CEC . Overall, the response surface models underscore the need to optimize NaOH concentration and temperature to maximize both water adsorption and CEC while minimizing adverse structural alterations. Although the solid-to-liquid ratio does play a part, its effect is comparatively small. XRD results indicate that an excessively high solid loading (30 %) can impede nucleation, leaving quartz as the dominant phase (Run 3). The highest CEC (192.43 mg CaCO₃ g⁻¹) was achieved at 3

M NaOH, 90 °C and 25 % solid-to-liquid ratio, whereas the maximum water adsorption (29.09 g H₂O/100 g adsorbent) occurred at 2.5 M NaOH, 75 °C and 25 % solid-to-liquid ratio. XRD analyses confirmed that these conditions favor an LTA-type zeolite phase, with the best crystallinity obtained at 3 M NaOH, 90 °C (Run 17), consistent with its elevated *CEC* value. A balanced set of conditions that simultaneously account for both properties emerge at 2.5 M NaOH, 75 °C and 25 % *S/L* ratio (Run 7–11), although 3 M NaOH and 90 °C (Run 17) remains the best choice if maximizing *CEC* is the primary goal. Furthermore, to identify optimal synthesis conditions, XRD analysis was performed. As shown in Table VII and Fig. 6, all samples obtained through the statistical design exhibited the LTA-type zeolite phase. Fig. 6 highlights the distinctive reflections of LTA-type zeolite, confirmed by matching peaks to the 73-2340 Zeolite LTA standard in the Inorganic Crystal Structure Database (ICSD).

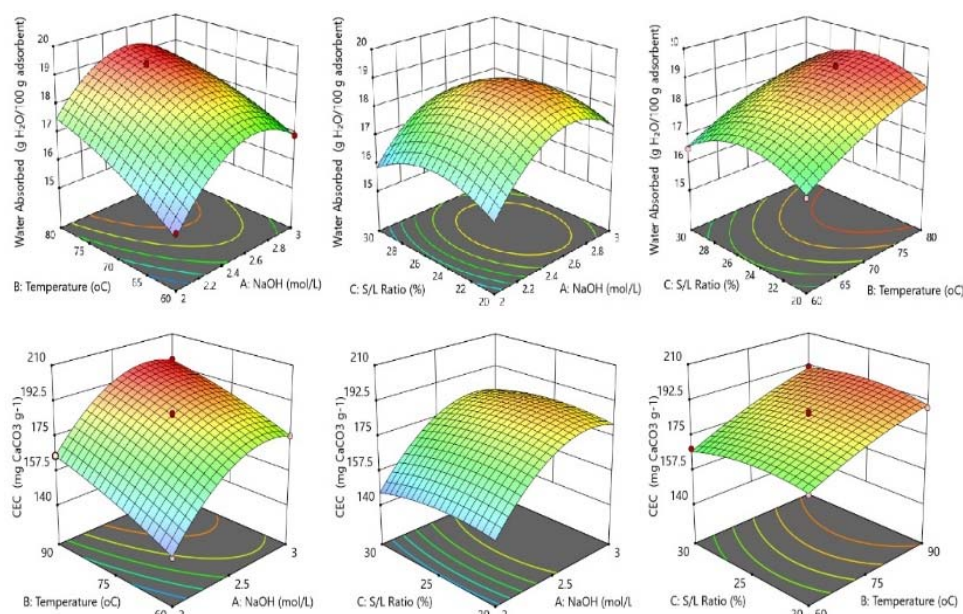


Fig. 5. Results of effecting variables on water adsorbed amounts and CEC value of LTA type zeolite.

Pawley refined X-ray patterns (Fig. 6, Table VII) confirm the synthesis window anticipated by the response surface model. At 2 M NaOH (Runs 1, 5, 6, 14) quartz dominates (63–78 %) and LTA remains below the 3 % detection limit, accompanied by 22–32 % amorphous aluminosilicate. Such behavior is characteristic of the dissolution reprecipitation constraint observed when alkalinity was inadequate for complete framework reconstruction.³⁶ Increasing the alkalinity to 2.5 M establishes a crystallization threshold even at 60 °C: Runs 2 and 3 contain 44

TABLE VII. XRD Results for of synthesized zeolite LTA

Run	Factor 1 A: NaOH (mol/L)	Factor 2 B: Temp., °C	Factor 3 C: S/L / %	LTA type zeolite %	Quartz %	Sodalite %	Amorphous %
1	2	60	25	<3	78	—	22
2	2.5	60	20	44	38	4	6
3	2.5	60	30	52	23	4	21
4	3	60	25	62	28	5	5
5	2	75	20	<3	64	2	30
6	2	75	30	<3	65	3	32
7–11	2.5	75	25	70	20	4–6	2–4
12	3	75	20	75	15	3–5	5–7
13	3	75	30	77	13	2–6	6–8
14	2	90	25	11	63	3	23
15	2.5	90	20	65	31	0–3	3–8
16	2.5	90	30	68	25	0–3	3–8
17	3	90	25	95–97	2–3	—	<1

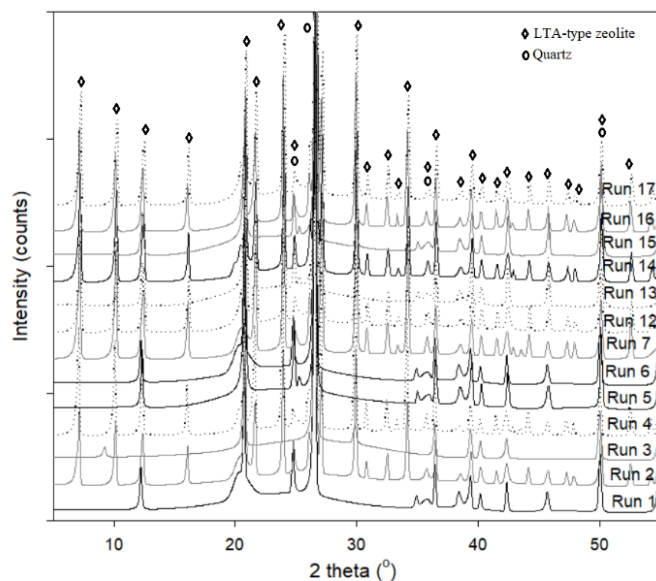


Fig. 6. XRD Results of diffractograms of the samples.

and 52 % LTA, respectively. The higher solid loading in Run 3 (30 % S/L) still leaves 21 % amorphous phase, illustrating the inhibitory effect of excessive slurry density on a ion mobility and nucleation.³⁹ With a concomitant rise in temperature to ≥ 75 °C, LTA crystallinity improves markedly. At 2.5 M NaOH and 75 °C (Runs 7–11), the products consistently contain approximately 70 % LTA, with quartz around 20 %, sodalite 4–6 % and only 2–4 % amorphous phase. The identical synthesis conditions applied to these runs resulted in similar phase compositions, as

summarized collectively in Table VII. The elevated water adsorption capacities observed in Runs 7–11 directly correlate with the high LTA content formed under these conditions. The highly porous LTA framework accounts for the enhanced water adsorption, while simultaneously elevated *CEC* values further confirm the dominant formation of the ion-exchangeable LTA zeolite phase. For Run 12 (3 M NaOH, 75 °C, 20 % *S/L*), the phase composition was estimated based on its similarity to neighboring runs, yielding approximately 75 % LTA, ~15 % quartz, 3–5 % sodalite, and 5–7 % amorphous content while at 3 M NaOH (Run 13) it reaches 77 % LTA with only 6–8 % amorphous residue. These observations mirror the positive interaction between the linear *A* (NaOH) and *B* (temperature) terms in the RSM surfaces. The optimum domain lies at high alkalinity and high temperature: Runs 15 and 16 (2.5 M NaOH, 90 °C) contain 65–68 % LTA with ≤8 % amorphous phase, whereas Run 17 (3 M NaOH, 90 °C, 25 % *S/L*) attains 95–97 % LTA ($a = 24.6127 \text{ \AA}$, $R_{wp} = 9.2 \%$) with only trace quartz and anatase. A residual line at $2\theta \approx 20.5^\circ$ ($d \approx 4.33 \text{ \AA}$) detected in partially crystallized samples corresponds to sodalite and indicates an intermediate stage in route to LTA formation 25. Collectively, these phase assemblages corroborate the statistical model: high alkalinity ($\geq 2.5 \text{ M}$) and elevated temperature ($\geq 75 \text{ }^\circ\text{C}$) are indispensable for phase-pure LTA, whereas lower NaOH or excessive solids loading suppresses nucleation, yielding quartz-rich or mixed products with diminished cation-exchange and water adsorption capacities.

Morphological and FTIR characterization results of best synthesis zeolite LTA (Run 17)

The scanning electron images show that the morphology of Run 17 sample was predominantly of cubic particles which are characteristic of LTA zeolite. High-magnification SEM images showed the presence of intergrown particles on the surface of cubes or between the cubes. The area marked with a black square in Fig. 7 was scanned by EDX. The EDX spectrum of sample Run 17 indicates that the main chemical elements present are Na, Al and Si, which are consistent with the chemical composition of LTA zeolite framework. The formation of the LTA structure was confirmed by the characteristic diffraction pattern observed in the XRD analysis.

High-magnification SEM images of Run 17 display well-defined cubic crystals ranging from sub-micron sizes up to approximately $2 \text{ }\mu\text{m}$, with sharp {100} faces and 90° edges, which is a morphology characteristic of low-silica zeolite LTA.³⁹ EDX analysis of the area highlighted in Fig. 7 yields an atomic ratio of $\text{Na} \approx \text{Al} \approx \text{Si}$, consistent with the ideal LTA framework composition ($\text{Na}_{12}[\text{Al}_{12}\text{Si}_{12}\text{O}_{48}]$). While cubic habit alone is not conclusive, the combination of this morphology, the stoichiometric Na–Al–Si balance, and the phase-pure LTA

reflections in the Pawley-refined XRD pattern (Fig. 6) collectively confirm that the product is LTA-type zeolite.

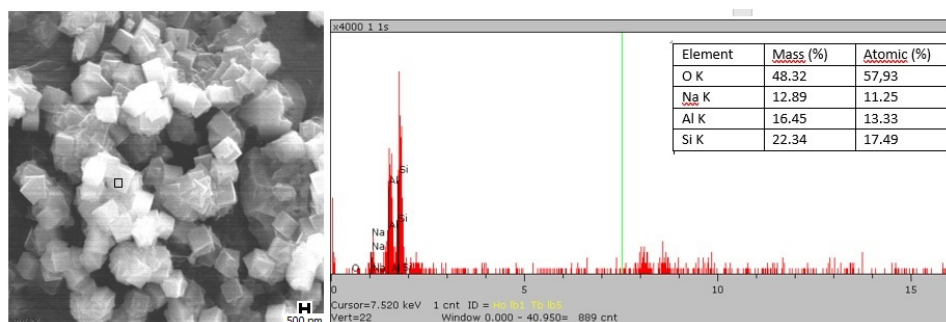


Fig. 7. SEM Results of Run 17 samples.

FTIR spectra were recorded from 4000 to 500 cm^{-1} using an FT-IR spectrometer and the KBr pellet technique. The FTIR spectrum of the sample synthesized under Run 17 conditions, which is the average yield of the synthesized zeolite LTA under optimal conditions (Run 17) was approximately 72 ± 3 wt. %, is shown in Fig. 8. It was compared the calcined kaolinite (MK). In the metakaolin sample, a broad band at 793.10 cm^{-1} corresponds to Al–O bonds in Al_2O_3 , while a vibration band at 1077.95 cm^{-1} is assigned to the Si–O stretch of SiO_2 . Although the spectrum for Run 17 shows overall similarity to that of commercial-grade LTA zeolite, a distinct additional band at 638 cm^{-1} is observed, which is absent in the commercial sample. Specifically, peaks at 546, 667 and 1007 cm^{-1} represent T–O

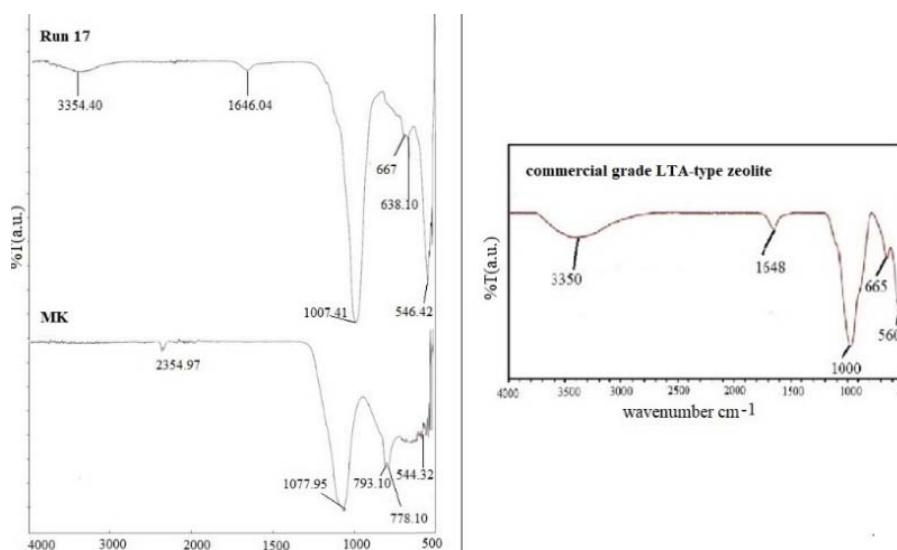


Fig 8. FTIR Results of Run 17 samples.

bending, double-loop bending, and TO_4 asymmetric stretching, respectively ($\text{T} = \text{Si}$ or Al). Additionally, bands between 3000 and 3600 cm^{-1} , as well as at 1646.04 cm^{-1} , indicate intermolecular hydrogen bonding and interstitial water. These observations are consistent with earlier reports,^{29,40} confirming the successful synthesis of LTA-type zeolite from MK under the selected optimal conditions. Moreover, the presence of strong absorption bands near $550\text{--}600\text{ cm}^{-1}$ and around 1000 cm^{-1} is widely recognized in the literature as indicative of a zeolite framework, reflecting the characteristic ring and tetrahedral vibrations of LTA-type structures. The obtained spectrum shows very good agreement with the reference FT-IR profile of commercial LTA-type zeolite (Fig. 8), while minor differences such as the 638 cm^{-1} band may reflect structural variations specific to the synthesized sample. Such shifts in vibrational modes from calcined kaolinite to the synthesized product highlight the reorganization of the aluminosilicate network, which is a key hallmark of the hydrothermal transformation into LTA zeolite.⁴⁰

CONCLUSION

Low-silica zeolite LTA was successfully synthesized in high yield from Balıkesir-region kaolin via a two-step process combining metakaolinization at $800\text{ }^\circ\text{C}$ and hydrothermal crystallization under alkaline conditions. Box–Behnken design and response-surface methodology (RSM) identified NaOH concentration and temperature as key factors controlling both cation-exchange capacity (CEC) and water adsorption, while excessive solid-to-liquid ratio inhibited nucleation. Crystallization toward the LTA framework occurred only above 2.5 M NaOH and $75\text{ }^\circ\text{C}$, with lower alkalinity or high slurry loading yielding quartz-rich or mixed phases. The optimal condition at 3 M NaOH, $90\text{ }^\circ\text{C}$ and $25\text{ }\%$ S/L produced nearly phase-pure LTA ($\approx 97\text{ }\%$) with lattice parameter $a = 24.6127\text{ }\text{\AA}$ and CEC of $192\text{ mg CaCO}_3\text{ g}^{-1}$. Water adsorption peaked at slightly milder conditions (2.5 M NaOH, $75\text{ }^\circ\text{C}$, $25\text{ }\%$ S/L), reflecting the narrow overlapping maxima predicted for both responses. XRD, SEM-EDX and FT-IR results demonstrated that the synthesized product exhibits cubic morphology and vibrational features consistent with LTA-type zeolite, closely resembling commercial materials. These results demonstrate that locally sourced kaolin can be converted into high-performance LTA zeolite without organic templates and under mild conditions, highlighting its potential as a cost-effective adsorbent or ion-exchange material for environmental applications.

ИЗВОД

СИНТЕЗА ЗЕОЛИТА LTA ИЗ КАОЛИНА И ЊЕГОВЕ ПЕРФОРМАНСЕ СВС И WAC
МОДЕЛА: ОПИМИЗОВАНО ЦЕНТРАЛНИМ КОМПОЗИТНИМ ДИЗАЈНОМ

GÜL AKAR ŞEN

Dokuz Eylül University, Faculty of Engineering, Mining Engineering Department, İzmir, Türkiye

У овом раду представљен је исплатив начин синтезе зеолиита LTA-типа из каолина који потиче из региона Balıkesir. Каолин је калцинисан на 800 °C да би се добио мета-каолин, који је затим третиран хидротермално у присуству NaOH при оптимизованим условима одређеним Box–Behnken експерименталним дизајном. Процесне променљиве концентрација NaOH, температура и однос чврсто/течно су систематски испитиване да се максимизира капацитет адсорпције воде и капацитет јонске измене (CEC). Модели квадратне регресије и ANOVA су потврдили да концентрација NaOH и температура имају најзначајнији утицај на формирање и перформансе зеолиита. Карактеризација XRD, SEM и FTIR спектроскопијом потврдила је да се производ синтетисан при оптимални условима претежно састоји од зеолитских кристала LTA-типа, што је потврђено карактеристичним рефлексијама, морфологијом и вибрационим тракама. Узорак који је имао најбоље перформансе је имао CEC до 192 mg CaCO₃ g⁻¹ и адсорпциони капацитет за воду до скоро 29 g H₂O по 100 g адсорбента. Ови резултати истичу потенцијал локално узоркованог каолина за производњу веома вредног зеолиита, нудећи одрживу алтернативу увозним сировинама.

(Примљено 10. марта, ревидирано 8. априла, прихваћено 22. јула 2025)

REFERENCES

1. C. Ronco, R. Bellomo, *Crit. Care* **26** (2022) 135 (<https://doi.org/10.1186/s13054-022-04009-w>)
2. S. Chatterjee, T. Chatterjee, S.H. Woo, *Chem. Eng. J.* **166** (2011) 168 (<https://doi.org/10.1016/j.cej.2010.10.047>)
3. M. Popaliya, A. Mishra, *Inter. J. Environ. Sci. Technol.* **20** (2023) 12919 (<https://doi.org/10.1007/s13762-022-04603-z>)
4. E. M. Flanigen, J. A. Rabo, *Micropor. Mesopor. Mater.* **47** (2001) 119 ([https://doi.org/10.1016/S1387-1811\(01\)00301-8](https://doi.org/10.1016/S1387-1811(01)00301-8))
5. J. B. Adeoye, J. A. Omoleye, M. E. Ojewumi, R. Babalola, *Inter. J. Appl. Eng. Res.* **12** (2017) 755 (https://www.ripublication.com/ijaer17/ijaerv12n5_27.pdf)
6. E. Victor, I. P. Okechukwu, C. N. Uchenna, *GSJ* **10** (2022) 1913 (http://www.globalscientificjournal.com/researchpaper/HYDROTHERMAL_SYNTHESIS_OF_ZEOLITE_Y_FROM_OKPELLA_KAOLIN_CLAY.pdf)
7. V. Verdoliva, M. Saviano, S. De Luca, *Catalysts* **9** (2019) 248 (<https://doi.org/10.3390/catal9030248>)
8. N. Yu. Ul'yanovaa, E. Yu. Brazovskayaa, O. Yu. Golubevaa, O. V. Shamovab, *Petroleum Chem.* **63** (2023) 790 (<https://doi.org/10.1134/S096554412305002X>)
9. C. Algieri, E. Drioli, *Sep. Pur. Technol.* **278** (2022) 119295 (<https://doi.org/10.1016/j.seppur.2021.119295>)
10. P. Bai, M. Y. Jeon, L. Ren, C. Knight, M. W. Deem, M. Tsapatsis, J. I. Siepmann, *Nat. Commun.* **6** (2015) 5912 (<https://doi.org/10.1038/ncomms6912>)
11. H. N. Tran, P. V. Viet, H. Chao, *Environ. Saf.* **147** (2018) 55 (<https://doi.org/10.1016/j.ecoenv.2017.08.027>)

12. P. Frontera, S. Candamano, A. Macario, F. Crea, L. A. Scarpino, P. L. Antonucci, *Mater. Lett.* **104** (2013) 72 (<https://doi.org/10.1016/j.matlet.2013.03.138>)
13. H. Zhang, A. Li, W. Zhang, C. Shuang, *J. Colloid Interface Sci.* **468** (2015) 128 (<https://doi.org/10.1016/j.jcis.2015.10.006>)
14. A. Ates, G. Akgül, *Pow Tech.* **287** (2016) 285 (<https://doi.org/10.1016/j.powtec.2015.10.021>)
15. A. A. Ahmed, Z. H. Yamani, *Mater. Chem. Phys.* **259** (2021) 124181 (<https://doi.org/10.1016/j.matchemphys.2020.124181>)
16. C. Baerlocher, L.B. McCusker, *Database of Zeolite Structures*, 2025, <http://www.iza-structure.org/databases/> (accessed on 24 April 2025)
17. T. Ohgushi, S. Komarneni, A. S. Bhalla, *J. Porous Mater.* **8** (2001) 23 (<https://doi.org/10.1023/A:1026518200875>)
18. W. Wang, Q. Feng, K. Liu, G. Zhang, J. Liu, Y. Huang, *Solid State Sci.* **39** (2015) 52 (<https://doi.org/10.1016/j.solidstatesciences.2014.11.012>)
19. X. Shen, G. Qiu, C. Yue, M. Guo, M. Zhang, *Environ. Sci. Pollut. Res. Int.* **24** (2017) 21829 (<https://doi.org/10.1007/s11356-017-9824-5>)
20. M. K. Seliem, S. Komarneni, *Micropor. Mesopor. Mater* **228** (2016) 266 (<https://doi.org/10.1016/j.micromeso.2016.04.010>)
21. K.S Hui, C. Y. H. Chao, *Micropor. Mesopor. Mater* **88** (2006) 145 (<https://doi.org/10.1016/j.micromeso.2005.09.005>)
22. W. J. Roth, P. Nachtigall, R. E. Morris, J. Cejka, *Chem. Rev.* **114** (2014) 4807 (<https://doi.org/10.1021/cr400600f>)
23. A. E. Gaidoumi, A. C. Benabdallah, B. E. Bali, A. Kherbeche, *Arab. J. Sci. Eng.* **43** (2017) 191-197 (<https://doi.org/10.1007/s13369-017-2768-8>)
24. Hartati, D. Prasetyoko, M. Santoso, I. Qoniah, W. L. Leaw, P. B. D. Firda, H. Nur, *J. Chin. Chem. Soc.* **67** (2020) 911 (<https://doi.org/10.1002/jccs.201900047>)
25. I. Bojaddayni, M. E. Küçük, Y. Ouardi, I. Jilal, S. Barkany, K. Moradi, E. Repo, K. Laatikainen, A. A. Ouammou, *Min. Eng.* **198** (2023) 108086 (<https://doi.org/10.1016/j.mineng.2023.108086>)
26. T. B. H. Nguyen, H. T. Van, *Technol. Agron.* **4** (2024) e002 (<https://doi.org/10.48130/tia-0023-0021>)
27. M. Senila, O. Cadar, *Heliyon* **10** (2024) 25303 (<https://doi.org/10.1016/j.heliyon.2024.e25303>)
28. M. Gougazeh, *J. Taibah Univ. Sci.* **12** (2018) 247 (<https://doi.org/10.1080/16583655.2018.1465714>)
29. Y. Cui, Y. Zheng, W. Wang, *Minerals* **8** (2018) 338 (<https://doi.org/10.3390/min8080338>)
30. M. A. V. Villaquirán-Cacedo, R. M. De Gutiérrez, M. Gordillo, N. C. Gallego, *Clays Clay Miner.* **64** (2016) 75 (<https://doi.org/10.1346/CCMN.2016.0640201>)
31. L. Ayele, J. Pérez-Pariente, Y. Chebude, I. Díaz, *Micropor. Mesopor. Mater.* **215** (2015) 29 (<https://doi.org/10.1016/j.micromeso.2015.05.022>)
32. L. Ayele, J. Pérez-Pariente, Y. Chebude, I. Díaz, *New J. Chem.* **40** (2016) 3440 (<https://doi.org/10.1039/c5nj03097h>)
33. S. K. Kirdeciler, B. Akata, *Adv. Powder Tech.* **31** (2020) 4336 (<https://doi.org/10.1016/j.apr.2020.09.012>)
34. B. Ait-Amir, P. Pougnet, A. El-Hami, *Embedded Mechatronic Sys. 2nd Ed.* **2** (2020) (ISBN: 9781785481901, eBook ISBN: 9780081019566)

35. M. R. Wang, D. C. Jia, P. G. He, Y. Zhou, *Mater. Lett.* **64** (2010) 2551
(<https://doi.org/10.1016/j.matlet.2010.08.007>)
36. C. Belviso, F. Cavalcante, A. Lettino, S. Fiore, *Appl Clay Sci.* **80–81** (2013) 162
(<https://doi.org/10.1016/j.clay.2013.02.003>)
37. B. B. Sousa, J. A. R. Rego, D. S. B. Brasil, M. C. Martelli, *Cerâmica* **66** (2020) 404
(<https://doi.org/10.1590/0366-69132020663802758>)
38. B. Fabbri, S. Gualtieri, C. Leonardi, *Appl. Clay Sci.* **73** (2013) 2
(<https://doi.org/10.1016/j.clay.2012.09.019>)
39. C. S. Cundy, P. A. Cox, *Micropor. Mesopor. Mater.* **82** (2005) 1
(<https://doi.org/10.1016/j.micromeso.2005.02.016>)
40. M. Alkan, Ç. Hopa, Z. Yilmaz, H. Güler, *Micropor. Mesopor. Mater.* **86** (2005) 176
(<https://doi.org/10.1016/j.micromeso.2005.07.008>).



J. Serb. Chem. Soc. 90 (10) 1241–1252 (2025)
JSCS–5451

Impact of drying, freezing and re-wetting events soil leachate in acidic *versus* calcareous soils

EMIRA HUKIĆ^{1*}, MILICA KAŠANIN-GRUBIN², MIREL SUBAŠIĆ¹, TOMISLAV
TOSTI², SVETLANA ĐOGO-MRAČEVIĆ³, SNEŽANA ŠTRBAC¹
and SANJA STOJADINOVIĆ²

¹University of Sarajevo – Faculty of Forestry, Sarajevo, Bosnia and Herzegovina, ²Institute of
Chemistry, Technology and Metallurgy, Belgrade, Serbia and ³University of Belgrade Faculty of
Pharmacy, Belgrade, Serbia

(Received 10 March, revised 24 April, accepted 30 June 2025)

Abstract: This study investigates the impact of drying-rewetting and freezing-rewetting events on soil leachate ion composition across two contrasting geochemical settings through a series of controlled laboratory experiments. Dissolution of ions (Na^+ , K^+ , Ca^{2+} , Mg^{2+} , Al^{3+} , Fe^{3+} , Mn^{2+} , F^- , Cl^- , NO_2^- , SO_4^{2-} , NO_3^- , PO_4^{3-}) in soil leachate was analysed following rewetting cycles after drying and freezing treatments. The results indicate that variations in leachate ion concentrations are primarily influenced by bedrock type, while drying-rewetting and freezing-rewetting treatments did not significantly impact overall variance. However, some inconsistent differences were observed: higher K^+ concentrations in calcareous soils and Al^{3+} , Fe^{3+} and Mn^{2+} in acidic soils after drying, higher anion concentrations in calcareous soils in both treatment leachates compared to controls. The findings highlight that the effects of drying, freezing, and rewetting are inherently linked to treatment type, ion characteristics and geochemical conditions.

Keywords: ions; forest soil; laboratory experiment; thermal conditions; limestone; sandstone.

INTRODUCTION

Analysing the composition of soil leachate is important for understanding stress factors affecting forest ecosystems.¹ Soil solution unravels climate change impacts, observed for instance in leaching losses of N.² The leaching of nitrate and sulphate ions is associated with the losses of soil base cations like Ca^{2+} and Mg^{2+} affected by increases in soil acidity, which causes potential decrease in forest productivity. Forest disturbance in relation to the climate changes can have significant effect on soil chemical properties, and on a relatively short-term it may

*Corresponding author. E-mail: e.hukic@sfsa.unsa.ba
<https://doi.org/10.2298/JSC250310040H>

affect soils' solution.³ The sediment and nutrient losses increase after freeze-thaw conditions.⁴ The similarity of ion availability is known to be affected by seasonal soil warming.⁵ The nutrient depletion from soil poses an environmental challenge for tree species, and its underlying factors are not yet fully understood.

Drying, freezing and re-wetting soil processes are controlled by meteorological conditions. Both processes, successional drying and wetting, or wetting, freezing and melting, are on-site processes controlled by the factor of soil temperature change. Soil temperature change accelerates soil dispersion forces and looseness of soil particles, and dissolvability of loosely bonded soil ions which are accordingly leached from soil. How specific ions, regarding different types of soil, site and regional level meteorology, react to alternations in temperature dynamic have not been sufficiently documented.

Limestone (with 61 %) and quartz sandstone (with 30 %) are among the most abundant bedrock types in Bosnia and Herzegovina.⁶ Two the most common forest soil types Calcic Cambisol and Dystric Cambisol are formed on these bedrock materials.⁷ While soils formed on limestone and dolomite are either calcic, calcareous and eutric, often not containing active carbonates, those formed on quartz reddish Werfen sandstone are highly acidic and dystric. Substantial distinctions are evident concerning their chemical and mineralogical properties. Calcic Cambisol formed on clear limestone (~99 % CaCO_3) have clay-like texture and contain montmorillonites, quartz, kaolinite and small amount of hematite.⁸ Dystric Cambisol formed on sandstones have sandy texture and they inherit quartz, mica and clay fraction.⁹ Although the most of the forest soils in the Dinaric region are not attributed to significant microclimate changes due to the applied close-to-nature silvicultural practices, their thermal stability is moderated by the multi-layered forest canopy.¹⁰ However, this buffering effect may be compromised by the anticipated increase in natural hazards causing large-scale forest disturbances.¹¹ The ability of soils to retain nutrients is anticipated to change. Hence, it is important to attain deeper understanding about the effect of increased soil temperature fluctuations on the ion dynamic behaviour.

In order to achieve better understanding of factors controlling leachate composition, simulation of soil temperature fluctuations was performed in laboratory conditions. The main hypothesis was that the thermal conditions determine soil leachate composition relative to soil geochemistry. Three main objectives were a) to determine an average leachate composition assuming light rain; b) to identify the main factor of soil leachate variation and c) to test the effect of treatments.

EXPERIMENTAL

Soil sample origin and pretreatment measurements

To analyse soil leachate composition, samples were collected from two contrasting soil and geological types. The soil samples originated from the Dinaric mountain beech and fir forests, developed on clear Triassic limestone on Mt. Bjelašnica (43.72735°N; 18.27205°E) and

Triassic quartz sandstone on Mt. Trebević (43.8332°N; 18.46439°E). The chosen bedrock types represent the most common geological settings in Bosnia and Herzegovina.¹² Soils were field described and named according to World Reference Base from 2022 as Calcaric Cambisol (Humic, Episceletic, Episiltic) with Oligomull humus on limestone (Calcareous soil) and as Dystric Cambisol (Chromic) with Hemimor humus on Werfenic sandstone (acidic sandstone soil, Table I).¹³ Four soil samples were collected from soil profile pits of calcareous and acidic sandstone soil at fixed depths from 0 to 10 cm and 10 to 20 cm. Approximately 3 kg of soil was taken from each layer, or 12 kg in total. Total number of composite samples was four: two calcareous and two sandstone soil.

TABLE I. Soil properties of calcareous and acidic sandstone soil (*N* – number of samples, depth of sample in cm, bulk density – *BD* (g cm⁻³), water field capacity – *FC* (vol. %), texture (CIL – clay loam, S – sandy loam), pH value, carbonates as CaCO₃ (%), soil organic carbon (*SOC*), total nitrogen (*TN*), C to N ratio – *C/N*; Bedrock, soil type and humus form were determined during site survey and compared with soil map

No.	Soil type	<i>N</i>	Depth cm	<i>BD</i> g cm ⁻³	<i>FC</i> vol. %	Texture US Soil	pH (CaCl ₂)	CaCO ₃ %	<i>SOC</i> %	<i>TN</i> %	<i>C/N</i>
Calcareous soil											
1.	Calcaric Cambisol	1	0–10	0.40	44.0	CIL	5.98	3.50	12.1	0.80	15.1
2.	(Limestone)	1	10–20	0.51	40.0	CIL	6.12	3.50	11.3	0.40	28.3
Acidic sandstone soil											
3.	Dystric Cambisol	1	0–10	1.30	31.8	SL	3.53	0.00	8.01	0.37	21.6
4.	(Sandstone)	1	10–20	1.42	21.5	SL	3.93	0.00	4.90	0.23	21.3

After the transportation to the laboratory, soil samples were manually cleaned, homogenized, and air-dried in preparation for subsequent drying, freezing, and re-wetting treatments. The natural aggregate structure was preserved; samples were not milled, but instead gently ground by hand and sieved through a 4 mm mesh. A portion of each sample was set aside for pre-treatment analysis of soil properties.

Pre-treatment measurements included determining following properties: bulk density (*BD*, gravimetrically), field capacity (*FC*, gravimetrically), soil texture (pipet method with 0.2M Na pyrophosphate), pH value (in 0.01M CaCl₂ dilution), amount of CaCO₃ (volumetrically, ISO 10693:1995),¹⁴ soil organic carbon (*SOC*, combustion with K₂Cr₂O₇, ISO 14235:1998)¹⁵ and total nitrogen (*TN*, Kjeldahl method, ISO 11261:1995)¹⁶ were determined per fixed layer depth prior to further analysis (Table I) at the laboratory of University of Sarajevo – Faculty of Forestry, Sarajevo (Bosnia and Herzegovina).

Experimental design

The experiment was designed to test the impact of drying–rewetting and freezing–rewetting cycles on the composition of soil leachate (Fig. 1). Applying a light drizzle with an intensity of approximately 0.25 mm h⁻¹, the concentrations of leached ions were quantified for each treatment after four rewetting cycles. Equal masses (~110 g) of air-dried calcareous soil (CS) and acidic sandstone soil (AS) were used to fill the porous plastic containers, six per soil type (twelve in total), for subsequent treatments.

The control soil (CS control 0-10, CS control 10-20, AS control 0-10, AS control 10-20) was soil in porous plastic containers left with approximate 40 % of water, corresponding to

average field capacity content for both soils. The soil was left at room temperature approximately 22–23 °C, overnight and re-wetting cycles were performed with the rain intensity of 122 ml during 30 min, *i.e.*, $\sim 0.25 \text{ mm h}^{-1}$.

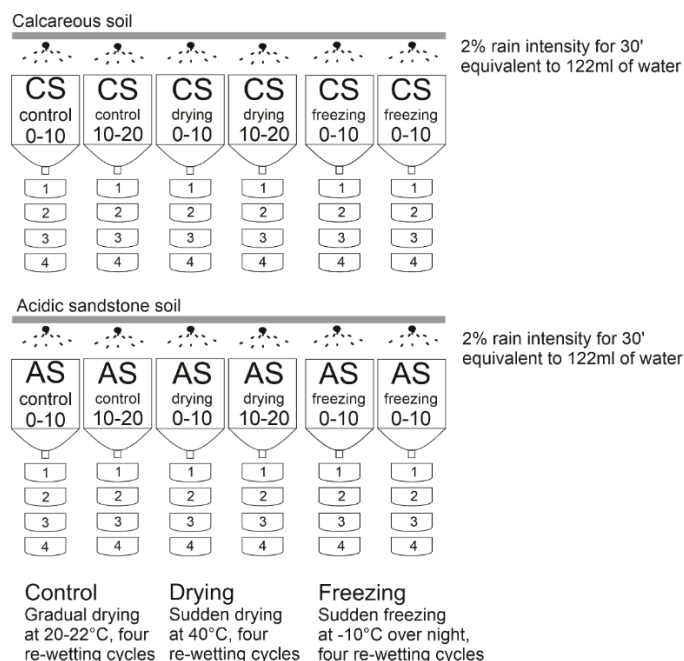


Fig. 1. Experimental design of drying-re-wetting and freezing-re-wetting treatment impact on soil leachate composition. Soil samples are marked as control calcareous (CS control 0-10, CS control 10-20, CS drying 0-10, CS drying 10-20, CS freezing 0-10, CS freezing 10-20) and acidic sandstone soil (AS control 0-10, AS control 10-20, AS drying 0-10, AS drying 10-20, AS freezing 0-10, CS freezing 10-20).

The drying treatment involved sudden drying event of soil sample (CS drying 0-10, CS drying 10-20, AS drying 0-10, AS drying 10-20) in the oven at 35 °C for 4 h, cooling at room temperature and re-wetting with simulated rain intensity of 122 ml in 30 min which corresponded to light rain intensity of $\sim 0.25 \text{ mm h}^{-1}$.

The freezing treatment involved freezing of soil sample (CS freezing 0-10, CS freezing 10-20, AS freezing 0-10, CS freezing 10-20) at -10 °C over night, leaving at room temperature for one hour and re-wetting with the same rainfall intensity of 122ml in 30 min which corresponded to light rain intensity of $\sim 0.25 \text{ mm h}^{-1}$.

Experiment was set up at the Institute of Chemistry, Technology and Metallurgy (ICTM), University of Belgrade (Serbia). All samples in plastic containers were connected to rain-event simulator with funnel so that no water is lost. Soil water leaching from plastic containers was collected and used for further measurements.

Leachate measurements

Leachate (soil water) volume, pH value and electric conductivity (EC , $\mu\text{S cm}^{-1}$) captured after each treatment and control were measured (electrometrically). Concentrations of soil

leached cations (K^+ , Ca^{2+} , Mg^{2+} , Na^+ , Al^{3+} , Fe^{3+} , Mn^{2+}) were measured on Inductively coupled plasma optical emission spectrometer with axial view (Thermo scientific iCAP 6000 series ICP spectrometer, USA). Concentrations of anions (F^- , Cl^- , NO_2^- , SO_4^{2-} , NO_3^- , PO_4^{3-}) were determined on Dionex ICS 3000, *i.e.*, ion chromatography with conductometric detection. The method refers to is EPA 314.7 (this method applies to anions in water) but at Institute of Chemistry, Technology and Metallurgy in Belgrade it is validated and verified it for anions in soil. Concentrations of cations and anions in soil leachate are given in $mg\ L^{-1}$. Ion measurements were made in the ICTM laboratories

Statistical analysis

Descriptive statistical methods were used to present the average composition of the leachate concentrations based on the control ($N = 16$), treatment drying ($N = 16$) and treatment freezing ($N = 16$). Total number of observations was $N = 48$. Soil leachate composition, means and standard deviations were calculated for calcareous (CS control 0-10, CS control 10-20) and acidic sandstone soil (AS control 0-10, AS control 10-20). Leachate concentrations of ions and anions represent means of two rain cycles. Principal component analysis (PCA) was used to address cumulative variance among variables and the effect of bedrock and treatment. The “prcomp” function from the base R package “stats” was employed for this purpose. Variables were scaled prior to model fit.¹⁷ Analysis were performed in RStudio version 4.3.1.¹⁸

RESULTS AND DISCUSSION

Soil leachate composition

Determined values of leachate pH, EC and ion concentrations were generally corresponded to those reported in the literature, although some deviations were observed (Table II). The only exception were the pH values in the calcareous soil,

TABLE II. Means and standard deviations (in brackets) of pH values, electrical conductivity (EC, $\mu S\ cm^{-1}$) and ion concentrations ($mg\ L^{-1}$) in leachate of control calcareous and acidic sandstone soils (combined M10 and M20) compared to typical forest soil ranges according to Blume *et al.* (2016)¹⁹

Feature	Calcareous soil (M10 and M20)	Acidic sandstone soil (M10 and M20)	Typical range for forest soils
pH	7.07 (0.25)	4.31 (0.09)	3.00–4.50
EC	747 (475)	97.7 (9.48)	200–1600
Al	0.16 (0.05)	1.71 (0.11)	0.20–3.00
Ca	127 (0.35)	5.35 (0.16)	<1.00–180
Mg	6.80 (0.39)	1.47 (0.06)	<0.01–30.0
Na	18.5 (14.7)	1.43 (0.14)	<1.00–40.0
K	1.51 (0.02)	0.58 (0.44)	0.30–50.0
Mn	0.11 (0.07)	2.35 (0.05)	0.02–3.00
Fe	0.13 (0.02)	0.50 (0.05)	0.00–10.0
F	0.01 (0.00)	0.00 (0.00)	0.20–30.0
Cl	0.96 (0.06)	0.89 (0.17)	3.00–170
NO ₂	0.01 (0.00)	0.00 (0.00)	<1.00
SO ₄	0.78 (0.21)	1.62 (0.02)	5.00–350
NO ₃	3.86 (2.37)	0.58 (0.05)	5.00–450
PO ₄	0.04 (0.03)	0.12 (0.02)	<0.05–12.0

and concentrations of Cl^- , SO_4^{2-} and NO_3^- in the acidic soil applying light rainfall of 0.25 mm h^{-1} the leaching rates may vary in respect to natural soil heterogeneity. Soil leachate composition was imparted by geochemical characteristic of the two soil sample sets, the acidic sandstone and the calcareous soil.

Soil leachate composition in relation to bedrock

The variation in ion concentrations of leachate are linked to soil pH, buffering capacity, and the presence of organic matter influenced by bedrock. This was revealed by the cumulative variance in PCA which indicates sample bedrock type as the main discriminating factor, while drying–re-wetting and freezing–re-wetting treatment did not significantly impact variance (Fig. 2).

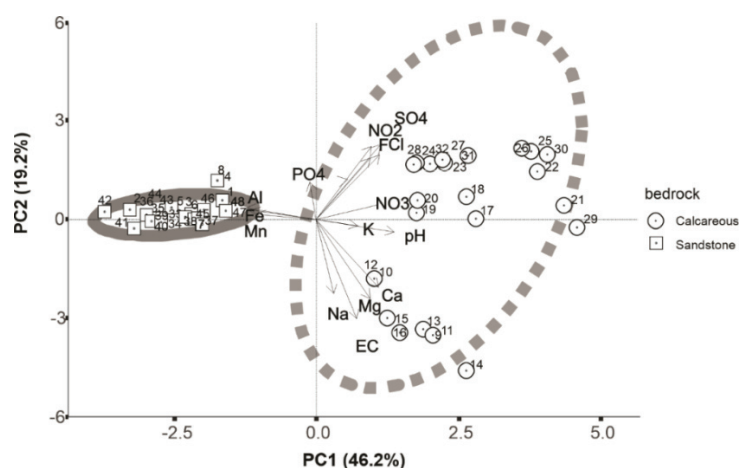


Fig. 2. Principal component analysis (PCA) plot of drying–re-wetting and freezing–re-wetting experiment showing variance in soil water composition impacted by soil geochemistry on two different soils calcareous soil (dashed line) and sandstone soil (solid line). The first two principal components (PCs) are plotted and colored according to bedrock. PCA was performed using all data (48 observations). Percentage of variation accounted for by each principal component is shown in brackets with the axis label.

The first two PCs account for approximately 65.4 % of the total variance. This suggests that these components effectively capture the essential patterns within the data. The eigenvalues associated with each PCs reveal the amount of variance explained by that component. Higher eigenvalues, $PC1 = 6.91$, $PC2 = 2.58$ explain the most variance. Variables Al^{3+} , Fe^{3+} and Mn^{2+} were negatively correlated with $PC1$ and pH, EC, all anions concentrations, as well as Ca^{2+} , Mg^{2+} , Na^+ and K^+ were positively correlated with $PC1$. The anion concentrations were correlated with the increase of $PC2$, EC, Ca^{2+} and Mg^{2+} were correlated with decrease of $PC2$, and there was no correlation to pH values and nitrite concentrations.

The primary outcome illustrates the influence of soil geochemistry on the ion leachate composition and ions concentrations (Fig. 2). The leachate ion concentrations varied according to *PC1* (eigenvalue, 6.91), followed by *PC2* (eigenvalue, 2.58). The strong correlation between Al^{3+} , Fe^{3+} and Mn^{2+} was specific for soil formed on acidic sandstone. Anions except nitrites correlated to each other and basic ions, Na^+ , K^+ , Ca^{2+} and Mg^{2+} , specific for calcareous soil formed on limestone. Many interrelated properties different for the two types of soil, like texture.²⁰ Also, the soil water holding capacity explain variation in soil ion diffusion.²¹

Effect of treatments

To assess the cumulative ion release and show overall treatment effects, concentrations from all four rewetting cycles were summed for each sample (Table III).

TABLE III. Summed ion concentrations (mg L⁻¹) in leachate from control, drying–rewetting (drying) and freezing–rewetting (freezing) treatments in calcareous and acidic sandstone soils (M10 and M20 layers); values of pH and electric conductivity (*EC*, $\mu\text{S cm}^{-1}$) are mean values

Feature	Calcareous soil						Acidic sandstone soil					
	Control		Drying		Freezing		Control		Drying		Freezing	
	M10	M20	M10	M20	M10	M20	M10	M20	M10	M20	M10	M20
pH	6.90	7.25	7.10	7.77	6.93	7.47	4.24	4.37	4.33	4.57	4.16	4.16
<i>EC</i>	411	1083	157	232	244	235	104	91.0	151	95.4	117	106
Al	0.76	0.48	0.76	0.24	0.93	0.39	7.14	6.51	17.1	5.02	9.53	5.60
Ca	506	508	142	308	226	290	20.9	21.8	39.6	25.7	21.9	17.6
Mg	28.3	26.1	10.3	13.2	20.2	13.0	5.73	6.07	12.1	7.39	7.88	5.56
Na	32.4	60.1	5.70	7.00	50.0	6.60	5.34	6.11	9.12	7.06	7.51	9.39
K	6.00	6.10	7.60	5.00	3.53	3.12	3.57	1.07	9.00	2.48	1.54	0.04
Mn	0.64	0.25	0.37	0.11	0.63	0.12	9.56	9.26	23.4	10.6	11.9	6.43
Fe	0.58	0.46	0.47	0.32	0.63	0.34	2.13	1.87	5.31	0.95	4.61	2.92
F	0.04	0.02	0.65	0.34	0.47	0.38	0.01	0.02	0.01	0.01	0.04	0.01
Cl	3.68	4.03	10.6	12.6	7.68	11.5	4.03	3.09	3.63	2.61	2.56	0.75
NO ₂	0.02	0.02	0.97	1.03	0.84	1.00	0.02	0.01	0.03	0.01	0.00	0.00
SO ₄	3.73	2.52	58.6	63.8	44.1	63.7	6.55	6.44	4.69	3.53	3.67	1.66
NO ₃	22.1	8.72	19.2	25.9	9.92	25.8	2.21	2.44	2.07	0.49	0.76	0.81
PO ₄	0.05	0.23	0.24	0.25	0.24	0.25	0.51	0.42	0.18	0.33	0.10	0.02

The leachate pH values, *EC* and the ion concentrations differed between the two bedrock types: calcareous and acidic sandstone (Figs. 3 and 4).

In calcareous soils, K^+ concentrations increased after the drying–rewetting treatment, while Na^+ concentrations were higher following the freezing–rewetting treatment (Fig. 3). No increase in the cation concentrations was observed in the calcareous soil following the treatments. In the acidic sandstone soils, the drying–rewetting treatment led to elevated concentrations of Al^{3+} , K^+ , Mg^{2+} , Mn^{2+} and Fe^{3+} in the layer M10 compared to the control leachate. No increase in the cation concentrations was observed in the acidic sandstone soil following the freezing–

–rewetting treatment. These effects were not observed in the M20 horizon of both soil types. Consequently, drying–rewetting vs freezing–rewetting treatments did not reveal a consistent and uniform effect with respect to the analysed variables of soil leachate in acidic sandstone and calcareous soil.

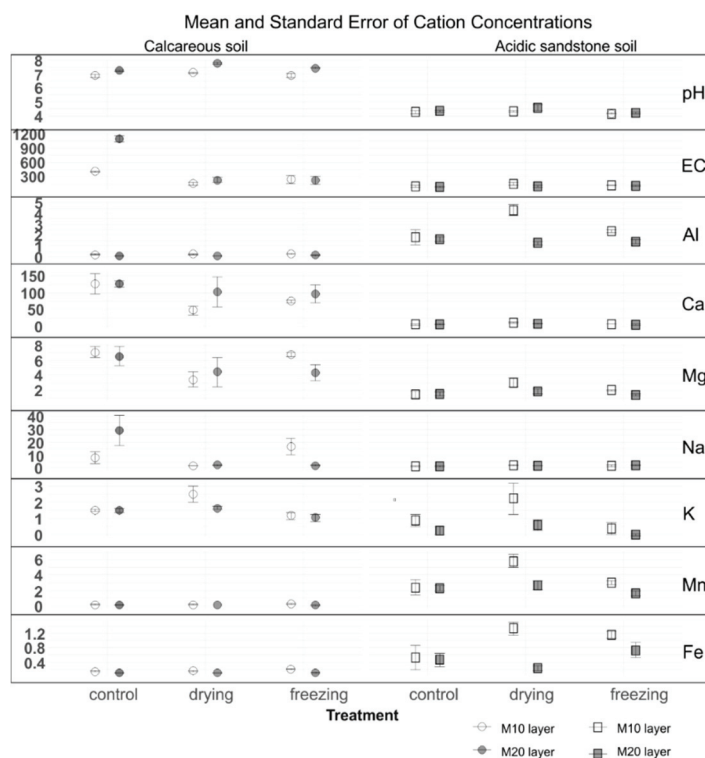


Fig. 3. Mean and standard error for leachate pH values, electric conductivity EC ($\mu\text{S cm}^{-1}$) and cation concentrations (mg L^{-1}) concentrations relative to bedrock, treatment and soil layer (0–10 cm M10; 10–20 cm M20).

The effect of drying–rewetting and freezing–rewetting treatments was evident in the concentrations of analysed anions in calcareous soil (Fig. 4). Anion concentrations were higher after both treatments compared to the control. In contrast, no significant differences in anion concentrations were observed in acidic sandstone soil.

No clear differences between treatments (drying–rewetting and freezing–rewetting) were observed.

The potassium concentration increased with higher temperature in calcareous soil was previously explained by higher K transmission factor with higher temperature in regard to water viscosity.²² Also in nutrient rich soils, drying–rewetting and freezing–rewetting treatments influenced increases in leached concentration

of anions, which are most likely linked to easily soluble ions in soil organic matter. Drying induces N and P mobilization which may influence their leaching from soils.²³ Drying and rewetting probably caused dissolution of the organic N in this soil organic matter rich soil.²⁴ Nitrogen availability in natural soils is predominantly linked to soil organic matter dynamic and microbial processes which are sensitive to drying and rewetting. Increase in SO_4^{2-} and Cl^- are linked to the increase in temperature and higher moisture content as highly susceptible to dissolution.²⁵ In calcareous soils ions, Ca^{2+} , Mg^{2+} , K^+ and Na^+ , stand in equilibrium with negatively charged surfaces of clay minerals and organic matter. Dissolved available ions, Al^{3+} , Fe^{3+} and Mn^{2+} , in calcareous soil did not show significant difference from control leachate, indicating their stability in such kinetic state.

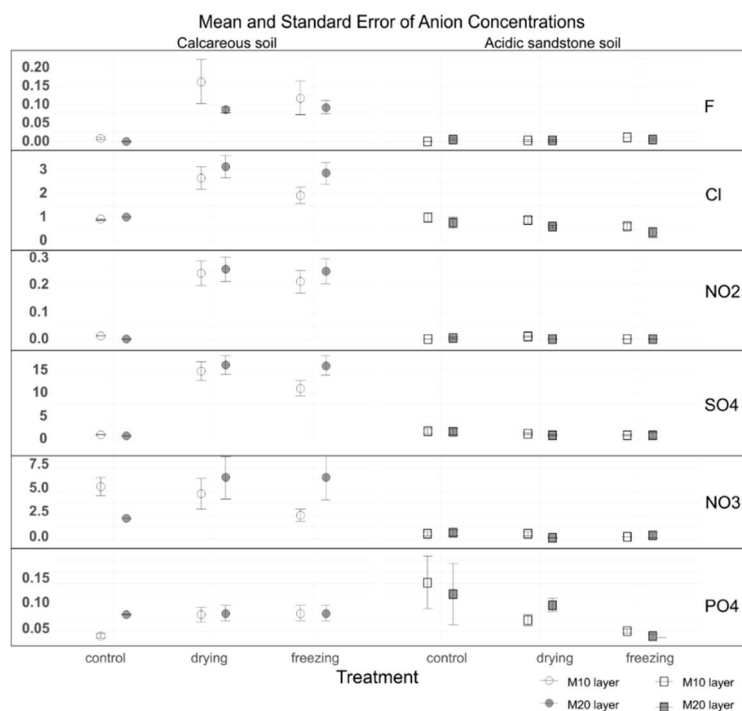


Fig. 4. Mean and standard error for leachate anion concentrations (mg L^{-1}) concentrations relative to bedrock, treatment and soil layer (0–10 cm M10; 10–20 cm M20).

In acidic soil leachate unclear treatment effect was found, observed in similar values of *EC*, pH values and ion concentrations among treatments. Only concentrations of Al^{3+} , Mn^{2+} were higher after drying–rewetting events, or Fe^{3+} also after freezing–rewetting treatment. Freezing–rewetting stimulated substantially higher Fe^{3+} concentrations in the acidic soil. Organic acids and rewetting may be linked

to metal leaching in the form of Al^{3+} and Mn^{2+} chelates. It was found that a solubilization of Al^{3+} , Fe^{3+} and Mn^{2+} is higher in low pH soil.²⁶ Most probably Fe chelated with organic acids or the non-chelating acidic agents is prone to leaching processes in acidic sandstone soil. It was found in field conditions that soil rewetting after dry periods can cause low pH and high amounts of dissolved metals in the water.²⁷ Depending on disturbance level acidic sandstone soil may cause periodically higher metal concentrations in water. The anion concentrations differed between treatments, but generally they were in the same range as control.

The dissolution of ions should be considered both thermodynamically and kinetically, meaning that changes in energy and kinetics may be favourable or not for ion dissolution.

It is known that implications of changes of thermodynamic conditions may be more intense in acidic soil on sandstone due to higher concentrations of Al^{3+} , Fe^{3+} and Mn^{2+} .²⁸ The acidification also affects calcareous soil, but due to the buffering effect of CaCO_3 these soils are not having increase in Al^{3+} , Fe^{3+} and Mn^{2+} concentrations in leachate. The ion concentrations variability in the soil leachate can be attributed to the inherent differences in ion dissolution rates, which are influenced by soil properties.²⁹

Additionally, the sample size and the number of cycles of repeating treatments in this study, in order to fully capture variability in leaching dynamics should be enlarged in further studies.

CONCLUSION

The results of this study indicate that the thermodynamic conditions significantly influence the composition of leachate in relation to the geochemical properties of the soil. The observed differences in ion concentrations between the drying–rewetting and the freezing–rewetting conditions suggest that ion solubility in agreement between both the type of ion and the prevailing thermodynamic conditions.

SUPPLEMENTARY MATERIAL

Additional data and information are available electronically at the pages of journal website: <https://www.shd-pub.org.rs/index.php/JSCS/article/view/13287>, or from the corresponding author on request.

Acknowledgements. This study was accomplished through support of the Ministry of science, higher education and youth in Canton of Sarajevo (public call for co-financing of scientific research/artistic research and research and development projects and programs from the budget of the Canton of Sarajevo for the year 2024, no. 27-02-35-33087-15/24 of 9.7.2024). Methodological design of preliminary study was designed through support of CA15226 – Climate-Smart Forestry in Mountain Regions (CLIMO) and STSM program ECOST-STSM-Request-CA15226-42653. This research has been financially supported by the Ministry of Science, Technological Development and Innovation of Republic of Serbia (Contract No. 451-03-136/2025-03/200026).

ИЗВОД

УТИЦАЈ СУШЕЊА, ЗАМРЗАВАЊА И ПОНОВНОГ ОВЛАЖИВАЊА НА ФИЛТРАТ
ЗЕМЉИШТА У КИСЕЛИМ И КАЛЦИТНИМ ЗЕМЉИШТИМАЕМИРА НУКИЋ¹, МИЛИЦА КАШАНИН-ГРУБИН², МИРЕЛ СУБАШИЋ¹, ТОМИСЛАВ ТОСТИ², СВЕТЛАНА
ЂОГО-МРАЧЕВИЋ³, СНЕЖАНА ШТРБАЦ² И САЊА СТОЈАДИНОВИЋ²¹ University of Sarajevo – Faculty of Forestry, Sarajevo, Bosnia and Herzegovina, ² Институт за хемију,
технолозију и металургију, Београд и ³ Универзитет у Београду, Факултет фармације, Београд

Истраживање проучава утицај догађаја сушења-поновног овлаживања и замрзавања–поновног овлаживања на састав јона у филтрату земљишта кроз серију контролисаних лабораторијских експеримената. реакције растворености јона (Na^+ , K^+ , Ca^{2+} , Mg^{2+} , Al^{3+} , Fe^{3+} , Mn^{2+} , F^- , Cl^- , NO_2^- , SO_4^{2-} , NO_3^- , PO_4^{3-}) у филтрату земљишта су анализиране након циклуса поновног овлаживања под различитим условима. Резултати указују да састав филтрата зависи од специфичног процеса поновног овлаживања (сушење у односу на замрзавање) и геохемијских својстава земљишта. Циклуси сушења–поновног овлаживања и замрзавања–поновног овлаживања су имали већи утицај на састав филтрата у калцитним земљиштима. Тако су циклуси замрзавања-поновног овлаживања снажно подстакли исцурење K^+ , Al^{3+} и Mn^{2+} , док су циклуси сушења-поновног овлаживања подстакли исцурење Ca^{2+} и Mg^{2+} и, за оба третмана, повећане концентрације аниона (F^- , Cl^- , NO_2^- , SO_4^{2-} , NO_3^- , PO_4^{3-}). Сушење и поновно овлаживање су утицали на веће концентрације Mn^{2+} и Fe^{3+} и мало веће концентрације аниона у киселом земљишту. Ова истраживања истичу да су ефекти сушења, замрзавања и поновног овлаживања неодвојиво повезани са геохемијским карактеристикама земљишта.

(Примљено 10. марта, ревидирано 24. априла, прихваћено 30. јуна 2025)

REFERENCES

1. W. de Vries, G.J. Reinds, E. Vel, *For. Ecol. Manage.* **174** (2003) 97 ([https://doi.org/10.1016/S0378-1127\(02\)00030-0](https://doi.org/10.1016/S0378-1127(02)00030-0))
2. P. S. J. Verburg, *Biol. Fertil. Soils* **41** (2005) 257 (<https://doi.org/10.1007/s00374-005-0831-1>)
3. J. D. Joslin, M. H. Wolfe, *Can. J. For. Res.* **23** (1993) 756 (<https://doi.org/10.1139/x93-099>)
4. Y. Cheng, P. G. Xu, Z. Li, T. Wang, S. Cheng, H. Zhang, T. Ma, *Catena* **166** (2018) 21 (<https://doi.org/10.1016/j.catena.2018.03.015>)
5. E. Kaštovská, M. Choma, P. Čapek, J. Kaňa, K. Tahovská, J. Kopáček, *PLoS ONE* **17** (2022) e0272143 (<https://doi.org/10.1371/journal.pone.0272143>)
6. H. Hrvatović, *Geological guide through Bosnia and Herzegovina*, Academy of Sciences and Arts of Bosnia and Herzegovina, Sarajevo, 2022 (in Bosnian)
7. Federal Agropedological Institute, , <https://agropedologija.gov.ba/pedoloska-karta-bosne-i-hercegovine> (September 20th, 2023)
8. M. Ćirić, in *Proceedings of the Faculty of Forestry and Institute of Forestry in Sarajevo* **10** (1966) 1 (in Bosnian)
9. R. Jovanović, M. Mojićević, S. Tokić, Lj. Rokić, *Basic geological map 1:100,000. Explanatory notes for sheet Sarajevo K 34-I*, Sarajevo, 1978
10. J. P. Schültz, M. Saniga, J. Diaci, T. Vrška, *Ann. For. Sci.* **73** (2016) 911 (<https://doi.org/10.1007/s13595-016-0579-9>)
11. R. Seidl, M. J. Schelhaas, W. Rammer, P. J. Verkerk, *Nature Clim. Change* **4** (2014) 806 (<https://doi.org/10.1038/nclimate2318>)

12. Federal Institute of Geology, <https://fzgg.gov.ba> (September 20th 2023)
13. IUSS Working Group World Reference Base for Soil Resources (WRB), *International soil classification system for naming soils and creating legends for soil maps*. International Union of Soil Sciences (IUSS), Vienna, 2022 (https://www.isric.org/sites/default/files/WRB_fourth_edition_2022-12-18.pdf)
14. *ISO 1069: Soil quality – Determination of carbonate content - Volumetric method*, 1995
15. *ISO 14235: Soil quality – Determination of organic carbon by sulfochromic oxidation*, 1998
16. *ISO 11261: Soil quality – Determination of total nitrogen - Modified Kjeldahl method*, 1995
17. A. Kassambara, *PCA: Principal component analysis* (version 0.3.2), CRAN, 2020 (<https://cran.r-project.org/package=PCA>)
18. RStudio Team, *RStudio: Integrated development environment for R* (version 4.3.1), RStudio, PBC, 2023 (<https://www.rstudio.com/>)
19. H. P. Blume, G. W. Brümmer, H. Fleige, R. Horn, E. Kandeler, I. Kögel-Knabner, R. Kretzschmar, K. Stahr, B. M. Wilke, *Scheffer/Schachtschabel Soil Science*, Springer-Verlag, Heidelberg, 2016 (<https://doi.org/10.1007/978-3-642-30942-7>)
20. S. R. Olsen, F. S. Watanabe, *Soil Sci. Soc. Am. Proc.* **27** (1963) 648 (<https://doi.org/10.2136/sssaj1963.03615995002700060024x>)
21. H. D. Scott, R. F. Paetzold, *Soil Sci. Soc. Am. J.* **42** (1978) 23 (<https://doi.org/10.2136/sssaj1978.03615995004200010006x>)
22. S.U. Khan, *Soil nutrients mobilization as influenced by climate-change driven soil drying–rewetting or drying–flooding*, School of Engineering and the Environment, Faculty of Science, Engineering and Computing, Kingston University, London, 2020
23. D. Gao, E. Bai, M. Li, C. Zhao, K. Yu, F. Hagedorn, *Soil Biol. Biochem.* **148** (2020) 107896 (<https://doi.org/10.1016/j.soilbio.2020.107896>)
24. D. Brödlín, K. Kaiser, F. Hagedorn, *Front. For. Glob. Change, Sec. Forest Soils* **2** (2019) 00066 (<https://doi.org/10.3389/ffgc.2019.00066>)
25. L. K. Heng, R. E. White, N. S. Bolan, D. R. Scotter, *N. Z. J. Agric. Res.* **34** (1991) 325 (<https://doi.org/10.1080/00288233.1991.10417672>)
26. K. Fujii, T. Ohmiya, *Catena* **206** (2021) 105490 (<https://doi.org/10.1016/j.catena.2021.105490>)
27. M. Preda, M. E. Cox, *Environ. Geol.* **39** (2000) 319 (<https://doi.org/10.1007/s002540050011>)
28. B. E. Schaff, E. O. Skogley, *Soil Sci. Soc. Am. J.* **46** (1982) 521 (<https://doi.org/10.2136/sssaj1982.03615995004600030015x>)
29. M. Bradová, V. Tejnecký, L. Borůvka, K. Němeček, C. Ash, O. Šebek, M. Svoboda, J. Zenáhlíková, O. Drábek, *Environ. Sci. Pollut. Res.* **22** (2015) 16676 (<https://doi.org/10.1007/s11356-015-4855-2>).

SUPPLEMENTARY MATERIAL TO
**Impact of drying, freezing and re-wetting events soil leachate in
acidic *versus* calcareous soils**

EMIRA HUKIĆ^{1*}, MILICA KAŠANIN-GRUBIN², MIREL SUBAŠIĆ¹, TOMISLAV
TOSTI², SVETLANA ĐOGO-MRAČEVIĆ³, SNEŽANA ŠTRBAC¹
and SANJA STOJADINOVIĆ²

¹University of Sarajevo – Faculty of Forestry, Sarajevo, Bosnia and Herzegovina, ²Institute of
Chemistry, Technology and Metallurgy, Belgrade, Serbia and ³University of Belgrade Faculty of
Pharmacy, Belgrade, Serbia

J. Serb. Chem. Soc. 90 (10) (2025) 1241–1252

Table S-Ia: Mean-M, standard deviation-SD, minimum-Min and maximum-Max values (N=4)
of averaged leachate pH, EC and ion concentrations for the control and treatment samples
(drying-re-wetting and freezing-re-wetting) of calcareous soil

Feature	Depth (cm)	M	SD	Min.	Max.	M	SD	Min.	Max.	M	SD	Min.	Max.	Sig. (≤0.05)
		Calcareous soil				Calcareous soil				Calcareous soil				
		control - gradual drying x re-wetting				drying x re-wetting				freezing x re-wetting				
pH	0-10	7.01	0.25	6.79	7.23	7.10	0.11	6.94	7.19	6.93	0.28	6.60	7.26	0.59
	10-20	7.38	0.16	7.24	7.53	7.77	0.14	7.59	7.88	7.47	0.01	7.41	7.60	0.06
EC (μS cm ⁻¹)	0-10	401	23.1	381	421	157	66.6	119	257	244	171	90.7	462	0.03
	10-20	813	258	606	1148	232	94.0	167	370	235	167.0	103	476	0.02
Al (mg L ⁻¹)	0-10	0.27	0.04	0.23	0.30	0.23	0.07	0.17	0.30	0.34	0.09	0.23	0.41	0.17
	10-20	0.11	0.01	0.10	0.12	0.11	0.00	0.11	0.12	0.13	0.02	0.11	0.15	0.13
Ca (mg L ⁻¹)	0-10	75.5	0.58	75.0	76.0	40.5	26.3	20.0	75.0	73.0	8.72	66.0	84.0	0.02
	10-20	157	33.6	124	204	86.3	79.8	37.0	204	84.2	49.3	47.0	151	0.05
Mg (mg L ⁻¹)	0-10	6.40	1.04	5.50	7.30	2.95	1.90	1.50	5.50	6.75	0.49	6.10	7.30	0.00
	10-20	7.35	1.21	6.20	8.90	3.70	3.51	1.60	8.90	3.80	2.09	2.20	6.60	0.11
Na (mg L ⁻¹)	0-10	12.8	11.8	2.60	23.0	1.75	0.61	1.30	2.60	2.00	-	2.00	2.00	0.22
	10-20	3.40	0.42	3.10	3.70	2.07	1.13	1.30	3.70	3.80	2.09	2.20	6.60	0.24
K (mg L ⁻¹)	0-10	1.55	0.17	1.40	1.70	2.65	0.84	1.40	3.20	1.11	0.40	0.89	1.70	0.01

*Corresponding author. E-mail: e.hukic@sfsa.unsa.ba

	10-20	1.60	1.82	1.40	1.80	1.65	0.17	1.50	1.90	0.93	0.38	0.62	1.40	0.07
Mn (mg L-1)	0-10	0.24	0.01	0.23	0.25	0.10	0.10	0.03	0.25	0.20	0.05	0.15	0.25	0.04
	10-20	0.75	0.01	0.07	0.09	0.03	0.04	0.01	0.09	0.03	0.03	0.10	0.70	0.10
Fe (mg L-1)	0-10	0.18	0.01	0.17	0.18	0.15	0.03	0.12	0.18	0.22	0.03	0.17	0.23	0.01
	10-20	0.11	0.00	0.11	0.12	0.11	0.01	0.09	0.12	0.11	0.01	0.10	0.12	0.75
F (mg L-1)	0-10	0.01	0.01	0.00	0.01	0.16	0.12	0.06	0.30	0.12	0.09	0.05	0.25	0.05
	10-20	0.00	0.00	0.00	0.01	0.09	0.02	0.07	0.10	0.09	0.03	0.06	0.14	0.01
Cl (mg L-1)	0-10	0.95	0.06	0.89	1.00	2.66	0.95	1.78	3.86	1.92	0.68	1.16	2.78	0.02
	10-20	0.58	0.49	0.08	1.01	3.15	0.98	2.12	4.11	2.89	0.91	2.10	3.88	0.03
NO2 (mg L-1)	0-10	0.01	0.00	0.01	0.01	0.24	0.09	0.15	0.36	0.21	0.09	0.13	0.31	0.00
	10-20	0.00	0.00	0.00	0.00	0.26	0.09	0.18	0.38	0.25	0.09	0.17	0.37	0.00
SO4 (mg L-1)	0-10	0.98	0.11	0.89	1.07	14.7	3.86	10.2	19.5	11.0	3.42	6.17	13.9	0.00
	10-20	0.37	0.30	0.05	0.63	16.0	4.06	12.1	19.8	15.9	4.09	11.8	19.7	0.00
NO3 (mg L-1)	0-10	6.47	2.18	4.59	8.36	4.79	3.29	1.24	9.13	2.48	1.20	1.33	3.66	0.05
	10-20	1.12	1.23	0.02	2.18	6.47	4.47	2.10	12.7	6.45	4.64	1.69	12.8	0.12
PO4 (mg L-1)	0-10	0.02	0.01	0.01	0.03	0.06	0.03	0.03	0.09	0.06	0.03	0.03	0.09	0.05
	10-20	0.03	0.02	0.01	0.06	0.06	0.03	0.03	0.09	0.06	0.03	0.03	0.09	0.37

Table S-Ib: Mean-M, standard deviation-SD, minimum-Min and maximum-Max values (N=4) of averaged leachate pH, EC and ion concentrations for the control and treatment samples (drying-re-wetting and freezing-re-wetting) of sandstone soils.

Feature	Depth (cm)	M	SD	Min.	Max.	M	SD	Min.	Max.	M	SD	Min.	Max.	Sig. (≤0.05)
		Sandstone soil				Sandstone soil				Sandstone soil				
		control - gradual drying x re-wetting				drying x re-wetting				freezing x re-wetting				
pH	0-10	4.24	0.21	4.10	4.54	4.37	0.08	4.26	4.43	4.13	0.07	4.06	4.22	0.04
	10-20	4.37	0.16	4.17	4.54	4.79	0.49	4.35	5.21	4.16	0.15	4.07	4.38	0.06
EC (μS cm-1)	0-10	104	35.9	69.1	135	125	49.5	88.6	194	111	15.3	98.2	128	0.72
	10-20	91.0	19.4	69.1	115	74.6	42.2	39.1	122	97.7	17.5	87.9	124	0.53
Al (mg L-1)	0-10	2.25	1.06	1.17	3.68	3.74	1.09	2.84	5.04	2.51	0.24	2.16	2.66	0.05
	10-20	1.63	0.52	1.17	2.21	1.14	0.23	0.95	1.42	1.62	0.44	1.10	1.99	0.22
Ca (mg L-1)	0-10	5.24	3.18	2.63	9.82	7.98	3.66	5.13	12.8	5.29	0.59	4.56	6.00	0.30
	10-20	5.46	1.85	3.54	7.94	5.14	2.48	3.16	8.30	3.61	1.78	2.07	5.26	0.43
Mg (mg L-1)	0-10	1.43	1.02	0.55	2.89	2.44	1.14	1.54	3.91	1.89	0.20	1.70	2.17	0.21
	10-20	1.52	0.55	1.02	2.29	1.46	0.75	0.87	2.43	1.21	0.40	0.87	1.57	0.74
Na (mg L-1)	0-10	1.33	0.45	0.83	1.86	1.80	0.91	1.23	3.14	2.18	0.71	1.16	2.82	0.29

	10-20	1.53	0.55	0.78	2.08	1.89	0.35	1.43	2.27	2.24	0.50	1.86	2.91	0.16
K (mg L ⁻¹)	0-10	0.89	0.76	0.01	1.55	1.29	1.82	0.01	3.86	0.38	0.75	0.01	1.51	0.59
	10-20	0.27	0.52	0.01	1.04	0.31	0.61	0.01	1.23	0.01	0.00	0.01	0.01	0.62
Mn (mg L ⁻¹)	0-10	2.39	1.91	0.74	5.14	4.88	1.89	3.33	7.17	2.78	0.42	2.43	3.39	0.05
	10-20	2.32	0.63	1.92	3.24	2.09	1.10	1.22	3.51	1.29	0.70	0.68	1.96	0.05
Fe (mg L ⁻¹)	0-10	0.53	0.64	0.01	1.46	1.16	0.44	0.79	1.64	1.25	0.19	0.98	1.37	0.05
	10-20	0.47	0.35	0.11	0.84	0.17	0.13	0.08	0.35	0.95	0.44	0.42	1.31	0.03
F (mg L ⁻¹)	0-10	0.00	0.00	0.00	0.00	0.00	0.00	0.00	0.01	0.01	0.00	0.01	0.01	0.00
	10-20	0.00	0.00	0.00	0.01	0.01	0.00	0.00	0.01	0.00	0.01	0.00	0.01	0.94
Cl (mg L ⁻¹)	0-10	0.94	0.38	0.40	1.22	0.79	0.23	0.63	1.12	0.75	0.28	0.46	0.99	0.65
	10-20	0.77	0.46	0.23	1.22	0.68	0.11	0.55	0.83	0.35	0.32	0.08	0.68	0.21
NO ₂ (mg L ⁻¹)	0-10	0.00	0.00	0.00	0.00	0.01	0.00	0.00	0.01	0.00	0.00	0.00	0.00	0.03
	10-20	0.00	0.00	0.00	0.01	0.00	0.00	0.00	0.00	0.00	0.00	0.00	0.00	0.18
SO ₄ (mg L ⁻¹)	0-10	1.70	1.09	0.51	3.14	1.04	0.26	0.88	1.43	0.85	0.16	0.72	1.08	0.05
	10-20	1.61	1.48	0.18	3.14	0.76	0.27	0.53	1.02	0.68	0.77	0.05	1.61	0.37
NO ₃ (mg L ⁻¹)	0-10	0.58	0.45	0.11	1.18	0.37	0.32	0.13	0.85	0.20	0.02	0.18	0.22	0.28
	10-20	0.61	0.61	0.08	1.18	0.13	0.03	0.09	0.16	0.24	0.37	0.02	0.79	0.28
PO ₄ (mg L ⁻¹)	0-10	0.14	0.11	0.04	0.29	0.05	0.02	0.03	0.08	0.03	0.01	0.02	0.04	0.03
	10-20	0.10	0.13	0.01	0.29	0.08	0.03	0.06	0.12	0.03	0.03	0.01	0.07	0.43



J. Serb. Chem. Soc. 90 (10) 1253–1266 (2025)
JSCS–5452

Unified method for multiresidue pesticide analysis in corn and sediment

LOURDES IMAS-GARAY, EMILENE DE CARVALHO LOURENÇO, FERNANDA RUBIO, ALINE THEODORO TOCI and MARCELA BOROSKI*

Federal University of Latin American Integration (UNILA), Environmental and Food Interdisciplinary Studies Laboratory (LEIMAA), 85867-970, Foz do Iguaçu, PR, Brazil

(Received 20 November, revised 17 December 2024, accepted 11 April 2025)

Abstract: Due to Brazil's significant role as a major global corn producer and the impact of pesticide accumulation in sediments on the health of aquatic ecosystems, this study addresses the need for a simplified method to assess pesticide residues in both matrices, corn and sediments. A modified QuEChERS method combined with gas chromatography-mass spectrometry, was validated for the analysis of seven common pesticides in Paraná State, Brazil: desisopropylatrazine (DIA), deethylatrazine (DEA), diazinon, methyl parathion, pirimiphos methyl, malathion and pirimiphos ethyl. Following the guidelines of INMETRO and SANTE 12682/2019, the method achieved quantification limits (8.40–15.00 $\mu\text{g kg}^{-1}$ for sediment and 8.80–13.00 $\mu\text{g kg}^{-1}$ for corn) below the maximum residue limits (MRL) established by EC 396/2005 for corn. The procedure demonstrated excellent linearity ($R^2 > 0.99$), recovery rates (70–120 %) and precision (relative standard deviations ≤ 20 %). This validated method provides a unified, reliable, and sensitive approach for the multiresidue analysis of pesticides in corn and sediment, which is beneficial for environmental monitoring and food safety, particularly in essential agricultural regions like Brazil.

Keywords: agricultural impact; food; environmental matrices; detection and quantification; environmental monitoring.

INTRODUCTION

Pesticide contamination of food and water resources poses a significant threat to human health and ecosystems integrity.^{1–3} Researchers have extensively studied pesticide residues in various food products and environmental matrices.⁴ These residues can persist in harvested crops, such as corn grains, and can also contaminate environmental matrices, like sediments.^{5,6} Sediments play a crucial role in the study of pesticide residues, as they act as reservoirs, accumulate contaminants

*Corresponding author. E-mail: marcelaboroski@yahoo.com.br
<https://doi.org/10.2298/JSC241120025I>

transported from agricultural areas via runoff or leaching.^{4–6} This issue is particularly concerning in regions with intensive agricultural activity.^{7,8}

Corn production in Brazil has experienced significant growth, making the country the third-largest producer of this cereal in the world.^{9,10} Within Brazil, the state of Paraná ranks as the second-largest agricultural producer, accounting for approximately 13 % of the nation's total corn and soybean production, based on the three-year average from 2021 to 2023.^{9,11} This increase in crop production has led to the extensive use of pesticides, primarily herbicides, fungicides and insecticides.^{8,11}

Many pesticides are classified as persistent organic pollutants due to their prolonged presence in the environment and the potential risks they pose to human health and ecosystems.^{6,7,10} Several commonly used pesticides in corn and soybean cultivation, including atrazine, diazinon, malathion, ethyl parathion, pirimiphos ethyl, methyl parathion and pirimiphos methyl, fall into this category.⁸ The classification of these substances as chronic residues by Brazil's National Health Surveillance Agency (ANVISA) underscores the urgent need for strict monitoring and management practices to mitigate risks to food safety and environmental health.^{8,12}

Current methods for analyzing pesticide residues often require separate, time-consuming procedures for different matrices.^{4,13} QuEChERS (Quick, Easy, Cheap, Effective, Rugged and Safe), developed by Anastassiades *et al.* in 2003,¹⁴ is an accessible, cost-effective extraction method with reduced solvent consumption, widely used for extracting organic and inorganic residues from various matrices.^{4,14} Its consistent application in food matrices has led to official validation by AOAC International and the European Committee for Standardization (CEN), underscoring its reliability for detecting pesticide residues in fruits and vegetables.^{13–15}

In recent years, the QuEChERS approach has been the focus of extensive research aimed at evaluating a variety of food and environmental samples.⁴ Numerous studies in Brazil have explored the application of QuEChERS for detecting pesticide residues in various materials, including rice,³ soy-based beverages,¹⁶ water,¹⁷ crop plants,¹⁸ soil¹⁹ and sediments.⁶ These studies underscore the importance of this methodology in ensuring food safety^{2,3,13,16} and promoting environmental conservation.^{6,17–19} However, there is a growing demand for more efficient and compatible methods capable of simultaneously assessing pesticide contamination in both food and environmental samples.^{4,10,15,20}

Although some studies have utilized QuEChERS methods to analyze individual matrices, such as food and environmental samples,⁴ the development and validation of a unified approach applicable to both corn and sediments remain limited.^{6,15,18} Establishing a standardized analytical method is crucial, as it enhance the efficiency of monitoring of these matrices.^{6,18}

The type of matrix used significantly influences the extraction efficiency of the QuEChERS method.^{6,15,18} In environmental matrices, such as soil and sediment, factors like organic matter and clay content can influence extraction performance.^{6,19} In food matrices, extraction efficiency may be impacted by water content, as well as the presence of fats and sugars.^{2,15,18,21} While matrix-matched calibrations are often recommended for various methodologies,^{6,15} a more straightforward approach can be applied to complex matrices.¹⁸ This involves using a single level standard addition in the sample (SLSAS),¹⁸ which is based on the standard addition method outlined in official guidelines (SANTE 12682/2019).²² To address these challenges, it is essential to continue applying the QuEChERS approach while enhancing its validation across different contexts (matrices and detection techniques). This will enable more efficient analysis and monitoring of pesticide residues.^{1,4}

This research aims to develop and validate a modified QuEChERS method combined with gas chromatography-mass spectrometry for the analysis of multiple pesticide residues in corn and sediment samples from the Paraná State in Brazil. The study addresses a critical gap in current analytical practices, which often depend on separate methods tailored to each matrix.^{1,4,18} It underscores the urgent need for a reliable and sensitive technique capable of simultaneously quantifying multiple pesticide residues in both food and environmental matrices. By integrating this approach, the study seeks to enhance monitoring capabilities in agricultural regions.

EXPERIMENTAL

Reagents

High-performance liquid chromatography (HPLC)-grade acetonitrile (MeCN) and the sorbents, primary secondary amine (PSA) and octadecylsilane (C18) were acquired from Supelco (Germany). Ethyl acetate (EtOAc) and dichloromethane (DCM) also HPLC grade, were acquired from Honeywell (USA). Glacial acetic acid (HAc) was sourced from Dinâmica (Brazil), heptahydrated magnesium sulfate from Vetec (Brazil), and sodium chloride from Synth (Brazil). Ultrapure water was acquired using a Purelab[®] ultra-purifier (Options-Q). All pesticide standards were obtained from Sigma–Aldrich with a purity of > 96.7 %. Individual pesticide standard solutions: desisopropylatrazine (DIA), deethylatrazine (DEA), atrazine-D5 (ATZ-D5), diazinon, methyl parathion, pirimiphos methyl, malathion and pirimiphos ethyl were prepared in EtOAc at a concentration of 1000 mg L⁻¹. An intermediate working standard was then prepared in MeCN at 10 mg L⁻¹. The solutions used for analyte addition to the samples were formulated from the separate intermediate solutions, creating a mixed standard in MeCN. The mixed standards were prepared at concentrations of 350, 450, 550, 650, 750, 850, 950 and 1050 µg L⁻¹. All solutions were stored at -18 °C until used.

According to recent studies, atrazine (ATZ) exhibits high water solubility, low sediment solubility and rapid degradation, forming its metabolites, as DIA and DEA under environmental conditions. This degradation is largely influenced by the high organic matter content and humidity associated with sediments, which promote increased microbial activity.²³⁻²⁶ These characteristics influence the detection and analysis of atrazine in environmental studies, shifting

the focus toward its more persistent metabolites. ATZ-D5 was selected as the internal standard, while ATZ was excluded due to the unavailability of the standard in the laboratory.

To monitor the primary pesticides used in corn cultivation, analyses were conducted on the following compounds: DIA, DEA, diazinon and methyl parathion. Additionally, to assess the methodology's effectiveness in sediment analysis, the following pesticides were selected: DIA, DEA, diazinon, malathion and ethyl parathion. The latter two are particularly significant due to their higher affinity for sediments (as organophosphates) and their widespread use in large-scale crops such as soybeans.^{27,28}

Sampling and localization

The corn grains samples were obtained from traditional cultivation, in the municipalities of São Miguel do Iguaçu (M1, M7, M8 and M9); Missal (M2, M3, M4 and M6); Foz do Iguaçu (M5, M10), in the Parana State, Brazil. However, sample M5 was sourced from a certified organic cultivation. In total, 10 different samples were collected. All methodology validation tests were conducted using sample M10. The samples were harvested between January and February 2021, with the grains in the milky stage, the optimal phase for fresh consumption (in natura). The collected samples correspond to the first annual harvest in the region.⁹

Quartering was employed for sample collection.²⁹ At each collection point, the grains were mixed separately in a clean container to create a homogeneous sample. The mixed sample was then divided into four equal parts. Two opposite quadrants were discarded, while the remaining two quarters were combined to form a composite sample. Small portions were taken from this composite until each sample reached a weight of 500 g. These 500 g samples were placed in airtight plastic bags and stored at $-18\text{ }^{\circ}\text{C}$ until analysis. While still frozen, the samples were crushed for 1 min using a Hamilton Beach® food processor.

Sediment samples were collected in the Tamanduá River basin, which supplies part of the municipality of Foz do Iguaçu, in the Parana State of Brazil. The five sediment collection points were in the Dourado stream; with points 1 and 2 (P1, P2) corresponded to the stream's springs, point 3 (P3) was situated upstream of the former municipal landfill, point 4 (P4) was downstream of the former landfill area and point 5 (P5) was at the intersection with the Tamanduá River (for details, see Supplementary material to this paper). The collected samples correspond to those cited in Da Silva *et al.*³⁰ At each collection point, 500 g of composite samples were obtained each consisting of a mixture of 16 subsamples.^{27,29} After collection, the samples were placed in stainless steel trays, dried at $40\text{ }^{\circ}\text{C}$ in a Limatec® (Brazil) forced-air oven, for 24 h and then macerated and sieved through a 28 mesh.²⁸ All methodology validation tests were conducted using sample P3. The maps displaying the locations of the collection points for both matrices are provided in Figs. S-1 and S-2 of the Supplementary material.

QuEChERS Method

The methodology is based on the QuEChERS approach developed by Anastassiades *et al.*,¹⁴ with modifications to enhance its applicability for both corn and sediment matrices. One of the simplest strategies involves reducing the sample size.¹⁴ Additionally, acidifying the extraction solvent with acetic acid (HAc) helps prevent pesticide hydrolysis in a basic pH environment.¹⁵ Increasing both the duration and speed of the mixing and separation stages can further improve extraction efficiency and enhance phase separation during these processes.¹⁴ Moreover, using a larger quantity of salts and adsorbents, along with the incorporation of a C18 adsorbent during the cleaning stage can significantly enhance the method's effectiveness.¹⁵ All these strategies were implemented to improve the overall efficiency of the process.

Similar analysis methodologies have been proposed for the matrices analyzed, specifically corn¹⁵ and sediments.⁶ These studies have confirmed the existence of a matrix effect in the validation of pesticide quantification methods. In both cases, matrix-matched calibrations were employed.^{6,15,22}

The use of the matrix-matched calibration is advantageous, as it enhances signal detection during the analysis stage, particularly in gas chromatography–mass spectrometry (GC–MS).^{2,6,15,31} When validating methods that involve complex matrices, and a blank or reference material is unavailable to prepare matrix-matched standard solutions, the standard addition approach can be employed.²² To address this limitation, Viera *et al.*¹⁸ proposed the single level standard addition in the sample (SLSAS) technique for analyzing pesticide residues in crops. This method enables validation to be carried out on a sample without requiring a specific target sample.¹⁸ The same approach was applied in the methodology validation stages using samples M10 for corn and P3 for sediments.

To construct the analytical curve, 5.00 g of corn grains or sediment samples were weighted in triplicate in a 50 mL polypropylene centrifuge tube. Subsequently, 9.0 mL of 1 vol. % MeCN acidified with HAc was added, followed by 1.0 mL of a standard solution containing the analytes in MeCN, resulting in a total solvent volume of 10 mL. The mixture was then homogenized for one minute using a Phoenix® (Brazil) vortex.

Subsequently, 4.00 g of MgSO₄ and 1.00 g of NaCl were added to the 50 mL polypropylene tube, followed by vortex mixing for 1 min and centrifugation at 4000 rpm for 15 min. After centrifugation, 2.0 mL of the supernatant was removed and transferred to a 15 mL polypropylene tube, where 300 mg of MgSO₄, 50 mg of PSA and 100 mg of C18 were added. The mixture was vortexed for 30 s and centrifuged at 4000 rpm for 15 min. Next, 1 mL aliquot of the supernatant was extracted and evaporated under a nitrogen stream using an evaporator. The dried residue was reconstituted in 400 µL of DCM for injection into the GC–MS system.

GC–MS Analysis

Chromatographic analyses were performed using a TRACE 1300 GC system equipped with a TriPlus RSH automatic sampler and coupled to an ISQ single quadrupole MS mass analyzer, all from Thermo Scientific (USA). The compounds were separated in a TR-5MS capillary column (30 m×0.25 mm×0.25 mm), also from Thermo Scientific (USA), with a stationary phase composed of 5 % phenyl polysilphenylene–siloxane. The injector temperature was set at 250 °C and the samples were injected (1 µL) in splitless mode. The temperature program used was from 50 °C (holding for 1 min) to 180 °C at a rate of 25 °C min^{−1} and increased to 280 °C at 3 °C min^{−1}. The carrier gas used was helium, of chromatographic purity, with a constant flow of 0.500 mL min^{−1}. Furthermore, in the mass spectrometry system, the ion source temperature was set at 280 °C and the transfer line temperature was set at 270 °C. The system was operated in the selective ion monitoring (SIM) mode using one target and three qualifier ions, as listed in Table I. Data processing was carried out using Thermo Xcalibur software, version 2.2, Thermo Scientific (USA).

TABLE I. Retention time, corresponding ions, CAS, molecular formula and log *K*_{ow} of the pesticides analyzed

Pesticide	Retention time, min	Ions (<i>m/z</i>)	CAS ^a	Formula ^a	log <i>K</i> _{ow} ^a
DIA	12.70	173, 158, 145	1007-28-9	C ₅ H ₈ ClN ₅	–
DEA	13.53	172, 174, 187	6190-65-4	C ₆ H ₁₀ ClN ₅	1.51
ATZ-D5	15.10	205, 178, 220	163165-75-1	C ₈ H ₁₄ ClN ₅	–

TABLE I. Continued

Pesticide	Retention time, min	Ions (<i>m/z</i>)	CAS ^a	Formula ^a	log <i>K</i> _{ow} ^a
Diazinon	17.87	179, 137, 152	333-41-5	C ₁₂ H ₂₁ N ₂ O ₃ PS	3.81
Methyl paration	18.85	109, 125, 263	298-00-0	C ₈ H ₁₀ NO ₅ PS	2.86
Pirimiphos methyl	20.92	290, 276, 305	29232-93-7	C ₁₁ H ₂₀ N ₃ O ₃ PS	4.12
Malathion	22.01	173, 125, 93	121-75-5	C ₁₀ H ₁₉ O ₆ PS ₂	2.36
Pirimiphos ethyl	23.19	318, 304, 168	23505-41-1	C ₁₃ H ₂₄ N ₃ O ₃ PS	5.00

^aData extracted from PubChem³²*Internal standard*

The internal standard (IS) was introduced in the step preceding injection to compensate for minor variations in injection volume and instrument performance, ensuring the normalization of relative peak areas of each pesticide.^{22,33} ATZ-D5 was selected as the internal standard due to its expected absent in the sample.²³⁻²⁶ The internal standard, maintained at a fixed concentration (10.00 µg L⁻¹), was added to each calibration solution. The response factor, based on the detector response of the analyte relative to the internal standard at each injected concentration, was plotted against the pesticide concentration. The adjusted analytical curve was determined using linear regression. Additionally, ATZ-D5 was incorporated into all final extracts as a quality control measure.

Method validation

The parameters evaluated for the quantitative analytical method were linearity, limit of detection (*LOD*), limit of quantification (*LOQ*), repeatability (in terms of relative standard deviation, *RSD*, %) and recovery. The criteria used to assess validation performance were those established in SANTE 12682/2019²² and by the National Institute of Metrology, Quality and Technology (INMETRO, Brazil).³³

The assessment of validation parameters, such as *LOD* and *LOQ* was conducted using the spreadsheet validation method developed by Ribeiro *et al.*³⁴ After obtaining the area ratios of the peaks for each pesticide relative to the internal standard peak (*A_p/A_{IS}*) at various concentrations during the linearity test (calibration solutions were injected in triplicate, *n* = 3), the data was entered into the spreadsheet created by Ribeiro *et al.*³⁴ This spreadsheet uses specific equations to estimate the limits of detection and quantification:

$$LOD = 2 \frac{s_{y,t}}{a_1} \sqrt{\frac{1}{N} + 1 + \frac{(y_c - \bar{y})^2}{a_1^2 \sum_{i=1}^n (x_i - \bar{x})^2}} \quad (1)$$

$$LOQ = \frac{y_h - a_0}{a_1} + \frac{s_{y,t}}{a_1} \sqrt{\frac{1}{N} + 1 + \frac{(y_c - \bar{y})^2}{a_1^2 \sum_{i=1}^n (x_i - \bar{x})^2}} \quad (2)$$

The calculations for each term in these equations are detailed in the work of Ribeiro *et al.*³⁴ and are also included in the Supplementary material. The spreadsheet was chosen because it simplifies the calculation of this parameters using information from the calibration curve.^{33,34}

To ensure repeatability, six concentration levels were established for each analyte, with three replicates for each level (*n* = 3). The assessment values for each analyte were adjusted according to the specific linearity of each pesticide. Repeatability was evaluated using the relative standard deviation (*RSD*, %), as detailed in Eq. (3) established by INMETRO.³³

$$RSD = \frac{100s}{\bar{x}} \quad (3)$$

In this context, s represents the standard deviation, and \bar{x} denotes the average of the measurements collected on the same day. This calculation helps evaluate the precision related to the repeatability of the applied methodology. Using the same levels evaluated for repeatability, a recovery study (representing accuracy) was conducted in accordance with INMETRO.³³ Eq. (4) was utilized for the quantification of recovery:

$$\text{Recovery} = 100 \frac{C_1 - C_2}{C_3} \quad (4)$$

The terms used in the Eq. (4), are referred to: C_1 , concentration of the analyte in the fortified sample; C_2 , concentration of the analyte in the unfortified sample; C_3 , as the concentration of the analyte added to the fortified sample.

RESULTS AND DISCUSSION

Linearity, LOD and LOQ limits

The results obtained were used to assess the linearity of the methodology for the analyzed pesticides, as shown in Tables II and III. Analytical curves were established within a concentration range of 17.50–52.50 $\mu\text{g kg}^{-1}$ for the pesticides DIA, DEA, diazinon, methyl parathion, pirimiphos methyl, malathion and pirimiphos ethyl. The correlation coefficients (R^2) for the identified analytes exceeded 0.990, confirming that the analytical curves met the established criteria for validating methodologies for pesticide residue extraction and quantification.^{2,22,33}

TABLE II. Values obtained from the assessment of linearity, limit of detection (LOD) and limit of quantification (LOQ) for sediments ($n = 3$)

Pesticide	Parameter				
	Range $\mu\text{g kg}^{-1}$	R^2 (A_p/A_{IS}) ^a	Equation $y = ax \pm b$	LOD $\mu\text{g kg}^{-1}$	LOQ $\mu\text{g kg}^{-1}$
DIA	17.50–42.50	0.9961	$y = 0.0012x - 0.0019$	5.60	8.40
DEA	17.50–52.50	0.9902	$y = 0.0017x - 0.0014$	7.30	10.90
Diazinon	17.50–42.50	0.9901	$y = 0.0062x - 0.0468$	6.10	9.10
Malathion	17.50–42.50	0.9937	$y = 0.0038x - 0.0273$	5.80	8.60
Pirimiphos ethyl	17.50–42.50	0.9935	$y = 0.0029x - 0.0252$	9.70	15.00

^aStandardized area with IS (Internal Standard, ATZ-D5)

The compiled data from Tables II and III, indicate that the LOD (5.60–9.70 $\mu\text{g kg}^{-1}$) and LOQ (8.40–15.00 $\mu\text{g kg}^{-1}$) obtained for sediments, closely align with values reported in the literature for Brazilian samples.⁶ In contrast, the LOD (5.00–8.70 $\mu\text{g kg}^{-1}$) and LOQ (8.80–13.00 $\mu\text{g kg}^{-1}$) for corn grains, are comparable to those obtained for the same detection techniques.¹⁵

The maximum residue levels (MRLs) for the pesticides analyzed in corn, are established by the values specified in European Union Regulation EC 396/2005 for food and feed.³⁵ This regulation aims to ensure a high level of food safety and

protect consumers from potential health risks associated with pesticide residues. The *MRL* values for the pesticides of interest, applicable to both sweet corn and maize, are as follows: atrazine, related to DIA and DEA ($50 \mu\text{g kg}^{-1}$); diazinon ($20 \mu\text{g kg}^{-1}$); methyl parathion ($20 \mu\text{g kg}^{-1}$) and for pirimiphos methyl ($500 \mu\text{g kg}^{-1}$). It is important to note that the *LOQ* must correspond to values $\leq MRL$ for each pesticide.^{2,22} The *LOQ* for corn ($8.80\text{--}13.00 \mu\text{g kg}^{-1}$) obtained using this methodological approach, is considerably lower than the *LOQ* suggested by the *MRL* found for each pesticide.^{15,22} Currently, no *MRL* values have been reported for sediments due to the exploratory nature of pesticide residue studies in this matrix.^{6,7} However, the *LOQs* obtained for the sediment matrix ($8.40\text{--}15.00 \mu\text{g kg}^{-1}$), are consistent with those obtained for the corn, demonstrating that the methodology is adaptable in both matrices.^{6,15,22}

TABLE III. Values obtained from the assessment of linearity, limit of detection (*LOD*) and limit of quantification (*LOQ*) for corn grains ($n = 3$)

Pesticide	Parameter				
	Range $\mu\text{g kg}^{-1}$	R^2 (A_P/A_{IS}) ^a	Equation $y = ax \pm b$	<i>LOD</i> $\mu\text{g kg}^{-1}$	<i>LOQ</i> $\mu\text{g kg}^{-1}$
DIA	17.50–42.50	0.9914	$y = 0.0014x - 0.0112$	6.00	8.80
DEA	22.50–52.50	0.9952	$y = 0.0023x - 0.0273$	6.70	9.70
Diazinon	17.50–52.50	0.9928	$y = 0.0039x - 0.0029$	5.00	7.40
Malathion	22.50–52.50	0.9953	$y = 0.0095x - 0.0144$	7.10	10.40
Pirimiphos ethyl	17.50–47.50	0.9921	$y = 0.0028x - 0.0313$	8.70	13.00

^aStandardized area with IS (Internal Standard, ATZ-D5)

Recovery and repeatability

Favorable findings regarding analyte recoveries are presented in Tables IV and V. The recovery percentages obtained are within the following ranges: for sediments, DIA (94.30–101.70 %), DEA (93.40–105.50 %), diazinon (88.10–109.80 %), malathion (95.00–108.30 %), pirimiphos ethyl (92.40–111.10 %); for corn, DIA (95.10–104.80 %), DEA (92.40–105.30 %), diazinon (88.40–106.60 %), methyl parathion (94.50–107.40 %), pirimiphos methyl (81.00–112.00 %).

Recoveries exceeding 100 % in pesticide residue analysis are often attributed to the matrix effect.^{6,15,18,22} The matrix effect occurs when co-extracted compounds from the sample matrix, such as corn or sediment, enhance the ionization of target analytes (pesticides) during mass spectrometry analysis.^{2,22,31} This enhancement can lead to an overestimation of pesticide concentration, resulting in a recovery rate greater than 100 %.²² The recovery percentages obtained in both matrices fall within the recommended range of 70–120 % for each spike level tested^{2,22,33} which ranged from 17.50 to 52.50 $\mu\text{g kg}^{-1}$, for the pesticides studied, as illustrated in Figs. 1 and 2. Importantly, the lowest recovery values exceed the recommended lower limit of 70 %.²²

TABLE IV. Mean recovery (%) and relative standard deviation (*RSD*, %) for DIA, DEA, diazinon, malathion and pirimiphos ethyl in sediments ($n = 3$)

Fortification level, $\mu\text{g kg}^{-1}$	Parameter	Pesticide				
		DIA	DEA	Diazinon	Malathion	Pirimiphos ethyl
17.50	Recovery	96.90	93.40	99.30	95.40	92.40
	<i>RSD</i>	2.90	3.00	4.60	7.70	4.70
22.50	Recovery	101.70	107.50	109.80	98.50	103.90
	<i>RSD</i>	5.10	4.50	7.00	5.60	5.50
27.50	Recovery	96.20	105.60	96.80	108.30	99.40
	<i>RSD</i>	5.50	5.20	2.90	11.90	2.80
32.50	Recovery	97.00	98.00	100.60	105.70	111.10
	<i>RSD</i>	5.30	7.10	4.40	9.80	2.90
37.50	Recovery	94.30	95.60	88.10	95.00	101.60
	<i>RSD</i>	2.40	3.80	12.50	9.80	8.50
42.50	Recovery	97.10	98.00	97.80	95.70	97.90
	<i>RSD</i>	3.80	2.90	13.20	8.00	12.20

TABLE V. Mean recovery (%) and relative standard deviation (*RSD*, %) DIA, DEA, diazinon, methyl parathion and pirimiphos methyl in corn grains ($n = 3$)

Fortification level $\mu\text{g kg}^{-1}$	Parameter	Pesticide				
		DIA	DEA	Diazinon	Methyl parathion	Pirimiphos methyl
22.50	Recovery	99.40	105.30	106.60	104.10	102.60
	<i>RSD</i>	1.90	1.50	6.80	0.50	2.80
27.50	Recovery	95.10	97.30	90.80	94.50	98.50
	<i>RSD</i>	1.20	0.80	5.20	1.10	3.60
32.50	Recovery	102.60	100.90	100.20	107.40	102.20
	<i>RSD</i>	5.90	5.10	3.20	2.50	8.90
37.50	Recovery	100.10	98.60	104.70	100.10	95.90
	<i>RSD</i>	3.00	3.40	3.80	4.00	7.50
42.50	Recovery	104.80	102.00	106.10	103.60	81.10
	<i>RSD</i>	5.10	4.70	2.30	3.70	3.10
47.50	Recovery	–	92.40	88.40	106.00	112.60
	<i>RSD</i>	–	3.50	1.60	3.00	3.60

Furthermore, the literature reviewed for similar studies reports comparable percentages, highlighting the effectiveness of the proposed methodology.^{5,6,15,21} This methodology employs an efficient and simplified calibration technique (SLSAS), based on the work of Viera *et al.*¹⁸ The relative standard deviation (*RSD*) for repeatability ranged from 0.80–13.20 %. A repeatability rate of less than 20 % is considered acceptable for multiresidue approaches.^{2,22,33}

Matrix effect

The matrix effect of the applied method was evaluated by comparing the chromatograms of the selected sample for SLSAS calibration (M10 for corn and

P3 for sediments) with a spiked level from the pesticide analysis curve. This comparison was conducted for both matrices: corn and sediments (see Figs. S-4 and S-5 of the Supplementary Material). It was observed that there was an incremental effect in the signals (GC–MS) of the analytes when using the matrix in the calibration curve with SLSAS,¹⁸ a finding that aligns with predictions from similar studies involving the analyzed matrices.^{6,15} Due to this signal enhancement, it was not possible to validate the methodology for the pesticides malathion and ethyl parathion in the corn matrix, as well as for methyl parathion and pirimiphos methyl in the sediment matrix.

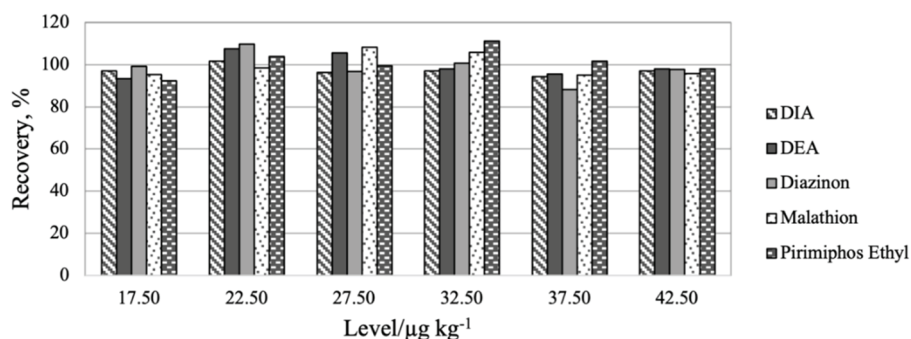


Fig. 1. Average recovery rates (%) for DIA, DEA, diazinon, malathion and pirimiphos ethyl, in sediments samples, obtained in triplicate ($n = 3$) for the modified QuEChERS/GC–MS method.

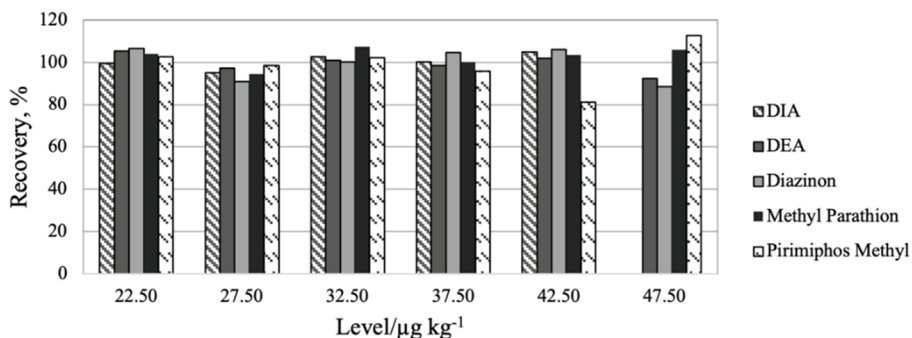


Fig. 2. Average recovery rates (%) for DIA, DEA, diazinon, methyl parathion and pirimiphos methyl, in corn grain samples, obtained in triplicate ($n = 3$) for the modified QuEChERS/GC–MS method.

Application of the proposed method to real samples

To assess the performance of the method, it was applied to 10 different corn samples and 5 sediment samples. Each samples were analyzed in triplicate; however, the analytes of interest were not quantified in these samples. All results were

below the limit of detection (*LOD*) for the pesticides analyzed in both matrices (see Tables S-1 and S-2 of the Supplementary Material).

Given the validation quality of the approach developed in this study, it is considered a suitable alternative to conventional laboratory methods. The modifications to the methodology of Anastassiades *et al.*¹⁴ enabled the simultaneous detection of seven pesticides: diazinon, malathion, pirimiphos ethyl, methyl parathion, pirimiphos methyl, DEA and DIA in two matrices with significantly different characteristics, corn and sediments. This was achieved using GC–MS/MS in selected ion monitoring (SIM) mode, a technique commonly employed for effectively analyzing pesticide residues in diverse matrices.^{2,31} Furthermore, this adaptation aligns with other methodologies applicable to multiple matrices and meets the analytical control parameters necessary to establish it a viable option for use in sediment and corn within similar agricultural contexts and pesticide applications.

CONCLUSION

This study presents a methodology for analyzing seven pesticides in corn and sediment samples, specifically for application in the agricultural regions of Paraná State, Brazil. The QuEChERS/GC–MS methodology proved to be both simple and effective. It was validated with recovery rates ranging from 70 to 120 %. The validation parameters were appropriate for analyzing pesticide residues in both matrices – corn and sediments – with concentrations between 17.50 to 52.50 $\mu\text{g kg}^{-1}$. These concentrations resulted in quantification limits (*LOQ*) below the maximum residue limits established for the analyzed food matrix. The use of GC–MS with selective ion monitoring (SIM) and SLSAS calibration enhanced the method's sensitivity, further reinforced by the inclusion of an internal standard (ATZ-D5).

The proposed method was applied to corn and sediment samples from Paraná State, where no significant levels of the targeted pesticides were found in the samples. This method achieved satisfactory limits of quantification, precision (repeatability) and accuracy (recovery), demonstrating its suitability for multiresidue pesticide analysis in both corn and sediments, serving both regulatory and routine residue monitoring purposes. Given the widespread use of pesticides, this study encourages the application of this methodology to other matrices involved in the environmental degradation cycles of pesticides, as well as on a broader range of pesticides used in various agricultural practices and application patterns.

SUPPLEMENTARY MATERIAL

Additional data and information are available electronically at the pages of journal website: <https://www.shd-pub.org.rs/index.php/JSCS/article/view/13136>, or from the corresponding author on request.

Acknowledgements. The authors are grateful to the City Hall of Missal and PRPPG-UNILA (104/2020-PIB2614-2020).

ИЗВОД

ОБЈЕДИЊЕНА МЕТОДА МУЛТИРЕЗИДУАЛНЕ АНАЛИЗЕ ПЕСТИЦИДА У КУКУРУЗУ И СЕДИМЕНТИМА

LOURDES IMAS-GARAY¹, EMILENE DE CARVALHO LOURENÇO¹, FERNANDA RUBIO¹, ALINE THEODORO TOCI¹
и MARCELA BOROSKI¹

¹Federal University of Latin American Integration (UNILA), Environmental u Food Interdisciplinary Studies Laboratory (LEIMAA), 85867-970, Foz do Iguaçu, PR, Brazil

Због значајне улоге Бразила као главног светског произвођача кукуруза и утицаја акумулације пестицида у седиментима на здравље водених екосистема, ова студија се бави потребом за поједностављеном методом за процену остатака пестицида у матрицама као што су кукуруз и седименти. Модификована QuEChERS метода комбинована са гасном хроматографијом–масеном спектрометријом, валидирана је за анализу седам уобичајених пестицида у држави Парана, Бразил: дезизопропилатразин (DIA), деетилатразин (DEA), диазинон, метилпаратион, метилпиримифос, малатион и етилпиримиф. Пратећи смернице INMETRO и SANTE 12682/2019, методом су постигнуте границе квантификације (8,40–15,00 $\mu\text{g kg}^{-1}$ за седимент и 8,80–13,00 $\mu\text{g kg}^{-1}$ за кукуруз) испод максималних граница остатка (MRL) утврђених од стране ЕС 396/2005 за кукуруз. Процедура је показала одличну линеарност ($R^2 > 0,99$), стопе опоравка (70–120 %) и прецизност (релативне стандардне девијације ≤ 20 %). Ова валидирана метода пружа јединствен, поуздан и осетљив приступ за анализу остатака већег броја пестицида у кукурузу и седименту, што је корисно за праћење животне средине и безбедност хране, посебно у кључним пољопривредним регионима као што је Бразил.

(Примљено 2. новембра, ревидирано 17. децембра 2024, прихваћено 11. априла 2025)

REFERENCES

1. M. Á. González-Curbelo, D. A. Varela-Martínez, D. A. Riaño-Herrera, *Molecules* **27** (2022) 4323 (<https://doi.org/10.3390/molecules27134323>)
2. P. Stefanelli, D. Attard Barbini, in *Pesticide Toxicology*, E. Gallardo, M. Barroso, Eds., Springer US, New York, 2022, pp. 1–26 (<https://doi.org/10.1007/978-1-0716-1928-5>)
3. M. G. Melo, A. Carqueijo, A. Freitas, J. Barbosa, A. S. Silva, *Foods* **9** (2019) 18 (<https://doi.org/10.3390/foods9010018>)
4. A. Santana-Mayor, R. Rodríguez-Ramos, A. V. Herrera-Herrera, B. Socas-Rodríguez, M. A. Rodríguez-Delgado, *TrAC Trends Anal. Chem.* **169** (2023) 117375 (<https://doi.org/10.1016/j.trac.2023.117375>)
5. J. Guo, A. Li, *TrAC Trends Anal. Chem.* **172** (2024) 117605 (<https://doi.org/10.1016/j.trac.2024.117605>)
6. D. R. Cassoli de Souza Dutra, M. Regina Assalin, R. Scanagatta Dos Santos, E. F. Gaspar de Carvalho Dores, *Int. J. Environ. Anal. Chem.* **100** (2020) 1536 (<https://doi.org/10.1080/03067319.2019.1657107>).
7. E. J. Didoné, J. P. G. Minella, T. Tiecher, R. Zanella, O. D. Prestes, O. Evrard, *Environ. Sci. Pollut. Res.* **28** (2021) 39370 (<https://doi.org/10.1007/s11356-021-13303-z>)
8. Brazilian Health Regulatory Agency (ANVISA), *Program of Agrototoxic Residues Analysis in Food – PARA, for cycle 2017/2018*, Brazil, Brasilia, 2019 (<https://www.gov.br/anvisa/pt-br/centraisdeconteudo/publicacoes/agrotoxicos/publicacoes/programa-de-analise-de-residuos-de-agrotoxicos-relatorio-2017-e-2018.pdf>)

9. USDA, *Country Summary – Brazil, Brazil Cron Area, Yield and Production*, <https://ipad.fas.usda.gov/countrysummary/Default.aspx?id=BR&crop=Corn> (accessed October 10, 2024)
10. M. Prado de Oliveira, A. B. Santana e Silva, C. V. Toniciolli Rigueto, R. Aparecida Loss, S. Ferreira Guedes, C. Aparecida Queli Geraldi, *Ciência Natura* **45** (2023) e2 (<https://doi.org/10.5902/2179460X70715>)
11. Agencia de Defensa Agropecuaria de Paraná – ADAPAR, *Agrotóxicos No Paraná, Datos del Sistema de Control de Comercio y Uso de Agrotóxicos en el Estado de Parana – SIAGRO*, <https://www.adapar.pr.gov.br/Pagina/Agrotoxicos-no-Parana> (accessed December 12, 2024)
12. W. A. Pignati, F. A. N. de S. e Lima, S. S. de Lara, M. L. M. Correa, J. R. Barbosa, L. H. D. C. Leão, M. G. Pignatti, *Ciencia Saude Coletiva* **22** (2017) 3281 (<https://doi.org/10.1590/1413-812320172210.17742017>)
13. R. Perestrelo, P. Silva, P. Porto-Figueira, J. A. M. Pereira, C. Silva, S. Medina, J. S. Câmara, *Anal. Chim. Acta* **1070** (2019) 1 (<https://doi.org/10.1016/j.aca.2019.02.036>)
14. M. Anastassiades, S. J. Lehotay, D. Stajnbaher, F. J. Schenck, *J. AOAC Int.* **86** (2003) 412 (<https://doi.org/10.1093/jaoac/86.2.412>)
15. Z. He, L. Wang, Y. Peng, M. Luo, W. Wang, X. Liu, *Food Chem.* **169** (2015) 372 (<https://doi.org/10.1016/j.foodchem.2014.07.102>)
16. M. M. May, G. Ferronato, N. M. G. Bandeira, O. D. Prestes, R. Zanella, M. B. Adaime, *Food Anal. Methods* **10** (2017) 369 (<https://doi.org/10.1007/s12161-016-0593-4>)
17. R. P. Gabardo, N. P. Toyama, B. do Amaral, M. Boroski, A. T. Toci, S. F. Benassi, P. G. Peralta-Zamora, G. A. Cordeiro, M. V. de Liz, *Microchem. J.* **168** (2021) 106392 (<https://doi.org/10.1016/j.microc.2021.106392>)
18. M. S. Viera, T. M. Rizzetti, M. P. de Souza, M. L. Martins, O. D. Prestes, M. B. Adaime, R. Zanella, *J. Chromatogr. A* **1526** (2017) 119 (<https://doi.org/10.1016/j.chroma.2017.10.048>)
19. B. do Amaral, P. Peralta-Zamora, N. Nagata, *Environ. Sci. Pollut. Res.* **29** (2022) 39102 (<https://doi.org/10.1007/s11356-021-18292-7>)
20. Clarivate, *Web of Science, Pesticides Residues in Food and Environmental Samples*, <https://clarivate.com/academia-government/scientific-and-academic-research/research-discovery-and-referencing/web-of-science/> (accessed December 10, 2024)
21. K. Arena, L. Martín-Pozo, R. Laganà Vinci, F. Cacciola, P. Dugo, L. Mondello, *Microchem. J.* **205** (2024) 111298 (<https://doi.org/10.1016/j.microc.2024.111298>)
22. Directorate General for Health and Consumer Affairs, *Guidance Document on Analytical Quality Control and Method Validation Procedures for Pesticide Residues Analysis in Food and Feed - SANTE/12682/2019*, European Commission, 2020 (https://www.eurl-pesticides.eu/userfiles/file/eurlall/aqcguidance_sante_2019_12682.pdf)
23. M. Triassi, P. Montuori, D. P. Provisiero, E. De Rosa, F. Di Duca, P. Sarnacchiaro, S. Diez, *Sci. Total Environ.* **803** (2022) 149972 (<https://doi.org/10.1016/j.scitotenv.2021.149972>)
24. W. Meng, D. Wang, S. Li, Y. Wang, C. Jiang, H. Tian, M. Ji, *Separations* **9** (2022) 397 (<https://doi.org/10.3390/separations9120397>)
25. H. Barchanska, M. Sajdak, K. Szczypka, A. Swientek, M. Tworek, M. Kurek, *Environ. Sci. Pollut. Res.* **24** (2017) 644 (<https://doi.org/10.1007/s11356-016-7798-3>)
26. T. Roh, P. S. K. Knappett, D. Han, G. Ludewig, K. M. Kelly, K. Wang, P. J. Weyer, *Int. J. Environ. Res. Public Health* **20** (2023) 5397 (<https://doi.org/10.3390/ijerph20075397>)

27. R. Exterkoetter, D. E. Rozane, W. C. da Silva, A. T. Toci, G. A. Cordeiro, S. F. Benassi, M. Boroski, *J. Soils Sediments* **19** (2019) 2240 (<https://doi.org/10.1007/s11368-018-2210-1>)
28. L. Lupi, K. S. B. Miglioranza, V. C. Aparicio, D. Marino, F. Bedmar, D. A. Wunderlin, *Sci. Total Environ.* **536** (2015) 687 (<https://doi.org/10.1016/j.scitotenv.2015.07.090>)
29. J. Park, D.-H. Kim, J.-Y. Moon, J.-A. An, Y.-W. Kim, S.-H. Chung, C. Lee, *Toxins (Basel)* **10** (2018) 319 (<https://doi.org/10.3390/toxins10080319>)
30. S. da Silva, F. Rubio, K. Gomes Ramirez, L. Martins Soares, J. Pires Frigo, P. Ferri Coldebella, C. Da Costa Silva Goncalves, M. Boroski, *Revista Tecnologia Sociedade* **19** (2023) (<https://doi.org/10.3895/rts.v19n55.13939>)
31. M. Hernández-Mesa, D. Moreno-González, *Separations* **9** (2022) 148 (<https://doi.org/10.3390/separations9060148>)
32. PubChem – National Library of Medicine, <https://pubchem.ncbi.nlm.nih.gov> (accessed August 24, 2024)
33. Brazilian National Institute of Metrology, Quality and Technology (INMETRO), *Guidance on Validation of Analytical Methods DOQ-CGCRE-008*, 2020 (http://www.inmetro.gov.br/credenciamento/organismos/doc_organismos.asp?torganismo=calibensaio)
34. F. A. de L. Ribeiro, M. M. C. Ferreira, S. C. Morano, L. R. da Silva, R. P. Schneider, *Quim. Nova* **31** (2008) 164 (<https://doi.org/10.1590/S0100-40422008000100029>)
35. European Parliament and of the Council, *Regulation (EC) 396/2005 - Maximum Residue Levels of Pesticides in or on Food and Feed of Plant and Animal Origin and Amending Council Directive 91/414/EEC*, Official Journal of the European Union, Legislation, ISSN 1725-2555, 2005 (<https://eur-lex.europa.eu/eli/reg/2005/396/oj>).

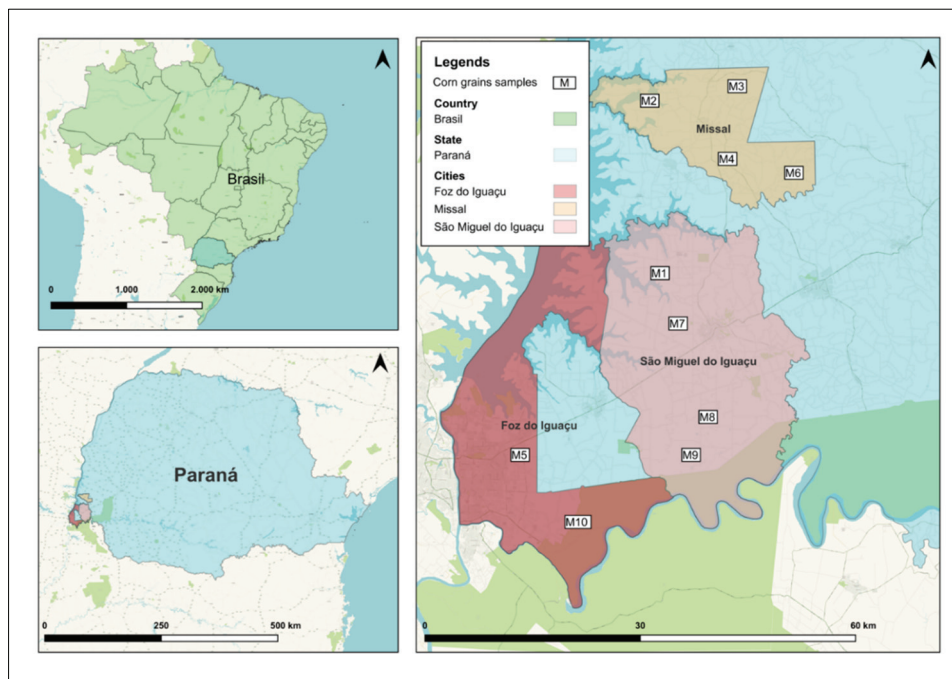


Fig. S-2. Spatial distribution of sampling sites selected for corn samples collection using the modified QuEChERS/GC-MS method in Paraná State, Brazil.

Method Validation (Cont.)

The limit of detection (LOD) refers to the smallest quantity of analyte in a sample that can be detected but not necessarily quantified under the conditions set for the assay conditions.¹ Estimating the limit of detection using parameters from the analytical curve provides greater statistical reliability, as it considers the confidence interval of the regression. In this context, the LOD is defined as the minimum concentration of a substance that can be measured and reported with either 99% or 95% confidence.

The estimation of the analytical signal from the regression equation introduces a standard error. By multiplying this error by the approximate value of t from Student's distribution, the confidence interval of the analytical curve can be calculated. This interval is represented by two hyperbolic lines surrounding the obtained curve, as illustrated in Figure S-3.²

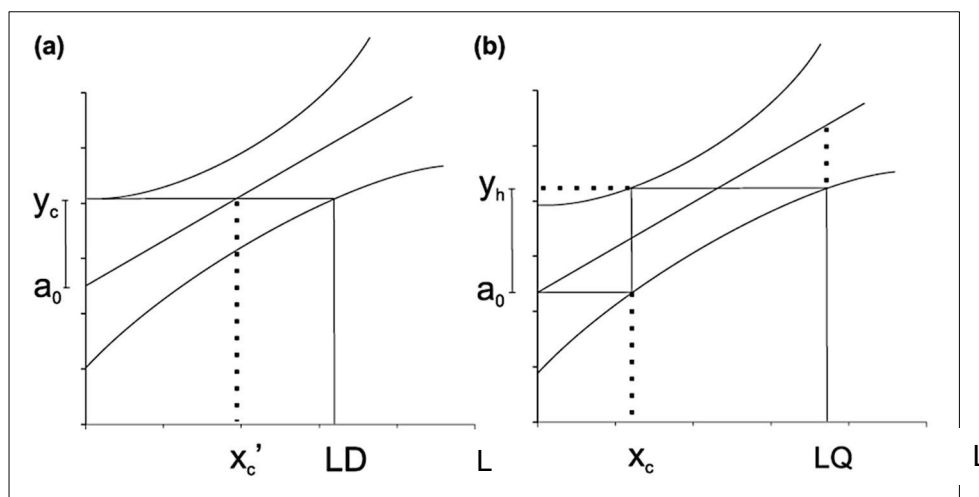


Fig. S-3. Calibration curve with illustration of the parameters used in the calculation of: (a) the limit of detection (LOD) and (b) limit of quantification (LOQ). Source: Ribeiro *et al.*³⁴

The upper limit of the confidence interval is referred to as y_c (y - critical). Its projection onto the lower limit provides an estimate of the minimum concentration that can be measured with a statistically validated level of confidence, known as the limit of detection (LOD) of the method. This limit is determined by calculating the standard deviation s_y , for a linear fit, as described in Equation S-1.

$$s_y = \sqrt{\frac{\sum (y_i - \hat{y}_i)^2}{N - 2}} \quad (\text{S-1})$$

Where N represents the number of measurements; y_i is the individual value of the instrumental signal (response); \hat{y}_i is the value of the response predicted by the analytical curve equation.

$$y_c = a_0 + s_y \cdot t \sqrt{\left(\frac{1}{N}\right) + 1 + \frac{\bar{x}^2}{\sum_{i=1}^n (x_i - \bar{x})^2}} \quad (\text{S-2})$$

On the other hand, the limit of quantification (LOQ) of an analytical procedure is the smallest amount of analyte in a sample that can be quantitatively determined

with acceptable precision and accuracy.³³ The LOQ is calculated from the confidence interval of the analytical curve. Specifically, x_c represents the concentration value at the point where the value of a_0 intercepts the regression line down to the lower hyperbola. y_h corresponds to the intensity value of y , which is projected from x_c to the upper hyperbola. With these values, it is possible to calculate the LOQ using the following equations:

$$x_c = \frac{s_y \cdot t}{a_1} \sqrt{\left(\frac{1}{N}\right) + 1 + \frac{\bar{x}^2}{\sum_{i=1}^n (x_i - \bar{x})^2}} \quad (\text{S-3})$$

$$y_h = a_0 + 2 \cdot s_y \cdot t \sqrt{\left(\frac{1}{N}\right) + 1 + \frac{(x_c - \bar{x})^2}{\sum_{i=1}^n (x_i - \bar{x})^2}} \quad (\text{S-4})$$

Matrix Effect (Cont.)

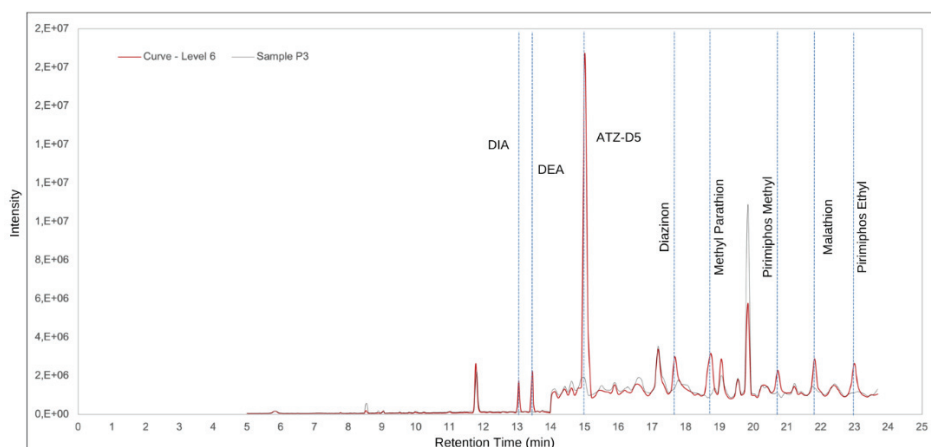


Fig. S-4. Total ion chromatogram (TIC) of pesticides obtained for a sediment sample (P3), and a calibration curve for Level 6 ($42.50 \mu\text{g kg}^{-1}$).

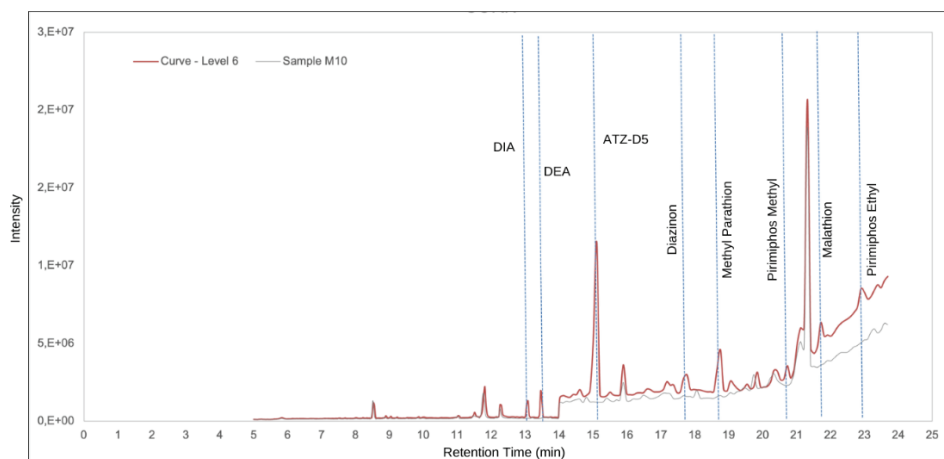


Fig. S-5. Total ion chromatogram (TIC) of pesticides obtained for a corn sample (M10), and a calibration curve for Level 6 ($52.50 \mu\text{g kg}^{-1}$).

Application of the proposed method to real samples (Cont.)

TABLE S-1. Results obtained using the linear equation derived from the modified QuEChERS/GC-MS method with sediment samples collected in the state of Paraná, Brazil.

Samples	SEDIMENTS				
	DIA	DEA	Diazinon	Malation	Pirimiphos Ethyl
P1	ND	ND	ND	ND	ND
P2	ND	ND	ND	ND	ND
P3	ND	ND	ND	ND	ND
P4	ND	ND	ND	ND	ND
P5	ND	ND	ND	ND	ND

ND: Not Detectable, below the LOD.

TABLE S-2. Results obtained using the linear equation derived from the modified QuEChERS/GC-MS method with corn samples collected in the state of Paraná, Brazil.

Samples	CORN				
	DIA	DEA	Diazinon	Methyl Parathion	Pirimiphos Methyl
M1	ND	ND	ND	ND	ND
M2	ND	ND	ND	ND	ND
M3	ND	ND	ND	ND	ND
M4	ND	ND	ND	ND	ND
M5	ND	ND	ND	ND	ND
M6	ND	ND	ND	ND	ND
M7	ND	ND	ND	ND	ND
M8	ND	ND	ND	ND	ND
M9	ND	ND	ND	ND	ND
M10	ND	ND	ND	ND	ND

ND: Not Detectable, below the LOD.

REFERENCES

1. Brazilian National Institute of Metrology, Quality and Technology (INMETRO), *Guidance on Validation of Analytical Methods DOQ-CGCRE-008*, 2020 (http://www.inmetro.gov.br/credenciamento/organismos/doc_organismos.asp?torganismo=calibensaio)
2. F. A. de L. Ribeiro, M. M. C. Ferreira, S. C. Morano, L. R. da Silva, R. P. Schneider, *Quim. Nova* **31** (2008) 164 (<https://doi.org/10.1590/S0100-40422008000100029>).



J. Serb. Chem. Soc. 90 (10) 1267–1284 (2025)
JSCS–5453

University students' scientific knowledge levels regarding chemical reaction arrows and electron arrows

GÖKÇE ÖZVEREN¹, BETÜL TURAN¹, MELİKE ULUCAN¹ and CEMAL TOSUN^{2*}

¹Bartın University, Bartın, Turkey and ²Bartın University, Faculty of Education, Department of Science Education, Bartın, Turkey

(Received 23 May, revised 27 June 2024, accepted 17 July 2025)

Abstract: This study investigated undergraduate students' recognition of chemical reaction arrows and electron arrows and their understanding of their functions. The research was conducted using a comparative research design. A four-tier diagnostic test for chemical reaction arrows and electron arrows was developed. 181 university students participated in the test development phase. The difficulty and discrimination indices of the test items were calculated. The reliability coefficient of the test was found to be 0.76. The four-tier diagnostic test was then administered to 174 university students to determine whether the participants' levels of scientific knowledge of chemical reaction arrows and electron arrows differed by gender, department and grade levels. The results showed that the university students had an inadequate level of scientific knowledge about chemical reaction arrows and electron arrows. It was found that more than half of the university students were deficient in all questions. It was also found that the level of scientific knowledge of the participants did not differ according to gender, but did differ according to grade level and department. These differences were in favour of fourth year students and against electrical and electronics engineering students.

Keywords: chemical reaction arrows; diagnostic test; electron arrows; university students.

INTRODUCTION

The arrow is known as “baan” or “teer” in Sanskrit, a language belonging to the Indo–Iranian branch of the Indo–European language family.¹ This word, which means curve, is used to describe the arc.² Arrows have been used in many fields for many years and continue to be used. One of the fields in which arrows are commonly used is chemistry. Arrows are the most basic and widely used symbols in chemistry. Arrows are among the symbols used in the early days of alchemy and

*Corresponding author. E-mail: E-mail: ctosun@bartin.edu.tr
<https://doi.org/10.2298/JSC240523053O>

chemistry. Arrows were used to represent processes such as purification, layering, and some substances. These arrows were removed from chemistry texts with the introduction of atomic symbols by Berzelius in 1814. Arrows regained their place in chemistry with the use of arrows to represent chemical reactions. Chemical reactions and equations are represented by arrows. Arrows are also used to show the movement of electrons. The use of arrows makes it possible to avoid countless sequences of words and sentences.

Lakshminarayanan classified the arrows used in chemistry as reaction arrows and electron arrows.¹ Chemical reaction arrows are used to describe the state or progress of the reaction, while electron arrows are used to show the movement of electrons. Chemical reaction arrows are chemical reaction arrow (right arrow, left arrow), balance arrows (dynamic balance arrows, balance arrows in favour of reactants/products), the upward arrow, the downward arrow, the retrosynthetic arrow, clockwise and anti-clockwise arrows, the reflux arrow, the wavy arrow, the rearrangement arrow, the dashed arrow, the broken arrow and the crossed arrow. Electron arrows are the curved or curled arrow, the fishhook arrow, the resonance arrow, the mid-hook arrow, the dipole moment arrow and electrons occupying an orbital.

Historical development of arrow symbols

The first chemical equation (primitive reaction diagram) was drawn by Jean Beguin in 1615.¹ Lavoisier was the first to propose a type of chemical equation, linking reactants and products with an equal sign, in describing the fermentation of sugar.^{3,4}

A chemical reaction arrow is a straight arrow showing the direction of chemical change. The most common arrow used in chemical reaction formulae is the right arrow. This arrow is shown with a straight line and a double hook at the right end of the line. The direction of the hook indicates the direction of the reaction. It indicates that the reactants are changing into products. If the direction of the arrow is reversed, it means that the products are changing into reactants.

Equilibrium arrows were first introduced by J.H. van't Hoff in 1884 in his book *Etude de Dynamique Chimique*.⁵ These arrows are used to show the reversible reaction. H. Marshall revised these arrows in 1902 and used half-hooked arrows showing opposite directions, which are widely used today.⁶ Half-hooked opposite double arrows are used to represent dynamic equilibrium. In equilibrium arrows in favour of the reactants, the arrow towards the products is shorter and there are more reactants than products at equilibrium. For equilibrium arrows in favour of products, the arrow towards the reactants is shorter and there are more products than reactants at equilibrium.

Curved arrows are the most important and widely used electron arrows. These arrows were introduced by Sir Robert Robinson in 1922.¹ This arrow is used to

write the reaction mechanism by showing the movement of the electron. Single-hook fishhook arrows are used to show the movement of a single electron.⁷ The resonance arrow is a double-hooked straight arrow that shows the similarity of two equivalent structures of the same molecule. Although the concept of resonance was first used by Linus Pauling in 1928, Fritz Arndt was the first to mention the resonance arrow.¹ This arrow links two structures of the same molecule with different electron distribution patterns.

Related studies

The number of studies focusing on arrow symbols in the educational research literature was limited. Some of these studies were in the form of reviews explaining the historical development of arrow symbols.^{1,8} Studies focusing on arrow symbols in chemistry education have generally been conducted in organic and inorganic chemistry. Electron arrows were the focus of these studies. These studies generally investigated the use of curved arrows in computer-based training.⁹ In another study that focused on the curved arrows representing electron flow in the organic reaction mechanism, researchers investigated the impact of an online learning module (interactive videos and activities with feedback) on undergraduate students' learning and experience.¹⁰ The results showed that students made significant learning gains on questions that required them to draw the products of a reaction.¹⁰ The most common type of error found in the research was drawing an arrow from an atom or charge. Berg and Ghosh investigated the value of the mechanistic approach in inorganic chemistry and found that this approach led to a participatory learning model.¹¹ They also reported that the arrow-pushing method created a descriptive, fun, reasoning-based and participatory classroom environment. Another study focusing on organic mechanisms showed that new bouncing curved arrows for electrophilic addition reactions can be a powerful teaching tool.¹² Ruder *et al.* used a method to assess students' use of curved arrows in multiple choice questions. The method was found to provide a deeper conceptual understanding of organic reactions and mechanisms.¹³ Ferguson investigated how they made sense of the arrow pushing formalism.¹⁴ The research was carried out with 16 university students studying chemistry. The barriers to their understanding in solving problems were discussed. A recent study investigated the effects of using diagrammatic arrows in an animation of salt dissolution.¹⁵

Current study and research questions

The studies described above were generally carried out by chemistry students in organic chemistry classes and fell within the scope of the curved arrow. The valuable contributions of these studies to the field of chemistry education should not be overlooked. Science students will encounter some reaction and electron arrows at every stage of their school, university or postgraduate studies. Arrow

symbols are an integral part of chemistry and contribute to its understanding. For this reason, it is important to assess students' knowledge of arrow symbols.

People often use diagrams to facilitate communication.¹⁶ Arrow symbols are often used in these diagrams and are one of the components of these diagrams. Arrow symbols have no specific meaning except in context. Arrow symbols provide information about other elements that are shown around them or that can be inferred from the context.¹⁶ Arrow symbols can have semantic roles such as labelling, indicating direction and indicating movement.¹⁶ Arrow symbols are the most powerful pictorial devices used in chemistry.¹ The semantic role of arrow symbols used to represent reactions and the movement of electrons was to indicate direction and movement. It is important for undergraduate science students to know the name and function of these arrow symbols, which are used to determine the direction of reactions and the movement of electrons. Recognising reaction arrows and knowing their functions provides information about the direction of the reaction. Recognising electron arrows and knowing their functions gives information about the movement of electron. It contributes to the understanding of chemical reactions and reaction mechanisms by providing information about other elements that are shown around them or can be inferred from context.

Chemistry, one of the branches of science, is difficult for many students of different ages to learn, because it contains abstract concepts.¹⁷ Chemistry is a branch of science that explains how macroscopic events occur at the particle level, using numbers and symbols.^{18,19} As can be seen from the definition, chemistry includes macroscopic, microscopic and symbolic representations.²⁰ According to Johnstone, one of the reasons why chemistry is difficult for students is that it requires multidimensional thinking.²¹ Understanding complex chemical processes requires making connections between the symbolic, microscopic and macroscopic levels.^{22,23} This connection contributes to more permanent learning of chemistry topics and understanding of chemical principles.²⁴ The present study revealed the levels of scientific knowledge, misconceptions, positive/negative errors, lack of confidence and lack of knowledge regarding reaction arrows and electron arrows of undergraduate science students. In this respect, it is believed that the research will make a significant contribution to the relevant literature.

In order to understand a drawing containing arrow symbols, the reader must infer the semantic role of each arrow symbol. It may be easy for adults with sufficient experience in drawing communication to make such comments.¹⁶ However, interpreting arrow symbols used in chemistry remains a problem for undergraduate science students. In addition, failure to learn basic principles in general chemistry makes it difficult to transfer this knowledge to courses such as organic chemistry.¹⁴ Undergraduate science students will struggle with problems related to the correct use of curved or reaction mechanisms. In the current research, it is important to identify the level of scientific knowledge of undergraduate students and their lack

of knowledge of arrow symbols. Chemical reactions and electrons are the fundamental topics of chemistry. In addition, understanding these topics ensures the understanding of other chemistry topics. Chemical reaction arrows and electron arrows are used in many topics in university chemistry. It is important for university students to recognise chemical reaction arrows and electron arrows and to understand their functions when learning chemistry topics. A chemical reaction has reactants and products. Chemical reactions are written in formulae. Chemical reaction arrows are used in formulae. The most common arrows used in chemical reactions are: right arrow, left arrow, balance arrow, dynamic balance arrow, balance arrow in favour of reactants/products, dashed arrow, crossed arrow and broken arrow. Electron arrows show the movement of electrons. The most commonly used electron arrows are: single-ended curved arrow (fishhook arrow), double-ended curved arrow (curved, curly) and resonance arrow. The aim of this research is to compare the level of scientific knowledge of university students about chemical reaction arrows and electron arrows. In this context, the research questions are presented below:

- 1) What was the validity and reliability evidence of the four-tier diagnostic test developed to determine university students' level of recognition of chemical reaction arrows and electron arrows and understanding of their functions?
- 2) What were the levels of scientific knowledge, misconceptions, positive/negative errors, lack of confidence and lack of knowledge of undergraduate science students about reactions and electron arrows?
- 3) Was there a difference between university students' levels of scientific knowledge regarding chemical reaction arrows and electron arrows according to gender?
- 4) Was there a difference between university students' levels of scientific knowledge regarding chemical reaction arrows and electron arrows according to department?
- 5) Was there a difference between university students' levels of scientific knowledge regarding chemical reaction arrows and electron arrows according to grade level?

EXPERIMENTAL

Research design

A quantitative research method was used in the study. A comparative research design, one of the non-experimental quantitative research designs, was used in the research. It is preferred as the best option when experimental models cannot be used.²⁵ This design is a step forward from survey research. This design was preferred in the research to find out whether there were statistically significant differences between university students' levels of scientific knowledge of chemical reaction arrows and electron arrows according to gender, department and grade level. In a comparative design, the researcher conducts research in the natural environment. Cause-effect relationships are not sought in the results of such studies.

Sample

The research was carried out with university students. 181 students participated in test development phase. The test was then administered to another group of 174 students. Convenience sampling, a non-random sampling techniques, was used in the research. The participants were favoured due to their proximity to the researchers. Due to time and labour constraints, the sample was selected from easily accessible and convenient locations.²⁶ The participants were second, third and fourth year students who taken chemistry courses during their undergraduate education. They were studying in the departments of science teachers, molecular biology and genetics, mechanical engineering, civil engineering, electrical and electronics engineering and biotechnology. Mechanical, civil and electronics engineering students took four or five hours of chemistry per week (one or two hours were laboratory or practical) in the first semester of their undergraduate education. Pre-service science teachers took four hours of chemistry per week (two hours were practical) in the first, second and third semesters of their undergraduate education. Biotechnology students took three or five hours of chemistry per week (two hours were practical) during the first six semesters of their undergraduate education. Molecular biology and genetics students took three or five or six hours of chemistry per week (two or three hours were practical) during the first six semesters of their undergraduate education. While students from the Faculty of Engineering were taught only general chemistry, students from the Faculty of Education (pre-service science teachers) were taught general, organic and analytical chemistry. The science faculty students (biotechnology and molecular biology and genetics) were taught general chemistry, organic chemistry and biochemistry. Participants were placed in their undergraduate programmes based on numerical scores. In order to be admitted to these departments in education and engineering faculties in Turkey, it was necessary to be in the top three hundred thousand in terms of numerical score in the university entrance exams. In the pilot study, the majority of participants (82.8 %) were studying at a state university (A university) in the Western Black Sea region. In addition, a small number of students studying at different universities in Turkey also participated in the pilot study (as online). This provided the missing sample for the validity and reliability stages of the test. For the main study, all participants studied at another state university (B university) in the Western Black Sea region. Participation in the research was completely voluntary. Ethics Committee approval was obtained and all ethical standards were followed during the research. The sample group is detailed in Table I.

Data collection tools

In recent years, two-, three- and four-tier diagnostic tests have emerged. The first tier of two-tier tests is content and the second tier is reasoning. Two-tier tests could not distinguish whether the student had a lack of knowledge or a misconception.²⁸ A confidence tier was added to the two-tier tests to create three-tier diagnostic tests. In three-tier tests, it is not known whether the student is confident about the content in the first tier, the reason in the second tier, or both answers. Therefore, a four-tier diagnostic test was developed and used in this study. We developed and used the Chemical Reaction Arrows and Electron Arrows diagnostic test as a data collection tool. The diagnostic test was constructed by the researchers and its validity and reliability were tested. The test included nine (9) chemical reaction arrows and three (3) electron arrows, which are commonly used in chemical reactions and the movement of electrons. This test was designed in four tiers and the questions were open-ended.

The first tier of this test was the content stage and it was the stage where the participants' knowledge was described. In this stage, the participants were presented with pictures of the arrows and it was determined whether they correctly named the chemical reaction arrows and

electron arrows. The third tier was the reasoning stage and included the reason for the answer given in the first tier. This stage determined the participants' level of understanding of the functions of the chemical reactions arrows and electron arrows. In the second and fourth tiers, participants were asked whether they were confident of their answers in the content and reason tiers respectively.²⁷ The diagnostic tests for chemical reaction arrows and electron arrows are presented in Appendix-1 of the Supplementary material to this paper.

TABLE I. The sample of the research

Sample		Pilot study (test development)		Main study	
		Frequency	%	Frequency	%
Gender	Female	125	69.0	75	43.1
	Male	56	31.0	99	56.9
	Total	181	100	174	100
Grade level	Sophomore	81	44.7	74	42.5
	Third grade student	48	26.5	65	37.4
	Fourth grade student	50	27.6	35	20.1
	Unspecified	2	1.2	—	—
	Total	181	100	174	100
Department	Science teacher	59	32.6	56	32.2
	Molecular biology and genetics	57	31.5	—	—
	Mechanical engineering	23	12.7	41	23.5
	Civil engineering	4	2.2	29	16.7
	Electrical-electronics engineering	2	1.1	48	27.6
	Biotechnology	29	16.0	—	—
	Other	7	3.9	—	—
	Total	181	100	174	100
University	A university	150	82.8	—	—
	B university	16	8.9	174	100
	Other	15	8.3	—	—
	Total	181	100	—	100

Data analysis

The first and third tier of the test contained short-answer and open-ended questions. The criteria used to analyse the two-tiers of open-ended questions were used to score the test.²⁹ Correct reasoning (third tier) was worth 2 points and correct content (a first tier) was worth 1 point. Confidence tiers were not included in the scoring and were used to determine the level of scientific knowledge of the participants. We conducted validity and reliability analyses of the test using data from the pilot study. For this purpose, the difficulty and discrimination indices of each test question were calculated. The reliability coefficient of the test was calculated using the KR-20 formula. These calculations followed the item analysis steps applied to short-answer and open-ended questions.³⁰ Pilot study data were analysed using Excel.

SPSS 22 was used for the analysis of the main study. Normality of data was checked for each group. First, the mode, median and arithmetic mean of the groups were examined and it was found that the values were not close to each other. The kurtosis and skewness values for each group were not in the range of -1 and $+1$. As the number of participants was more than 50, the results of the Kolmogorov-Smirnov test were examined and it was found that the p -values

were less than 0.05. The histogram graphs of the data were not in the form of a symmetrical curve. Therefore, non-parametric tests were performed on the main study data. The Mann-Whitney U test was used to compare the means of two groups, and the Kruskal-Wallis test was used to compare the means of more than two groups.

In this study it was determined whether the students had scientific knowledge, misconceptions, positive errors, negative errors, lack of confidence and lack of knowledge. For this purpose, decisions were made about the questions from the participants' responses to the four-tier diagnostic test according to the criteria in Table II.^{31,32} The second and fourth tiers of the four-tier tests were the confidence tier. The confidence level of three or four-tier diagnostic tests should be constructed using *Likert*-type³³ or binary logic.³⁴ Students must be confident in their answers in order to avoid misconceptions.³⁵ The binary confidence tier was preferred in the current research. If the student answered the first and third tiers correctly and was confident in his/her answer for the second and fourth tiers, it meant that the student had scientific knowledge. If the student answered the first and third tiers incorrectly and was confident about the second and fourth tiers, the student had a misconception. If the student was confident in his/her answers and answered the first tier of the test correctly but the reason was wrong, he/she had a positive false. If the student was confident in his/her answers and answered the third tier of the test correctly but the first tier was wrong, he/she had a negative false. If the student's answers are correct but he/she is not confident about at least one tier of his/her answer, there is a lack of confidence. If a student is unconfident in at least one tier of their answers and at least one tier of their answer is incorrect, there is a lack of knowledge.

TABLE II. Comparison of decisions for all possibilities in the four-tier test

Arrow name	The state of being confident	Function	The state of being confident	Decision of the question
True	Confident	True	Confident	Scientific knowledge
True	Confident	False	Confident	M-Positive false
False	Confident	True	Confident	M-Negative false
False	Confident	False	Confident	Misconception
True	Confident	True	Not Confident	Lack of confident
True	Not confident	True	Confident	Lack of confident
True	Not confident	True	Not confident	Lack of confident
True	Confident	False	Not Confident	Lack of knowledge
True	Not confident	False	Confident	Lack of knowledge
True	Not confident	False	Not confident	Lack of knowledge
False	Confident	True	Not Confident	Lack of knowledge
False	Not confident	True	Confident	Lack of knowledge
False	Not confident	True	Not confident	Lack of knowledge
False	Confident	False	Not Confident	Lack of knowledge
False	Not confident	False	Confident	Lack of knowledge
False	Not confident	False	Not confident	Lack of knowledge

RESULTS

Findings for the first research question

The difficulty and discrimination indices of the test items were calculated from the test scores of 181 university students. There were 50 participants in each

of the lower and upper groups. The difficulty and discrimination indices of each question are shown in Table III. The difficulty indices of the 12 questions ranged from 0.18 to 0.40. The discrimination indices were between 0.36 and 0.67. The average difficulty index of the test was 0.28 and the average discrimination index was 0.52. According to these results it can be said that the developed diagnostic test is a difficult test for university students. The reliability coefficient of the test was determined to be 0.76 using the KR-20 formula.

TABLE III. Item analysis

Question	Difficulty index	Discrimination index
1	0.32	0.51
2	0.26	0.45
3	0.40	0.61
4	0.36	0.64
5	0.18	0.37
6	0.18	0.36
7	0.25	0.49
8	0.35	0.67
9	0.31	0.61
10	0.32	0.63
11	0.24	0.48
12	0.20	0.41
Mean	0.28	0.52

Descriptive findings

After ensuring the validity and reliability, the diagnostic test was administered to 174 participants. There were 12 questions in the test and each question had a maximum of three points and a total of 36 points could be obtained from the test. It was found that the minimum score obtained from the test was 0 and the maximum score was 27. The average score of the test was 6.72 (see Table IV). It was found that the easiest question of the test was the second question (mean = 1.20) and the most difficult question was the seventh question (mean = 0.10). It was found that the average score obtained from the first two questions of the test was above one, while the average score obtained from the other questions was below one.

TABLE IV. Descriptive findings; *SD* = standard deviation

Question	Mean	<i>SD</i>
1	1.18	1.04
2	1.20	1.04
3	0.91	1.12
4	0.95	1.30
5	0.14	0.41
6	0.14	0.41
7	0.10	0.47

TABLE IV. Continued

Question	Mean	SD
8	0.29	0.72
9	0.27	0.67
10	0.46	0.75
11	0.18	0.69
12	0.83	1.07
Total	6.72	5.60

Findings for the second research question

Participants' understanding of chemical reaction arrows and electron arrows was grouped and presented in Table V. The percentage of participants with scientific knowledge ranged from 0.5 to 17.2 %. Lack of confidence was highest in the third (8.0 %) and fourth (8.6 %) questions. The rate of students with misconceptions was less than 10 % in all questions. Students had the most positive false (17.8 %) in the first question and the most negative false (9.1 %) in the twelfth question. More than half of the university students had lack of knowledge in all questions.

TABLE V. Grouping participants' understanding of chemical reactions and electron arrows; SK = scientific knowledge; LC = lack of confident; M = misconception; PF = positive false; NF = negative false; LK = lack of knowledge; *f* = frequency

Question	SK		LC		M		PF		NF		LK	
	<i>f</i>	%	<i>f</i>	%	<i>f</i>	%	<i>f</i>	%	<i>f</i>	%	<i>f</i>	%
1	30	17.2	5	2.8	10	5.7	31	17.8	3	1.7	95	54.5
2	30	17.2	5	2.8	8	4.5	30	17.2	4	2.2	97	55.7
3	18	10.3	14	8.0	16	9.1	12	6.8	3	1.7	111	63.7
4	30	17.2	15	8.6	12	6.8	3	1.7	2	1.1	112	64.3
5	1	0.5	0	0	4	2.2	4	2.2	0	0	165	94.8
6	1	0.5	0	0	5	2.8	3	1.7	0	0	165	94.8
7	3	1.7	0	0	12	6.8	0	0	1	0.5	158	90.8
8	7	4.0	1	0.5	7	4.0	1	0.5	1	0.5	157	90.2
9	6	3.4	0	0	7	4.0	1	0.5	2	1.1	158	90.8
10	5	2.8	4	2.2	2	1.1	4	2.2	0	0	159	91.3
11	6	3.4	2	1.1	5	2.8	0	0	0	0	161	92.5
12	9	5.1	3	1.7	4	2.2	0	0	16	9.1	142	81.6

The third, fourth and fifth research questions investigated whether there was a statistical difference between the levels of scientific knowledge of the participants according to gender, department and grade level. Prior to the analyses, it was examined whether the data met the assumption of normal distribution for all variables (see Table VI). It was found that the kurtosis and skewness values for all variables were not within the range of -1 and $+1$. Kurtosis and skewness values between -1 and $+1$ are considered indicators of normal distribution.³⁶ In addition,

the results of the Kolmogorov-Smirnov test were examined and it was found that the p -values were less than 0.05. As the data were not normally distributed, differences between two groups were analysed using the Mann Whitney U test, and differences between more than two groups were analysed using the Kruskal-Wallis test.

TABLE VI. Normal distribution of data according to variables

Sample		N	Mean	Median	SD	Kurtosis	Skewness
Gender	Female	75	7.29	6.00	5.54	1.401	1.019
	Male	99	6.29	5.00	5.64	0.256	0.998
Grade level	Second	74	5.31	5.00	4.30	-0.093	0.715
	Third	65	7.61	5.00	6.38	-0.405	0.783
	Fourth	35	8.05	8.00	5.98	1.540	1.007
Department	Science teacher	56	8.28	8.00	4.92	2.739	1.204
	Mechanical engineering	41	6.58	5.00	4.75	-0.504	0.702
	Civil engineering	29	8.65	8.00	7.32	-0.944	0.507
	Electrical-electronics engineering	48	3.85	3.00	4.74	3.750	1.905

Findings for the third research question

The third research question was: Is there a difference between university students' level of scientific knowledge regarding chemical reaction arrows and electron arrows according to gender? The Mann Whitney U test was used to determine whether there was a statistically significant difference between the groups according to gender (see Table VII). According to the analysis results, it was found that there was no statistically significant difference between male and female participants' levels of scientific knowledge regarding chemical reaction arrows and electron arrows.

Table VII. Comparison of test scores by gender

Group	N	Mean ranks	Sum of ranks	U	p
Female	75	94.29	7072.00	3203.000	0.120
Male	99	82.35	8153.00		

Findings for the fourth research question

Another research question was: Is there a difference between university students' levels of scientific knowledge regarding chemical reaction arrows and electron arrows according to department? The data were analysed using the Kruskal Wallis test (see Table VIII) and according to the results of the analysis, there were significant differences between the groups according to departments. These differences were between science teachers and electrical and electronics engineering students ($U = 550.500$; $p < 0.05$). In addition, significant differences were found between mechanical engineering ($U = 602.500$; $p < 0.05$), civic engineering ($U =$

= 424.000 $p < 0.05$) and electrical and electronics engineering students. These differences were against electrical and electronics engineering students.

Table VIII. Comparison of test results by undergraduate program

Department	<i>N</i>	Mean ranks	<i>df</i>	χ^2	<i>p</i>
Science teacher	56	106.88	3	26.996	0.000
Mechanical engineering	41	88.73			
Civil engineering	29	98.24			
Electrical-electronics engineering	48	57.35			

Findings for the fifth research question

Another question of the research was: Is there a difference between university students' level of scientific knowledge regarding chemical reaction arrows and electron arrows according to grade level? The data were analysed using the Kruskal-Wallis test (see Table IX) and according to the results of the analysis, there were significant differences between the groups according to grade levels. These differences were between the second and fourth grades ($U = 942.000$; $p < 0.05$) and in favour of the fourth grade.

Table IX. Comparison of test results by grade level

Grade level	<i>N</i>	Mean ranks	<i>df</i>	χ^2	<i>p</i>
Second	74	77.04	2	6.000	0.050
Third	65	92.88			
Fourth	35	99.63			

DISCUSSION AND CONCLUSION

A four-tier diagnostic test was developed to determine the level of scientific knowledge of university students regarding chemical reaction arrows and electron arrows. Item analysis was used to calculate the difficulty and discrimination indices of the test items. The average difficulty index of the test was 0.28, and the average discrimination index was 0.52. In addition, the reliability coefficient of the test was found to be 0.76 using the KR-20 formula. Item difficulty scores must be between 0 and 1. If the score is below 0.30, it is a difficult item; if it is between 0.30 and 0.70, it is an item of medium difficulty; and if it is above 0.70, it is an item of easy difficulty.³⁷ The average difficulty of the test is expected to be 0.50. If the item discrimination value is 0.19 and below, the item should be removed from the test, items in the range 0.20–0.29 should be corrected, items in the range 0.30–0.39 are good items, and items 0.40 and above are very good items.³⁷ Based on these results, it can be said that the diagnostic test is difficult and distinctive for university students. In addition, if the reliability coefficient is greater than 0.70, the test is reliable.³⁸ When these results were evaluated together, a diagnostic test was developed that ensured reliability and validity. In addition, for most of the

questions, the percentage of participants with positive and negative false was less than 10 %. Researchers recommend that the percentage of positive and negative false in a test should be less than 10 %.³⁹ The lower this percentage, the higher the validity of the test. The first task of the research was to develop a four-tier diagnostic test, tested for validity and reliability, for researchers wishing to determine the level of scientific knowledge of university students in relation to chemical reaction arrows and electron arrows. There have been studies in the literature to develop a four-tier diagnostic test.^{40–42} Researchers developed a four-tier diagnostic test to assess upper secondary school students' understanding of isomers.⁴⁰ Researchers reported that the Cronbach alpha coefficient of the test was greater than 0.70 for each tier and dimension. In another study, researchers developed a four-tier diagnostic test to identify high school students' misconceptions about alcohols and carbonyl compounds.⁴¹ The researcher calculated the McDonald's ω value of the test to be 0.85 for the response tier, 0.83 for the reason tier, and 0.86 for both tiers. In another study, a four-tier diagnostic test was developed to assess university students' understanding of transition metal chemistry, a topic in inorganic chemistry.⁴² The researchers reported that the diagnostic test was difficult for students to complete and the Cronbach alpha reliability coefficient of the test was 0.60. Similar to the current research findings, the above studies also reported modest reliability values for their four-tier tests. Diagnostic tests can be used both to identify misconceptions and to determine students' levels of scientific knowledge. Studies on misconceptions have generally considered misconceptions detected at 10 % or more.^{28,34} The percentage of students with misconceptions was below 10 % for all questions. For this reason, the test developed in this study was used to determine the level of students' scientific knowledge about chemical reaction arrows and electron arrows.

Another result of the research was that university students were deficient in recognizing chemical reaction arrows and electron arrows and in understanding their functions. The percentage of those who had scientific knowledge about chemical reaction arrows and electron arrows was between 0.5 and 17.2 %. In addition, more than half of the university students lacked knowledge on all questions. It was found that the participants' level of scientific knowledge about chemical reaction arrows was higher than their level of scientific knowledge about electron arrows. The percentage of those with a lack of knowledge in the questions about right arrows, left arrows, balance arrows and dynamic balance arrows was between 54.5 and 64.3 %. This rate was over 90 % for the questions on electron arrows. The researcher states that the use of curved arrows in organic chemistry is an excellent way of showing the flow of electrons as products are formed from reactants.⁹ In his study, he noted that some students had difficulty using curved arrows correctly and attributed this to the fact that the basis of curved arrows was explained in few textbooks. A possible reason for the higher level of scientific knowledge about

chemical reaction arrows than electron arrows among the participants in the current study may be that chemical reaction arrows are mentioned in more topics in chemistry courses. On the other hand, lack of confidence was greatest in the third (8.0 %) and fourth (8.6 %) questions. Although students answered the first and third tiers of these questions correctly, they were not confident of their answers. The third question was about the balance arrow and the fourth question was about the dynamic balance arrow. It was found that students were not confident in their answers to the arrows used to represent reversible reactions and chemical reactions at equilibrium. The reason why students are not confident in their answers may be that the balance arrows used to represent reversible reactions are now represented with half-hooked opposite double arrows to represent dynamic equilibrium.

In the research, it was found that university students' level of scientific knowledge about right arrow (it shows that the reactants are transformed into product), left arrow (it shows that products are transformed into reactants), balance arrow (it shows a reversible reaction) and dynamic balance arrow (it shows a chemical reaction in equilibrium) was higher than other chemical reaction arrows (balance arrows in favor of reactants/products, dashed arrow, broken arrow and crossed arrow) and electron arrows (resonance arrow, single-ended curved arrow, double-ended curved arrow). It was observed that the level of scientific knowledge of university students about resonance arrows (it shows the resonance relationship between two molecules) and balance arrows in favor of reactants/products (it shows the strong preference in the equilibrium reaction) was quite low (it was between 0.10 and 0.14 points out of 3 points). The percentage of those with no knowledge in the questions about resonance arrows and balance arrows in favor of reactants/products was over 90 %. The percentage of those with scientific knowledge was between 0.5 and 1.7 %. On the other hand, the level of scientific knowledge of the university students was below one out of three for the single-ended curved arrow (it shows the path of a single electron), the double-ended curved arrow (it shows the path of a pair of electrons), the dashed arrow (it shows that a chemical reaction is taking place but the conditions are unknown), the broken arrow (it shows reactions that have been tried but do not work) and the crossed arrow (it shows a reaction that cannot take place). The percentage of those with lack of knowledge on those questions was over 80 %. The percentage of those with scientific knowledge was between 2.8 and 5.1 %. Alchemists included arrows into their symbols hundreds of years before modern chemists included arrows in chemical equations.⁸ Different types of arrows have different roles in chemistry. The complexity of the environment in which chemicals, glassware and other laboratory equipment are displayed in the virtual chemistry laboratory creates a cognitive load. For this reason, researchers conducted an experimental exercise in a virtual chemistry laboratory supported by arrow texts and found that the exercise improved students'

performance in terms of time and errors.⁴³ Studies of the use of arrows in chemistry have tended to be in the area of organic chemistry. As students did not develop a conceptual understanding of organic chemistry, studies in the literature generally focused on the techniques of using, meaning and usefulness of the curved arrow in organic chemistry.¹² Researchers focused on how students made sense of the arrow and the common barriers to understanding.^{14,44} The literature included module development studies that guided students to learn and apply the electron repulsion approach.¹⁰ Another study found that using the arrow pushing approach in inorganic chemistry significantly increased the sense of participation in the lesson.¹¹ In another study, researchers described a new assessment technique that allows lecturers to ask open-ended questions about curved arrow representation in a multiple-choice format.¹³ The above studies were generally conducted in the context of organic and inorganic chemistry courses and generally focused on curved arrows.

Finally, it was found that there was no statistically significant difference between participants' level of scientific knowledge about chemical reaction arrows and electron arrows according to gender. The effect of using labels and arrows in salt dissolution animation has been investigated in the literature.¹⁵ The study reported that students with high spatial ability performed better than students with low spatial ability. It was also found that females outperformed males in the post-test. It was found that students in the animation group, where only arrows were used, scored lower than the other groups. The current study revealed differences in the scores of the chemical reaction arrows and the electron arrow diagnostic test between groups by department and grade level. These differences were in favor of fourth year students and against electrical and electronics engineering students. According to the researchers, advanced courses in chemistry education strengthened students' conceptual understanding. These courses introduced and used different arrow symbols to deepen understanding of chemical processes.⁴⁵ While students from the Faculty of Education (science teacher) took courses in analytical chemistry and organic chemistry in addition to general chemistry, students from the Faculty of Engineering only took courses in general chemistry. This situation showed that the educational process and advanced courses played an important role in increasing the scientific knowledge level of university students regarding chemical reaction arrows and electron arrows.

RECOMMENDATIONS AND LIMITATIONS

We developed a test to determine the scientific knowledge level of university students regarding chemical reaction arrows and electron arrows. This test was designed to determine whether there were differences in university students' scientific knowledge of chemical reaction arrows and electron arrows according to gender, department and grade level. Data were collected from students studying in

four different undergraduate programs. It is recommended that future studies include students from other undergraduate programs taking chemistry courses. In addition, most of the research data was collected from students studying at two different universities. This situation is considered a limitation of the study. Students studying at different universities could be included in future studies.

Diagnostic tests can be used to reveal both misconceptions and students' level of scientific knowledge. The percentage of students with misconceptions was below 10 % for all questions in this study. Therefore, the test developed in this study was used to determine the level of students' scientific knowledge about chemical reaction arrows and electron arrows. Future studies could investigate students' misconceptions about chemical reaction arrows and electron arrows.

This study revealed university students' level of scientific knowledge about chemical reaction arrows and electron arrows. Future studies could investigate whether university students' use chemical reaction arrows and electron arrows correctly in concrete examples.

The study developed a four-tier diagnostic test. The second and fourth tier of this test were the confident tier. The confidence level had two options: confident and not confident. Future studies may prefer five-point Likert-type scales for confident tiers.

SUPPLEMENTARY MATERIAL

Additional data and information are available electronically at the pages of journal website: <https://www.shd-pub.org.rs/index.php/JSCS/article/view/12942>, or from the corresponding author on request.

Acknowledgement. The authors would like to thank TUBITAK (The Scientific and Technological Research Council of Turkey) for financial support (Project Number: 1919B012214484).

Ethics approval. Data was collected from human participants in the study. All ethical standards were taken into account and followed during the research. Ethical approval was obtained.

ИЗВОД

НИВОИ НАУЧНОГ ЗНАЊА УНИВЕРЗИТЕТСКИХ СТУДЕНАТА О СИМБОЛИЦИ СТРЕЛИЦА У ЈЕДНАЧИНАМА ХЕМИЈСКИХ РЕАКЦИЈА И О КРЕТАЊУ ЕЛЕКТРОНА

GÖKÇE ÖZVEREN¹, BETÜL TURAN¹, MELİKE ULUCAN¹ и CEMAL TOSUN²

Bartın University, Bartın, Turkey и ²Bartın University, Faculty of Education, Department of Science Education, Bartın, Turkey

Ово истраживање је имало за циљ да испита у којој мери студенти основних академских студија препознају и разумеју значење и функцију стрелица у једначинама хемијских реакција и о кретању електрона. Истраживање је спроведено применом компаративног истраживачког дизајна. Развијен је четворостепени дијагностички тест намењен процени знања о наведеним типовима стрелица. У фази развоја инструмента учествовао је 181 студент, а на основу добијених резултата израчунати су индекси тежине и дискриминативности

задатака. Коефицијент поузданости теста износио је 0,76. Након тога, тест је примењен на узорку од 174 студента с циљем утврђивања разлика у нивоу научног знања у зависности од пола, студијског програма и године студија. Резултати су указали на недовољан ниво научног знања студената о значењу и функцији стрелица у једначинама хемијских реакција и о кретању електрона. Више од половине испитаника показало је недовољно разумевање у свим питањима теста. Утврђено је да не постоје статистички значајне разлике у нивоу знања у односу на пол, док су уочене значајне разлике у односу на студијски програм и годину студија. Ове разлике су биле у корист студената четврте године, док су студенти електро-технике и рачунарства остварили слабије резултате.

(Примљено 23. маја, ревидирано 27. јуна 2024, прихваћено 17. јула 2025)

REFERENCES

1. A. Lakshminarayanan, *Resonance* **15** (2010) 51 (<https://doi.org/10.1007/s12045-010-0006-8>)
2. E. R. Lujan-Martinez, *J. Ind. Celtic Stud.* **6** (2006) 715 (<https://dc.uwm.edu/ekeltoi/vol6/iss1/16>)
3. H. M. Leicester, *Panorama historico de la quamica*, Alhambra, Madrid, 1967
4. A. Lavoisier, *Traite elementaire de Chimie*, Cuchet, Paris, **1** (1789)
5. Nobel Lectures, Chemistry, 1901–1921, Elsevier Publishing Company, Amsterdam, 1966
6. H. Marshall, *Proc. Roy. Soc. Edin.* **24** (1902) 85 (<https://doi.org/10.1017/S0370164600007720>)
7. G. Bhattacharyya, G. Bodner, *J. Chem. Educ.* **82** (2005) 1402 (<https://doi.org/10.1021/ed082p1402>)
8. S. Alvarez, *Angew. Chem. Int. Ed.* **51** (2012) 590 (<https://doi.org/10.1002/anie.201101767>)
9. W. N. Turek, *J. Chem. Educ.* **69** (1992) 45 (<https://doi.org/10.1021/ed069p45>)
10. M. S. Carle, R. Visser, A. B. Flynn, *Chem. Educ. Res. Pract.* **21** (2020) 582 (<https://doi.org/10.1039/C9RP00274J>)
11. S. Berg, A. Ghosh, *J. Chem. Educ.* **88** (2011) 1663 (<https://doi.org/10.1021/ed200166z>)
12. A. R. Straumanis, S. M. Ruder, *J. Chem. Educ.* **86** (2009) 1389 (<https://doi.org/10.1021/ed086p1389>)
13. S. M. Ruder, A. R. Straumanis, *J. Chem. Educ.* **86** (2009) 1392 (<https://doi.org/10.1021/ed086p1392>)
14. R. Ferguson, G.M. Bodner, *Chem. Educ. Res. Pract.* **9** (2008) 102 (<https://doi.org/10.1039/B806225K>)
15. D. A. Falvo, J.P. Suits, *J. Educ. Comp. Res.* **41** (2009) 83 (<https://doi.org/10.2190/EC.41.1.d>)
16. Y. Kurata, M.J. Egenhofer, *Spat. Cogn. Comp.* **8** (2008) 306 (<https://doi.org/10.1080/13875860802148843>)
17. A. Ayas, A. Demirbaş, *J. Chem. Educ.* **74** (1997) 518 (<https://doi.org/10.1021/ed074p518>)
18. J. Gilbert, D. Treagust, *Multiple Representations in Chemical Education. Models and Modelling*, 4, Springer, Amsterdam, 2009
19. K. S. Taber, *Chem. Educ. Res. Pract.* **14** (2013) 156 (<https://doi.org/10.1039/C3RP00012E>)
20. A. H. Johnstone, *J. Comp. Ass. Learn.* **7** (1991) 75 (<https://doi.org/10.1111/j.1365-2729.1991.tb00230.x>)

21. B. Demirdöğen, F. Nur-Akın, G. Demircan-Akman, *YYU J. Educ. Fac.* **18** (2021) 524 (<https://doi.org/10.33711/yyuefd.1029070>)
22. D.L. Gabel, *Handbook on science teaching and learning: A project of the National Science Teacher Association*, Macmillan, New York, 2005
23. A.H. Johnstone, *J. Chem. Educ.* **70** (1993) 701 (<https://pubs.acs.org/doi/pdf/10.1021/ed070p701>)
24. B. Ekiz-Kıran, E. S. Kutucu, A. Tarkin-Çelikkıran, M. Tüysüz, *YYU J. Educ. Fac.* **15** (2018) 1081 (<https://dergipark.org.tr/en/download/article-file/594855>)
25. N. Karasar, *Bilimsel Araştırma Yöntemi*, Ankara, Nobel, 2005
26. J. H. McMillan, S. Schumacher, *Research in Education: Evidence-Based Inquiry*, 7th ed., Pearson, Boston, MA, 2001
27. D. Kaltakçı, *Unpublished PhD Thesis*, Middle East Technical University, Ankara
28. I. Caleon, R. Subramaniam, *Int. J. Sci. Educ.* **32** (2010) 939 (<https://doi.org/10.1080/09500690902890130>)
29. F.Ö. Karataş, S. Köse, B. Coştu, *Pamukkale Üniversitesi Eğitim Fakültesi Dergisi* **1** (2003) 54 (<https://dergipark.org.tr/tr/download/article-file/114820>)
30. S. Bayrakçıken, in *Test Geliştirme*, E. Karip, Ed., Ölçme ve Değerlendirme Pegem A, Ankara, 2015, pp. 244–277
31. S.A. Kiray, S. Şimsek, *Int. J. Sci. Math. Educ.* **19** (2021) 935 (<https://doi.org/10.1007/s10763-020-10087-5>)
32. T. Taban, S.A. Kiray, *Int. J. Sci. Math. Educ.* **20** (2022) 1791 (<https://doi.org/10.1007/s10763-021-10224-8>)
33. S. Hasan, D. Bagayoko, E.L. Kelley, *Physics Educ.* **34** (1999) 294 (<https://doi.org/10.1088/0031-9120/34/5/304>)
34. E. Taslidere, *Res. Sci. Tech. Educ.* **34** (2016) 164 (<https://doi.org/10.1080/02635143.2015.1124409>)
35. A. Eryılmaz, *Eurasian J. Educ. Res.* **40** (2010) 53 (https://ejer.com.tr/wp-content/uploads/2021/01/ejer_2010_issue_40.pdf)
36. G.A. Morgan, N.L. Leech, G.W. Gloeckner, K.C. Barret, *SPSS for Introductory Statistics: Use and Interpretation (2nd ed.)*, Lawrence Erlbaum Associates, London, 2004
37. H. Tekin, *Eğitimde Ölçme ve Değerlendirme*, 20th ed., Yargı Yayınevi, Ankara, 2010
38. Ş. Büyüköztürk, *Sosyal Bilimler için Veri Analizi El Kitabı*, 28th ed., Pegem Yayınevi, Ankara, 2020
39. D. Hestenes, I. Halloun, *Interpreting The Force Concept Inventory: A Response, Department of Physics and Astronomy, Arizona State University, Tempe, AZ, 85287-1504*, 1995
40. M. Wu, P. Tian, D. Sun, D. Feng, M. Luo, *Int. J. Sci. Math. Educ.* **23** (2024) 907 (<https://doi.org/10.1007/s10763-024-10494-y>)
41. K. B. Putica, *J. Chem. Educ.* **101** (2024) 1442 (<https://doi.org/10.1021/acs.jchemed.3c01343>)
42. B. Sreenivasulu, R. Subramaniam, *Res. Sci. Educ.* **44** (2014) 801 (<https://doi.org/10.1007/s11165-014-9400-7>)
43. N. Ali, S. Ullah, D. Khan, *Educ. Inf. Tech.* **27** (2022) 7629 (<https://doi.org/10.1007/s10639-022-10936-6>)
44. A.B. Flynn, R.B. Featherstone, *Chem. Educ. Res. Pract.* **18** (2017) 64 (<https://doi.org/10.1039/C6RP00126B>)
45. G. M. Bodner, D. S. Domin, *Univ. Chem. Educ.* **4** (2000) 24 (<https://edu.rsc.org/download?ac=517097>).

SUPPLEMENTARY MATERIAL TO
**University students' scientific knowledge levels regarding
chemical reaction arrows and electron arrows**


GÖKÇE ÖZVEREN¹, BETÜL TURAN¹, MELİKE ULUCAN¹ and CEMAL TOSUN^{2*}

¹Bartın University, Bartın, Turkey and ²Bartın University, Faculty of Education, Department of
Science Education, Bartın, Turkey


J. Serb. Chem. Soc. 90 (10) (2025) 1267–1284

**APPENDIX-1: CHEMICAL REACTION AND ELECTRON ARROWS DIAGNOSTIC
TEST (NEXT PAGE)**

Table S-I. Write the names of the arrows given in the table below and explain in what
sense/function they are used in chemical reaction formulas and the movement of electrons?

	Arrow name	Are you sure?	Function	Are you sure?
1a	$R \longrightarrow P$	<input type="checkbox"/> I am sure <input type="checkbox"/> I am not sure		<input type="checkbox"/> I am sure <input type="checkbox"/> I am not sure
1b	$R \longleftarrow P$	<input type="checkbox"/> I am sure <input type="checkbox"/> I am not sure		<input type="checkbox"/> I am sure <input type="checkbox"/> I am not sure
1c	$R \rightleftharpoons P$	<input type="checkbox"/> I am sure <input type="checkbox"/> I am not sure		<input type="checkbox"/> I am sure <input type="checkbox"/> I am not sure
1d	$R \rightleftharpoons P$	<input type="checkbox"/> I am sure <input type="checkbox"/> I am not sure		<input type="checkbox"/> I am sure <input type="checkbox"/> I am not sure
1e	$R \rightleftharpoons P$	<input type="checkbox"/> I am sure <input type="checkbox"/> I am not sure		<input type="checkbox"/> I am sure <input type="checkbox"/> I am not sure
1f	$R \rightleftharpoons P$	<input type="checkbox"/> I am sure <input type="checkbox"/> I am not sure		<input type="checkbox"/> I am sure <input type="checkbox"/> I am not sure
1g	\longleftrightarrow	<input type="checkbox"/> I am sure <input type="checkbox"/> I am not sure		<input type="checkbox"/> I am sure <input type="checkbox"/> I am not sure
1h		<input type="checkbox"/> I am sure <input type="checkbox"/> I am not sure		<input type="checkbox"/> I am sure <input type="checkbox"/> I am not sure

*Corresponding author. E-mail: E-mail: ctosun@bartin.edu.tr

1i		<input type="checkbox"/> I am sure <input type="checkbox"/> I am not sure	<input type="checkbox"/> I am sure <input type="checkbox"/> I am not sure
1i	$R \cdots \cdots \rightarrow P$	<input type="checkbox"/> I am sure <input type="checkbox"/> I am not sure	<input type="checkbox"/> I am sure <input type="checkbox"/> I am not sure
1j	$R \xrightarrow{\#} P$	<input type="checkbox"/> I am sure <input type="checkbox"/> I am not sure	<input type="checkbox"/> I am sure <input type="checkbox"/> I am not sure
1k	$R \xrightarrow{\times} P$	<input type="checkbox"/> I am sure <input type="checkbox"/> I am not sure	<input type="checkbox"/> I am sure <input type="checkbox"/> I am not sure

R= Reactants; P= Products